ROYAUME DU MAROC
Université Mohammed V - RABAT -
جامعة محمد الخامس – الرباط –
Faculté des sciences
كلية العلوم
CENTRE D'ETUDES DOCTORALES - SCIENCES ET TECHNOLOGIES

N° d'ordre : **3552**

THESE

En vue de l'obtention du : ***DOCTORAT***

Centre de Recherche*: Centre de Recherche en Energie*
Structure de Recherche *: Équipe d'Énergétique et Physique des Réacteurs, Sécurité Nucléaire et Environnement (PRESN)*
Discipline *: Physique*
Spécialité *: Physique Nucléaire*

Présentée et soutenue le 29/11/2021 par :

Ouadie KABACH

Possible Scenarios for a Transition to a Thorium-Based Fuel Cycle in a Pebble-Bed High-Temperature Reactor

JURY

Hamid EZ-ZAHRAOUY	PES, Faculté des Sciences, Université Mohammed V - Rabat	Président
Abdelmajid MAGHNOUJ	PES, Faculté des Sciences, Université Sidi Mohamed Ben Abdellah - Fès	Rapporteur/ Examinateur
Abdelmajid SAIDI	PES, Faculté des Sciences, Université Mohammed V - Rabat	Rapporteur/ Examinateur
Mohammed CHERRAJ	PH, Faculté des Sciences, Université Mohammed V - Rabat	Rapporteur/ Examinateur
El Mahjoub CHAKIR	PES, Faculté des Sciences, Université Ibn Tofail - Kenitra	Examinateur
Abdelouahed CHETAINE	PES, Faculté des Sciences, Université Mohammed V - Rabat	Directeur de Thèse
Abdelfettah BENCHRIF	Docteur Ès Sciences, CNESTEN - Rabat	Co-Encadrant

Année Universitaire: 2021/2022

List of publications

This thesis is based on the work contained in the following papers:

[1] **O. Kabach**, A. Chetaine, A. Benchrif, H. Amsil, The use of burnable absorbers integrated into TRISO/QUADRISO particles as a reactivity control method in a pebble-bed HTR reactor fuelled with (Th,^{233}U)O2, Nucl. Eng. Des. 384 (2021) 111476. doi:10.1016/j.nucengdes.2021.111476.

[2] **O. Kabach**, A. Chetaine, A. Benchrif, H. Amsil, F. El Banni, A comparative analysis of the neutronic performance of thorium mixed with uranium or plutonium in a high-temperature pebble-bed reactor, Int. J. Energy Res. (2021) er.6935. doi:10.1002/er.6935.

[3] **O. Kabach**, A. Chetaine, A. Benchrif, H. Amsil, An inter-comparison between ENDF/B-VIII.0-NECP-Atlas and ENDF/B-VIII.0-NJOY results for criticality safety benchmarks and benchmarks on the reactivity temperature coefficient, Nucl. Eng. Technol. (2021) 106192. doi:10.1016/j.net.2021.02.012.

[4] **O. Kabach**, A. Chetaine, A. Benchrif, Processing of JEFF-3.3 and ENDF/B-VIII.0 and testing with critical benchmark experiments and TRIGA Mark II research reactor using MCNPX, Appl. Radiat. Isot. 150 (2019) 146–156. doi:10.1016/j.apradiso.2019.05.015.

[5] **O. Kabach**, A. Chetaine, A. Darif, A. Jalil, A. Saidi, A. Benchrif, H. Amsil, Processing of the ENDF/B-VIII.0B6 Neutron cross-section data library and testing with critical benchmarks and oktavian shielding benchmarks, in: Fourth Int. Conf. Phys. Technol. React. Appl., 2018.

[6] **O. Kabach**, A. Chetaine, A. Darif, A. Jalil, A. Saidi, A. Benchrif, H. Amsil, Processing of the ENDF/B-VIII.0β6 neutron cross-section data library and testing with critical benchmarks, oktavian shielding benchmarks and the doppler reactivity defect benchmarks, Ann. Univ. Craiova, Phys. 28 (2018) 78–98.

[7] **O. Kabach**, A. Chetaine, A. Jalil, A. Darif, A. Saidi, Processing and benchmarking of evaluated nuclear data file/b-viii.0β4 cross-section library by analysis of a series of critical experimental benchmark using the Monte Carlo code MCNP(X) and NJOY2016, Nucl. Eng. Technol. 49 (2017) 1610–1616. doi:10.1016/j.net.2017.08.017.

List of publications not included in this thesis:

[1] **O. Kabach**, A. Chetaine, A. Benchrif, Physical Protection System, Corrective Actions, and Weaknesses Identification Based on Nuclear Security Series: The Hypothetical Atomic Research Institute (HARI) Case, Int. J. Nucl. Secur. 6 (2020). doi:10.7290/ijns060104.

[2] **O. Kabach**, A. Chetaine, A. Benchrif, H. Amsil, Neutronic investigation of the thorium-based mixed-oxide as an alternative fuel in the TRIGA Mark-II research reactor – Part I: A beginning of life calculations, Ann. Nucl. Energy. 140 (2020) 107075. doi:10.1016/j.anucene.2019.107075.

[3] H. Amsil, A. Jalil, **O. Kabach**, H. Chahidi, H. Bounouira, C. Elyounoussi, A. Chetaine, Neutron beam characterization for the Moroccan TRIGA Mark II reactor, J. Radioanal. Nucl. Chem. 327 (2021) 1063–1072. doi:10.1007/s10967-021-07613-2.

[4] A. Chetaine, **O. Kabach**, T. Bouassa, A. Saidi, H. Amsil, The Physical protection systems: evaluation and assessment, in: Int. Conf. Nucl. Secur. 2020 (ICONS 2020), 2020.

[5] J. Abdelhamid, A. Hamid, C. Abdelouahed, **K. Ouadie**, S. Abdelmajid, Generation of thermal scattering cross sections for sapphire (Al2O3) and bi crystal filters used in nuclear facilities, Ann. Univ. Craiova, Phys. 29 (2019) 45–49.

[6] R. Achraf, **K. Ouadie**, C. Abdelouahed, Nuclear Security in Middle East and North Africa: Problems and Challenges, in: 5ème Ec. Fr. La Mes. l'Instrumentation Nucléaires, 2018.

[7] S. Charouq, H. Amsil, A. Chetaine, A. Benchrif, **O. Kabach**, A. Jalil, O. Lebied, Optimization of a new cuboid nuclear fuel cell concept for long life SMR, in: Fourth Int. Conf. Phys. Technol. React. Appl., 2018.

[8] A. Jalil, C. Abdelouahed, **K. Ouadie**, H. Amsil, K. Embarch, K. Laraki, H. Marah, OpenMC Monte Carlo modelling of TRIGA research reactor, in: Fourth Int. Conf. Phys. Technol. React. Appl., 2018.

[9] H. Amsil, A. Chetain, A. Benchrif, S. Charouq, O. Lebied, **O. Kabach**, A. Jalil, Optimization of a new cuboid nuclear fuel cell concept for long life SMR, in: Eur. Res. React. Conf. RRFM2018, 2018.

[10] A. Darif, A. Chetaine, M. Mghar, **O. Kabach**, Investigation of the influence of various reflector elements material types on the core nuclear parameters of the 2 MW Triga Mark-II

research reactor using the Monte Carlo code, TURKISH J. Phys. 42 (2018) 41–46. doi:10.3906/fiz-1707-1.

[11] A. Chetaine, A. Jalil, **O. Kabach**, A. Darif, A. Saidi, A. Benchrif, A. Hamid, Evaluation of the IAEA 2D PWR benchmark problem using TRIVAC and OpenMOC codes, Ann. Univ. Craiova, Phys. 28 (2018) 24–30.

[12] A. Darif, A. Chetaine, **O. Kabach**, M. Mghar, A. Saidi, Neutronic analysis of Moroccan TRIGA MARK-II research reactor using the DRAGON.V5 and TRIVAC.v5 codes, Ann. Univ. Craiova, Phys. (2017).

Acknowledgments

I must first sincerely thank my research supervisor, Mr. Abdelouahed CHETAINE, Professor at the Faculty of Sciences, University Mohammed V - Rabat, for proposing this thesis subject and for directing my scientific work. He has given me the advantage of his comprehensive experience in the field of reactor physics and has shown great availability. Without his support and assistance, the completion of this work would have been impossible.

My deepest gratitude also goes to my co-supervisor, Mr. Abdelfettah BENCHRIF, Researcher at CNESTEN - Rabat, for his patience, continuous encouragement, support, and assistance from start to finish. Also, for his contribution to the revision of this thesis.

I would also like to express my gratitude to Mr. Hamid EZ-ZAHRAOUY, Professor at the Faculty of Sciences, University Mohammed V - Rabat, for the honor he gave me by accepting chair the Jury of this thesis.

I would like to express my sincere gratitude to Mr. Abdelmajid MAGHNOUJ, Professor at the Faculty of Sciences, University Sidi Mohamed Ben Abdellah - Fès, for honoring me by consenting to revise, and judge this work.

I am extremely grateful to Mr. Abdelmajid SAIDI, Professor at Faculty of Sciences, University Mohammed V- Rabat, for honoring me by accepting to participate on the jury for this work.

Also, extend sincere gratitude to Mr. Mohammed CHERRAJ, Professor at Faculty of Sciences, University Mohammed V- Rabat, for agreeing to the assessment of this work and for his attention in the evaluation of this manuscript. I also thank him for the honor he bestowed upon me by agreeing to be a member of the jury.

I owe a deep sense of gratitude to Mr. El Mahjoub CHAKIR, Professor at Faculty of Sciences, University Ibn Tofail - Kenitra, for honoring me by accepting to participate on the jury for this work.

This thesis owes a lot to Mr. Hamid AMSIL, Researcher at CNESTEN - Rabat, who helped me with the simulation code and shared his views and vast experience with me.

I owe a debt of gratitude to my parents, who have always kept me in their prayers and surrounded me with their unconditional love and support.

At last, I would like to thank Mr. Abdelaziz DARIF, Mr. Taoufiq BOUASSA, Mr. Fadi EL BANNI, and all the PRESN researchers who helped me with their friendly attitude. A lot of them helped me to carry out this work directly, through suggestions or patient discussions. I would like to express my gratitude to the people that have influenced my studies and time at University Mohammed V.

Résumé

"les scénarios possibles pour une transition vers un cycle du combustible à base de thorium dans un réacteur à haute température à lit de boulets"

Les bibliothèques de données nucléaires fiables et la durabilité de l'énergie nucléaire, avec l'évacuation des stocks de croissance en monde tel que les déchets radioactifs et les matières nucléaires de qualité militaire en excès, sont les deux défis les plus actuels auxquels fait face la recherche en ingénierie nucléaire. Par conséquent, cette thèse est divisée en deux grandes parties : la première partie concentrée sur le traitement des bibliothèques de sections efficace en utilisant des évaluations de données nucléaires base sur les bibliothèques ENDF/B et JEFF et traitées par les systèmes de codes NJOY et NECP-Atlas. Les bibliothèques traitées ont été validées à l'aide d'expériences incluses dont le guide ICSBEP puis par rapport à d'autres expériences consolidées telles que les benchmarks d'effet Doppler qui sont basées sur des cellules de réacteur PWR (élargissement doppler dans le combustible) et de blindage Oktavian. Une fois les bibliothèques développées, les analyses préliminaires ont été effectuées sur le réacteur TRIGA afin d'évaluer les paramètres-clés de réacteur (le facteur de multiplication effective des neutrons, la fraction effective de neutrons retardés, le temps effectif de génération de neutrons, les coefficients de sûreté…etc.). La deuxième partie de cette thèse examine les potentiels combustibles à base de thorium avec divers isotopes 'driver' pour les intégrer dans l'une des conceptions les plus prometteuses des réacteurs, le réacteur à lit de boulets refroidi par gaz (HTR) basé sur les particules TRISO, pour identifier les mélanges potentiels et pour analyser leurs performances neutroniques et physiques. Les combustibles évalués dans cette thèse incluent le combustible à dioxyde de thorium mélangé avec l'uranium faiblement enrichi à dosage élevé (High-Assay Low-Enriched Uranium), le plutonium issu du recyclage de combustible de réacteur utilise, le plutonium issu de combustible militaire et U-233. De plus, tous les paramètres ont été évalués en utilisant nos bibliothèques générées. Enfin, dans cette thèse, les nouvelles méthodes de contrôle de réactivité pour le combustible (Th,^{233}U)O_2 ont été proposées en utilisant les absorbeurs consommables incorporés dans TRISO/QUADRISO afin de disposer d'une anti-réactivité neutronique au début de cycle, de réduire l'excédent de réactivité et d'augmenter les longueurs de cycle de fonctionnement.

Mots-clés: Codes de traitement nucléaires, Bibliothèques données nucléaires, Benchmarks, Réacteur TRIGA, Combustibles à base de thorium, Réacteur HTR.

Abstract

"Possible scenarios for a transition to a thorium-based fuel cycle in a pebble bed high temperature reactor"

Reliable nuclear data libraries and the sustainability of nuclear energy, with the disposal of the world's growth stocks as radioactive waste or surplus weapons material, are two of the most current challenges facing nuclear engineering research. Hence, this thesis is divided into two major parts: the first part deals with neutron cross-section libraries using state-of-the-art nuclear data evaluations (ENDF/B and JEFF) processed by the NJOY and NECP-Atlas code systems. The processed libraries have been validated using integral experiments from the ICSBEP Handbook and expansively validated against other consolidated experiments such as Oktavian shielding and the Doppler reactivity defect benchmarks. Once libraries were developed, preliminary analyses were carried out for the TRIGA reactor to estimate the reactor key parameters (effective neutron multiplication factor, effective delayed neutron fraction, effective neutron generation time, safety coefficients …). The second part of this thesis examines potential thorium-based fuels with various 'driver' isotopes in one of the most promising reactor designs, the high-temperature pebble-bed reactor (HTR) based on TRISO coating particles, to identify the potential mixtures and to analyze their physical performance. The fuels evaluated in this thesis include thoria fuel mixed with High-Assay Low Enriched Uranium, reactor-grade plutonium, weapon-grade plutonium and U-233. Moreover, all parameters were evaluated using our generated libraries. Additionally, in this thesis, new reactivity control methods for the (Th,^{233}U)O_2 fuel were proposed using burnable absorbers incorporated into TRISO/QUADRISO to enhance de discharge burnup in this type of reactor.

Keywords: Processing codes, libraries, Benchmarks, TRIGA reactor, thorium-based fuels, HTR Reactor.

Table of contents

List of tables

List of figures

Introduction

Several physical problems can be addressed in nuclear engineering simulations using Monte Carlo transport techniques. The accuracy of the results is primarily determined by the accuracy of the geometry model and the estimated statistical uncertainty of the calculation. There is, however, another potential source of error, namely the nuclear data used in the codes. Reliable nuclear data are, therefore, crucial key components for nuclear engineering research. Two types of data are needed for simulations: data describing interaction with the nuclei conforming to the system; and data describing the nuclear changes in the system components as a result of fission, activation, etc... All these data are considered nuclear data. Several studies have shown that there can be significant differences between the calculated results using cross-section libraries based on various evaluated nuclear data files or processed using different processing code methods (processing codes allows the acquisition of application libraries, which are input data to computations for a wide range of applications.).

On the other hand, the study of the behavior of nuclear materials and fuels constitutes also a major line of nuclear engineering research. In order to; support the operation of nuclear power (better use of fuels, improved material resistance, etc.); and to improve the technologies required for the design of future nuclear reactors. Which will allow, in particular, the optimization of natural resources and the production of less waste. Thorium-based fuels are one of these fuels that can achieve most of these properties. Although thorium-based fuels have been explored since the early reactor production in the 1960s. In the last decade, there has been a renewed interest in thorium fuel, which has now become the primary focus of studies and proposed for next-generation nuclear reactors due to the decreasing availability of uranium. Besides, thorium and thorium-based fuels produce substantially less long-lived radioactive waste compared to uranium and its fuel cycles, and the fissile content can be reprocessed for additional fuel cycles.

As a result, this research work is consistent with the international trend of obtaining accurate nuclear data by providing an overview of processing methods and the preparation of incident neutron data libraries (ENDF/B and JEFF) with the processing codes (NJOY/NECP-Atlas) for their implementation in MCNP code, as well as the analysis of new thorium fuel concepts for nuclear reactors. It mainly concerns the evaluation of certain safety parameters by modeling the

pebble-bed HTR reactor with different thorium-based fuel mixtures to maximize its discharge burnup and minimize radioactive waste.

For data libraries preparation, in the current work, we describe how the neutron data file is processed with NJOY and NECP-Atlas into ACE libraries. As well, numerical tests, along with statistical tests, were carried out to provide a library-to-library and code-to-code comparison to obtain more comprehensive impression and understanding of the criticality quality of the processed neutron data libraries. As a tool of the comparison processes, the processed libraries were checked using integral experiments from the International Handbook of Evaluated Criticality Safety Benchmark Experiments (ICSBEP) and extensively verified against other benchmarks including Oktavian and Doppler. The developed libraries were also tested with the TRIGA reactor by analyzing the most important criticality safety parameters of comprehensive complex reactor designs from a neutronic viewpoint, namely effective multiplication factors, effective delayed neutron fraction, mean generation times and reactivity coefficients.

For, the second objective of the thesis, which is to evaluate various thorium-based fuels in HTR reactors in order to optimize discharge burnup and minimize radioactive waste. We model a reference reactor based on the high-temperature pebble-bed reactor HTR-10 with High-Assay Low Enriched Uranium (HALEU 17 wt.%) fuel. This was accomplished by determining the effective multiplication factors for various processed data libraries at the beginning of the life and comparing these to the results published in IAEA reports. Based on the developed core, the HTR-10 was then investigated with different thorium-based fuel mixtures namely thoria (ThO_2) fuel mixed with High-Assay Low Enriched Uranium (HALEU 20 wt.%), reactor-grade plutonium ($RGPuO_2$), weapon-grade plutonium ($WGPuO_2$), and U-233 to examine the possibility of using thorium in such reactors.

The evaluation of thorium-based in power reactors is not a novel concept; yet, there is no comprehensive cross-comparison of multiple prospective pebble-bed HTR reactor thorium-based fuels in the open literature (evaluated but never completely compared in a single document). Therefore, this thesis evaluates potential thorium-based fuels to see if any fuel composition is especially favorable for use in a pebble-bed HTR reactor setting. The thesis also includes the use of two burnable absorbers as a reactivity control strategy in the modeled HTR reactor fueled with $(Th,^{233}U)O_2$. Burnup analysis, actinides, and fission product inventories for each of the fueled cores were determined as necessary for the reactor criticality-safety design studies. To achieve

these goals and obtain a thorough understanding, we carried out the works outlined in the following chapters of this thesis:

The first chapter is dedicated to the theoretical background required to understand the approaches presented in the rest of the thesis such as the definition of interaction cross-sections. Contains an overview of how the processing codes and the evaluated data can be used to produce cross-section libraries. The next part of the chapter is a comprehensive outline of the fundamental parameters such as the Boltzmann equation, neutron flux, multiplication and reactivity, and four-factor formula. And the last part of the chapter focuses on the support codes that are used for reactor analysis and benchmarking.

The second chapter provides detailed descriptions of the benchmarks used; these benchmarks are part of standard problem exercises aimed at determining the robustness of criticality safety computational for large arrays of fissile materials and spent fuel, shielding benchmarks, and reactivity benchmarks.

The third chapter is reserved to present the results of the comparisons and verifications made for the data libraries and processing code used in the study. The results are presented through the research articles published by the author.

Chapter four provides a comprehensive review of a reactor's operational requirements, which will be required to discuss the findings of chapter sixth. This chapter discusses the kinetic coefficients, control rod effect, and poison effect.

The fifth chapter delves into the history of thorium, as well as the various forms of thorium-based fuels used in nuclear reactors, the physical properties of thorium dioxide, and the neutronic properties of mixed thorium fuels.

The results of the neutronic and safety evaluation of the use of thorium-based fuels in the HTR-10 reactor are presented in the sixth chapter. We also highlight the major impact of the investigated fuels on reactor lifetime (discharge burnup) and various safety parameters, such as mass and fission product poisons evolution. The results are presented through the research articles published by the author. The final chapter contains a discussion of the results together with recommendations for future research.

Part I: Nuclear data processing and benchmarking

Chapter 1: Nuclear fundamentals

Chapter 1 focuses on the theoretical background required to understand the approaches presented in the subsequent chapters. The first part of the chapter elaborates on principles in nuclear physics, such as neutron cross-sections, and contains an overview of how the processing codes and the data libraries can be used to generate such cross-sections. The next part of the chapter is a comprehensive outline of the key parameters such as the Boltzmann equation, neutron flux, multiplication and reactivity, and four-factor formula. Whereas the last part of the chapter focuses on the support codes that are used for reactor analysis and benchmarking. We concentrate in particular on MCNP codes because they were used in most of the calculations for this work.

1.1. Introduction to neutron physics

In reactor design theory, knowledge of the neutron population i.e. predicting how the neutrons will be distributed in the system is important as it describes the rate at which various nuclear reactions occur. Unfortunately, evaluating the neutron population is a difficult problem in general because the population depends on the neutron source population, which depends on the neutron population itself in the case of the fission source, and on the neutron nuclei interactions undergone by the neutrons when they move away from the source. Thus, a thorough meticulous and understanding of neutron transport is imperative when determining the neutron population. Where it is the motion of neutrons in the reactor that eventually leads to scattering, absorption, or leakage. Other important applications of neutron population analysis in reactors include radiation-shielding design, heating measurements, and even nuclear plant life, which is measured by the amount of damage caused by radiation heating [1, 2, 3, 4, 5]. In the following sections, we describe the basic neutron interactions of importance in nuclear reactors and the data used in reactor physics calculations.

1.1.1. Definition of interaction cross-sections

Neutrons are released from a source and for some distance continue to travel in lines, at which point they leak out of the system or collide and interact with matter. On collision, scattering or absorption may occur. There are two types of scattering phenomena. The first type is elastic scattering (n, n), while the second type is inelastic scattering (n, n'). There are also two possibilities of reactions that can occur in absorption. The first is capture reaction, referred to as

$((n,\gamma),(n,p),(n,\alpha),(n,2n),(n,3n)$), and the second is fission reaction, referring to as (n,f) (see **Figure1.1)**.

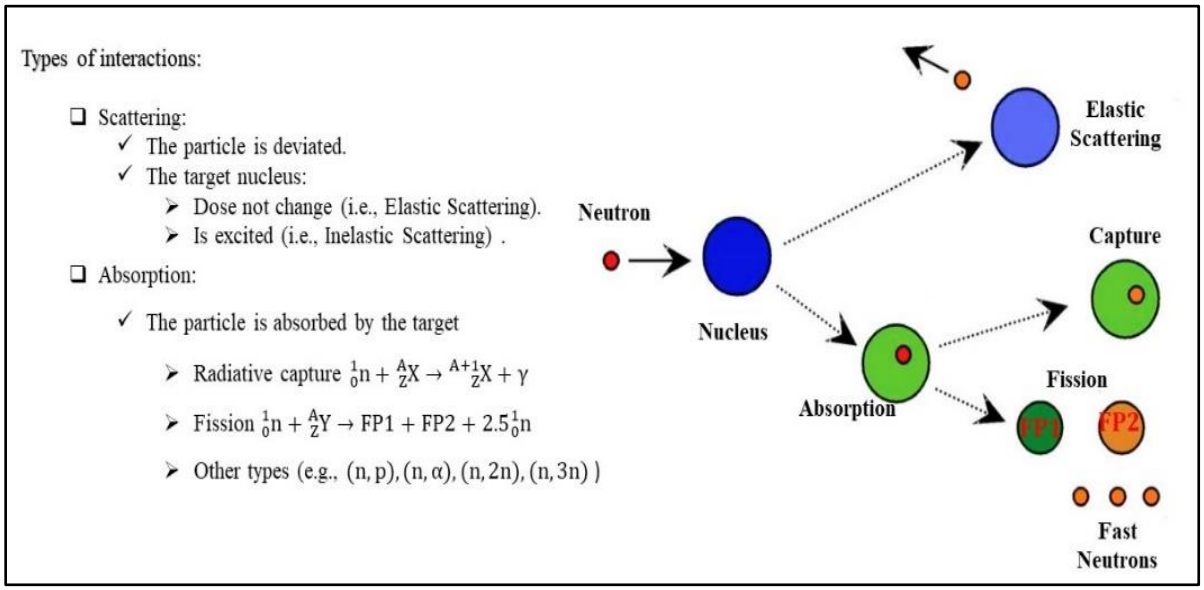

Figure 1. 1. Types of interactions; (FP= Fission Product).

In general, the expression "cross-section" usually characterizes how particles interact with matter. This quantity presents a measure of the likelihood of a reaction or reactions occurring. The cross-section is expressed in barn units(b), where one barn is equal 10^{-24}cm^2.

If we consider a particle beam (ϕ particles per cm^2 per second) that perpendicularly strikes a target of monoatomic material containing N atoms, the number of nuclear reactions category i observed per unit of surface and unit of time is determined by the reaction rate τ_i:

$$\tau_i = N.\sigma_i.\phi \tag{1.1}$$

Where σ_i is the cross-section (microscopic) of interaction type i on the monoatomic material. Then we designate another form of cross-section known as the macroscopic cross-section (Σ). The macroscopic cross-section is the probability that a given neutron reaction occurs per unit travel (cm^{-1}). Σ is related by the relation shown below to the microscopic cross-section.

$$\Sigma = N.\sigma \tag{1.2}$$

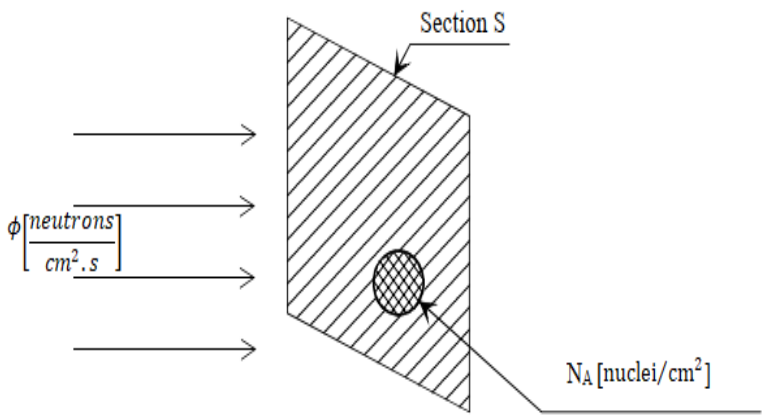

Figure 1. 2. A neutron beam striking a target.

For neutrons, the different probabilities of particle interaction with the nuclei are defined by the neutron cross-sections, which depend on the velocity of the incident neutrons (**Figure 1.3**), the nature of the target nuclei, and the temperature of the material. As well, each of the processes described in **Figure 1.1** by which neutrons interact with nuclei is denoted by a specific cross-section. Hence, elastic scattering is described by the elastic scattering cross-section, σ_{el}; inelastic scattering is described by the inelastic scattering cross-section, σ_{inel}; the radiative capture (n, γ) by the capture cross-section, σ_{γ}; fission (n, f) by fission cross-section, σ_f [3, 6]. The sum of the cross-sections for all possible interactions is known as the total cross-section and is symbolized by σ_t **Equation (1.3)**, and it quantifies the probability of any type of interaction occurring when neutrons strike a target [1].

$$\sigma_t = \sigma_{el} + \sigma_{inel} + \sigma_{\gamma} + \sigma_f + \text{other types} \tag{1.3}$$

The sum of the cross-sections of all absorption reactions is known as the absorption cross-section and is indicated by σ_a.

$$\sigma_a = \sigma_{\gamma} + \sigma_f + \sigma_p + \sigma_{\alpha} \tag{1.4}$$

where σ_p and σ_{α} are the cross-sections for the (n, p) and (n, α) reactions, as shown in **Equation (1.4)**, conversion fission, is traded as an absorption process. Likewise, the total scattering cross-section is the sum of the elastic and inelastic scattering cross-section [1]. Thus:

$$\sigma_s = \sigma_{el} + \sigma_{inel},$$

$$\sigma_t = \sigma_s + \sigma_a.$$

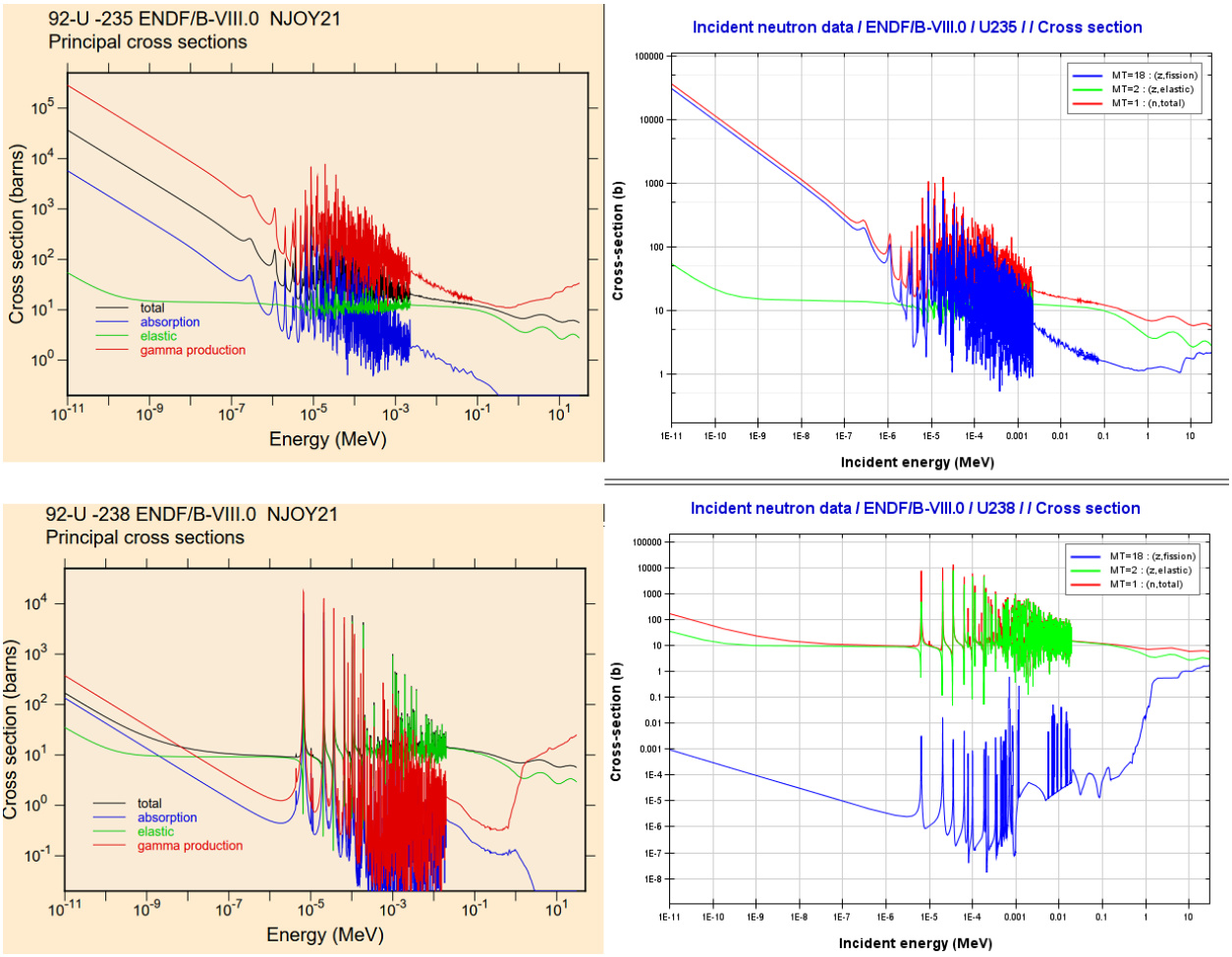

Figure 1. 3. Cross-sections for U-235 and U-238 as a function of the incident neutron energy.

There are four major areas of variation in neutron cross-sections as a function of incident neutron energy [4]:

- The thermal domain describes energies below 1 eV. The sections there generally show slow variations with slow gradients.
- The domain of resolved resonances for energies between 1 eV and a few tens of keV, where the sections present sudden localized variations.

- The domain of unresolved resonances for energies between a few tens and a few hundred of keV, where the sections have such resonance density (of decreasing amplitudes with energy) that we cannot distinguish them, so they are represented by mean parameters.
- The continuum domain, for energies greater than a few hundred keV, where the resonances are so numerous and similar that they overlap each other, causing slow variations of the sections with the energy again.

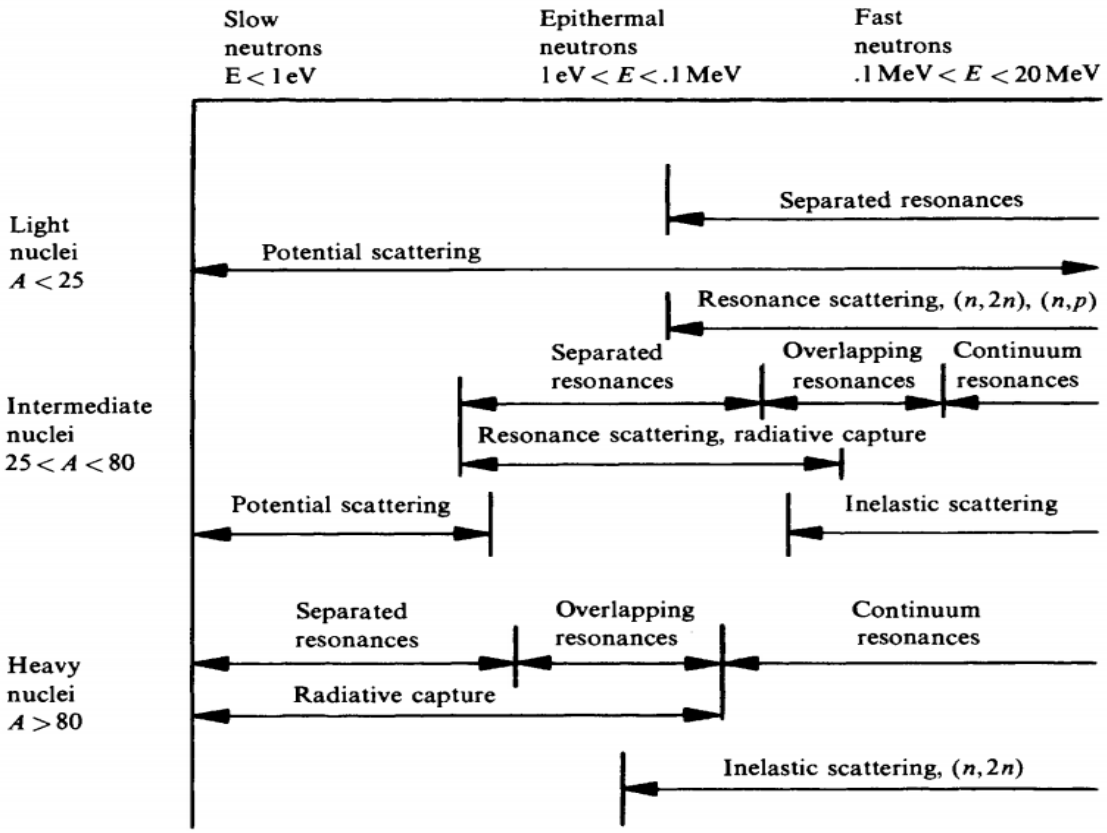

Figure 1. 4. Cross-section behavior for nuclei of various mass numbers [7].

1.1.2. Temperature effects on neutron cross-section

As discussed before, the microscopic cross-section varies significantly as neutron energy varies. The most microscopic cross-sections are provided at a standard neutron velocity of 2200 m/s (thermal), which corresponds to the room temperature [≈ 293 K (20 °C)]. Consequently, if the material is at a different temperature, the cross-section will be different from the 293 K value (**Figure 1.5)**. The formulation below is used to correct microscopic temperature cross-sections.

Although the example highlights the absorption cross-section, the same formula can be used to correct the capture and fission cross-sections [8, 9]:

$$\sigma_a = \sigma_{a,T_0} \cdot \sqrt{\frac{T_0}{T}} \tag{1.5}$$

Where σ_a is the cross-section corrected for the desired temperature, $\sigma_{a,0}$ cross-section at the reference temperature, T_0 the reference temperature, and T temperature for which the corrected value is being calculated.

Example:

The absorption cross-section for U-238 at 293 K is:

$$\sigma_{a,(293\text{K})} = 2.68 \text{ barn}$$

Then, the absorption cross-section for U-238 at 1000 K is equal to:

$$\sigma_{a,(1000\text{K})} = \sigma_{a,(293\text{K})} \cdot \sqrt{\frac{293}{1000}} = 1.45 \text{ barn}$$

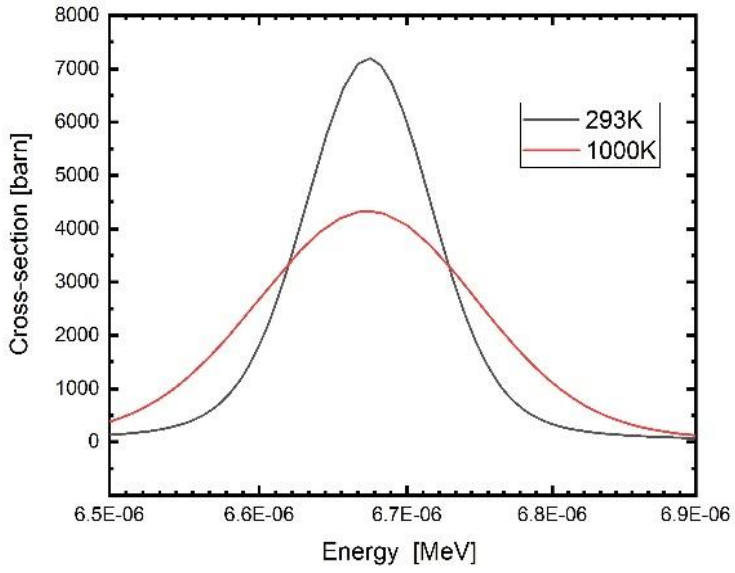

Figure 1. 5. The absorption cross-section for U-238 evaluated at 293 K and 1000 K showing the temperature effect.

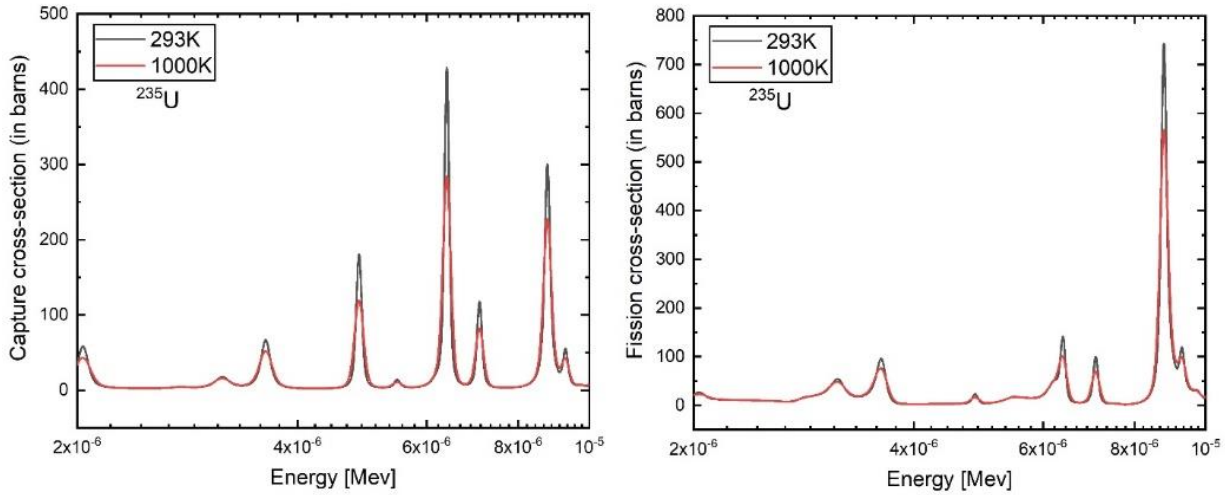

Figure 1. 6. Capture and fission cross-section for U-235 evaluated at 293 K and 1000 K.

1.1.3. Evaluated nuclear data file

All of the experimental data associated with cross-section measurements, or even more specifically all of the basic work of evaluating nuclear data, is the data required for modeling nuclear systems. These data are stored in international standard format computer files called "Evaluated Nuclear Data Files" or ENDF. The ENDF format provides representations for neutron cross-sections and contains information such as the energy and angular distributions for secondary neutrons, radioactive decay data, fission product data, etc.

The Nuclear data libraries consist of ASCII format files the size of which can reach multiple tens of thousands of lines. These data are provided in a tabulated form "tape" with correct interpolation laws, and others in the form of model parameters used to recreate hundreds of thousands of points reflecting those energy fields (see **Figure 1.7**) [10, 11]. The data stored in the evaluation files in ENDF format are listed according to three quantities: MAT, MF, and MT. The MAT number labels a material or an isotope. The MF number indicates the data type (i.e. spectrum, neutron cross-sections, photon cross-sections, general data, etc.). The MT number indicates the reaction form (e.g. elastic or inelastic scattering, fission, photoelectric effect, etc.) or other nucleus-specific details (e.g. period, radioactive decay spectrum, energy released subsequent fission, etc.). The organization of nuclear data evaluation is illustrated in **Figure 1.8**.

There are a collection of nuclear data libraries available e.g., the U.S. Evaluated Nuclear Data Library (ENDF/B) {the CSEWG (Cross Section Evaluation Working Group), which is in charge of the US ENDF/B libraries and the ENDF format. It is coordinated by the national nuclear data

center “NNDC” at Brookhaven National Laboratory}; the Evaluated Nuclear Data Library of the Lawrence Livermore National Laboratory (ENDL); Japanese Evaluated Nuclear Data Library (JENDL); Joint Evaluated File of NEA Nations (JEFF); and Russian Evaluated Nuclear Data File (BROND) [3].

Each of these organizations has adopted the ENDF-6 format as the standard format for publishing their nuclear data libraries, but each has defined its methods for using the format, reviewing the evaluation, and testing the results.

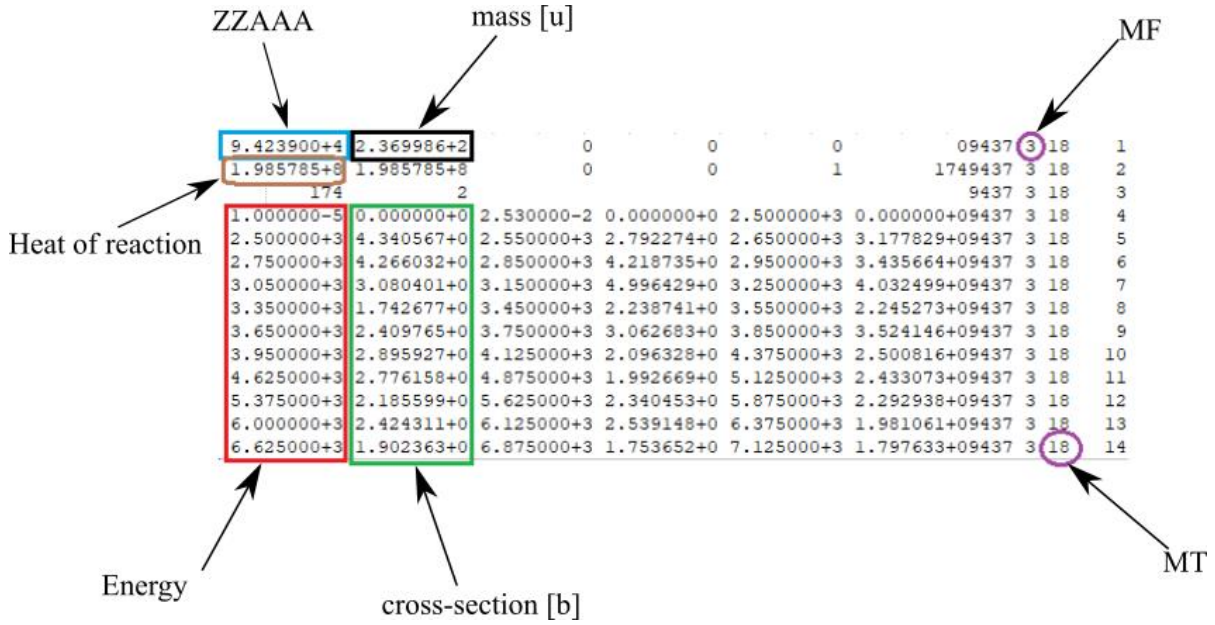

Figure 1. 7. Description of nuclear data contained in an ENDF-6 file (the latest version of the ENDF file). The isotope described in the figure is Pu-239.

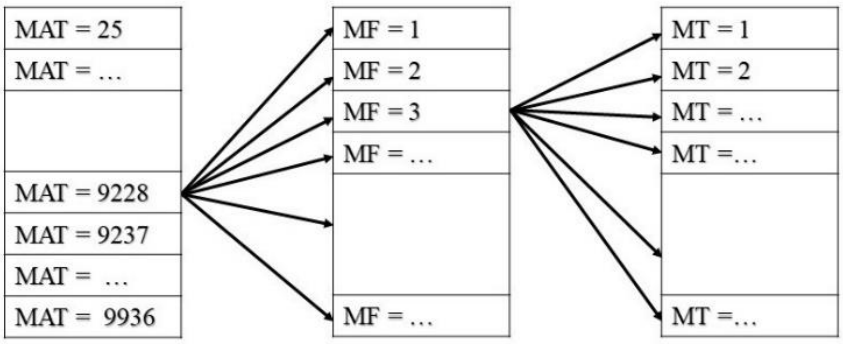

Figure 1. 8. The organization of an evaluation. Example: U-235 is designated by MAT = 9228 and U-238 by MAT = 9237.

Table 1. 1. Description of MF files.

MF	Description
1	General information
2	Resonance parameters
3	Pointwise cross-sections
4	Angular distribution of emitted particles
5	Energy distribution of emitted particles
6	Energy-angle distribution of emitted particles
7	Thermalization data

Table 1. 2. Description of MT files (example).

MT	Description: type of interaction cross-section
1	Total
2	Elastic scattering
4, 51-91	Inelastic scattering
102	Capture
16	$(n, 2n)$
17	$(n, 3n)$
18	(n, f)
37	$(n, 4n)$
104	(n, d)
105	(n, t)
106	$(n, {}^{3}He)$
107, 800-849	(n, α)

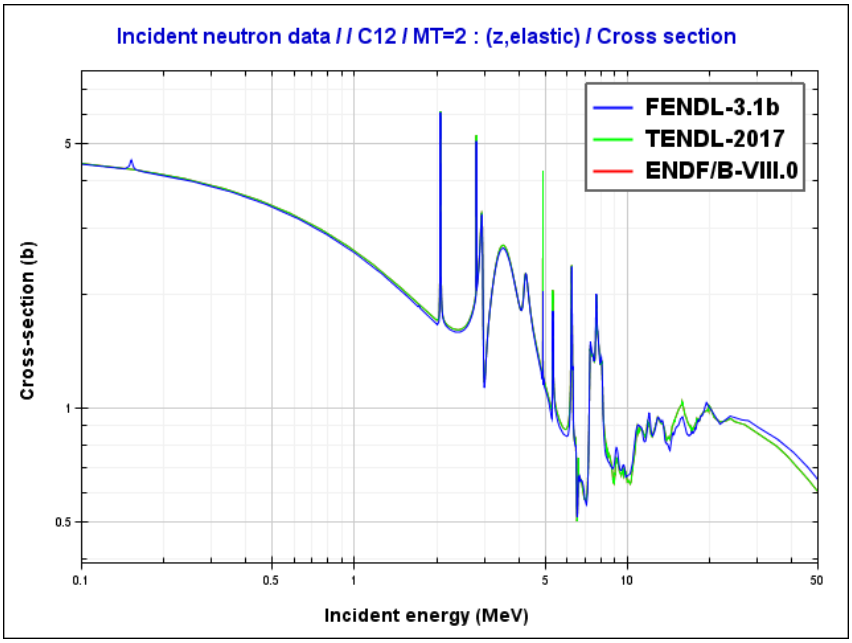

Figure 1. 9. Elastic cross-section for C-12, comparison between FENDL-3.1b, TENDL-2017, and ENDF/B-VIII.0.

1.1.4. Processing codes, creating cross-section libraries

The ENDF files are representations of the data extracted from experimental data and theoretical predictions coded in a unified computer-readable format. The ENDF files cannot be used directly; they must be translated into suitable forms for applications such as multi-group calculations of particle transport, determinist, or Monte Carlo techniques. As a result, cross-section processing codes such as NJOY [12], NECP-Atlas [13], PREPRO [14], and AMPX [15] have to be used to convert and modify data from the single universal ENDF format into a variety of formats accessible via particle transport codes [5]. The subsequent sections address the main processing codes used in this thesis.

1.1.4.1. NJOY data processing codes (NJOY2016 and NJOY21)

NJOY is a nuclear data processing system developed at the Los Alamos National Laboratory in 1974. It is a modular code allowing, from nuclear data evaluations (ENDF), to create pointwise or multi-groups neutron parameters (multi-group cross-sections, fission spectra, etc.) necessary for probabilistic and deterministic transport codes [11, 12, 16]. To prepare the standard MCNP libraries, NJOY code uses the ENDF format to create ACE files (A Compact ENDF). The ACE formatted files can be implemented directly in MCNP to perform criticality and shielding calculations. The $S(\alpha,\beta)$ thermal scattering data treatments for light nuclei and the structural materials were also generated by NJOY since these thermal scattering data are fundamental for finer modeling of the neutron interactions at energies below ~4 eV. These modules are described below, the reason for running the **acer** module twice is that it is used to evaluate the consistency of the ACE format, which is checked and for which problems are corrected. For the MCNP transport calculations performed in this thesis, **gaspr** and **heatr** modules (described in the next paragraphs) are not generally needed, but they are important and necessary to construct a complete processed file [17, 18, 19, 20]. In the following thesis, the NJOY input file has been prepared for each material and at the desired temperature. Each module executes a precise processing task, and they are linked by input and output files (tapes). An example of NJOY input is given in **Figure 1.10**. The Thermal Scattering Libraries (TSL) have been also processed but by using another special NJOY input file (example **Figure 1.12**) [12, 17].

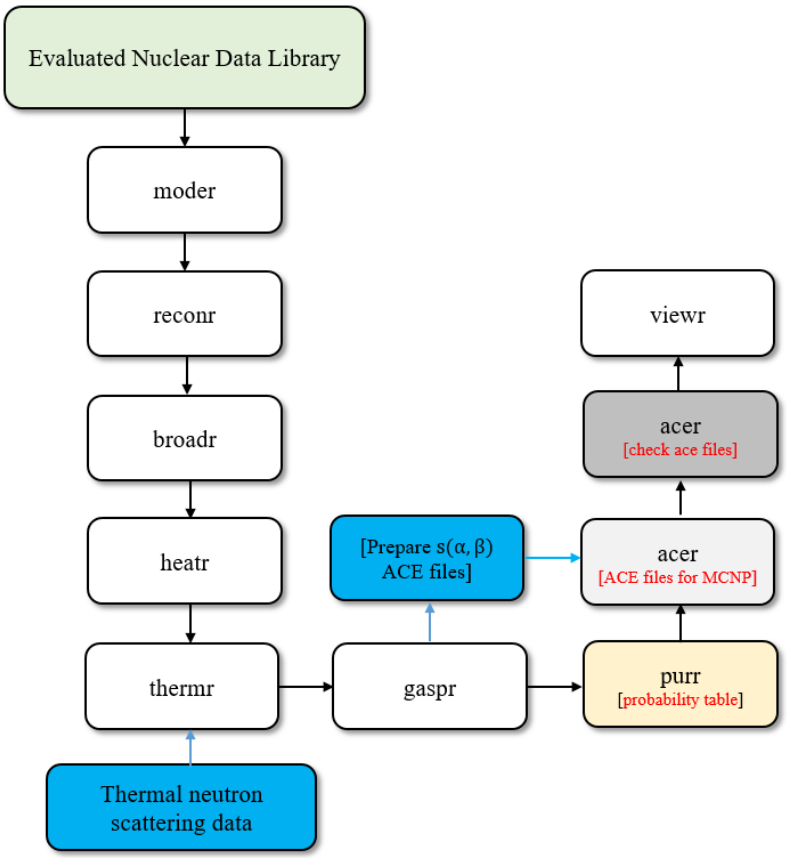

Figure 1. 10. NJOY sequence to process the latest libraries in ACE format.

- The **moder** module is used to convert ENDF "tapes" back and forth between ASCII format and the special NJOY blocked-binary format.
- The **reconr** module is used to produce pointwise (energy-dependent) cross-sections for all reactions on a common energy grid, which is described by linear interpolation to correctly represent the cross-sections. These cross-sections are reconstructed from the evaluated nuclear data, stored in a file in the ENDF format divided into different types according to the energy range considered. We can distinguish:
  - The resonance parameters established for a given formalism (BREIT et WIGNER, REICH et MOORE...) in the resolved resonances range;
  - The mean resonance parameters associated with statistical distribution laws in the range of the unresolved resonance;
  - The pointwise cross-sections, associated with an interpolation law between the points, for the energy ranges specified in the evaluation;

The file created by the **reconr** module is a file of a specific type called PENDF format; it contains pointwise cross-sections at a temperature of 0 K over the entire energy range. To create cross-sections at any temperature, we use the **broadr** module.

- The **broadr** module used to Doppler broadens and thins pointwise cross-sections at a given temperature. **Broadr** module produces a file in a PENDF format similar to the file from the **reconr** module.
- The **heatr** module is used to add pointwise heating cross-sections called KERMA factors and radiation damage energy production to the ENDF-file.
- The **gaspr** module is used to add the production of charged particles (also called gas-production). The module takes any cross-sections of reactions in which secondary particles are created (i.e. protons and alpha particles) and adds to the library the production of particles from those cross-sections. These results can be converted to multigroup form using **groupr**; they are then passed to **acer** or displayed using plotr.
- The **thermr** module is used to produce cross-sections and energy-to-energy matrices for free or bound scatterers in the thermal energy range.
- The **purr** module can prepare the probability tables in MCNP for the treatment of unresolved self-shielding resonance. This module will construct a series of resonance ladders, which will follow the statistical distributions given in the ENDF file. Each of those ladders will be randomly sampled to produce contributions to a probability table. When no unresolved resonances are present, NJOY will pass this module as no probability tables will be produced.
- The **acer** module prepares libraries for the continuous Monte Carlo energy codes in ACE format. The ACE format contains all the information regarding the standard ENDF format. The second run of **acer** will perform accuracy tests of this ACE file and if necessary fix the problems.

```
moder
1 21
'Process 92-U-235 from ENDFB-VIII.0'/
20 9228
0/
reconr
21 22
'PENDF for 92-U-235'/
9228 2/
0.001 0.0 0.003/ err tempr
0/
broadr / doppler broaden XS
21 22 23
9228 3 0 0 0. /
0.001 2.0E6 0.003/
293.6 600.  900.
0/
heatr / add heating kerma and damage energy
21 23 24/
9228 7 0 0 0 2/
302 303 304 318 402 443 444/
gaspr / add gas production
21 24 25
thermr / thermal calculation
 0 25 61
0 9228 20 3 1 0 0 1 221 0/
293.6 600.  900.
0.001 4.0
purr / process unresolved resonance range
21 61 26
9228 3 5 20 64/
293.6 600.  900.
1.E+10 1.E+04 1.E+03 1.E+02 1.E+01
0/
acer / prepare ACE files
21 26 0 27 28
1 0 1 .80 /
'92-U-235 from ENDFB-VIII.0'/
9228 293.6
1 1/
/
acer / check the prepared ACE files
0 27 0 29 30
7 1 1 -1/
/
- convert Acer plot file to photo scrip format
viewr
 29 37
stop
```

Figure 1. 11. NJOY input used to generate the ACE library for U-235 at 293.6 K.

```
moder
 20 -30
moder
 21 -40
reconr
 -30 -31 /
 'PENDF tape for ENDFB-VIII.0' 1-H-1'/
 125 2 0 /
 0.001 0. 0.003 /
 '1-H-1 from ENDFB-VIII.0'' /
 0 /
broadr
 -30 -31 -32
 125 1 0 0 0./
 0.001 1.0E6 0.003 /
 293.6
 0 /
heatr
 -30 -32 -33 0/
 125 7 /
 302 303 304 318 402 443 444 /
thermr / Add thermal scattering data (free gas)
  0 -33 -34
 0 125 12 1 1 0 0 1 221 1/
 293.6
 0.001 4.0
thermr / Add thermal scattering data (bound)
 -40 -34 -35
 1 125 20 1 2 1 0 2 235 1/
 293.6
 0.001 4.0
gaspr
 -30 -35 -37
 moder
 -37 38
acer
 40 38 0 41 42                          / Card1
 2 0 1 .01                              / Card2
 'H in H20 293.6k from ENDFB-VIII.0'    / Card3
 125 293.6 'hh2o'                       / Card8
 1001    0    0                         /
 222 64   0 0 1 4.0 0                   / Card9
acer
 0 41 45 43 44 /
 7 1 1 -1/
 'H in H20 293.6k from ENDFB-VIII.0'    /
viewr
45 46 /
stop
```

Figure 1. 12. NJOY input used to generate ACE (TSL) for H in H2O.

1.1.4.2. NECP-Atlas data processing code (version 1.2)

NECP-Atlas data processing code developed at Xi'an Jiaotong University in China. NECP-Atlas is a modular system with a variety of sub-programs each performing a specific task in a multi-step sequence starting from the initial ENDF-formatted file and ending with an ACE file appropriate for use in MCNP calculation. To generate cross-section libraries, NECP-Atlas uses **atlas_mod**, **recon_calc**, **doppler**, **table_calc**, and **ace_outp** modules. **Recon_calc** is used to build a unionized energy grid for all cross-sections of the evaluated file in question. If there are resolved resonance parameters, they are expanded to the appropriate pointwise cross-sections, typically scattering, capturing, and possibly fissioning. The recon **calc_output** is transferred to the **doppler** module, where the Doppler effect is extended to the desired temperature for the cross-sections.

NECP-Atlas allows the user to define a specific linear tolerance of interpolation as part of its doppler input. **Table_calc** is used for creating unresolved probability resonance tables. Lastly, **ace_outp** is used to accumulate different quantities into an ACE format [13, 21, 22]. An example of NECP-Atlas input is given in **Figures 1.14** and **1.15.**

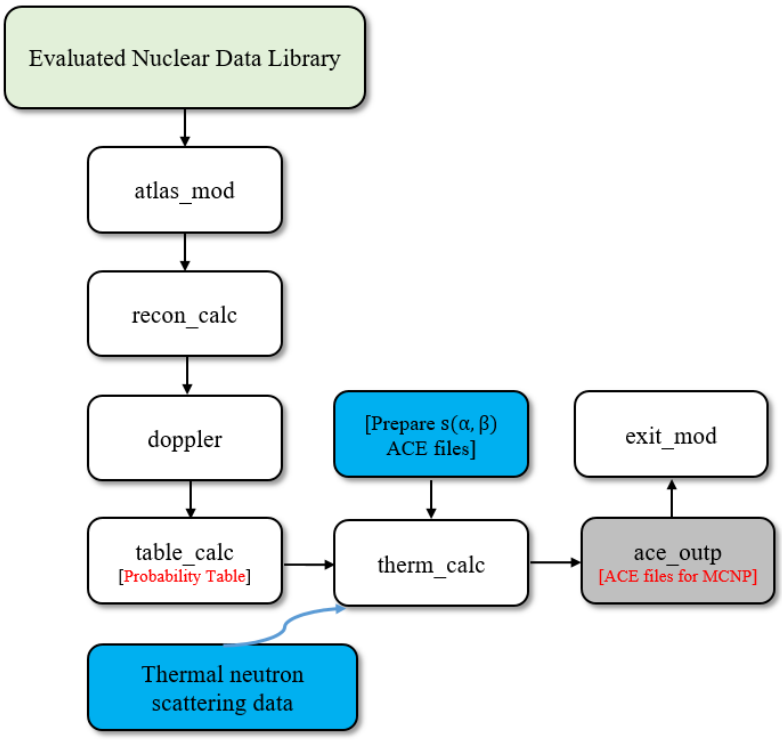

Figure 1. 13. NECP-Atlas nuclear data processing sequence for the Monte Carlo code MCNP.

```
--          9228g
-- process U-235
n_9228_92-U-235.dat
exit_file
atlas_mod
reconstruct/
9228/
0.001 0. 0.003/
doppler/
9228 1 /
0.001 2.0E6 0.003/
293.6/
pro_unres/
9228 1 5 /
293.6/
1.E+10 1.E+04 1.E+03 1.E+02 1.E+01 /
0 /
table_calc/
9228 1 5 /
293.6/
1.E+10 1.E+04 1.E+03 1.E+02 1.E+01 /
thermal_calc/
0 9228 12 1/
293.6/
4. 0.001/
ace_outp/
1 0.80/
9228 293.6
exit_mod
stop
```

Figure 1. 14. NECP-Atlas input used to generate the ACE library for U-235 at 293.6 K.

```
--
-- process H in H2O at 293.6 K
tape20
tape30
exit_file
atlas_mod
reconstruct /
 128 /
0.001 0. 0.003/
doppler /
 128 1 /
0.001 2.0E6 0.003/
293.6 /
table_calc /
 128 1 10 /
293.6 /
1.E+10 1.E+04 1.E+03 1.E+02 1.E+01 /
thermal_calc /
11  128 12 1 1/
293.6 /
4. 0.001/
ace_outp/
2 0.11/
128 293.6 'hh2o'/
1002/
16/
exit_mod/
stop
```

Figure 1. 15. NECP-Atlas input used to generate ACE (TSL) for H in H_2O.

1.1.5. Nuclear data validation process

In the criticality safety studies, which cover the various stages of the fuel cycle, require the knowledge of precise nuclear data on many nuclei (i.e. fissile, neutronic absorbents, moderators, reflectors) and the neutron spectrum (i.e. thermal, epithermal, or fast). Therefore, the knowledge of nuclear data is essential for the development and implementation of nuclear science and technology. It is indeed been the nuclear data libraries, which supply nuclear data to neutronic simulation codes. However, before being used for any application, those data are subject to thorough review, correction, and analysis. They have to go through the following steps to be directly usable:

- Measurements
- Evaluation (creation from measurements and theoretical models);
- Processing (creation of data library);
- Verification and validation against internationally accepted benchmarks (criticality safety benchmarks) or in a power reactor.

1.2. Basic nuclear concepts

1.2.1. Nuclear fission

The use of nuclear energy is to take advantage of the high binding energy of the nuclei through exothermic reactions. The two main types of reactions are fission and fusion. There are two types of fission known as fast fission and thermal fission, depending on a neutron's energy as it bombards a nucleus. The neutron energy in thermal fission is about 0.0025 eV, and fast fission typically occurs at an energy of 1 MeV or greater. Yet, the overwhelming majority of research on power reactors focuses on the thermal region, which produces the majority of the power, thus, understanding fission is fundamental to understanding reactor design, operation, and licensing [8]. In the fission reaction, the incident neutron enters a heavy target nucleus forming a composite nucleus excited to such a high degree of energy, that the nucleus divides into two large fragments and other neutrons (2 to 3 prompt fast neutrons) plus a considerable amount of energy emitted in the form of radiation and fragmentation of kinetic energy. An example of a typical fission reaction is given below. Obviously, the fission fragments are also excited nuclei, heavily charged, they repel each other and then stop by spreading their kinetic energy in the form of heat on the

surrounding nuclei. Then they become fission products (FP). They partially stabilize during their time-of-flight by first releasing neutrons, and then gamma rays. Through radioactive decay of these fission products, all forms of radiation ($\beta, \gamma, \ldots$) are released, plus a so-called delayed neutron is emitted approximately 10 seconds after fission on average. These delayed neutrons are fast but slightly below the prompt neutrons (about 500 keV). These few delayed neutrons play a fundamental role in controlling the reactor [1].

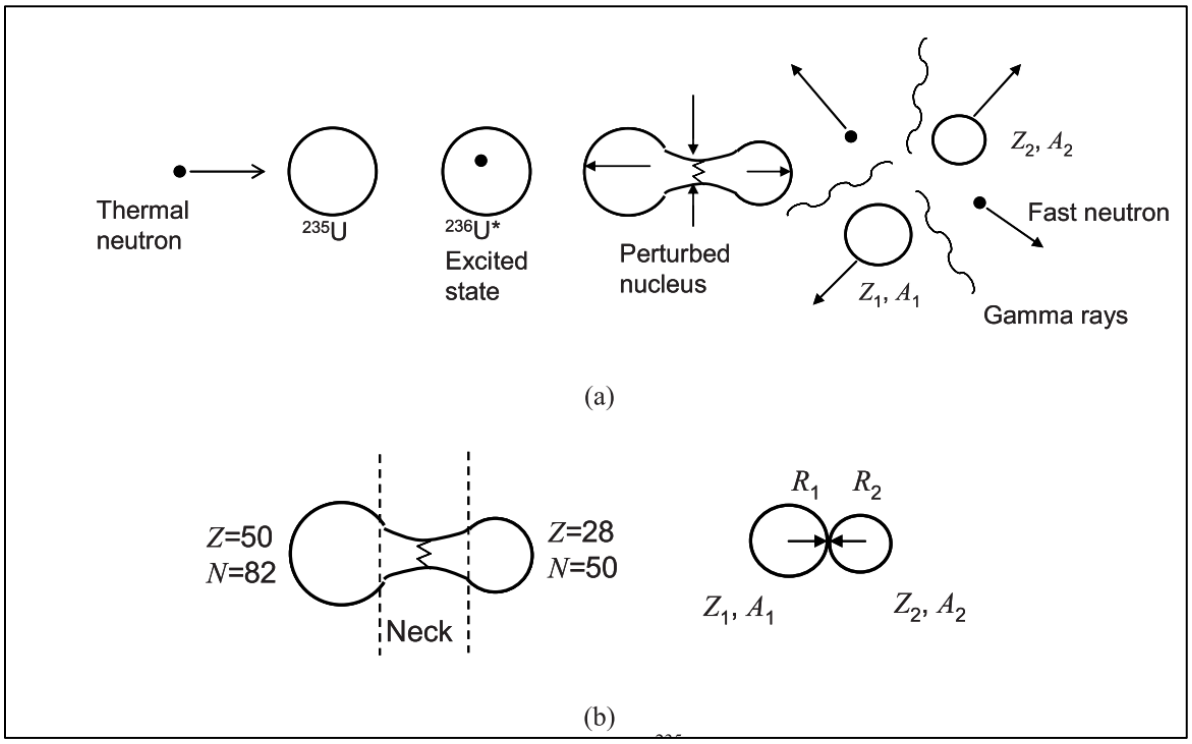

Figure 1. 16. (a) Schematics of a fission process for U-235; (b) perturbed nucleus at the moment of fission according to the liquid drop model. (From: Jevremovic, 2009 [23]). The fission process can be explained using the liquid drop model of a nucleus. In the ground state, the nucleus is a nearly spherical shape. After absorption of a neutron, the nucleus will be in an excited state and will begin to oscillate and deform. If the oscillations cause the nucleus to behave like a dumbbell, the nuclear attractive short-range forces will be overcome by the repulsive electrostatic forces and the nucleus will separate in two [8].

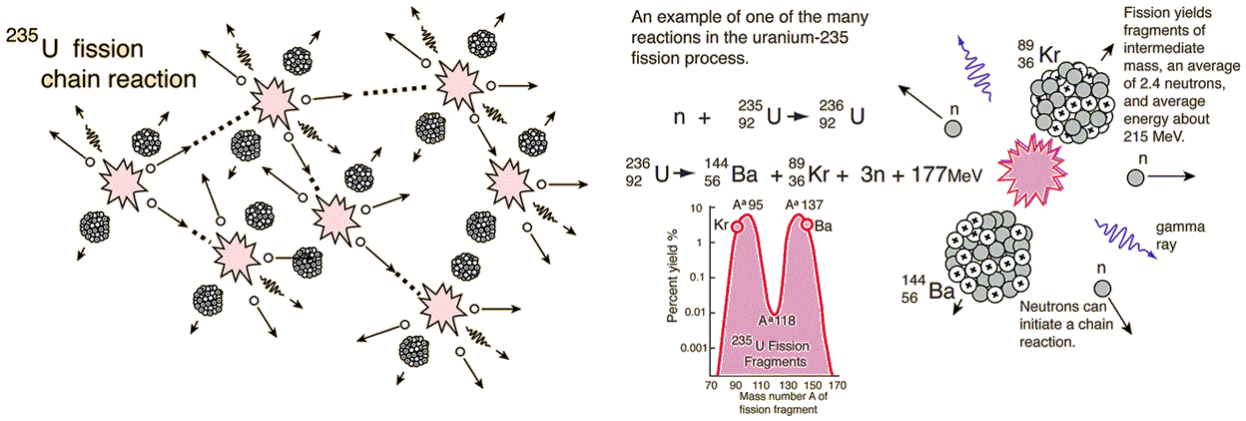

Figure 1. 17. Schematic of a fission chain reaction. (From: hyperphysics.phy-astr.gsu.edu/).

Another thing to observe from **Figure 1.17** is that there are more free neutrons present at the end of the fission process and than there were at the start. Although the actual number of neutrons released per fission depends on the fissioning isotope (referred to as $\overline{\nu}$), this emitted neutron could repeat the process of fission with other nearby fissile atoms. This mechanism could then continue unless all available fissile atoms are split or are so remote that continuing the chain reaction becomes impossible reactor principle. Therefore, when $\overline{\nu} > 1$, it is conceived that a multiplicative effect will occur; the neutrons multiply from generation to generation and the reaction rate increases correspondingly. We call that process a chain reaction. It is necessary to know what number k of fission neutrons can induce fission again to assess the possibility of a chain reaction. For U-235, $\overline{\nu}$ is about 2.42, that's, an average of 2.42 new neutrons are created for each U-235 fission that occurs. However, since not all the absorbed neutrons lead to fission (this process is called radiative capture), it does not necessarily give a complete picture of the neutron production rate. Therefore, an extremely significant factor is the balance between the probability of fissions and radiative capture. This balance is distinguished by the capture-to-fission ratio, defined by **Equation (1.6)**. While the number of neutrons released in fission per neutron absorbed by a fissile nucleus is commonly referred to as η and can be evaluated by **Equation (1.7)** [7].

$$\alpha = \frac{\sigma_\gamma}{\sigma_f} \tag{1.6}$$

$$\eta = \overline{\nu} . \frac{\sigma_f}{\sigma_a} \tag{1.7}$$

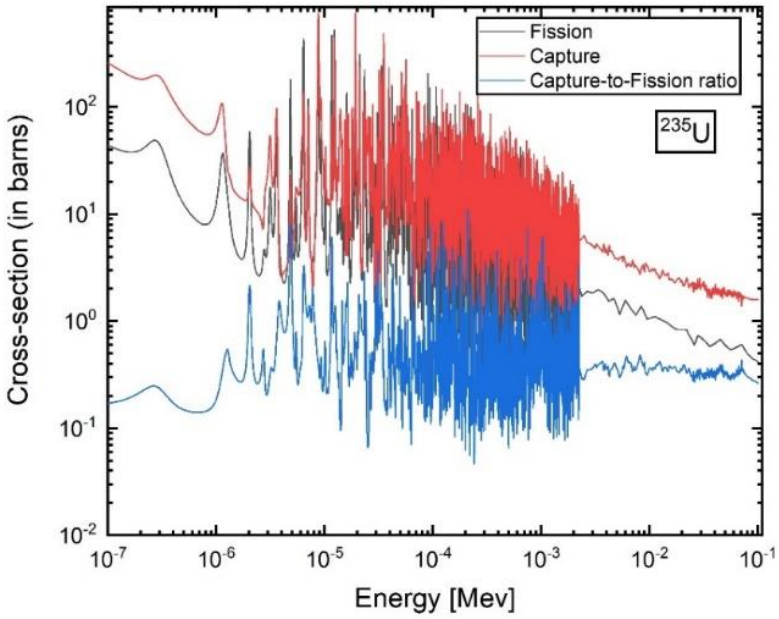

Figure 1. 18. Capture-to-fission ratio ($\frac{\sigma_\gamma}{\sigma_f}$) for U-235; results obtained using NJOY21.

Table 1. 3. Cross-sections and average number of fission for various nuclei with thermal neutrons [1, 24].

Isotopes	U-233		U-235		Pu-239	
Spectrum	Thermal	Fast	Thermal	Fast	Thermal	Fast
σ_f (in barns)	531	2.79	582	1.81	743	1.76
σ_γ (in barns)	46	0.33	101	0.52	270	0.46
α	0.09	0.12	0.17	0.29	0.36	0.26
$\overline{\nu}$	2.49	2.53	2.42	2.43	2.87	2.94
η	2.29	2.27	2.07	1.88	2.11	2.33

1.2.2. Neutron flux

It was shown in Section 1.1.1 that, the reaction rate τ_i is related to the macroscopic cross-section Σ_i and the flux ϕ by:

$$\tau_i = \Sigma_i . \phi$$

The quantity ϕ is called the neutron flux, in the case of monoenergetic neutrons is defined by the following formulate:

$$\phi = n.\boldsymbol{v}_n$$
$$\left[\frac{\text{neutrons}}{\text{cm}^2.\text{s}}\right] = \left[\frac{\text{neutrons}}{\text{cm}^3}.\frac{\text{cm}}{\text{s}}\right] \quad (1.8)$$

Usually, a single neutron inside a reactor is described by; the vector position coordinates ($\vec{\boldsymbol{r}} = x\vec{\imath} + y\vec{\jmath} + z\vec{k}$), the velocity coordinates ($\boldsymbol{v}_n$), the angular directions ($\vec{\Omega} = \frac{\boldsymbol{v}_n}{|\boldsymbol{v}_n|}$), and the time ($t$). However, if we want to know how many reactions are going to occur, we need to know how many neutrons propagate through the material and how many centimeters they travel each second. This number is called neutron density, and is represented by $n(\vec{\boldsymbol{r}}, \boldsymbol{v}_n, \vec{\Omega}, t)$ such that $n(\vec{\boldsymbol{r}}, \boldsymbol{v}_n, \vec{\Omega}, t)d^3rd^2\Omega d\boldsymbol{v}_n$ is the total amount of neutrons per unit volume at an instance t [1, 3]. Therefore, the neutron flux, which describes the local motion of neutrons in a reactor, can be expressed by **Equation (1.9)**. However, the equation that governs neutron transport is the Boltzmann equation and will be presented in the next sections.

$$\phi(\vec{\boldsymbol{r}}, \boldsymbol{v}_n, \vec{\Omega}, t) = n(\vec{\boldsymbol{r}}, \boldsymbol{v}_n, \vec{\Omega}, t).\boldsymbol{v}_n \quad (1.9)$$

1.2.3. Multiplication factor

Since not all neutrons created after the previous fission generation will have the potential to cause new fissions, as non-fissionable materials will absorb some neutrons, others will be parasitically absorbed into fissionable materials and will not cause fission, while others will leak out of the reactor. However, to ensure a self-sustaining chain reaction, the basic requirement for each nucleus undergoing fission is to generate, on average, at least one neutron triggering another fission. This condition is expressed conveniently as a multiplication factor (k), which helps us to know the ratio of the number of neutrons between two successive generations of fission neutrons [7]. There is a difference between the infinite multiplication factor (k_{inf}) and the effective multiplication factor (k_{eff}). k_{inf} is commonly used in lattice cell calculations i.e., infinitely large system, which expresses there is no neutron leakage. To describe the neutrons' life cycle in a real, finite reactor, the account must be taken of the neutrons that leak out. The multiplication factor that takes into such criterion is the k_{eff}.

$$\mathrm{k_{inf}} = \frac{\text{Production}}{\text{Absorption}} \qquad \mathrm{k_{eff}} = \frac{\text{Production}}{\text{Absorption} + \text{Leakage}}$$

For a reactor that creates exactly as many neutrons as it consumes is known to be exactly critical and has $k = 1$ and $n(t)$ is constant. If a reactor consumes more neutrons than it generates, it is said to be subcritical and has a value of $k < 1$, $n(t)$ decreases with time. A supercritical reactor, on the other hand, has $k > 1$ and produces more neutrons than it absorbs, $n(t)$ increases with time. Subcritical reactors are unable to maintain the required chain reaction and supercritical reactors are difficult to control if not impossible. Reactor designers, therefore, set $k = 1$ as their goal for the operation [7]. Another useful term expressed in nuclear physics is reactivity (ρ), which normalizes the multiplication factor and is represented as follows:

$$\rho = \frac{\mathrm{k} - 1}{\mathrm{k}} = \frac{\delta \mathrm{k}}{\mathrm{k}} \tag{1.10}$$

From this equation, it is evident that the reactivity varies according to:

$$\rho = \frac{\delta \mathrm{k}}{\mathrm{k}} = \begin{cases} k = 1 \rightarrow \rho = 0 \\ k > 1 \rightarrow \rho > 0 \\ k < 1 \rightarrow \rho < 0 \end{cases}$$

1.2.4. The four-factor formula

The four-factor formula (i.e. Fermi's four-factor formula) is obtained by performing a neutron balance that is, by studying the evolution of a neutron population from one generation to the next, taking into account the various interactions that a neutron can undergo during its life. It allows for the breakdown of a neutron's life into different phases, which reflect the events in the three energy domains: fast, epithermal, and thermal. This formula can be applied to an infinite system, which is homogenous or heterogeneous [4]. This formula is described as:

$$\mathrm{k_{inf}} = \epsilon f p \eta \tag{1.11}$$

The fast fission factor:
$$\epsilon = \frac{\text{number of fast neutrons produced by all fissions}}{\text{number of fast neutrons produced by thermal fissions}}$$

Thermal utilization factor:
$$f = \frac{\text{number of thermal neutrons absorbed in the fuel}}{\text{total neutron absorption}}$$

Resonance escape probability: $$p = \frac{\text{number of neutrons that reach thermal energy}}{\text{number of fast neutrons that start to slow down}}$$

Reproduction factor: $$\eta = \frac{\text{rate of production of fast neutrons by thermal fission}}{\text{rate of absorption of thermal neutrons by the fuel}}$$

The fast fission factor reflects the probability that fission happens beyond the thermal range. This mainly happens in the energy spectrum of the fast fission spectrum. The thermal utilization factor is the probability that the absorption of neutrons is in the fuel and not in other components (i.e. moderator, coolant, and other structural materials). The resonance escape factor describes the likelihood that a neutron will manage to be thermalized without being absorbed by the fuel. The reproduction factor reflects the amount of neutrons in the thermal range produced from fission compared to the total thermal neutron absorption by the fuel.

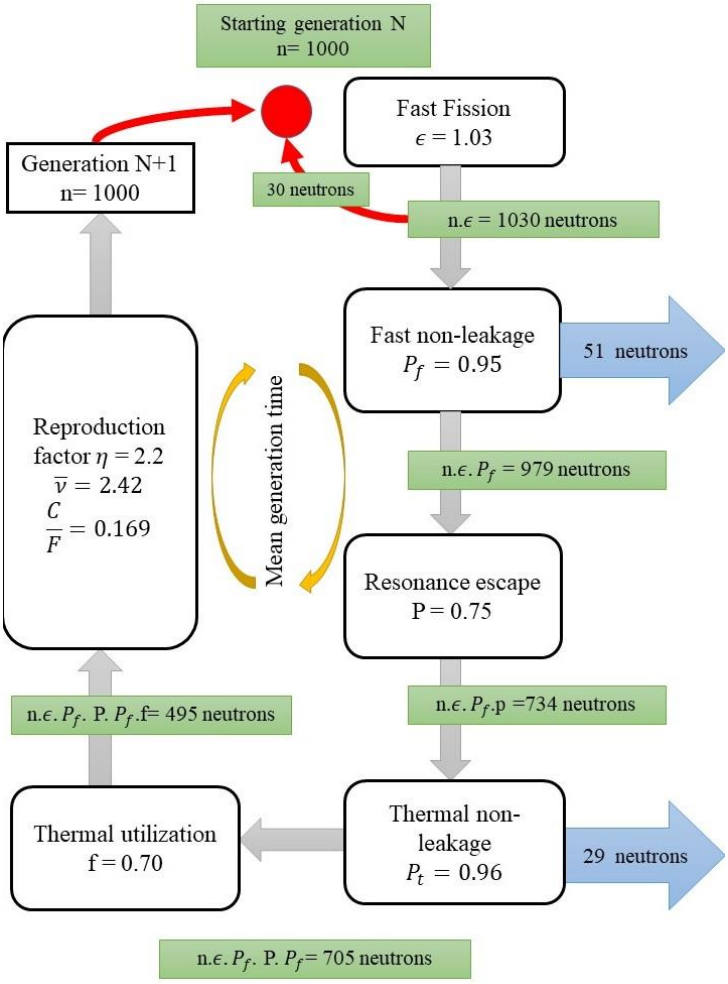

Figure 1. 19. Example of neutrons cycle.

1.3. The Boltzmann transport equation

We need to identify two entities to determine the reaction rates within a nuclear system. We need to know the nuclear cross-sections and the neutron population (as a function of time, space, and position). Thus, it is necessary to define the neutron population in a balanced mathematical format. Typically, there are two ways to interpret this behavior. There is the integrodifferential equation approach and the integral equation approach. However, we will present the integral equation in the following thesis, since it is the equation that can be solved by the Monte Carlo transport codes. As it was shown in Section 1.2.2, the neutron population is represented by a function called neutron density and denoted $n(\vec{r}, \boldsymbol{v}, \vec{\Omega}, t)$. In reactor physics, it is more convenient to refer to the flux function that designates the product of density $n(\vec{r}, \boldsymbol{v}, \vec{\Omega}, t)$ by the velocity $\boldsymbol{v}$ of the neutrons **Equation (1.9)** since this function provides complete access to the only observable physical quantities of the reaction rates. The expression of the integral form of the Boltzmann equation requires the precision of certain quantities. It is, therefore, necessary to introduce, for example, the definition of the curvilinear coordinate s which links the location of a neutron at time t with that of s_0 at time t_0, by:

$$\vec{r}(s) = s\vec{\Omega} + \vec{r}_0 \text{ with } t(s) = \frac{s}{v} + t_0 \qquad (1.12)$$

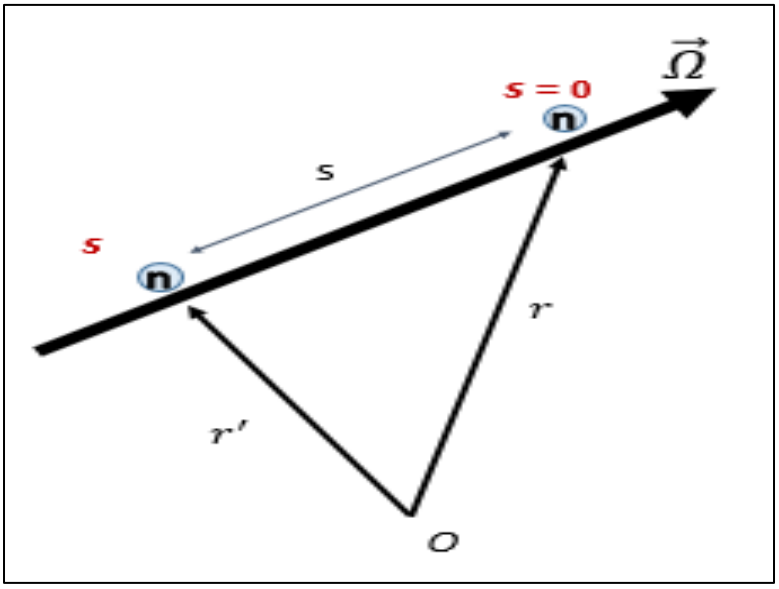

Figure 1. 20. Neutron motion along the direction $\vec{\Omega}$.

It is also necessary to define the quantity ω (the optical path), obtained by integration of the total macroscopic cross-section (Σ_t) on the path of this neutron, between its starting point $\vec{\boldsymbol{r}}_0$, defined by $s = 0$, and the point $\vec{\boldsymbol{r}}$ defined by s:

$$\omega(s) = \int_0^s \Sigma_t(\boldsymbol{v}, s')ds' \tag{1.13}$$

and the emission density Q defined as:

$$Q(\vec{\boldsymbol{r}}, \boldsymbol{v}, \vec{\Omega}, t) = \overbrace{\int_{(4\pi)} d\vec{\Omega'} \int_0^{\infty} d\boldsymbol{v}' \left[\Sigma_s\left((\vec{\boldsymbol{r}}(\boldsymbol{v}', \vec{\Omega'}) \rightarrow (\boldsymbol{v}, \vec{\Omega}), t\right)\right] \phi(\vec{\boldsymbol{r}'}, \boldsymbol{v}', \vec{\Omega'}, t)}^{(1):\ \textbf{scattering}} + \underbrace{S(\vec{\boldsymbol{r}}, \boldsymbol{v}, \vec{\Omega}, t)}_{\substack{(2):\ \text{sources} \\ \text{(in the case of fissions)}}} \tag{1.14}$$

Then, the general form of the integral transport equation can then be written as:

$$\phi(\vec{\boldsymbol{r}}, \boldsymbol{v}, \vec{\Omega}, t) = \int_0^{\infty} e^{-\omega(s)} Q\left(\vec{\boldsymbol{r}} - s\vec{\Omega}, \boldsymbol{v}, \vec{\Omega}, t - \frac{s}{\boldsymbol{v}}\right) ds \tag{1.15}$$

From this form, and under simplifying assumptions (the neutrons are monokinetic, the sources and the neutron population are stationary in time, the sources are isotropic), we can express a simplified form of this equation **Equation (1.16)** [4].

$$\phi(\vec{\boldsymbol{r}}) = \int_{\vec{r'} \in \boldsymbol{D}} \frac{e^{-\omega(s)}}{4\pi \left|\vec{\boldsymbol{r}} - \vec{\boldsymbol{r}'}\right|^2} Q(\vec{\boldsymbol{r}'})\, d^3\boldsymbol{r}' \tag{1.16}$$

1.4. Monte Carlo solution of the neutron transport equation

For simulation and modeling of neutron transport in a reactor, two methods can be employed. The first category of methods is deterministic; these methods numerically solve the Boltzmann transport equation by applying approximations around the modeled structure. The second is probabilistic and uses Monte Carlo simulations to model statistically the almost exact reactor system and by tracking each particle individually using predetermined nuclear data libraries to determine the average particle behavior [5, 25].

1.4.1. The Monte Carlo method

The Monte Carlo method is a stochastic process based on the selection of random numbers, analogous to throwing “rolling dice” in a gambling casino, thus it is called "Monte Carlo". The Monte Carlo method is essential for simulating nuclear systems also; this method is extremely useful for modeling simulations of shielding criticality, dosimetry, and detector response analysis, etc., with the recent advances in computing technology. The fundamental advantage of Monte Carlo against deterministic codes is that they do not require typical space, energy, and time approximations. This means that somehow the Monte Carlo codes are very well suited to complex problems that cannot be modeled using deterministic methods.

The Monte Carlo technique is very practical in the context of particle transport, as it follows each of several particles from a source throughout their life to their death (e.g. absorption or escaping). To assess the type of interaction, probabilities are coupled with randomly generated numbers at each event in that period, such as crossing a material boundary or undergoing a collision. Probabilities are then again combined to determine the scattering angle and direction, energy transfer, secondary particle output, etc., depending on the form of interaction. The cycle is repeated for each subsequent particle interaction until the end of its life is reached. Moreover, the cycle is repeated over and over until adequate particle history is tracked to ensure a reasonable approximation of actual behavior within the system being studied [26, 27].

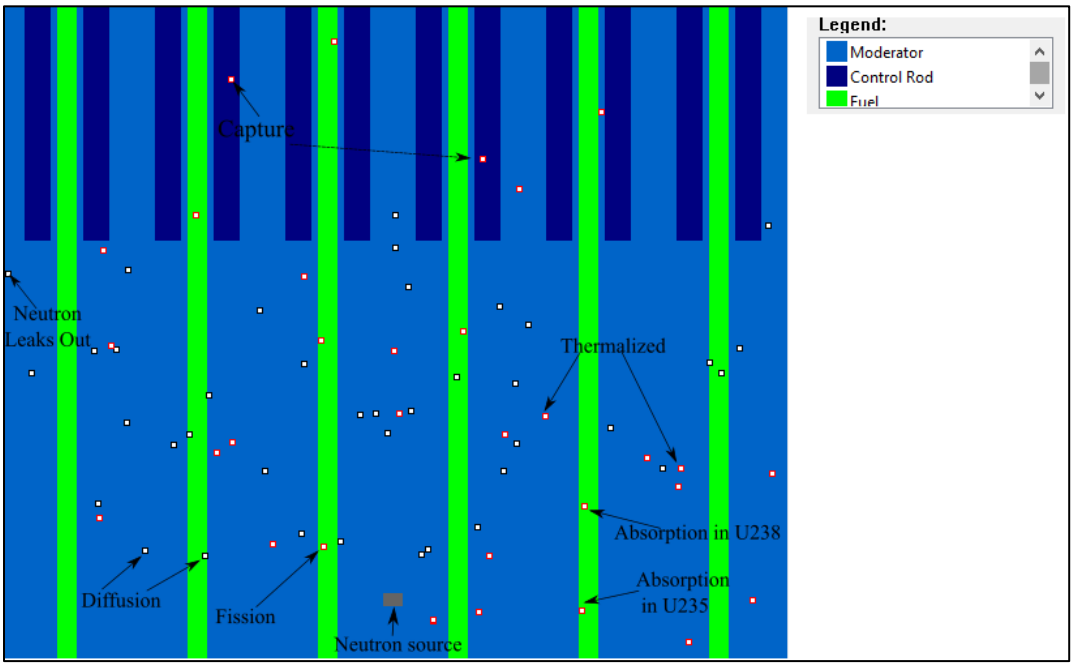

Figure 1. 21. A random history of a neutron incident.

1.4.2. The Monte Carlo N-Particle codes

With recent advances in computing technology, Monte Carlo N-Particle codes are becoming increasingly appealing in the nuclear research field for their ability to simulate a wide range of particle transport scenarios including reactor design, shielding, and dosimetry problems. The MCNP and its variants (i.e. Monte Carlo N-Particle eXtended "MCNPX") were developed by Los Alamos National Laboratory to address the needs of the nuclear engineering community since the codes can describe complex three-dimensional geometries and treat a model using continuous energy, space, and angle. Besides, MCNP codes were extensively benchmarked and widely used as a benchmarking tool for other codes and applications in nuclear engineering. In this thesis, we have used MCNP5, MCNPX 2.6.0, and MCNP6, all codes are briefly described in the following Subsections.

1.4.2.1. MCNP5 code system

The Monte Carlo N-Particle (MCNP) code is an internationally recognized code for analyzing the transport of different particles at varying energies [28]. It is capable of simulating 3D models based on constructive solid geometry with second-order surfaces. MCNP can be used to calculate k_{eff} and many other reactor parameters of interest. Simulations with MCNP or MCNPX require, among other things, an input file that defines the geometry, what isotopes the materials consist of and which nuclear data libraries to use. The continuous-energy particle interaction data is based on an ACE format (A Compact ENDF) that can be generated by NJOY code.

1.4.2.2. MCNPX and MCNP6 code system

MCNPX and MCNP6 [29, 30] are general-purpose, continuous-energy, generalized-geometry, and Monte Carlo transport codes derived from the MCNP code. It can be used for neutron, photon, electron, or coupled neutron/photon/electron transport, including the capacity to figure eigenvalues for critical systems. It helps to generate the 3D model of either simple or complex geometry in detail. It also contains physics subroutines and packages that allow the user to compute phenomena related to fuel burnup including the capability to track fission products. MCNPX performs individual criticality calculations for each time step within the “Burn” card of the input file. The “Burn” card, responsible for burnup calculations, allows the user to pre-define the power level, the duration, the burnable materials, and to specify the fission products MCNPX/MCNP6 should track, as well as the omitted list of isotopes for which cross-section data does not exist in

MCNPX/MCNP6 library. MCNPX/MCNP6 obtains its burnup capability using the CINDER90 library file (Depletion and Decay Chain Calculation for Fission Products in Thermal Reactors) that contains both decay and fission yield data, needed to perform depletion calculations and generate new number densities correspond to the end of each time step (**Figure 1.22**) [29, 31, 32, 20, 33]. An example of data entries for the BURN card in MCNPX/MCNP6 is presented in **Table 1.4** and **Figure 1.23.**

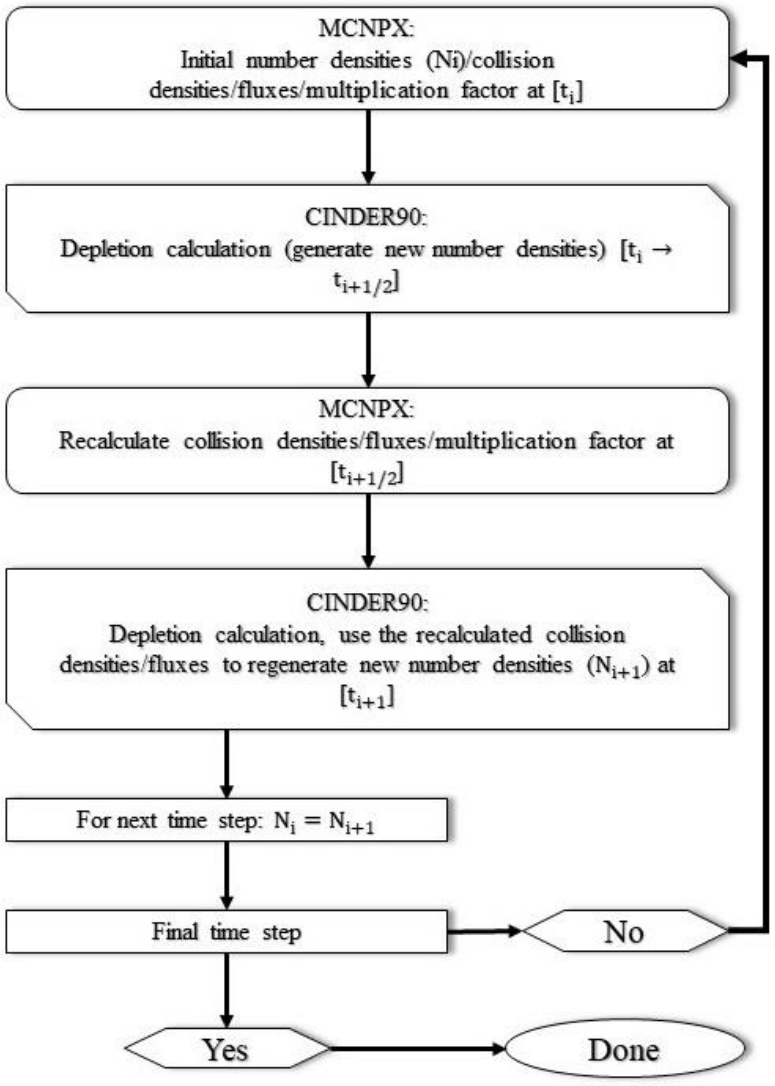

Figure 1. 22. Steady-state Monte Carlo using MCNPX/MCNP6, depletion utilizing CINDER.

Table 1. 4. Depletion/Burnup (BURN) keyword [29].

Data Card	Descriptions
POWER	The reactor operating power in MW (thermal) (e.g. 2MW).

TIME	The reactor operating time in days for each burn cycle (e.g. 50, 50, 100).
PFRAC	The power fraction.
MAT	The materials to be burned.
OMIT	The omitted list of isotopes for which cross-section data does not exist in MCNPX/MCNP6 library.
BOPT = b_1, b_2	b_1 = 1.0; The Q value multiplier. b_2 = -14; b_2 with a value of -14 indicates that the burn output will include the 2-tier fission products arranged based on increasing ZZZAAA displayed at the end of each time step.
MATVOL	The total volume of the materials to be burned (i.e. fuel materials).

```
c ============================================================================================
c data card
c ======================
c ======================
c     Burnup
c ======================
 burn  time= 1,10,20,20,50,50,50,100,100,100,100,100,100,100,100
       mat=1,2,3
       power= 19.63 $ MWt
       PFRAC=1 14r
       AFMIN=1e-20
       omit=1,16,6012,6013,6014,7016,8018,9018,10020,88227,89228
            64151,64159,66159,66157,91230,91232,91233
            2,16,6012,6013,6014,7016,8018,9018,10020,88227,89228
            64151,64159,66159,66157,91230,91232,91233
            3,16,6012,6013,6014,7016,8018,9018,10020,88227,89228
            64151,64159,66159,66157,91230,91232,91233
       BOPT =1 24 1
       MATVOL= 38916.024 10701.9066 972.9006 $ Total fuel volume [312 is the number of fuel rod in the fuel assembly]
c ======================
```

Figure 1. 23. Example of a depletion entry.

1.4.3. Particle tracking in MCNP

As already noted, a particle is followed throughout its lifetime from its birth (e.g. source) to its death (e.g. capture) **Figure 1.21**. When following a neutron, MCNP begins checking whether it interacts with a mechanism or not [34]. The probability of the first collision between s and $s + ds$ occurring along its flight line is:

$$p(s)ds = e^{-\Sigma_t s}\Sigma_T ds \tag{1.17}$$

Σ_t is the total macroscopic cross-section. Creating a random number $\boldsymbol{\zeta}$ distributed uniformly on $[0, l)$, with the flight line to l, to be:

$$\boldsymbol{\zeta} = \int_0^{\boldsymbol{l}} p(s)ds = 1 - e^{-\Sigma_t l} \tag{1.18}$$

That could be written as:

$$l = -\frac{1}{\Sigma_t} ln(1 - \boldsymbol{\zeta}) \tag{1.19}$$

Since $(1 - \boldsymbol{\zeta})$ is distributed in the same way as $\boldsymbol{\zeta}$, it is possible to rewrite the equation and obtain an expression for the distance to the collision [34];

$$l = -\frac{1}{\Sigma_t} ln(\boldsymbol{\zeta}) \tag{1.20}$$

Besides, the following pattern occurs when a particle (representing any number of neutrons, depending on the weight of the particle) collides with a nucleus:

a) The collision nuclide is identified;

If the material in which the collision occurred is formed by *N* different nuclides, and if $\boldsymbol{\zeta}$ is a random number at the unit interval $[0, l)$, then the j^{th} nuclide is chosen as the collision nuclide if;

$$\sum_{i=1}^{j-1} \Sigma_{t,i} < \boldsymbol{\zeta} \sum_{i=1}^{N} \Sigma_{t,i} < \sum_{i=1}^{j} \Sigma_{t,i} \tag{1.21}$$

$\Sigma_{t,i}$ is the total macroscopic cross-section of nuclide "i".

b) Either the thermal scattering treatment $\mathbf{S(\alpha, \beta)}$ is used or the velocity of the target nucleus is sampled for low-energy neutrons;

The wavelengths of neutrons at high energies are low; it is fair to treat scattering as classic particle collisions (i.e. based on velocity). However, at thermal energies, neutron wavelengths approach the size of molecules and the spacing of crystalline lattices. Scattering is indeed a quantum mechanical problem. In MCNP applications, the thermal motion cannot be ignored without obtaining significant errors in the estimated results. MCNP uses a thermal treatment based on the free gas approximation to correct the thermal motion. This procedure assumes that the medium is a free gas and therefore that the elastic scattering cross-section at zero temperature is almost independent of the energy of the neutron in the context of atomic weight and neutron energy where thermal effects are important and the reaction cross-sections are nearly independent of temperature [34].

With the assumptions set out above, the free gas thermal treatment consists of adjusting the elastic cross-section and taking into account the velocity of the target nucleus when measuring the kinematics of a collision. The MCNP free gas thermal treatment applies effectively only to elastic scattering. Besides, cross-section libraries processed by NJOY already include Doppler broadening of elastic, capture, fission, and other low-threshold absorption cross-sections(< 1 eV). Contrariwise, NJOY does not broaden the inelastic cross-sections. For more information about the theoretical basis for the thermal scattering treatment, we refer to the following References [12, 17, 28, 34].

c) The neutron absorption is accrued (i.e. the disappearance of neutrons by any process);

Capture can be treated in two ways: analog (explicit) absorption and implicit absorption. Either way, the incoming neutron energy incident does not involve the relative velocity of the targeted nucleus from the free gas thermal treatment since it is presumed that the nonelastic reaction cross-sections are almost independent of temperature [34]. Furthermore, the terms "absorption" and "capture" are used interchangeably for non-fissile nuclides, both meaning $(\mathrm{n}, 0\mathrm{n})$. However, "absorption" involves all capture and fission reactions for fissile nuclides.

- Analog absorption, which is normal capturing, when the neutron is absorbed with the probability of $\frac{\sigma_a}{\sigma_t}$, where σ_a and σ_t are the absorption and total cross-sections of the collision nuclide at the incoming neutron energy.
- Implicit absorption, also called survival biasing (default in MCNP), occurs when the neutron has a weight W_n to which the absorption is reduced. (After capture, the neutron is still alive but its contribution is smaller).

$$W_n = \left(1 - \frac{\sigma_a}{\sigma_t}\right) * W_n \tag{1.22}$$

d) Elastic and inelastic scattering;

Whereby the treatment $S(\alpha, \beta)$ is not used, either elastic scattering or inelastic reactions are chosen. The new energy and direction of the outgoing track is determined. The probability of the reaction being elastic scattering is:

$$\frac{\sigma_{el}}{\sigma_{inel} + \sigma_{el}} = \frac{\sigma_{el}}{\sigma_t - \sigma_a} \tag{1.23}$$

Where

σ_{el} is the elastic scattering cross-section.

σ_{inel} is the inelastic cross-section; includes any neutron-out process; (n, n'), (n, f), (n, np), etc.

σ_a is the absorption cross-section; $\sum \sigma(n, x)$, where x ≠ n that is, all neutrons disappearing reactions

σ_t is the total cross-section; $\sigma_t = \sigma_{el} + \sigma_{el} + \sigma_a$

both σ_{el} and σ_t are adjusted for the free gas thermal treatment at thermal energies.

If the collision is determined to be inelastic, the type of inelastic reaction, N, is sampled from

$$\sum_{i=1}^{j-1} \sigma_i < \zeta \sum_{i=1}^{N} \sigma_i < \sum_{i=1}^{j} \sigma_i \tag{1.24}$$

where σ_i is the i^{th} inelastic reaction cross-section at the incident neutron energy.

e) The S(α, β) treatment is used instead of elastics/inelastic scattering if the energy of the neutron is low enough and the appropriate S(α, β) table is present

The S(α, β) thermal scattering treatment is a clear reflection of the molecules and crystalline solids scattering thermal neutrons. Two processes are required: i) inelastic dispersion with a cross-section σ_{in}, and a mixed energy-angle representation derived from an ENDF S(α, β) scattering law; ii) and elastic dispersion without any change in the outgoing neutron energy for solids with a cross-section σ_{el} and angular treatment derived from lattice parameters. The elastic scattering treatment is fundamental for finer modeling of the neutron interactions at energies below ~ 4 eV. This thermal scattering treatment also allows the representation of scattering by multiatomic molecules (for example, ZrH, BeO, UO_2, etc.) [18, 19, 20, 34, 35].

1.4.4. Depletion calculation in MCNPX and MCNP6

Over time, the composition of the irradiated locations varies by nuclear reactions and phenomena of radioactive decay. The concentrations $N_i(t)$ of the radioactive nuclei of species "i", obey linear coupled differential equations called Bateman's equations [5, 31], generally written in the form:

$$\frac{dN_i(t)}{dt} = B_i + \sum_{j \neq i} C_{ij}.N_j(t) - C_{ii}.N_i(t) \quad (1.25)$$

where the coefficient C_{ij} is the transmutation rate of the nucleus of species j into the nucleus of species i following a radioactive decay or nuclear reaction phase. The coefficient C_{ii} is the disappearance rate of the nucleus of species i, and the coefficient B_i indicates a constant source term per irradiation step and feeding nuclide i. For a single fissile isotope, the evolution of the concentrations of fission products, which mainly contribute to the so-called delayed photonic emissions, can be expressed as follows:

$$B_i = N_f.\sigma_f.\varphi.Y_{fi}$$

$$C_{ij} = \lambda_{ij} + \sigma_{ij}.\varphi$$

$$C_{ii} = \lambda_i + \sigma_i.\varphi$$

with N_f the number of fissile nuclei, σ_f the fission cross-section, Φ the neutron flux, Y_{fi} the fission yield of isotope i, λ_{ij} the radioactive decay constant from isotope j to isotope i, σ_{ij} the reaction cross-section from j to i, λ_i the radioactive decay constant of isotope i, and σ_i the absorption cross-section of isotope i.

There are various ways to solve Bateman's equations. CINDER90, therefore, uses a simplified form to solve the Bateman differential equations to characterize the depletion of a particular nuclide [36][37][31].

$$\frac{dN_i(t)}{dt} = -N_i(t)\beta_i + \sum_{j \neq i} N_j(t)\gamma_{j \to i} + \overline{Y_i} \quad (1.26)$$

where $\frac{dN_i(t)}{dt}$ is the rate of change of the nuclide density of i, $-N_i(t)\beta_i$ is the destruction rate of nuclide i, $\sum_{j \neq i} N_j(t)\gamma_{j \to i}$ is the creation of nuclide i via other nuclides in the system, $\overline{Y_i}$ is the production rate of i from an external source.

In fact, solving the time-dependent change of a specified nuclide often requires an understanding of the time-dependent variation of each participating nuclide. Thus, the solution of

each time-dependent change in nuclides requires the resolution of a set of coupled differential equations. Although it is a clear mathematical mechanism to solve a series of coupled linear differential equations, the coefficients in the coupled depletion equations are nonlinear thus making the equations unsolvable without approximation [31]. Expanding the coefficient of destruction, β, and the coefficient of creation, $\gamma_{j\to i}$:

$$\beta_i = \lambda_i + \sum_r \int \sigma_{i,r}(E)\varphi(r,E,t)dE$$

$$\gamma_{j\to i} = \sum_{i\neq j} L_{ji}\lambda_j + \sum_{i\neq j}\sum_r \int \gamma_{ji,r}(E)\sigma_{j,r}(E)\varphi(r,E,t)dE$$

where λ_i is the destruction rate of i by radioactive decay, $\sum_r \int \sigma_{i,r}(E)\varphi(r,E,t)dE$ is the destruction of nuclide i by transmutation reaction, $\sum_{i\neq j} L_{ji}\lambda_j$ is the creation of nuclide i by some isotope radioactively decaying to isotope i, $\sum_{i\neq j}\sum_r \int \gamma_{ji,r}(E)\sigma_{j,r}(E)\varphi(r,E,t)dE$ is the summation of the production rate of i by transmutation of all other nuclides summed over all transmutation reactions.

1.4.5. Convergence of keff

Since the majority of the investigation focuses on determining the criticality characteristics, the KCODE card in MCNP conducts the criticality calculations, which specify the criticality source used to evaluate the keff. A typical KCODE card is represented by the following variables (all the italicized variables display given values by the user) in the input file:

KCODE nrsck rkk ikz kct

Where "nrsck" is the number of source histories (neutrons) per cycle, "rkk" is the initial guess of keff, "ikz" is the number of cycles to be skipped (to guarantee convergence before averaging calculations) and "kct" is the number of cycles to be performed. An example of a KCODE input is {KCODE 20,000 1.0 100 600}. This means that for each cycle (i.e. each generation of neutrons), MCNP will sample and track 20,000 starting neutrons, and the initial estimate for keff is 1.0. The first 100 cycles will be skipped so that equilibrium can be reached between the fission positions. MCNP will start an average of the measured keff from each cycle from the 101^{th} cycle. When all 600 cycles are complete, a final result is obtained for the keff. Besides, there are several available

methods to determine a neutron source in the input file, e.g. the KSRC or the SDEF card. The KSRC card allows the user to predefine neutron sources with Cartesian coordinates (i.e. x, y, and z). While the SDEF card is used to uniformly describe source points in a volume with specific source parameters.

Another point to consider in the calculation of the MCNP is the expected statistical uncertainty associated with the result (i.e. estimated standard deviation), since such a Monte Carlo result without associated uncertainty is essentially meaningless [27]. The result of a simulation in Monte Carlo designed to calculate a parameter defined x, an average value $\bar{x}$ (obtained on a set of N simulated histories) and a standard deviation σ proportional to $1/\sqrt{N}$ as defined in the central limit theorem. When N tends to infinity, the central limit theorem allows the confidence intervals to be defined at 1σ and 2σ as $P(\bar{x} - \sigma < x < \bar{x} + \sigma) = 68\%$ and $P(\bar{x} - 2\sigma < x < \bar{x} + 2\sigma) = 95\%$ [27, 34]. The simplest method to reduce the standard deviation and have an acceptable confidence interval is to simulate more histories (i.e. the number of particles tracked in the simulation). In general, according to the Strong Law of Large Numbers, the relative error (R) for certain measured quantities determined in each iteration is defined by **Equation (1.27)** [38]. However, that requires more computing time and is not enough for some problems since the confidence statements correspond only to the precision of the Monte Carlo calculation itself and not to the accuracy of the results of the true physical value. Hence, a combination between the desired accuracy and computational time must be achieved. The sensitivity of a sample criticality measure to, active cycles, inactive cycles, and particles per cycle is shown in **Table 1.5**.

$$R = \frac{1}{\bar{x}}\sqrt{\frac{\overline{x^2} - \bar{x}^2}{N-1}} \tag{1.27}$$

where:

$$\bar{x} = \frac{1}{N}\sum_n x_n \;\; and \;\; \overline{x^2} = \frac{1}{N}\sum_n {x_n}^2 \tag{1.28}$$

and, the measured standard deviation by MCNP calculation is given by:

$$S = \sqrt{\frac{\sum_{i=1}^{N}(x_i - \bar{x})^2}{N-1}} \cong \sqrt{\overline{x^2} - \bar{x}^2} \tag{1.29}$$

Table 1. 5. Multiplication factor sensitivity to, active cycles, inactive cycles, and particles per cycle; benchmark name “heu-met-fast-001-case-1 (Godiva)”.

Test on: Number of Active Cycles					
Particles per cycle	Inactive cycle	Active cycle	Total Active Particles	keff	σ
50,000	100	100	5,000,000	0.99986	0.00028
50,000	100	200	10,000,000	1.00007	0.00018
50,000	100	300	15,000,000	0.99990	0.00015
50,000	100	400	20,000,000	0.99986	0.00013
50,000	100	500	25,000,000	0.99989	0.00012
Test on: Number of Inactive Cycles					
Particles per cycle	Inactive cycle	Active cycle	Total Active Particles	keff	σ
50,000	25	500	25,000,000	0.99994	0.00012
50,000	50	500	25,000,000	0.99995	0.00012
50,000	75	500	25,000,000	0.99993	0.00012
50,000	100	500	25,000,000	0.99989	0.00012
50,000	125	500	25,000,000	0.99990	0.00012
Test on: Number of Particles Per Cycle					
Particles per cycle	Inactive cycle	Active cycle	Total Active Particles	keff	σ
10,000	100	500	5,000,000	0.99963	0.00027
20,000	100	500	10,000,000	0.99987	0.00018
30,000	100	500	15,000,000	1.00028	0.00015
40,000	100	500	20,000,000	0.99999	0.00012
50,000	100	500	25,000,000	0.99989	0.00012

1.4.6. Source convergence use of Shannon's entropy

Convergence in MCNP is examined by the user and is done by checking convergence for both keff and the fissions source distribution using Shannon entropy. In Shannon entropy, the convergence for keff is checked by measuring the number of cycles at each cycle against the keff values. This allows visual control of whether or not the keff has converged. Shannon entropy is a

quantity determined by MCNP5/MCNP6 for the distribution of the fission source. The Shannon entropy converges to a steady-state value as the source distribution approaches convergence, which indicates convergence. If any of these measurements (i.e. keff and Shannon entropy) does not converge before the start of the active cycles, then the measurement results would be biased. Therefore, convergence can be achieved by maximizing the number of cycles missed or by increasing the number of source neutrons [39, 40]. The Shannon entropy (H_{src}) is then defined to be:

$$H_{src} = -\sum_{j=1}^{N_s} P_J \ln(P_J) \tag{1.30}$$

where N_s is the total number of grid boxes in the imposed mesh, and P_J is the source distribution normalized to unity, it is the number of fission points in a bin divided by the total number of fission points in the system.

1.4.7. Flux and power estimators in MCNP

In general, Monte Carlo physics obtains results by simulating individual particles and tracking their average behavior by certain physical quantities (Tallies). Examples of Monte Carlo Tallies' cards include surface flux, cell flux, energy deposition, and fission energy deposition or pulse height Tally. In the MCNP calculations, the user should first specify the type of particle to be tracked in the Tally. All Tallies are normalized per source particle. In a fixed source simulation, the number of source particles per second is known. However, in a reactor-specific criticality calculation, reaction rates must be normalized by the equivalent number of neutrons per second for a user-specified power value supposed to be constant. The power in a given geometry can be estimated by the deposition of the cell fission energy "F7 Tally", and the flux in the geometry by "F4 Tally". MCNP estimates the cell flux using **Equation (1.31)** and the fission energy deposition by **Equation (1.32)**.

$$\Phi_{\mathrm{F4}}\left[\frac{particles}{cm^2}\right] = \int dE \int dt \int dV \int \frac{1}{V} d\Omega \phi(\vec{\boldsymbol{r}},, \vec{\Omega}, t) = wT_i \frac{\rho}{V} \tag{1.31}$$

where w is the particle weight, T_i is the track length cm, it is the transit time by particle velocity, ρ is the atom density, and V is the cell volume.

$$H_{fission}\left[\frac{MeV}{g}\right] = wT_i\sigma_f(E)\frac{\rho}{m} = Q\frac{\rho}{m}\int dE\int dt\int dV\int d\Omega\sigma_f(E)\phi\left(\vec{r},,\vec{\Omega},t\right) \qquad (1.32)$$

where $\sigma_f(E)$ is the microscopic fission cross-section at the energy E, Q is the energy emitted per fission of the fissioning nuclide, and m is the cell mass.

To get the absolute comparison with the measured quantities, the MCNP results should be properly normalized to the steady-state thermal power of the system. The Monte Carlo source normalization factor for the F4 and F7 Tallies was estimated as follows [28]:

$$\mathrm{S} = \frac{\bar{\nu}\left(\frac{\text{neutron}}{\text{fission}}\right) * \mathrm{P[W]}}{\epsilon\left(\frac{\text{MeV}}{\text{fission}}\right) * 1.602.10^{-13}\left(\frac{\text{J}}{\text{MeV}}\right) * \mathrm{k_{eff}}} \qquad (1.33)$$

Where $\bar{\nu}$ is the average number of neutrons released by fission, P the reactor power and $\epsilon\left(\frac{\text{MeV}}{\text{fission}}\right)$ the energy released by fission.

Therefore:

$$\Phi\left(\frac{\text{neutron}}{\text{cm}^2.\text{s}}\right) = \mathrm{S} * \Phi_{\mathrm{F4\ Tally}}\left(\frac{particles}{\text{cm}^2}\right) \qquad (1.34)$$

Chapter 2: Benchmark problem

Benchmarking the processed library is a very important step towards creating a validated application library for its use in the analysis of nuclear systems. This is mainly achieved by validating them against experimental data or standard benchmarks. The main aim of a benchmark is to decouple the relative contribution to the error in the measured parameters from the basic nuclear data and those resulting from the limitations of the library format, data processing assumptions, and approximations in the calculation models. These benchmarks are usually chosen as a function of the application purpose to which the library is to be applied, such as nuclear reactors or shielding applications. In general, the benchmark choices are selected on the basis that they include a variety of material types used in the existing nuclear systems because it is difficult to provide comparisons for every material.

The selected benchmarks described below are part of standard problem exercises aimed at establishing the robustness of criticality safety computational methods (i.e. they were used as a tool to check computational procedures or to check data) for large arrays of fissile materials and spent fuel (i.e. criticality benchmarks), shielding benchmarks (i.e. Oktavian benchmarks), and reactivity benchmarks ((i.e. Doppler benchmarks).

2.1. Characteristics of the analyzed benchmark problems

2.1.1. ICSBEP criticality benchmarks

The criticality benchmarks used were taken from the International Handbook of Evaluated Criticality Safety Benchmark Experiments (ICSBEP) [41]. As well known, the ICSBEP handbook contains a large verified collection of criticality data of various kinds of systems. The benchmarks are defined using an XXX-YYY-ZZZ-aaa.b abbreviation. The XXX defines the fuel system and includes Pu for Pu-239 fueled systems, and HEU, IEU, and LEU for highly-enriched, intermediate-enriched, and low-enriched U-235 fuel systems, respectively. U233 defines the U-233 fueled systems, and MIX is used for mixed fuel systems (e.g. U-235 and Pu-239). The YYY defines the chemical form of the fuel, with MET meaning a metal system, SOL being a solution, and COMP a compound. ZZZ is used to define the average fission energy. FAST is used for a fast energy spectrum (i.e. more than 50% of the fissions occur above 100 KeV). THERM is used for a thermal energy spectrum (i.e. more than 50% of the fissions occur below 0.625 eV), INTER is used when

50% or more of the fissions occur between these energy limits, and MIXED is used when no energy interval has 50% or more fissions. Finally, aaa.b is a simple numerical index, and .b represents the case number when multiple experiments are described for one evaluation. Besides, the ordinary water acting as the primary moderator and reflector, other reflectors were also included such as graphite, beryllium, molybdenum, and other materials or unreflected systems. The list of ICSBEP abbreviations and brief descriptions of the experiments are listed in **Table 2.1**.

Table 2. 1. Summary of ICSBEP abbreviations used [42].

Abbreviation	Meaning
Fissile material	
HEU	High enriched uranium (^{235}U ≥ 60 wt.%)
IEU	Intermediate or mixed enrichment uranium (60 wt.% > ^{235}U > 10 wt.%)
LEU	Low enriched, natural, or depleted uranium (^{235}U ≤ 10 wt.%)
PU	Plutonium
MIX	Mixed uranium and plutonium
U-233	Uranium ^{233}U systems
Physical form of fissile material	
MET	Metal
SOL	Solution
COMP	Compound system, e.g. lattice in water
Spectrum	
FAST	Fast system (≥50% of fissions above 100 keV)
THERM	Thermal system (≥50% of fissions below 0.625 eV)

2.1.2. Time-of-flight experiment benchmarks at oktavian facility

The Oktavian neutron source facility at Osaka University was designed to provide an intense 14 MeV D-T neutron source for fusion nuclear engineering studies. The project studies were carried out in the mid-1970s, and the construction period lasted from late 1978 until early 1980. The experimental arrangement is highlighted in **Figure 2.1**. The D-T neutrons were produced by bombarding a 370 GBq tritium target placed at the center of the pile with a 250 keV deuteron beam. The pile covers multiple types of materials like Aluminum (Al), Cobalt (Co), Chromium (Cr), Copper (Cu), Lithium Fluoride (LiF), Manganese (Mn), Molybdenum (Mo), Niobium (B), Silicon Si), Titanium (Ti), Tungsten (W), and Zirconium (Zr). A cylindrical liquid-organic scintillator NE-218 was used as a neutron detector, which was located at about 11 m from the tritium target and 55 deg. concerning the deuteron beam axis, surrounded by concrete and heavy concrete. To reduce the background neutrons, a pre-collimator made of polyethylene-iron multi-

layers was set between the pile and the detector. The neutron leakage spectra from the piles were measured by the time-of-flight (TOF) technique [43, 44, 45, 46, 47, 48]. Examples of the studied piles are presented in **Figures 2.2** and **2.3**. The material densities and outer diameters of the vessels are summarized in **Table 2.2,** and an example of MCNP input is given in **Figure 2.4**.

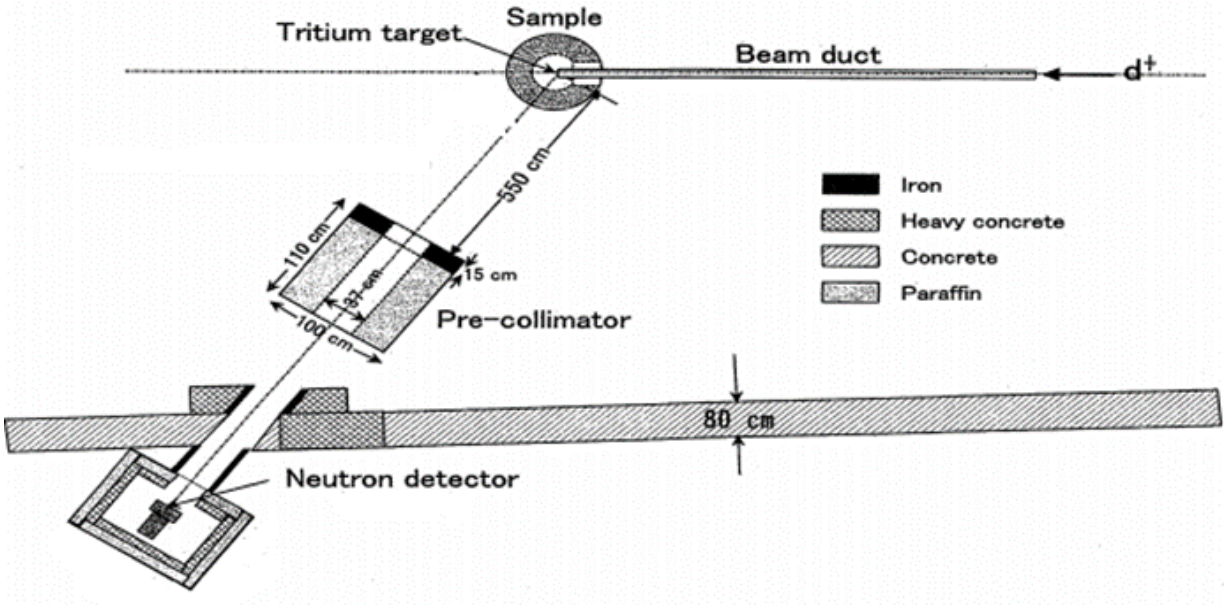

Figure 2. 1. The experimental arrangement at Oktavian.

Table 2. 2. Material density and the outer diameter of the vessel.

Material		Apparent density (g/cm3)	The outer diameter of the vessel (Cm)
Aluminum	Al	1.22	40
Cobalt	Co	1.94	40
Chromium	Cr	3.72	40
Copper	Cu	6.23	61
Lithium Fluoride	LiF	1.79	61
Manganese	Mn	4.37	61
Molybdenum	Mo	2.15	61
Niobium	Nb	4.39	28
Silicon	Si	1.29	60
Titanium	Ti	1.54	40
Tungsten	W	4.43	40
Zirconium	Zr	2.84	61

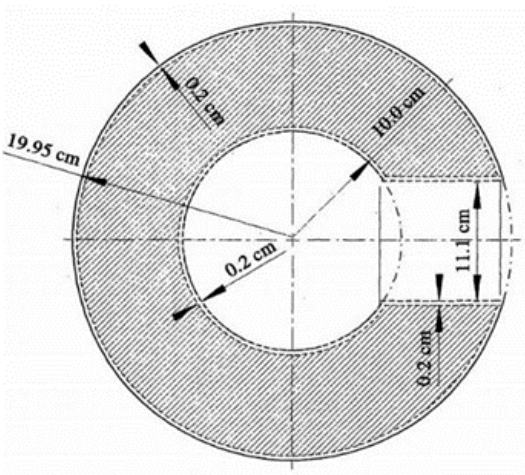

Figure 2. 2. Schematic drawing of the Oktavian geometry for the Al benchmark.

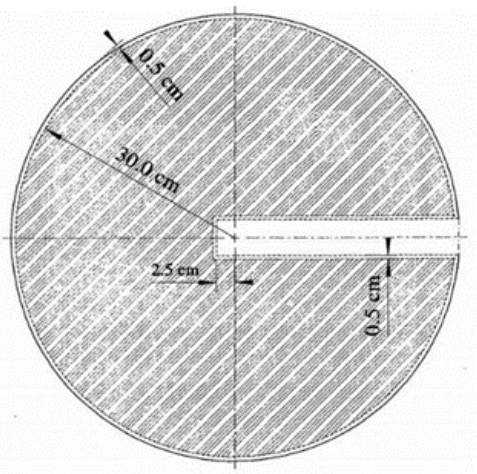

Figure 2. 3. Schematic drawing of the Oktavian geometry for the Zr benchmark.

```
c     Created on: Friday, December 01, 2017 at 10:49
    1     3 -0.001225 (-3 -8 ):(8 -1 -6 )
    2     2  -7.824 (-4 3 -8 ):(8 -2 1 -6 )
    3     1   -1.22 (-5 4 -8 ):(-5 2 8 )
    4     2  -7.824 (-6 5 -8 ):(-6 5 8 2 )
    5     3 -0.001225 -7 6
    6     0         7

    1        cx 5.5
    2        cx 5.7
    3        so 10
    4        so 10.2
    5        so 19.8
    6        so 20
    7        so 100
    8        px 8.32

mode  n
m1    13027.80c             -1  $MAT1
m2    6000.80c      -0.0003  $MAT2
      14000.80c      -0.005 15031.80c   -0.000225 16000.80c    -0.00015
      24050.80c    -0.00793 24052.80c   -0.159031 24053.80c   -0.018378
      24054.80c   -0.004661 25055.80c       -0.01 26054.80c   -0.039996
      26056.80c   -0.644764 26057.80c   -0.015026 26058.80c   -0.002039
      28058.80c    -0.06234 28060.80c   -0.024654 28061.80c   -0.001085
      28062.80c   -0.003504 28064.80c   -0.000917
m3    7014.80c    -0.755636  $MAT3
      8016.80c    -0.231475 18000.80c   -0.012889
imp:n   1 3r         0 1r          $ 1, 6
sdef  pos = 0.0 0.0 0.0 cel=1 erg = d1
c     *** ENERGY BIN FOR SOURCE NEUTRON ***
si1   1.000E-01 1.120E-01 1.260E-01 1.410E-01 1.590E-01
      1.780e-01 2.000E-01 2.240E-01 2.520E-01 2.830E-01
      3.170e-01 3.560E-01 4.000E-01 4.490E-01 5.040E-01
      5.660e-01 6.350E-01 7.130E-01 8.000E-01 8.780E-01
      9.640e-01 1.058E+00 1.162E+00 1.275E+00 1.400E+00
      1.542e+00 1.698E+00 1.871E+00 2.061E+00 2.270E+00
      2.500e+00 2.704E+00 2.924E+00 3.162E+00 3.419E+00
      3.699e+00 4.000E+00 4.165E+00 4.337E+00 4.516E+00
      4.703e+00 4.897E+00 5.099E+00 5.310E+00 5.529E+00
      5.757e+00 5.995E+00 6.242E+00 6.500E+00 6.765E+00
```

```
     7.041e+00 7.327E+00 7.627E+00 7.938E+00 8.261E+00
     8.598e+00 8.949E+00 9.314E+00 9.693E+00 1.009E+01
     1.050e+01 1.082E+01 1.114E+01 1.148E+01 1.183E+01
     1.218e+01 1.255E+01 1.277E+01 1.300E+01 1.324E+01
     1.348e+01 1.372E+01 1.397E+01 1.422E+01 1.447E+01
     1.474e+01 1.500E+01 1.527E+01 1.554E+01 1.583E+01
     1.611e+01 1.640E+01
c    *** SOURCE DISTRIBUTION ***
sp1   0.000E-04 0.000E-00 0.000E-00 1.270E-04 5.774E-05
     2.536e-04 2.722E-04 2.076E-04 4.366E-04 3.873E-04
     4.756e-04 6.161E-04 6.727E-04 6.648E-04 8.581E-03
     1.098e-03 1.184E-03 1.412E-03 1.616E-03 1.546E-03
     1.556e-03 1.631E-03 1.771E-03 1.804E-03 1.823E-03
     1.891e-03 1.935E-03 2.002E-03 2.052E-03 2.004E-03
     2.068e-03 2.091E-03 3.354E-03 1.492E-03 1.322E-03
     1.451e-03 1.401E-03 7.112E-04 6.423E-04 6.514E-04
     6.195e-04 6.428E-04 6.209E-04 5.788E-04 5.227E-04
     5.250e-04 5.456E-04 5.106E-04 5.789E-04 5.391E-04
     4.998e-04 4.813E-04 5.300E-04 5.756E-04 5.230E-04
     5.394e-04 6.256E-04 7.047E-04 7.729E-04 7.951E-04
     8.659e-04 8.106E-04 8.923E-04 1.022E-03 1.281E-03
     1.687e-03 2.286E-03 1.825E-03 2.479E-03 3.794E-03
     7.010e-03 1.565E-02 3.634E-02 7.492E-02 1.279E-01
     1.768e-01 1.916E-01 1.500E-01 8.676E-02 3.950E-02
     1.430e-02 4.269E-03
c    ***** TALLY CARDS *****
F21:n 6
c    ***** ENERGY BIN *****
E21   1.000E-03 1.290E-03 1.670E-03 2.150E-03
     2.780e-03 3.590E-03 4.640E-03 5.990E-03 7.740E-03
     1.000e-02 1.290E-02 1.670E-02 2.150E-02 2.780E-02
     3.590e-02 4.640E-02 5.990E-02 7.740E-02
     1.000e-01 1.120E-01
     1.260e-01 1.410E-01 1.590E-01 1.780E-01 2.000E-01
     2.240e-01 2.520E-01 2.830E-01 3.170E-01 3.560E-01
     4.000e-01 4.490E-01 5.040E-01 5.660E-01 6.350E-01
     7.130e-01 8.000E-01 8.780E-01 9.640E-01 1.058E+00
     1.162e+00 1.275E+00 1.400E+00 1.542E+00 1.698E+00
     1.871e+00 2.061E+00 2.270E+00 2.500E+00 2.704E+00
     2.924e+00 3.162E+00 3.419E+00 3.699E+00 4.000E+00
     4.165e+00 4.337E+00 4.516E+00 4.703E+00 4.897E+00
     5.099e+00 5.310E+00 5.529E+00 5.757E+00 5.995E+00
     6.242e+00 6.500E+00 6.765E+00 7.041E+00 7.327E+00
     7.627e+00 7.938E+00 8.261E+00 8.598E+00 8.949E+00
     9.314e+00 9.693E+00 1.009E+01 1.050E+01 1.082E+01
     1.114e+01 1.148E+01 1.183E+01 1.218E+01 1.255E+01
     1.277e+01 1.300E+01 1.324E+01 1.348E+01 1.372E+01
     1.397e+01 1.422E+01 1.447E+01 1.474E+01 1.500E+01
     1.527e+01 1.554E+01 1.583E+01 1.611E+01 1.640E+01
c    ***** ************************** *****
cut:n   1.0e6 0.0 -0.5 -0.25 0
c    ***** NEUTRON HISTORY *****
nps    500000000
print
```

Figure 2. 4. Example of input data for MCNP calculations.

2.1.3. Benchmarks for the Doppler reactivity defect

The Doppler-defect Benchmarks have been proposed in 1991 to assess the Doppler coefficient of reactivity feedback for 2D cells. They have relatively simple geometries (**Figure 2.6**) and they hold all of the important contributors to Doppler reactivity feedback. The benchmark data are based on previous benchmark studies and they include seven different fuel enrichments of a typical pressurized water reactor (PWR) LWR-UO_2 lattice, five different mixed oxides (MOX)

concentrations of Reactor-grade fuel and four different MOX concentrations of Weapons-grade fuel. The benchmark configuration corresponds to an infinite corresponding pair of cells (the hot zero and the hot full power) at the beginning of life consisting of fuel. At the Hot Zero Power (HZP), the temperature for fuel, cladding, and the borated moderator is a uniform 600 K. At the Hot Full Power (HFP), the fuel temperature is 900 K, while the temperature of everything else still at 600 K. The Doppler defect is evaluated as the reactivity change between HFP and HZP conditions [49, 50, 51, 52]. The geometry specification and the isotopic concentrations in the fuel, the cladding, and the moderator are given in **Tables 2.3** to **2.6**. The Doppler defect theory and the calculation method are defined in chapter 4.

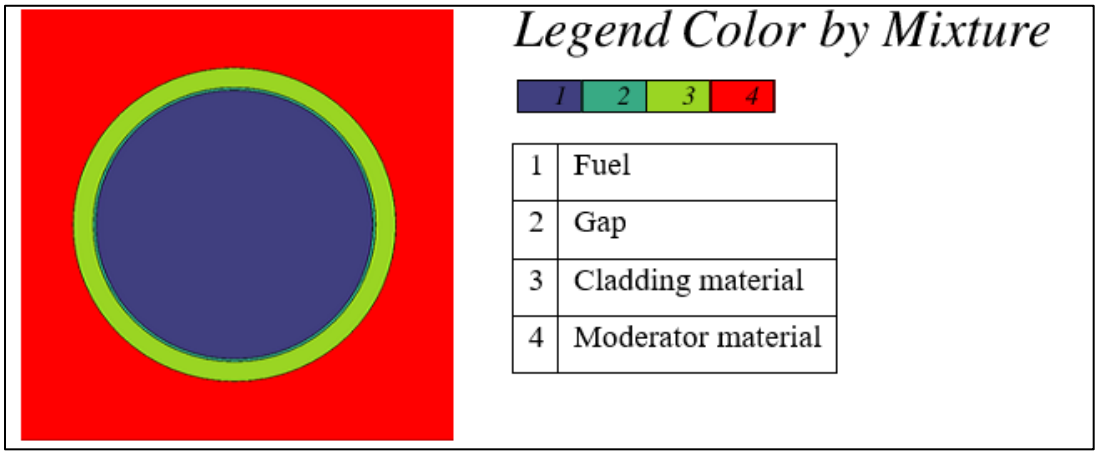

Figure 2. 5. Pin cell model.

Table 2. 3. Pin cell dimensions for different temperatures.

Parameter	HZP	HFP
Unit cell pitch, (cm)	1.26678	
Outer radius of fuel, (cm)	0.39398	0.39433
Inner radius of cladding, (cm)	0.40226	0.40226
Outer radius of cladding, (cm)	0.45972	0.45972
Cladding material	Zirconium	
Moderator material	Water with 1400 ppm of Boron	

Table 2. 4. Plutonium isotopics (wt.%).

Fuel	Pu-239	Pu-240	Pu-241	Pu-242
Reactor-Recycle MOX	45.0	30.0	15.0	10.0
Weapons-Grade MOX	93.6	5.9	0.4	0.1

Table 2. 5. Fuel density for different temperatures.

		The density of fuel (g/cm3)
UO_2 fuels	600K	10.3390
	900K	10.3120
Reactor-Recycle MOX fuels	600K	10.3376
	900K	10.3106
Weapons-Grade MOX fuels	600K	10.3376
	900K	10.3106

Table 2. 6. Atomic densities for cladding and moderator.

Materials	Isotope	Number density (atoms/b-cm)
Cladding	Zr-Nat	4.21838E-02
Moderator	^{1}H	4.42326E-02
	^{10}B	1.02133E-05
	^{11}B	4.11098E-05
	^{16}O	2.21163E-02

2.2. Appendix

Table 2. 7. Characteristics of the ICSBEP benchmarks.

LEU Benchmarks				
Spectrum	Form	Shape	Moderator and/or Reflector	Benchmark name
Thermal	UO_2	Lattice	UO_2 rods, Water	leu-comp-therm-008-case_1
				leu-comp-therm-008-case_2
				leu-comp-therm-008-case_5
				leu-comp-therm-008-case_7
				leu-comp-therm-008-case_8
				leu-comp-therm-008-case_11
	Solution	Sphere	Water	leu-sol-therm-002-case1
			Unreflected	leu-sol-therm-002-case2
IEU Benchmarks				
Fast	Metal	Spheres	Unreflected	ieu-met-fast-003-case2
			Steel	ieu-met-fast-005-case2
			Duralumin	ieu-met-fast-006-case2
			Graphite	ieu-met-fast-004-case2
		Cylinder	Unreflected	ieu-met-fast-001-case1
				ieu-met-fast-001-case2
				ieu-met-fast-001-case3
				ieu-met-fast-001-case4
			Normal U	ieu-met-fast-002
			Depleted U	ieu-met-fast-007-case1
Intermediate	Plate	Lattice	Normal U, steel	mix-met-fast-008-case7

Thermal	UO_2	Lattice	Water	ieu-comp-therm-002-case3
	Solution	Cylinder	Unreflected	leu-sol-therm-007-case14
				leu-sol-therm-007-case30
				leu-sol-therm-007-case32
				leu-sol-therm-007-case36
				leu-sol-therm-007-case49
HEU Benchmarks				
Fast	Metal	Spheres	Unreflected	heu-met-fast-001
				heu-met-fast-008
				heu-met-fast-018-case2
				heu-met-fast-003-case1
				heu-met-fast-003-case2
				heu-met-fast-003-case3
				heu-met-fast-003-case4
				heu-met-fast-003-case5
				heu-met-fast-003-case6
				heu-met-fast-003-case7
				heu-met-fast-028
			Depleted Uranium	heu-met-fast-014
			Tungsten carbide	heu-met-fast-003-case8
				heu-met-fast-003-case9
				heu-met-fast-003-case10
				heu-met-fast-003-case11
			Nickel	heu-met-fast-003-case12
			Steel	heu-met-fast-013
				heu-met-fast-021-case2
			Duralumin	heu-met-fast-022-case2
			Aluminum	heu-met-fast-012
			Graphite	heu-met-fast-019-case2
			Beryllium	heu-met-fast-009-case1
			Beryllium Oxide	heu-met-fast-009-case2
			Polyethylene	heu-met-fast-011
				heu-met-fast-020-case2
			Water	heu-met-fast-004-case1
		Cylinder	Unreflected	heu-met-fast-015
		Lattice	Paraffin	heu-met-fast-026-case9
Intermediate	UH_3	Cylinder	Natural U	heu-comp-inter-003-case7
	Metal	Cylinder	Graphite, copper	heu-met-inter-006-case1
				heu-met-inter-006-case2
				heu-met-inter-006-case3
				heu-met-inter-006-case4
Thermal	UO_2+ZrO_2	Lattice	Water, ThO_2	u233-comp-therm-001-case6
	Solution	Sphere	Unreflected	heu-sol-therm-013-case1
				heu-sol-therm-013-case2
				heu-sol-therm-013-case3
				heu-sol-therm-013-case4
				heu-sol-therm-032
U-233 Benchmarks				
Fast	Metal	Spheres	Unreflected	u233-met-fast-001
			HEU	u233-met-fast-002-case_1
				u233-met-fast-002-case_2
			Normal Uranium	u233-met-fast-003-case_1

				u233-met-fast-003-case_2
				u233-met-fast-006
			Tungsten	u233-met-fast-004-case_1
				u233-met-fast-004-case_2
			Beryllium	u-233-met-fast-005-case_1
				u-233-met-fast-005-case_2
Intermediate	Solution	Sphere	Beryllium	u233-sol-inter-001-case1
Thermal	UO_2+ZrO_2	Lattice	Water	u233-comp-therm-001-case3
	Solution	Sphere	Unreflected	u233-sol-therm-001-case1
				u233-sol-therm-001-case2
				u233-sol-therm-001-case3
				u233-sol-therm-001-case4
				u233-sol-therm-001-case5
				u233-sol-therm-008
Plutonium Benchmarks				
Fast	Metal	Spheres	Unreflected	pu-met-fast-001-case_1
				pu-met-fast-002-case_1
				pu-met-fast-022
			HEU	mix-met-fast-001-case_1
				mix-met-fast-003
			Normal Uranium	pu-met-fast-006
				pu-met-fast-010-case_1
			Depleted Uranium	pu-met-fast-020
			Thorium	pu-met-fast-008-case2
			Tungsten	pu-met-fast-005-case_1
			Steel	pu-met-fast-025
				pu-met-fast-026
			Aluminum	pu-met-fast-009-case_1
			Graphite	pu-met-fast-023
			Beryllium	pu-met-fast-018-case_1
				pu-met-fast-019
			Polyethylene	pu-met-fast-024
			Water	pu-met-fast-011-case_1
		Cylinder	Beryllium	pu-met-fast-021-case1
			Beryllium Oxide	pu-met-fast-021-case2
		Lattice	Unreflected	pu-met-fast-003-case103
Intermediate	Mixture	Homog	Hydrogen, graphite	pu-comp-inter-001
Thermal	MOX	Lattice	Water	mix-comp-therm-002-case-pnl30
				mix-comp-therm-002-case-pnl31
				mix-comp-therm-002-case-pnl32
				mix-comp-therm-002-case-pnl33
				mix-comp-therm-002-case-pnl34
				mix-comp-therm-002-case-pnl35
	Solution	Sphere	Unreflected	pu-sol-therm-009-case3a
				pu-sol-therm-011-case_5.16
				pu-sol-therm-011-case_1.18
				pu-sol-therm-011-case_6.18
				pu-sol-therm-021-case_1.t9a
				pu-sol-therm-021-case_3.t9a
		Cylinder	Water	pu-sol-therm-018-case_9
				pu-sol-therm-034-case_01

Chapter 3: Numerical results

The objective of this chapter is to present the results of the validation made for the nuclear data libraries used in the study, namely ENDF/B-VI.8, ENDF/B-VII.0, ENDF/B-VII.1, ENDF/B-VIII.0, JEFF-3.2, and JEFF-3.3. The study was made by analyzing different criticality benchmarks, Octavian Shielding benchmarks, and Doppler reactivity [18, 53, 19, 20, 54]. The second main objective of this section was to model the research reactor TRIGA Mark II using the MCNP code and the benchmarked libraries. This was done by determining effective multiplication factor (keff), heat distribution, neutron flux distribution, effective delayed neutron fraction (β_{eff}), prompt removal lifetime (τ_r) and the mean neutron generation time (Λ) at the beginning of life (BOL) and comparing it with published results. The study results presented in this chapter will be based on documents published in international peer-reviewed journals by the author of this thesis.

To ensure fluent reading, tables and figures are integrated directly into the text.

3.1. Processing and benchmarking of ENDF/B-VIII.0β4 cross-section library by analysis of a series of critical experimental benchmarks using the Monte Carlo code MCNPX and NJOY2016.

Modified from a paper published in Nuclear Engineering and Technology - Journal.

DOI: https://doi.org/10.1016/j.net.2017.08.017.

Ouadie Kabach *, Abdelouahed Chetaine, Abdelhamid Jalil, Abdelaziz Darif, Abdelmajid Saidi

Nuclear Reactor and Nuclear Security Group Energy Center, Nuclear Physics Laboratory, Physics Department, Faculty of Science, Mohammed V University, Rabat, Morocco.

*Corresponding author e-mail address: ouadie.kabach10@gmail.com

Abstract: For the validation of the ENDF/B-VIII.0β4 library, thirty-one different critical cores were used for the benchmark test of the key parameter, keff. The four libraries that were used are processed using NJOY2016. The results obtained with the ENDF/B-VIII.0β4 library were compared with those calculated with the ENDF/B-VI.8, ENDF/B-VII.0 and ENDF/B-VII.1 libraries using the Monte Carlo MCNPX code. All calculations of keff values were compared with the experimentally measured results available in the ICSBEP with these four libraries. The obtained results are discussed and analyzed in this section.

3.1.1. Introduction

The evaluated nuclear data library ENDF/B-VIII.0β4 was released on February 28, 2017 [55]. The Neutron General Purpose Library contains incident neutron data for 446 isotopes from $^{1}_{1}$H to $^{255}_{100}$Fm, and the Scattering Thermal Library $S(\alpha,\beta)$ covers twenty-six different moderators. The code system used for processing and generating the ACE format is NJOY2016 [56] for all isotopes and $S(\alpha,\beta)$ thermal scattering, especially the ACER module, for the correct processing of the libraries. A local executable of NJOY2016 was created using 64-bits under a Linux system. As part of the validation process, comparisons with the ENDF/B-VI.8, ENDF/B-VII.0 and ENDF/B-VII.1 libraries were carried out. In this study, the MCNPX v2.6.0 [32] calculations were done with an HP Pro Intel® i5 CPU 3.20 GHz, third-generation (4 cores), 4 Gb RAM and 6 Mb Cache Memory under Win 10 system and using MPICH2 [57]. Keff calculations were made using 600 iterations with a nominal source size of 60,000 particles per cycle to reduce statistical error estimates. Initial 100 cycles were skipped to ensure homogeneous distribution of the neutrons source.

3.1.2. Benchmark results and discussion

In this part, we present all the keff values, which are given in a graphical form. The columns contain the following items.

- The benchmark values [58].
- The results obtained from MCNPX calculations based on ENDF/B-VI.8. In the four benchmarks, namely LEU-SOL-THERM-002-case-1, MIX-COMP-THERM-002-case-pnl30, HEU-MET-INTER-006-case-1, and HEU-SOL-THERM-013-case-1, Cu replaced the element Zn because Zn is missing in the original library [Release 8, 2001].
- The results obtained from MCNPX calculations based on ENDF/B-VII.0.
- The results obtained from MCNPX calculations based on ENDF/B-VII.1.
- The results obtained from MCNPX calculations based on the new library ENDF/B-VIII.0β4.

Results of keff calculations obtained using MCNPX code with ENDF/B-VI.8, ENDF/B-VII.0, ENDF/B-VII.1, and ENDF/B-VIII.0β4 libraries, as well as the benchmark keff values, are presented in **Figure 3.1**. The $\frac{C}{E} - 1$ values ('E' = expected and 'C' = calculated value) and its uncertainty in pcm are presented in **Figure 3.2** for each of the benchmark systems. The average values of $\frac{C}{E} - 1$ (in pcm) per benchmark category are represented in **Table 3.1**. As can be seen in

Figure 3.1, deviations from the benchmark values decrease as we move from ENDF/B-VI.8 to ENDF/B-VIII.0β4 library in nine-benchmark cases. Also, the calculation results prove that the best performance is for modern ENDF/B-VII.0, ENDF/B-VII.1, and notably ENDF/B-VIII.0β4 libraries because deviations from the benchmark values are less than 200 pcm in the large majority of cases. In addition, deviations are less than 100 pcm for the last library in about half of the benchmark cases. There are, however, some cases, which the $\frac{C}{E} - 1$ value deviates by more than 1000 pcm from the benchmark value. It should be noted that the largest deviations are seen for the U233-SOL-INTER-001-case-1 benchmark for all libraries except the ENDF/B-VII.0 library.
In the "U233-SOL-INTER-001-case-1" benchmark, beryllium is used as the reflector. It is the authors' opinion that this may be due to Be data, as the ENDF/B-VIII.0β4, ENDF/B-VII.1 and ENDF/B-VI.8 data libraries perform worse for Be reflected systems. Besides, it can be observed that the curves representing the main Be cross-sections, as a function of the energies (see **Figure 3.3**), are almost identical for all libraries, but differ from that of the ENDF/B-VII.0 library, especially for the elastic cross-sections in the energy interval [4 MeV to 6 MeV].

To confirm this presumption, we carried out calculations of keff values with the ENDF/B-VIII.0β4, ENDF/B-VII.1, and ENDF/B-VI.8 data libraries, where the Be data $S(\alpha, \beta)$ thermal scattering in these three libraries were replaced with those in the original ENDF/B-VII.0. The results, which are presented in **Table 3.2**, show very good agreement with each other according to $\frac{C}{E} - 1$ values.

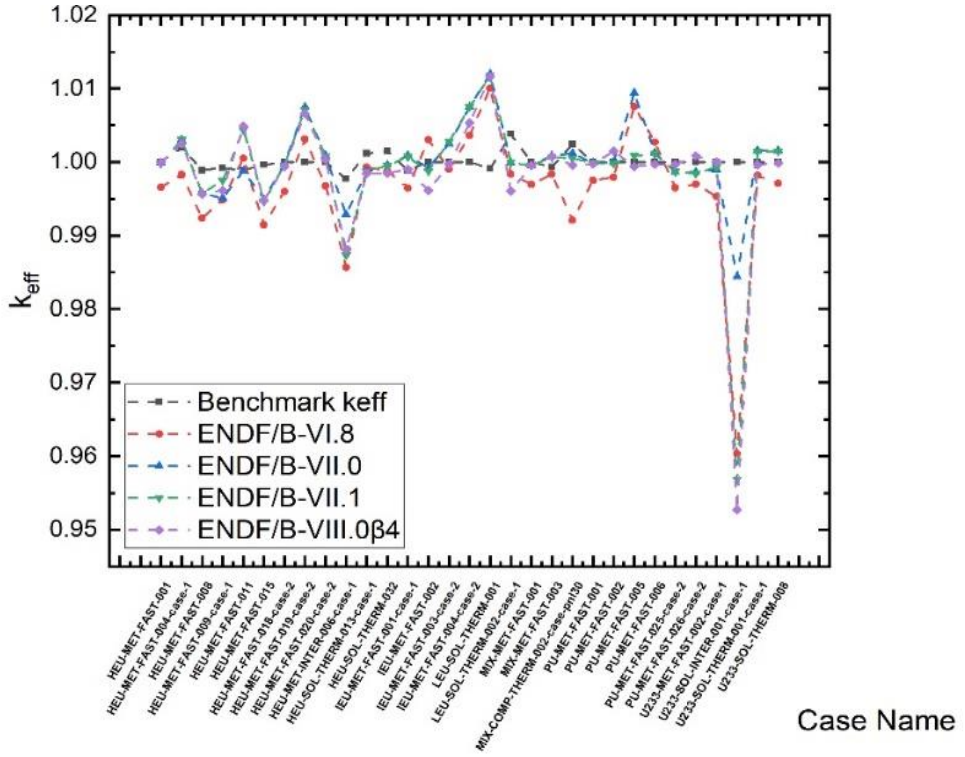

Figure 3. 1. MCNPX calculations of keff with four data libraries.

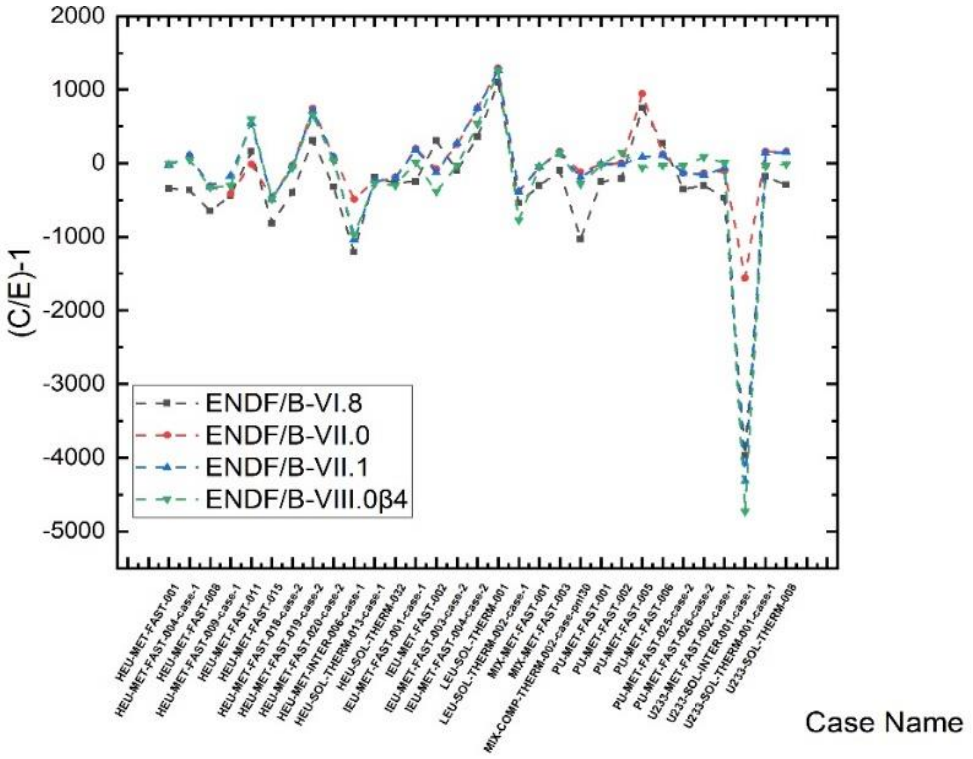

Figure 3. 2. $\frac{C}{E} - 1$ (in pcm) values with the evaluated data libraries.

Table 3. 1. Average values of $\frac{C}{E} - 1$ (in pcm) per benchmark category. N is the number of benchmarks in the category.

Category	N	ENDF/B-VI.8	ENDF/B-VII.0	ENDF/B-VII.1	ENDF/B-VIII.0β4
HEU-MET-FAST	9	-318.3869	-34.8974	44.1899	16.9735
HEU-MET-INTER	1	-1205.7733	-485.1158	-1038.3883	-967.2246
HEU-SOL-THERM	2	-229.6839	-220.7061	-223.2024	-287.6099
IEU-MET-FAST	4	80.9326	278.8042	271.8004	31.2530
LEU-SOL-THERM	2	277.5186	453.3140	438.3028	241.5317
MIX-MET-FAST	2	-199.5340	52.0550	44.5480	47.0501
MIX-COMP-THERM	1	-1030.5267	-122.7055	-190.5427	-282.3224
PU-MET-FAST	6	-13.1667	131.5000	-21.0000	13.8333
U233-MET-FAST	1	-470.0000	-103.0000	-67.0000	3.0000
U233-SOL-INTER	1	-3967.0000	-1560.0000	-4316.0000	-4732.0000
U233-SOL-THERM	2	-237.0000	157.0000	96.0000	-24.5000

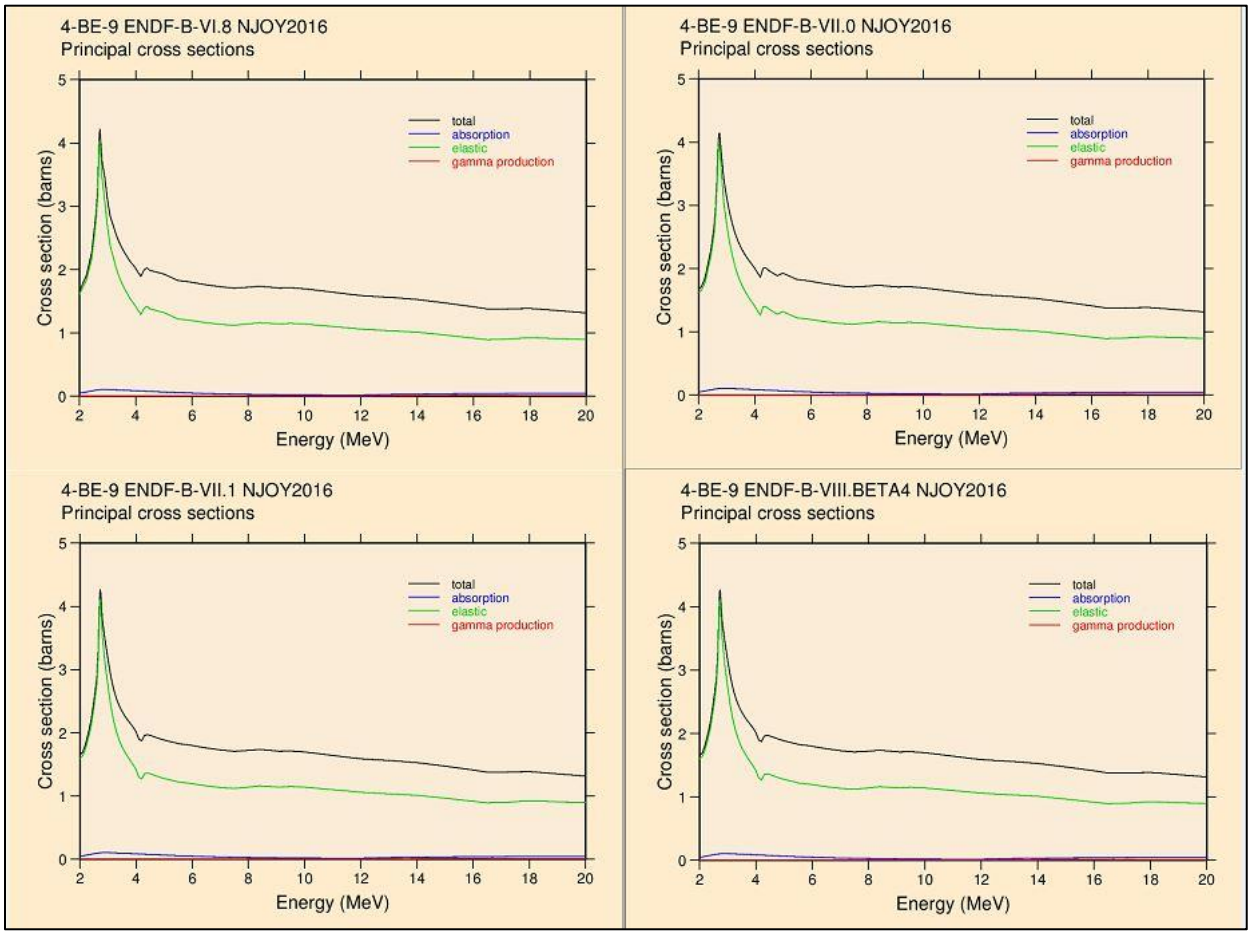

Figure 3. 3. Principal Be (beryllium) cross-sections as a function of energies.

Table 3. 2. MCNPX calculations of keff value - Benchmark keff. Values of $\frac{C}{E} - 1$ (in pcm) - Replacement of Be data in the ENDF/B-VIII.0β4, ENDF/B-VII.1, and ENDF/B-VI.8 by those in ENDF/B-VII.0.

U233-SOL-INTER-001-case-1			
Library/Benchmark keff	keff	$(\frac{C}{E} - 1)$ in pcm	
Benchmark keff	1.00000 ± 0.0083		
ENDF/B-VI.8 [Be from ENDF/B-VII.0]	0.98516 ± 0.0002	-1484.0000	± 12.3209
ENDF/B-VII.0	0.98440 ± 0.0002	-1560.0000	± 12.9519
ENDF/B-VII.1 [Be from ENDF/B-VII.0]	0.98444 ± 0.0002	-1556.0000	± 12.9187
ENDF/B-VIII.0β4 [Be from ENDF/B-VII.0]	0.98316 ± 0.0002	-1684.0000	± 13.9814

3.1.3. Conclusion

The obtained ENDF/B-VIII.0β4 results for most cases of benchmarks improved, except for the U233-SOL-INTER-001-case-1 system. Indeed, the calculated values of $\frac{C}{E} - 1$ and their uncertainties are better, especially for certain benchmark cases, compared to older evaluations. On the other hand, for the rest of the benchmark cases, the differences with older evaluations are not large. In addition, the improvement of this library can also be observed for calculations of the average values of $\frac{C}{E} - 1$ per benchmark category (see **Table 3.1**).

The keff values calculated using the Be data in ENDF/B-VIII.0β4, ENDF/B-VII.1, and ENDF/B-VI.8 data libraries were replaced with those in the original ENDF/B-VII.0 and show very good agreement with each other.

From this work, we can underline the following remark:

Based on the obtained results for the U233-SOL-INTER-001-case-1 benchmark, incident neutron data and thermal neutron scattering data need to be revised for Be (beryllium) in ENDF/B-VIII.0β4 evaluation when this Be is used as a reflector.

3.2. Processing of the ENDF/B-VIII.0β6 neutron cross-section data library and testing with critical benchmarks, oktavian shielding benchmarks, and the doppler reactivity defect benchmarks

Modified from a paper published in Annals of the University of Craiova, Physics - Journal.

Physics AUC, vol. 28, 79-98 (2018)

Ouadie Kabach [1,*], Abdelouahed Chetaine [1], Abdelhamid Jalil [1], Abdelaziz Darif [1], Abdelmajid Saidi [1], Abdelfettah Benchrif [2], Hamid Amsil [2]

[1)] Nuclear Reactor and Nuclear Security Group Energy Center, Nuclear Physics Laboratory, Physics Department, Faculty of Science, Mohammed V University, Rabat, Morocco.

[2)] National Centre of Sciences, Energy and Nuclear Techniques (CNESTEN/CENM), POB 1382, Rabat, Morocco.

*Corresponding author e-mail address: ouadie.kabach10@gmail.com

Abstract: The ENDF/B-VIII.0β6 cross-section data library has been processed and tested using benchmark calculations. The computations were performed with the NJOY2016 processing code and the MCNPX continuous energy Monte Carlo code. The benchmark assessment has been conducted through the calculations for 31 criticality benchmarks taken from the ICSBEP handbook, fusion shielding based on Oktavian (for Al, Cr, Cu, LiF, Mn, Mo, Nb, Si, Ti, W, Zr), experiments, and three fuel types of Doppler benchmark. The obtained results were compared with the ENDF/B-VI.8, ENDF/B-VII.0, ENDF/B-VII.1, ENDF/B-VIII.0β4, ENDF/B-VIII.0β5 data libraries, and the published values.

3.2.1. Introduction

In this section, the main objective is to validate the ENDF/B-VIII.0β6 neutron cross-section data library. The evaluated nuclear ENDF/B-VIII.0β6 data library was released on December 15, 2017. The main revised data are available on the CSEWG website [59]. To validate some of these data, three series of benchmark calculations were performed. Testing with 31 different criticality data contained in the ICSBEP handbook [41], 12 Octavian Shielding Benchmarks from the IAEA [43], and Doppler-Defect benchmarks from [60]. Adequate calculations based on ENDF/B-VI.8, ENDF/B-VII.0 ENDF/B-VII.1, ENDF/B-VIII.0β4, and ENDF/B-VIII.0β5 [59] have also been done and compared with measurements. The ACE libraries used in the calculations were prepared with the LANL nuclear data processing system NJOY2016 [12]. The thermal scattering [35] data were used for H in H_2O processed at 293.6 K and 600K. For H in CH_2, graphite and Be in

Beryllium metal, the data were processed at room temperature, which in some cases implied 293.6 K and in others 296 K, as necessary for consistency with the data file.

3.2.2. Calculation methods

The MCNPX calculations were carried out with an HP Elite Book 8560 workstation Intel® i7 CPU 2.20 GHz, 8 cores, 8 Gb RAM, and 6 Mb Cache Memory under Win 10 system and using MPICH2 [57]. The keff parameter of criticality and Doppler defect calculations were performed using these six libraries with 600 iterations on a nominal source size of 60,000 particles per cycle to decrease statistical error estimates, initial 100 cycles were skipped to insure homogeneous neutrons source distribution. For Oktavian benchmarks, 500,000,000 neutron histories were run.

3.2.3. Benchmark results and discussion

Results of criticality calculations

The results of keff calculations with ENDF/B-VI.8, ENDF/B-VII.0, ENDF/B-VII.1, ENDF/B-VIII.0β4 [18], ENDF/B-VIII.0β5, and ENDF/B-VIII.0β6 data libraries for the suite of benchmarks as well as the benchmark keff values are illustrated in **Figure 3.4**. The $\frac{C}{E} - 1$ values and their uncertainties are shown in **Figure 3.5**.

Results using the ENDF/B-VIII.0β6 data library have been improved in the fourteen among the thirty-one benchmark systems because deviations from the benchmark values are <100 pcm. In addition, the values of $\frac{C}{E} - 1$ deviate from the benchmark values by > 1000 pcm in just two cases. It should be pointed out that the largest deviations have been observed for the U233-SOL-INTER-001-case-1 benchmark for all libraries except the ENDF/B-VII.0, ENDF/B-VIII.0β5, and ENDF/B-VIII.0β6 libraries. In the "U233-SOL-INTER-001-case-1" benchmark, Beryllium (Be) is employed as the reflector. In the latter library, the Be data are significantly more accurate than those of the ENDF/B-VIII.0β4 library discussed in [18] since deviations from the benchmark values are < 2000 pcm for this benchmark.

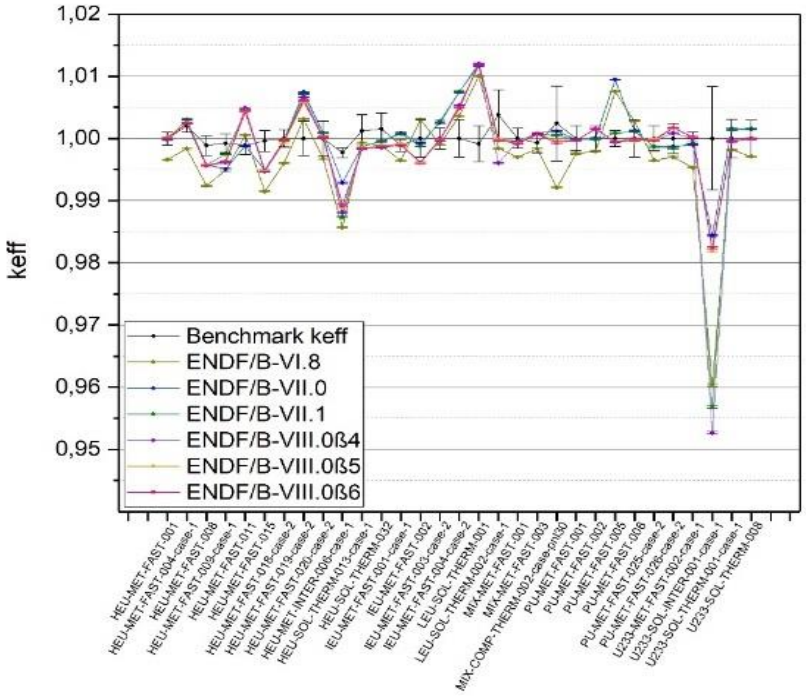

Figure 3. 4. MCNPX calculations of keff values and its uncertainty with six data libraries and benchmark keff.

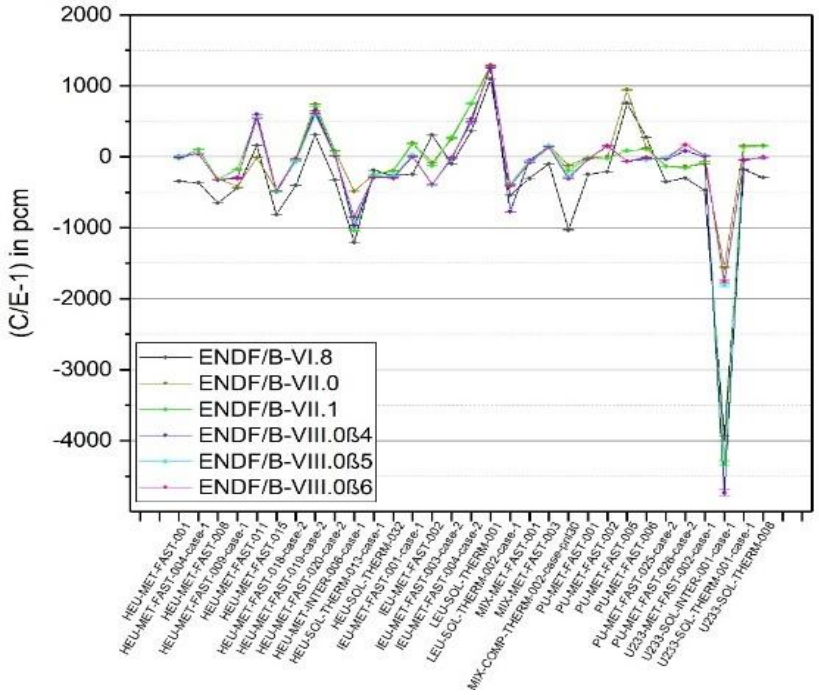

.

Figure 3. 5. $\frac{C}{E} - 1$ values and their uncertainties (in pcm) for all benchmark cases.

Results of Oktavian shielding calculations

In this section, we present the calculation results with ENDF/B-VIII.0β6, ENDF/B-VIII.0β5, ENDF/B-VIII.0β4, ENDF/B-VII.1, ENDF/B-VII.0, and ENDF/B-VI.8 libraries. These results are reported as graphs of the neutron spectrum, as well as $\frac{C}{E}$ values for the neutron spectrum for each specific energy region of 0.1 to 0.5 MeV, 0.5 to 1 MeV, 1 to 5 MeV, 5 to 10 MeV, and > 10 MeV. From the results, the following remarks can be underlined:

- Oktavian Al benchmark:

For each specific energy region, the calculated and measured values of the neutron spectra and the $\frac{C}{E}$ values using the data of six libraries are illustrated in **Figures 3.6** and **3.7**, respectively. The calculation results demonstrate that all the libraries perform the same way including the new one. Also, these results are generally good in the interval between 0.5 to 1 MeV.

- Oktavian Co benchmark:

Figures 3.8 and **3.9** indicate the experimental and calculated neutron spectra and the $\frac{C}{E}$ for each specific energy region, respectively. The calculation results based on ENDF/B-VIII.0β6 data are closest to the values of the benchmark in the range between 0.1 to 10 MeV.

- Oktavian Cr benchmark:

Figures 3.10 and **3.11** show the experimental and computational values of neutron spectra and the $\frac{C}{E}$ values for each specific energy region, respectively. The calculation results using the new ENDF/B-VIII.0β6 are almost the same as those obtained with the other libraries.

- Oktavian Cu benchmark:

The measured and calculated neutron spectra and the $\frac{C}{E}$ values for each specific energy region are shown in **Figures 3.12** and **3.13**, respectively. The calculation results with ENDF/B-VIII.0β6 data are improved between 0.1 to 5 MeV, but these results tend to be high in energy intervals between 5 to 10 MeV.

- Oktavian LiF benchmark:

The experimental and computational values of neutron spectra and the $\frac{C}{E}$ values for each specific energy region are presented in **Figures 3.14** and **3.15**, respectively. The calculation results show that all the libraries perform equally, except for the ENDF/B-VI.8 data library. Note that these results are the best in the energy range between 10 to 20 MeV.

- Oktavian Mn benchmark:

Figures 3.16 and **3.17** give the measured and calculated neutron spectra and the $\frac{C}{E}$ values for each specific energy region, respectively. The calculation results using the new ENDF/B-VIII.0β6 data library are closest to the benchmark values in the interval between 5 to 10 MeV, but this library was not improved in the other intervals. It can be seen that the ENDF/B-VII.0 library performs well between 0.1 to 1 MeV.

- Oktavian Mo benchmark:

Figures 3.18 and **3.19** summarize the measured and calculated values of neutron spectra and the $\frac{C}{E}$ values for each specific energy region, respectively. The calculation results indicate that all the libraries perform the same way, except ENDF/B-VI.8 which performs better between 0.5 to 1 MeV.

- Oktavian Nb benchmark:

The measured and calculated neutron spectra and the $\frac{C}{E}$ values for each specific energy region are illustrated in **Figures 3.20** and **3.21**, respectively. The calculation results show that all the libraries perform the same way. These results tend to be high between 1 to 5 MeV, but they are closest to benchmark values in both energy intervals 0.5 to 1 MeV and 5 to 20 MeV.

- Oktavian Si benchmark:

The experimental and calculated neutron spectra and the $\frac{C}{E}$ values for each specific energy region can be seen in **Figures 3.22** and **3.32**, respectively. The calculation results are generally identical for ENDF/B-VIII.0β6, ENDF/B-VII.0, ENDF/B-VII.1, ENDF/B-VIII.0β4, and ENDF/B-VIII.0β5. It is observed that these results are good between 1 to 20 MeV.

- Oktavian Ti benchmark:

The measured and computed neutron spectra and the $\frac{C}{E}$ values for each specific energy region are summarized in **Figures 3.24** and **3.25**, respectively. The performed calculations demonstrate that the results are good from 0.1 to 1 MeV using ENDF/B-VI.8 and from 5 to 10 MeV with ENDF/B-VII.0. For the new ENDF/B-VIII.0β6 library, the results are located between those of the other libraries.

- Oktavian W benchmark:

Figures 3.26 and **3.27** show the measured and calculated values of neutron spectra and the $\frac{C}{E}$ values for each specific energy region, respectively. From these figures, it can be observed that all the libraries perform the same way between 0.5 to 20 MeV, but they perform poorly between 5 to 10 MeV.

- Oktavian Zr benchmark:

The experimental and computed neutron spectra and the $\frac{C}{E}$ values for each specific energy region are shown in **Figures 3.28** and **3.29**, respectively. The ENDF/B-VIII.0β6 library is better performing between 0.1 to 1 MeV. Furthermore, the results are closest to the benchmark values between 5 to 10 MeV.

From the results of this work, it could be noted that, on the one hand, the computed values using ENDF / B-VIII.0β6 for Oktavian shielding benchmarks are generally good, but in some cases, there are strong deviations from the benchmark values. Instead, there is little difference between libraries in most of the calculations. As far as there are major differences, this is likely to be attributed to the original nuclear data in many cases.

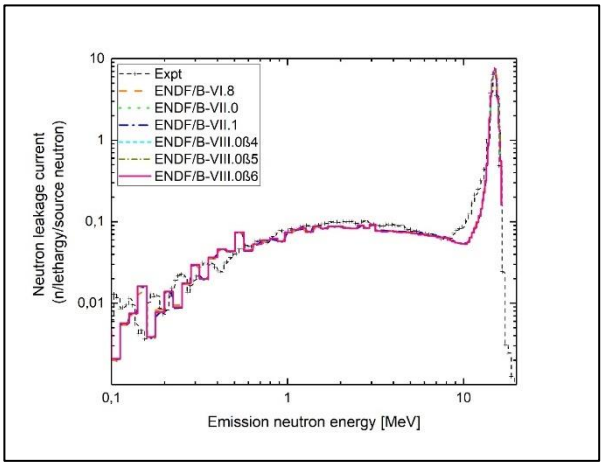

Figure 3. 6. Measured and calculated leakage neutron spectrum for the Al benchmark.

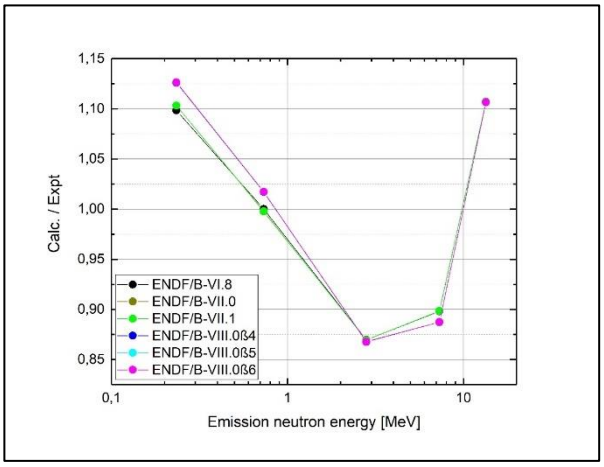

Figure 3. 7. $\frac{C}{E}$ values for the neutron spectrum of the Al benchmark.

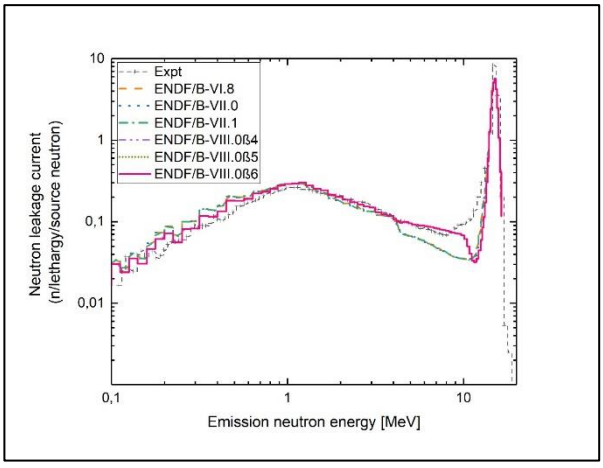

Figure 3. 8. Measured and calculated leakage neutron spectrum for the Co benchmark.

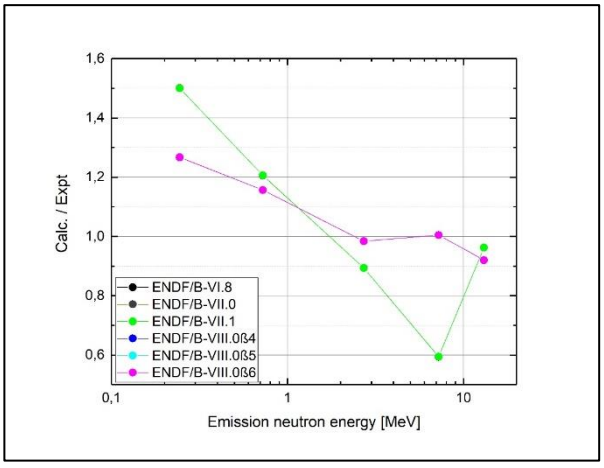

Figure 3. 9. $\frac{C}{E}$ values for the neutron spectrum of the Co benchmark.

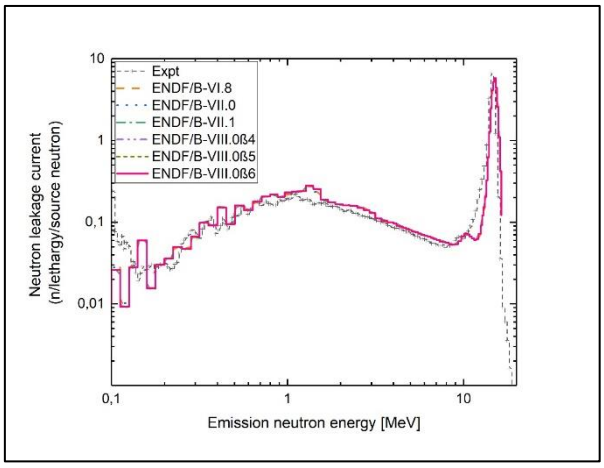

Figure 3. 10. Measured and calculated leakage neutron spectrum for the Cr benchmark.

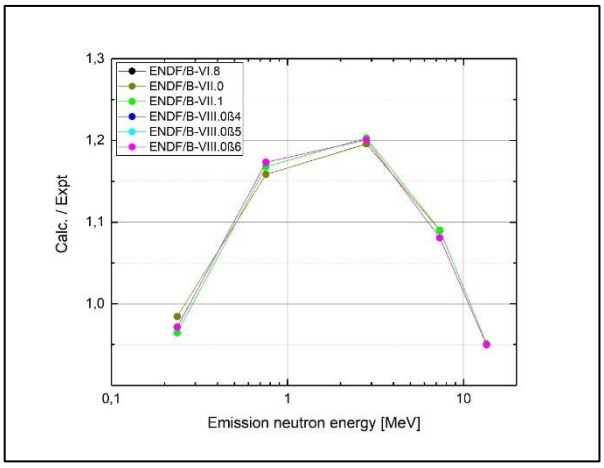

Figure 3. 11. $\frac{C}{E}$ values for the neutron spectrum of the Cr benchmark.

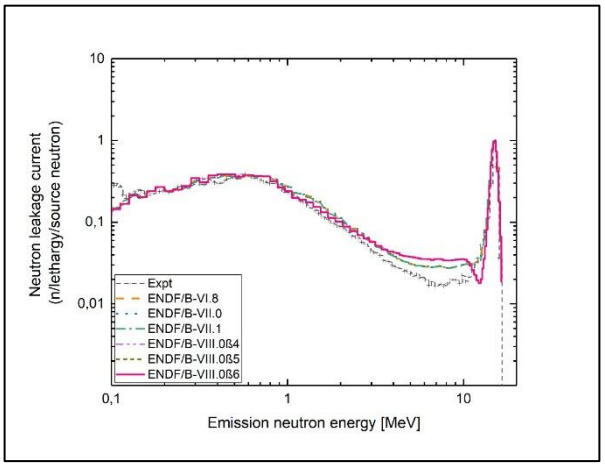

Figure 3. 12. Measured and calculated leakage neutron spectrum for the Cu benchmark.

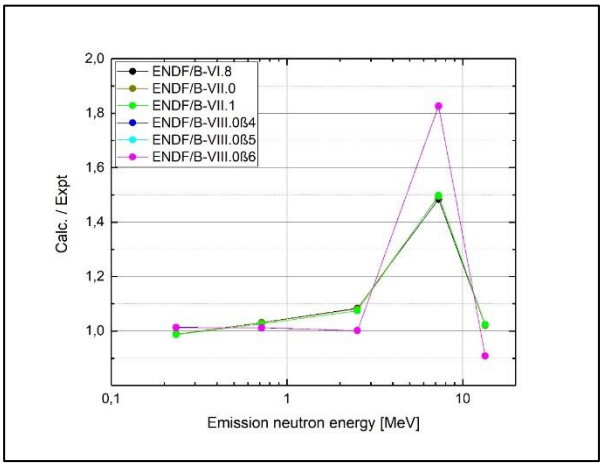

Figure 3. 13. $\frac{C}{E}$ values for the neutron spectrum of the Cu benchmark.

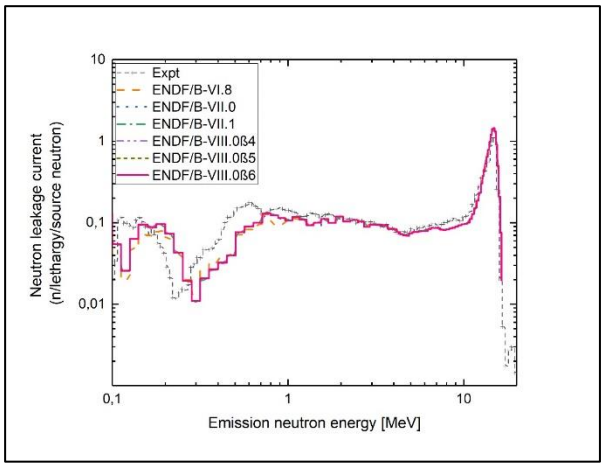

Figure 3. 14. Measured and calculated leakage neutron spectrum for the LiF benchmark.

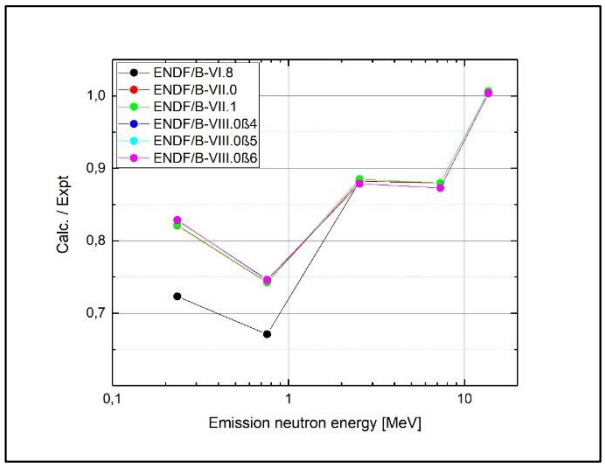

Figure 3. 15. $\frac{C}{E}$ values for the neutron spectrum of the LiF benchmark.

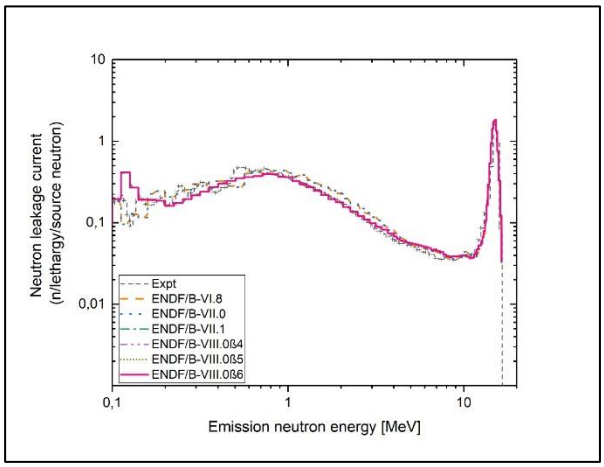

Figure 3. 16. Measured and calculated leakage neutron spectrum for the Mn benchmark.

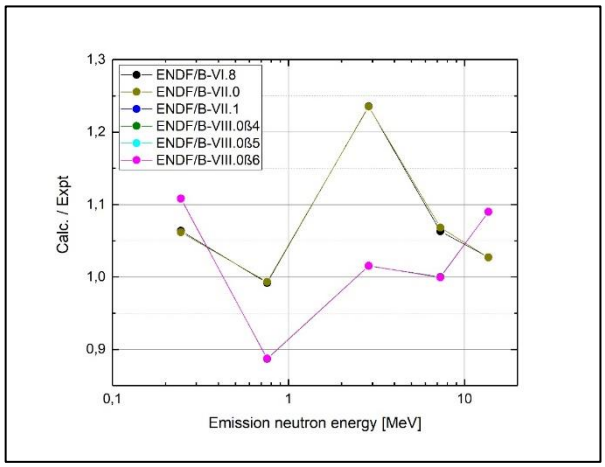

Figure 3. 17. $\frac{C}{E}$ values for the neutron spectrum of the Mn benchmark.

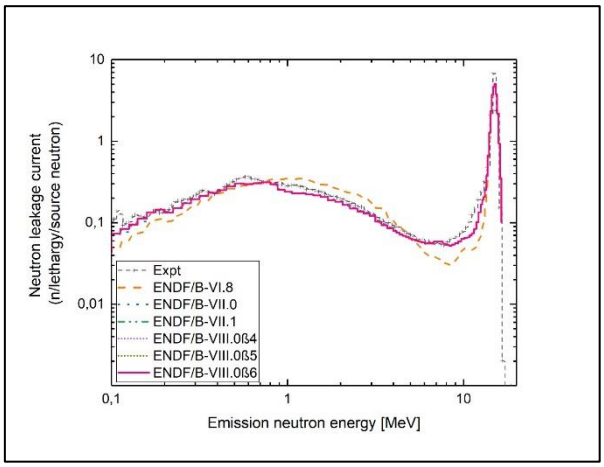

Figure 3. 18. Measured and calculated leakage neutron spectrum for the Mo benchmark.

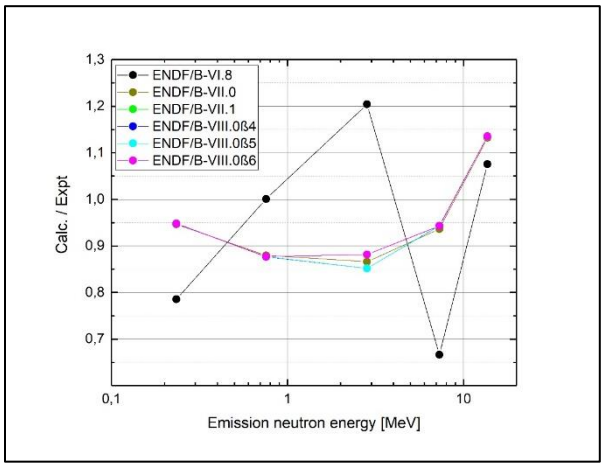

Figure 3. 19. $\frac{C}{E}$ values for the neutron spectrum of the Mo benchmark.

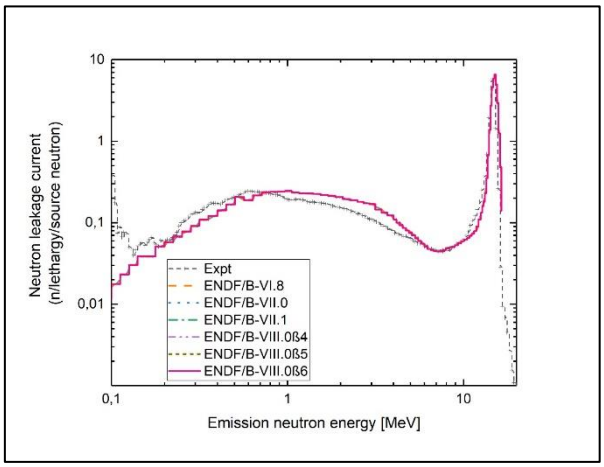

Figure 3. 20. Measured and calculated leakage neutron spectrum for the Nb benchmark.

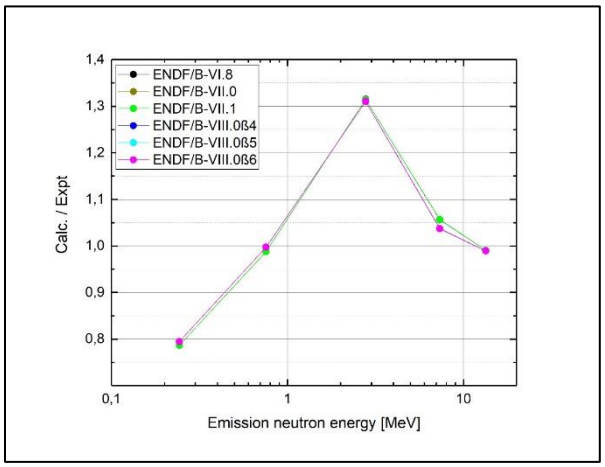

Figure 3. 21. $\frac{C}{E}$ values for the neutron spectrum of the Nb benchmark.

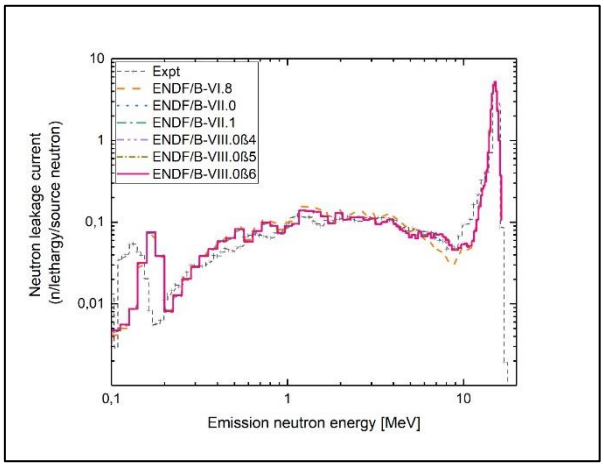

Figure 3. 22. Measured and calculated leakage neutron spectrum for the Si benchmark.

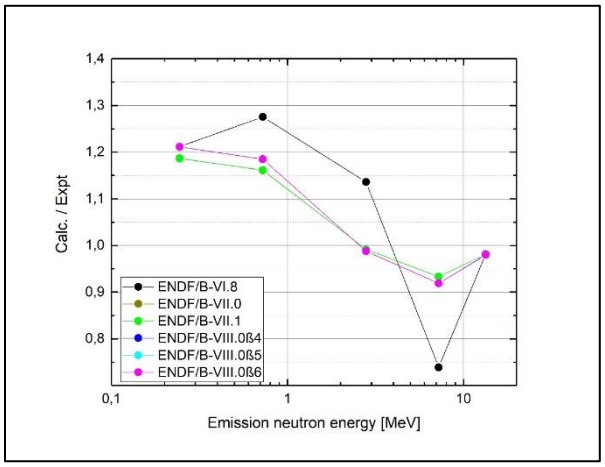

Figure 3. 23. $\frac{C}{E}$ values for the neutron spectrum of the Si benchmark.

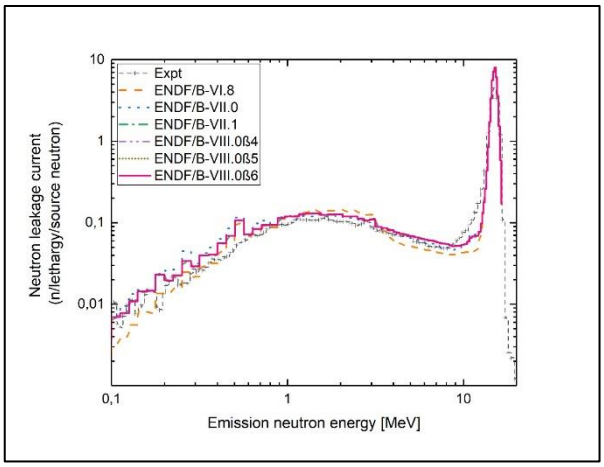

Figure 3. 24. Measured and calculated leakage neutron spectrum for the Ti benchmark.

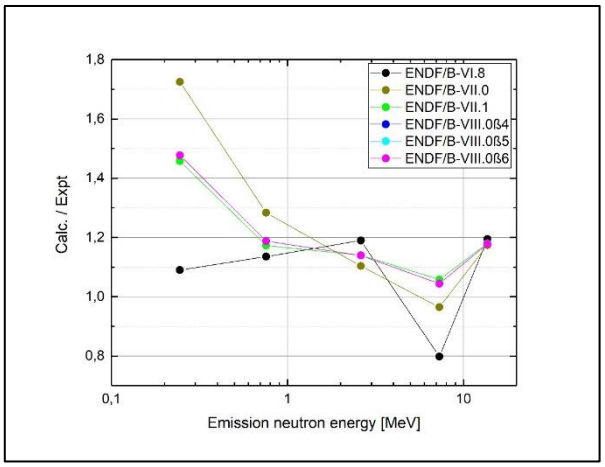

Figure 3. 25. $\frac{C}{E}$ values for the neutron spectrum of the Ti benchmark.

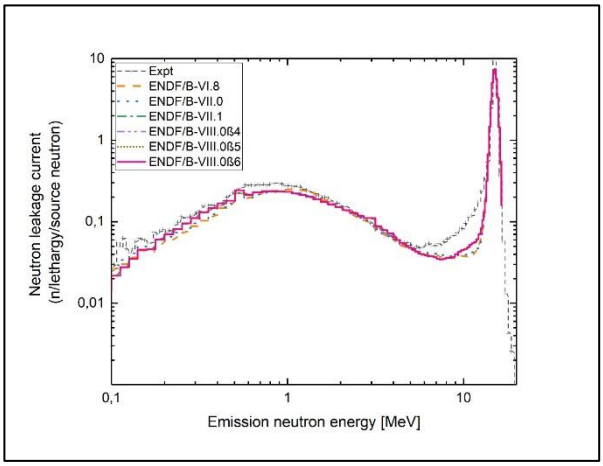

Figure 3. 26. Measured and calculated leakage neutron spectrum for the W benchmark.

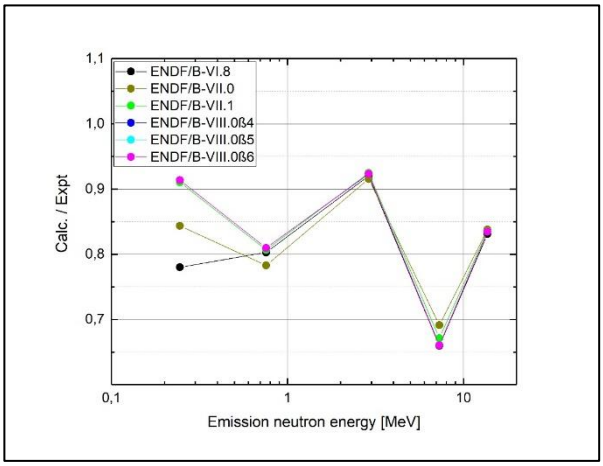

Figure 3. 27. $\frac{C}{E}$ values for the neutron spectrum of the W benchmark.

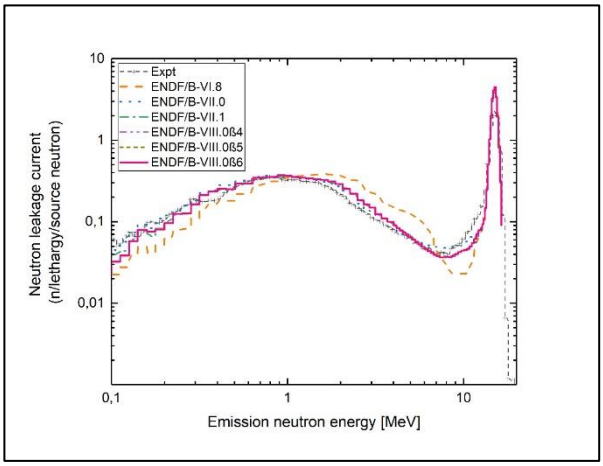

Figure 3. 28. Measured and calculated leakage neutron spectrum for the Zr benchmark.

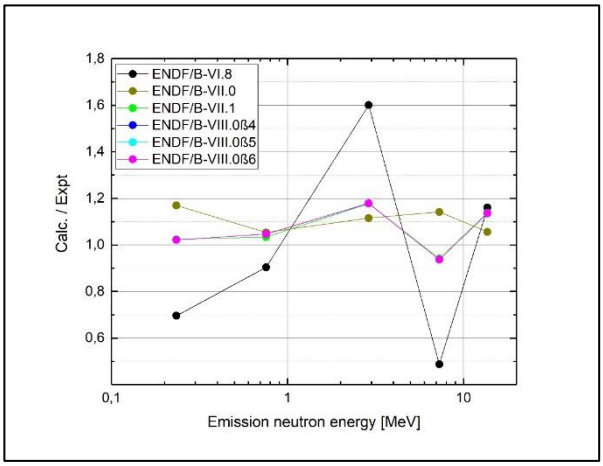

Figure 3. 29. $\frac{C}{E}$ values for the neutron spectrum of the Zr benchmark.

Results of Doppler reactivity defect benchmarks

As it is known, the Doppler coefficient of reactivity is generally negative and increases with uranium enrichment or MOX concentration. It is becoming consistently less negative as the enrichment or PuO_2 content increases. However, the change is much smaller for the MOX fuel than for the UO_2 fuel behavior. Besides, the Doppler coefficient for heavy loadings of MOX fuel is significantly more negative than the Doppler coefficient for highly enriched UO_2 fuel. Natural uranium has been included in all three fuel types. In this work, the Doppler coefficient in the MOX fuel is used just as a reference.

For UO_2 pin cells, it is clear from the results that the six versions of the cross-section libraries produce generally very similar values of the keff parameter; statically the higher and lower values for keff are produced by ENDF/B-VII.1 and ENDF/B-VI.8 for every case, respectively. The obtained results using ENDF/B-VIII.0β6 are good. Additionally, all the libraries produce very similar results for Doppler Coefficients. Also, they produce a very similar standard deviation (σ) for each case. The uranium fuel shows an increasing function to an asymptotic value (see **Figure 3.30** and **Figure 3.33**).

For Reactor-Recycle MOX pin cells, from the results, it can be noted that ENDF/B-VIII.0β4, ENDF/B-VIII.0β5, and ENDF/B-VIII.0β6 produce higher values for keff and ENDF/B-VI.8 the lower values. However, all the libraries including ENDF/B-VIII.0β6 produce again very similar Doppler Coefficients and standard deviations (σ), the deviations between σ are less than (1%). The ENDF/B-VI.8 and ENDF/B-VII.0 produce curves that have been slightly less negative with increasing PuO_2 content and ENDF/B-VIII.0β6 has a middle curve between the others when increasing PuO_2 content (see **Figure 3.31** and **Figure 3.34**).

For Weapons-grade MOX pin cells, it can be observed that all the libraries produce the very same values of Doppler Coefficients and (σ). The Doppler Coefficients have curves that are in the form of a shoulder for the variation between (1 wt.%) and (3 wt.%) Furthermore, ENDF/B-VI.8 and ENDF/B-VII.0 libraries produce nearly flat curves. It is deduced that the results with ENDF/B-VIII.0β6 are good (see **Figure 3.32** and **Figure 3.35**).

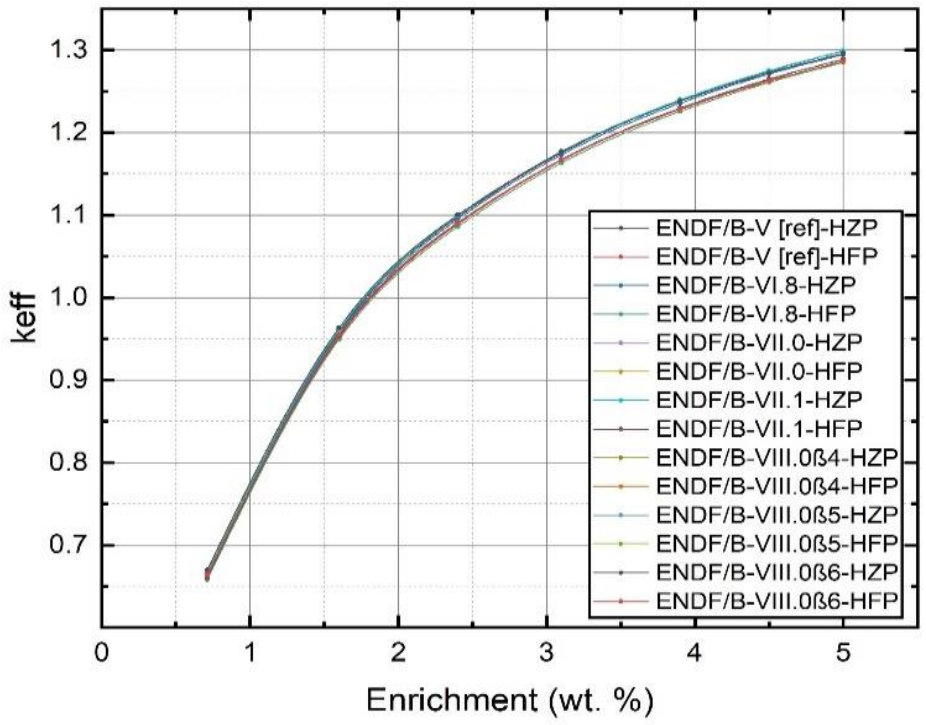

Figure 3. 30. keff results for UO_2 pin cells.

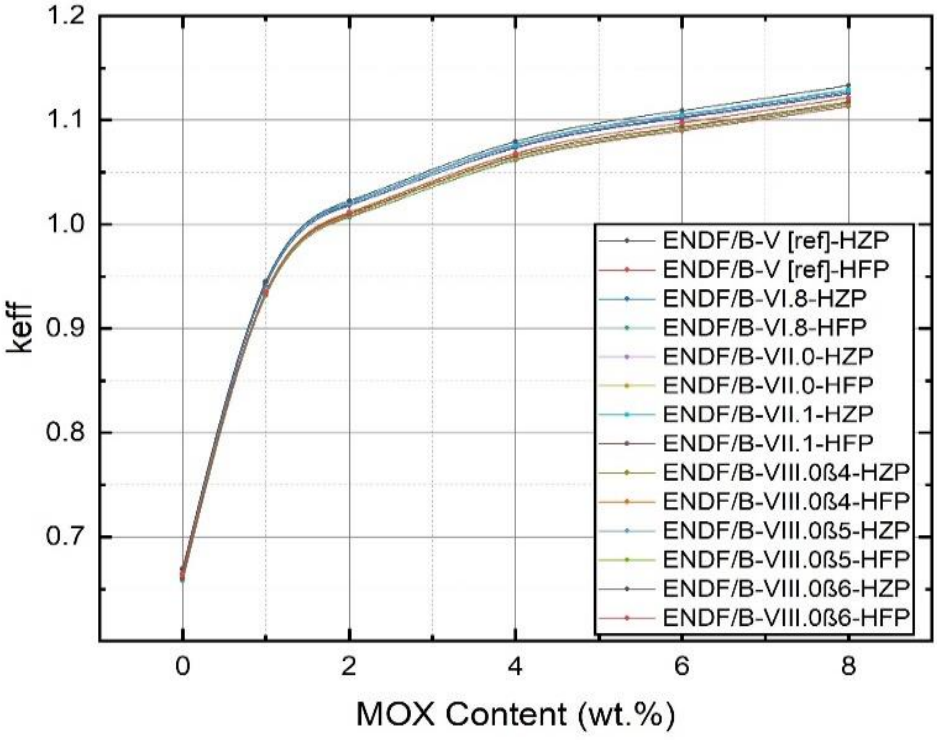

Figure 3. 31. keff results for Reactor-recycle MOX pin cells.

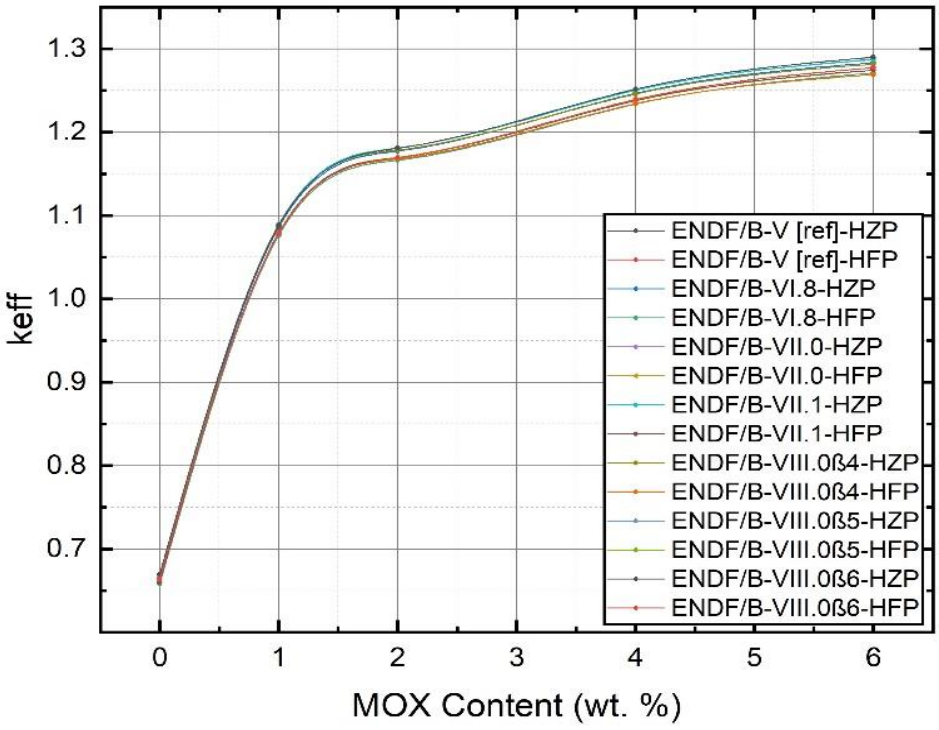

Figure 3. 32. keff results for Weapons-grade MOX pin cells.

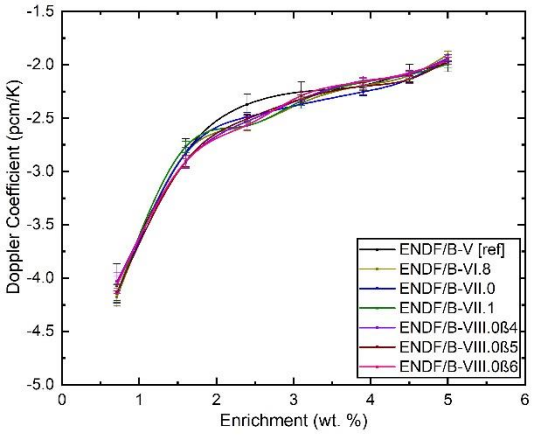

Figure 3. 33. Doppler coefficient for normal and enriched UO_2 fuel.

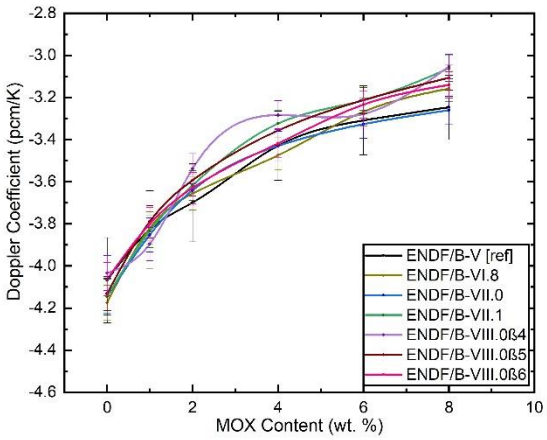

Figure 3. 34. Doppler coefficient for reactor-recycle MOX fuel.

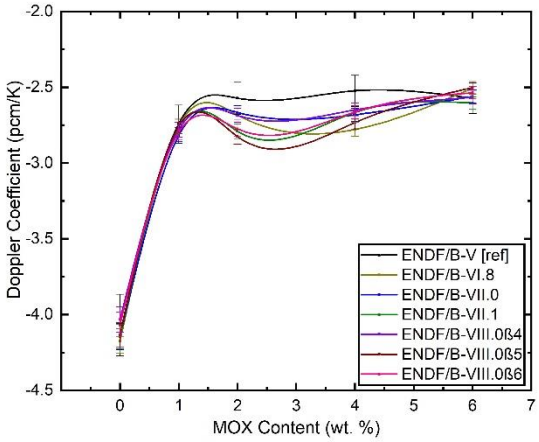

Figure 3. 35. Doppler coefficient for weapons-grade MOX fuel.

3.2.4. Conclusion

The performance of the library for the criticality benchmarks in combination with NJOY2016 and MCNPX is shown to be a good agreement with the benchmark values. The result for the U233-SOL-INTER-001-case-1 benchmark based on Beryllium has been improved since the obtained value is very close to that of ENDF/B-VII.0 and the difference is less than 200 pcm. For most other benchmarks, the results are also in good agreement with the published values. For shielding benchmarks, we benchmarked ENDF/B VIII.0β6 with the TOF Oktavian experiments. Generally, it can be concluded that ENDF/B VIII.0β6 is improved in some cases for each specific energy region by comparing it with the other libraries. However, small differences in values exist between the libraries in the majority of applications. The largest differences can likely be due to original nuclear data in many cases. Also, there are strong deviations between computed and benchmark values in some cases. The behavior of the Doppler coefficients is similar in almost all cases. The coefficients and the standard deviation (σ) from the studied libraries including ENDF/B VIII.0β6 are statistically indistinguishable. However, differences can be observed in the values for keff'. In other terms, the keff parameter does not much matter when it is used to compute the Doppler coefficients. In conclusion, the ENDF/B-VIII.0β6 library has shown much better performance than the previous ENDF evaluations for most applications, except in some cases, and some energy ranges.

3.3. An Inter-comparison between ENDF/B-VIII.0-NECP-Atlas and ENDF/B-VIII.0-NJOY results for criticality safety benchmarks and benchmarks on the reactivity temperature coefficient

Modified from a paper published in Nuclear Engineering and Technology - Journal.

DOI: https://doi.org/10.1016/j.net.2021.02.012

Ouadie Kabach [1,*], Abdelouahed Chetaine [1], Abdelfettah Benchrif [2], Hamid Amsil [1,2]

[1)] Nuclear Reactor and Nuclear Security Group Energy Center, Nuclear Physics Laboratory, Physics Department, Faculty of Science, Mohammed V University, Rabat, Morocco.

[2)] National Centre of Sciences, Energy and Nuclear Techniques (CNESTEN/CENM), POB 1382, Rabat, Morocco.

*Corresponding author e-mail address: ouadie.kabach10@gmail.com

Abstract: Since the nuclear data forms a vital component in reactor physics computations, the nuclear community needs processing codes as tools for translating the Evaluated Nuclear Data Files (ENDF) to simulate nuclear-related problems such as an ACE format that is used for MCNP. Errors, inaccuracies, or discrepancies in library processing may lead to a calculation that disagrees with the experimentally measured benchmark. This paper provides an overview of the processing and preparation of ENDF/B-VIII.0 incident neutron data with NECP-Atlas and NJOY codes for implementation in the MCNP code. The resulting libraries are statistically inter-compared and tested by conducting benchmark calculations, as the mutual comparison is a source of strong feedback for further improvements in processing procedures. The database of the benchmark experiments is based on a selection taken from the International Handbook of Evaluated Criticality Safety Benchmark Experiments (ICSBEP handbook) and those proposed by Russell D. Mosteller. In general, there is quite good agreement between the NECP-Atlas1.2 and NJOY21$^{(1.0.0.json)}$ results with no substantial differences, if the correct input parameters are used.

3.3.1. Introduction

Nuclear evaluations are physics representations of the data derived from experimental data and theoretical predictions encoded in a unified computer-readable format called Evaluated Nuclear Data File (ENDF) released by the U.S. Cross Section Evaluation Working Group (CSEWG) [11]. ENDF files cannot be used directly, they need to be converted into suitable forms for applications, such as calculations of particle transport using multi-group, pointwise for deterministic and Monte Carlo techniques. As a result, cross-section processing codes such as NJOY [12], NECP-Atlas

[13], PREPRO [14], and AMPX [15] must be used to translate and manipulate the data from the single universal [5] ENDF format to a variety of formats accessible via particle transport codes.

Another point to be taken into account is that the use of different sets of processing codes in the analysis of a benchmark problem is both an essential feature and a source of strong feedback for further improvements in data through mutual comparison of results. In fact, the differences observed in the results obtained are not only due to cross-sections but also to the calculation methodologies used by these codes (i.e. interpolation, cross-section tolerances, probability tables, etc.) [17, 61]. Other relevant information is the type of verification tests conducted and the types of benchmarks used to validate the libraries. This can be done by checking the processed libraries against benchmarks that are recognized internationally to ensure that the libraries are capable of providing accurate and reliable results. Further, the Monte Carlo approach is the most suitable for directly validating nuclear data libraries since processed pointwise cross-section data in terms of ACE format (A Compact ENDF) can be used directly without the need of a preceding resonance treatment [17].

In the current work, we describe how the neutron data file is processed with NECP-Atlas and NJOY into ACE libraries. Besides, numerical tests, along with statistical tests, are carried out to provide a code-to-code comparison, and to obtain a more comprehensive impression and understanding of the criticality quality of the processed neutron libraries. The results presented in this paper are based on a set of benchmark calculations, including 120 criticality safety benchmarks, and a set of numerical benchmarks for the Doppler coefficient of reactivity. The criticality benchmarks are taken from the ICSBEP handbook [41], whereas the Doppler benchmarks are given by **Refs**. [49, 60, 52]. The Monte Carlo N-Particle transport code (MCNPX) was used for the present computations [29].

3.3.2. Methodology

Descriptions of processing methods

The nuclear data processing codes used for this work are NECP-Atlas and NJOY. Both codes can be used to convert the ENDF-6 format into pointwise and multigroup cross-sections, but in this work, they are being used to produce pointwise cross-section data in terms of ACE libraries. In order to eliminate any differences in the processed libraries, we decided to generate libraries with the same basic set of input parameters for all available nuclear data evaluations (including the

$s(\alpha, \beta)$ thermal scattering data treatments) as given in **Table 3.3**. Additionally, the temperatures treated are 293.6, 600, and 900 K.

Table 3. 3. Processing options used in a typical input file for NECP-Atlas and NJOY codes.

Reconstruction tolerance:	0.1%
Resonance integral check tolerance	0.3%
Reconstruction temperature:	0.0 K
Thinning tolerance	0.1%
Maximum energy for Doppler broadening	2 MeV

Monte Carlo simulations

All Monte Carlo simulations described in the following have been carried out by resorting to MCNPX computer code [29]. MCNP [28], the general-purpose Monte Carlo radiation transport code developed at Los Alamos National Laboratory and dedicated to criticality safety, reactor physics with depletion, and shielding. The code offers criticality and fixed source simulation mode and several options for the keff value accompanied by an associated uncertainty $|\Delta k_{eff}|$. For this study, the combined average of the absorption, collision, and track-length estimator is quoted as the keff value. Each of the cases employed 600 generations of 50,000 neutron histories each and the results from the first 100 generations were discarded for the determination of the keff. Consequently, the results reported herein are based on 25,000,000 active neutrons histories for each case. Statistical uncertainties with 1σ reliability of keff values are less than 22 pcm in all cases.

Comparison methods

In this section, we explain the methods used to measure the values reported in this paper. The comparison between the codes is reported using the calculated k_{eff} normalized to the benchmark ($\frac{C}{E}$) and its estimated uncertainty ($\sigma_{(C/E)}$) together with the relative difference from the unity value (Δk_{eff}) [42, 62]. For the criticality benchmarks, the expected k_{eff} value were taken from the ICSBEP and are presented with the results. The $\frac{C}{E}$ is calculated as shown in **Equation (3.1)**, and its uncertainty is determined as presented in **Equation (3.2)**. In **Equation (3.3)**, ΔX indicates the relative difference, and X is the analyzed parameter (k_{eff} and D_C).

$$\frac{C}{E}=\frac{k_{eff}^{calculated}}{k_{eff}^{expected}} \tag{3.1}$$

$$\sigma_{(C/E)}=\frac{C}{E}\left[\sqrt{\left(\frac{\sigma_{expected}}{k_{eff}^{expected}}\right)^2+\left(\frac{\sigma_{calculated}}{k_{eff}^{calculated}}\right)^2}\right] \tag{3.2}$$

$$\Delta X=\left(\frac{X^{calculated}}{X^{expected}}-1\right) \tag{3.3}$$

Besides the $\frac{C}{E}$ values, several statistical metrics are compared to determine the accuracy between the calculations and which result shows the better fit to the benchmark values. These metrics include:

- The uncertainty of the expected results ($\sigma_{expected}$), and the uncertainty of the calculated results ($\sigma_{calculated}$) are combined statistically to give a combined statistical uncertainty (σ_s) **Equation (3.4)**. The combined uncertainty is also employed to determine if the results of both processing codes are statistically identical. we can adopt that the results are identical when the relative difference is within a ±3 σ_s interval (99.6% of confidence)[62].

$$\sigma_s=\sqrt{\left(\sigma_{expected}\right)^2+\left(\sigma_{calculated}\right)^2} \tag{3.4}$$

- The χ^2 (chi-square) goodness-of-fit test, and the average difference between calculated and expected keff $\langle|\Delta|\rangle$ [63], **Equations (3.5)** and **(3.6)**.

$$\chi^2=\sum\frac{((k_{calc}-k_{exp})/\sigma_{expected})^2}{n} \tag{3.5}$$

$$\langle|\Delta|\rangle=\sum\frac{|k_{calc}-k_{exp}|}{n} \tag{3.6}$$

The statistical analysis was also conducted by determining the weighted mean multiplication factor ($\overline{k_{eff}}$) **Equation (3.7)**, and the bias uncertainty (S_p) **Equation (3.8)**. The two approaches involve determining the variance about the mean (s^2) **Equation (3.9)**, and the total average

uncertainty ($\overline{\sigma_s}^2$) **Equation (3.10)** [64, 65, 66]. Where n is the number of critical experiments used in the validation and $k_{eff,i}$; is the i^{th} value of the multiplication factor.

$$\overline{k_{eff}} = \frac{\sum_i \frac{1}{\sigma_{s,i}^2}(k_{eff,i})}{\sum_i \frac{1}{\sigma_{s,i}^2}} \tag{3.7}$$

$$S_p = \sqrt{s^2 + \overline{\sigma_s}^2} \tag{3.8}$$

$$s^2 = \frac{\frac{1}{(n-1)}\sum_i \frac{1}{\sigma_{s,i}^2}(k_{eff,i} - \overline{k_{eff}})}{\frac{1}{n}\sum_i \frac{1}{\sigma_{s,i}^2}} \tag{3.9}$$

$$\overline{\sigma_s}^2 = \frac{n}{\sum_i \frac{1}{\sigma_{s,i}^2}} \tag{3.10}$$

3.3.3. Results

Results of criticality calculations

This section presents the analysis of the 120 critical benchmarks results. This takes account of the MCNP results of the calculations (i.e. NECP-Atlas and NJOY results compared to the benchmark values) and a detailed statistical inter-comparison between NECP-Atlas and NJOY by benchmark category. **Figure 3.36** to **Figure 3.40** show the results of the MCNP calculations based on the ENDF/B-VIII.0 data library expressed as normalized to the benchmark value ($\frac{C}{E} \pm \sigma_{(C/E)}$) along with Δk_{eff}. The benchmark uncertainty is also plotted (marked in grey) to visualize the tendencies in the results. Besides, the majority of studied cases converged to a Monte Carlo stochastic uncertainty between ±7 pcm and ± 22 pcm in keff.

It can be marked from **Figure 3.36** to **Figure 3.40** that most of the computed keff values are inside of experimental error bands (95% of cases are within 1σ level), within Δk_{eff}'s around 1000 pcm except for five-benchmark problems. Both uranyl-fluoride solutions (i.e. 'leu-sol-therm-001' and 'u233-sol-inter-001-1') and plutonium-nitrate solutions (i.e. 'pu-sol-therm-009-3a' and 'pu-

sol-therm-011-181') categories show poor agreement with the expected results since the obtained Δk_{eff} is around 1.5% on an absolute basis. The largest deviations from unity also occur for the IEU (37.5 wt.%) reflected by uranium and steel (mix-met-fast-008) and are more than 2% Δk_{eff} on an absolute basis. However, it is worth mentioning that this pattern also has been reported for earlier ENDF/B releases [67, 68, 58, 69, 20].

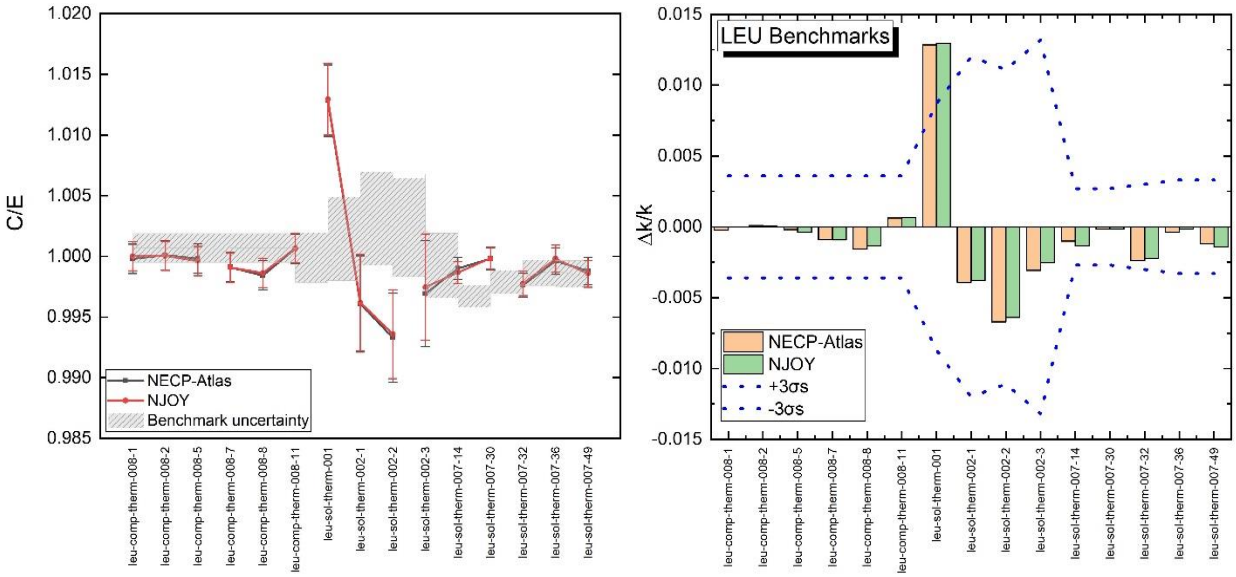

Figure 3. 36. $(\frac{C}{E})$ and $\Delta k_{eff}/k$ results for the LEU benchmarks.

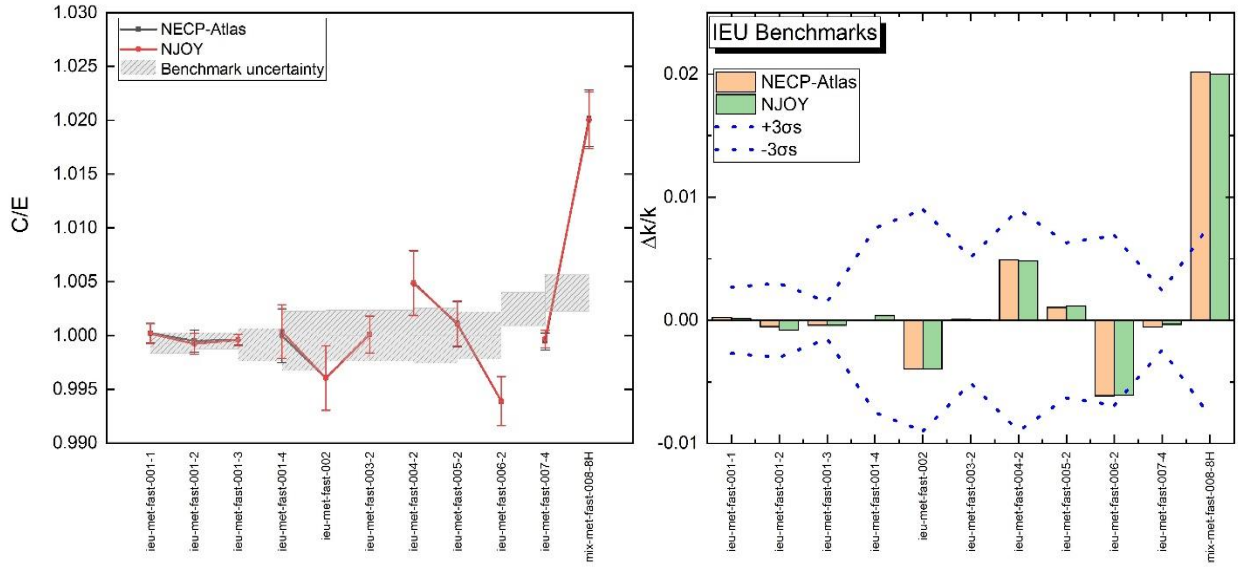

Figure 3. 37. $(\frac{C}{E})$ and$\Delta k_{eff}/k$ results for the IEU benchmarks.

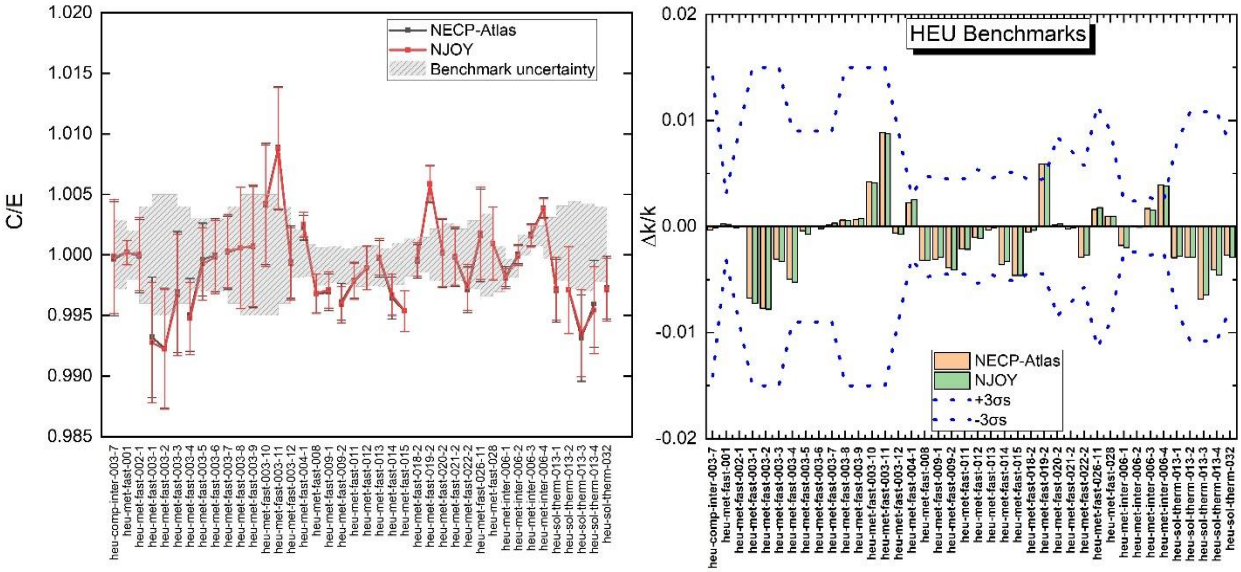

Figure 3. 38. $(\frac{C}{E})$ and $\Delta k_{eff}/k$ results for the HEU benchmarks.

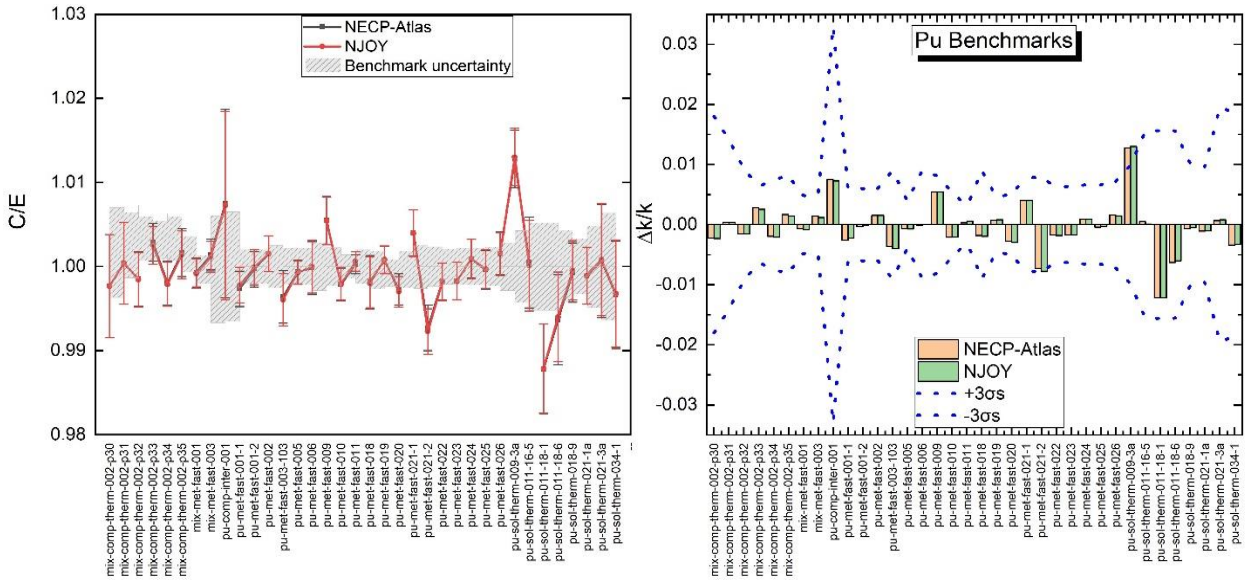

Figure 3. 39. $(\frac{C}{E})$ and $\Delta k_{eff}/k$ results for the Pu benchmarks.

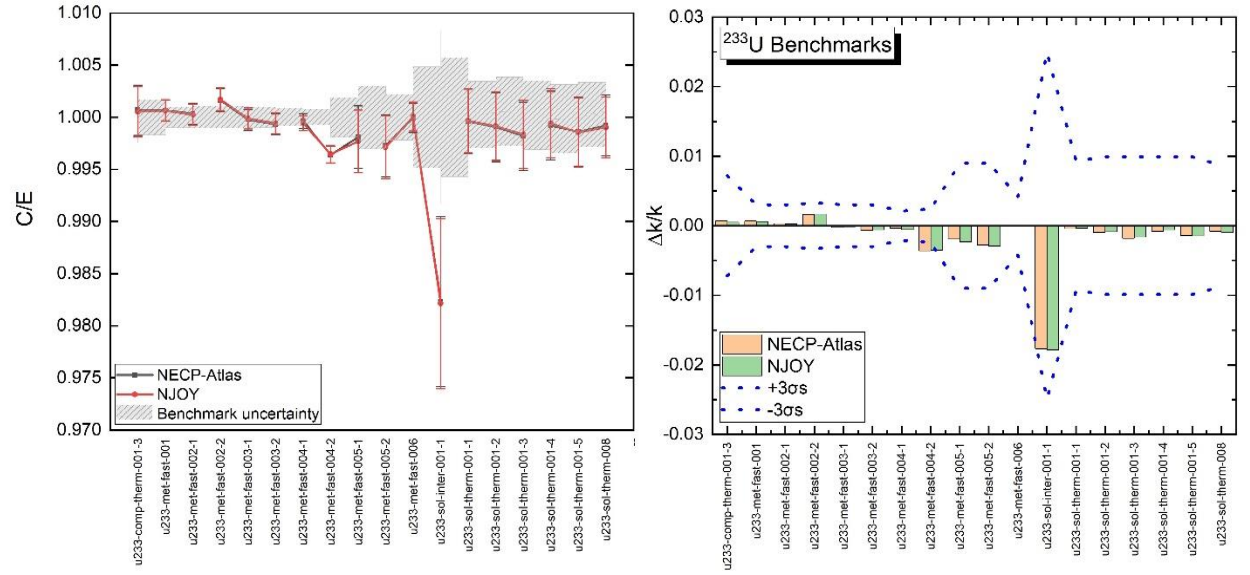

Figure 3. 40. $(\frac{C}{E})$ and $\Delta k_{eff}/k$ results for the U-233 benchmarks.

Statistical analysis

Using the data in **Figure 3.36** to **Figure 3.40**, this subsection provides a statistical evaluation between NECP Atlas and NJOY for each case in each category of benchmarks. **Figure 3.41** to **Figure 3.45** show comparisons between NECP-Atlas and NJOY based $\frac{\Delta k_{eff}}{k_{eff}}$ and $\frac{\Delta k_{eff}}{\sigma_s}$ metrics for each of the benchmark systems regrouped by benchmarks category. **Tables 3.4** and **3.5** show the

validation metrics as calculated by **Equations** (**3.3 to 3.10**) for the whole category. From the plotted results, it is observed that the majority of the cases show good agreement between NECP-Atlas and NJOY with $|\Delta k_{eff}|$ values within 0.02% of each other. Few cases exhibit differences between 0.04% and 0.05%. However**,** more than 54% of keff values based on NECP-Atlas were higher than NJOY values. Concerning the obtained uncertainties, 93% of the cases are within 3σ, 77% of the cases are within 2σ and 47% of the cases are within 1σ. Moreover, the LEU systems show the most significant difference NECP-Atlas and NJOY results (93% of cases). Yet, based on the virtually identical values of χ^2, $\langle|\Delta|\rangle$ and $\overline{k_{eff}} \pm S_p$, show that there are minor differences between NECP-Atlas and NJOY processing codes.

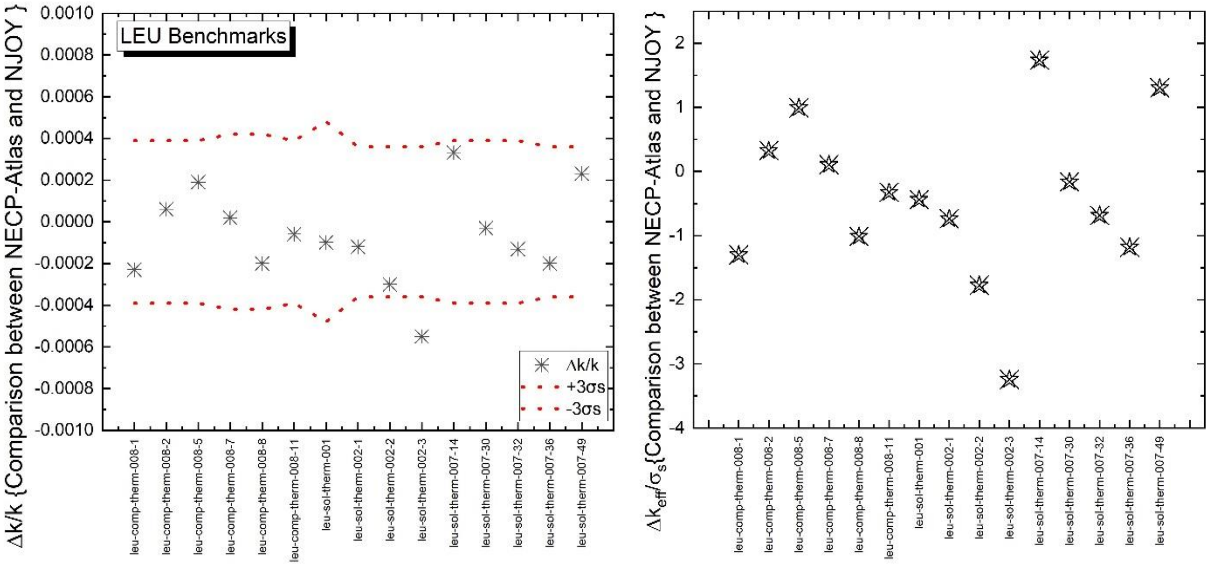

Figure 3. 41. $\frac{\Delta k_{eff}}{k_{eff}}$ and $\frac{\Delta_{keff}}{\sigma_s}$, comparison between NECP-Atlas and NJOY, LEU benchmarks.

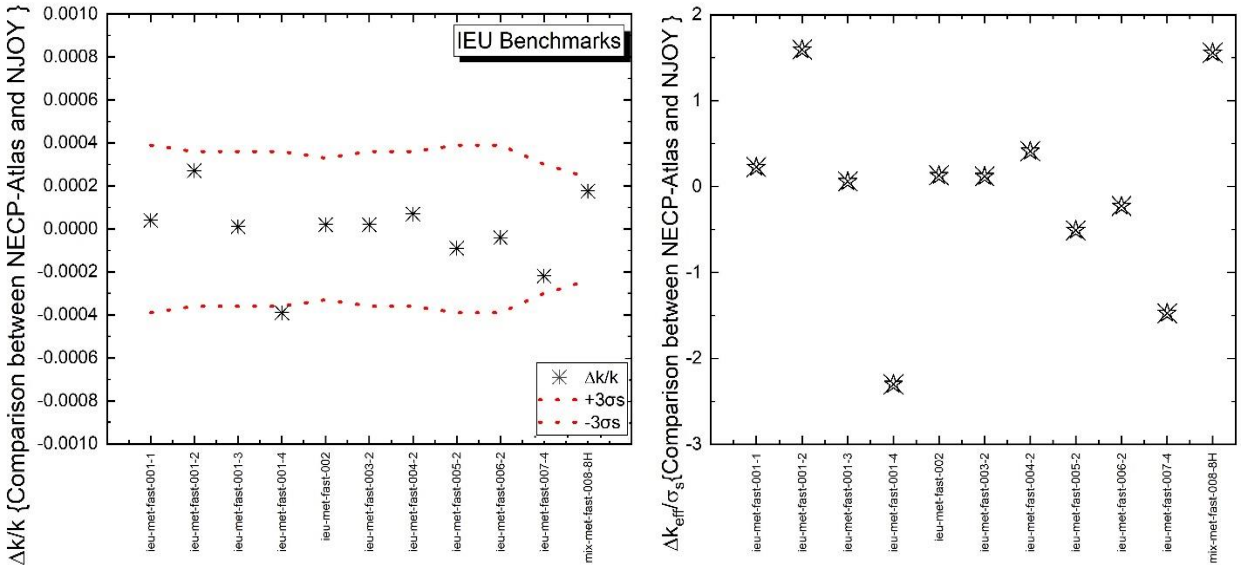

Figure 3. 42. $\frac{\Delta k_{eff}}{k_{eff}}$ and $\frac{\Delta_{keff}}{\sigma_s}$, comparison between NECP-Atlas and NJOY, IEU benchmarks.

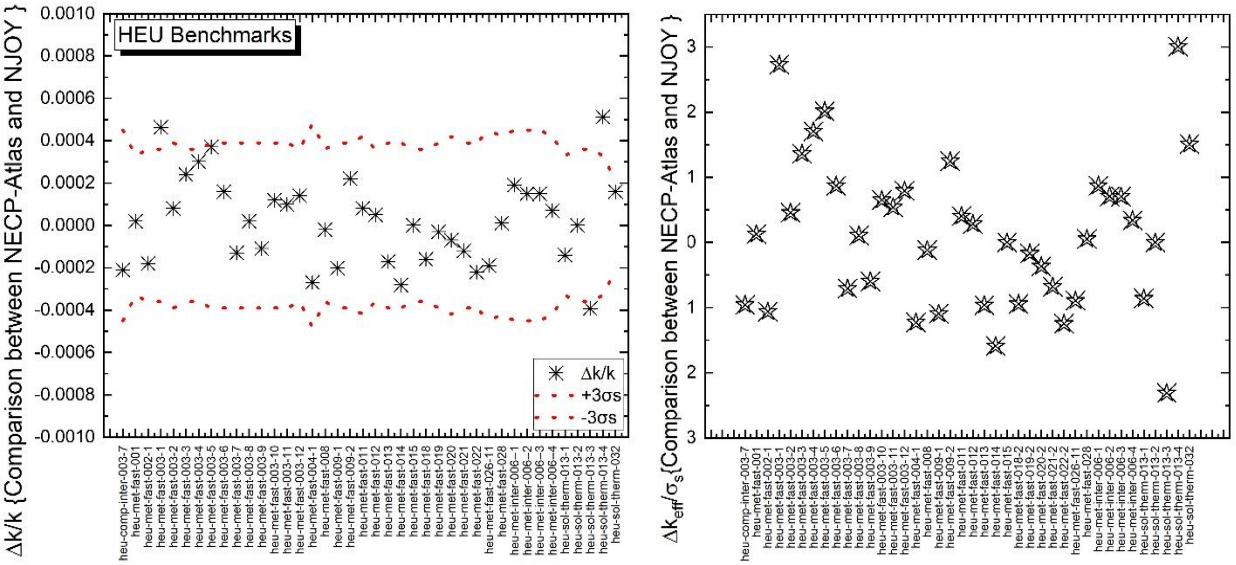

Figure 3. 43. $\frac{\Delta k_{eff}}{k_{eff}}$ and $\frac{\Delta_{keff}}{\sigma_s}$, comparison between NECP-Atlas and NJOY, HEU benchmarks.

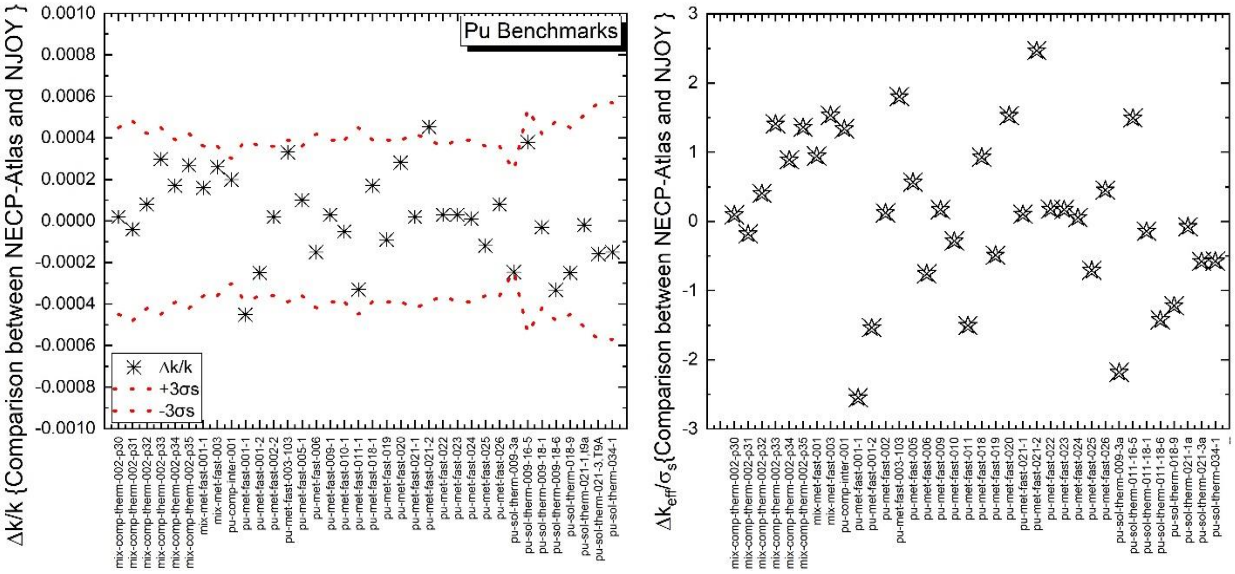

Figure 3. 44. $\frac{\Delta k_{eff}}{k_{eff}}$ and $\frac{\Delta_{keff}}{\sigma_s}$, comparison between NECP-Atlas and NJOY, Pu benchmarks.

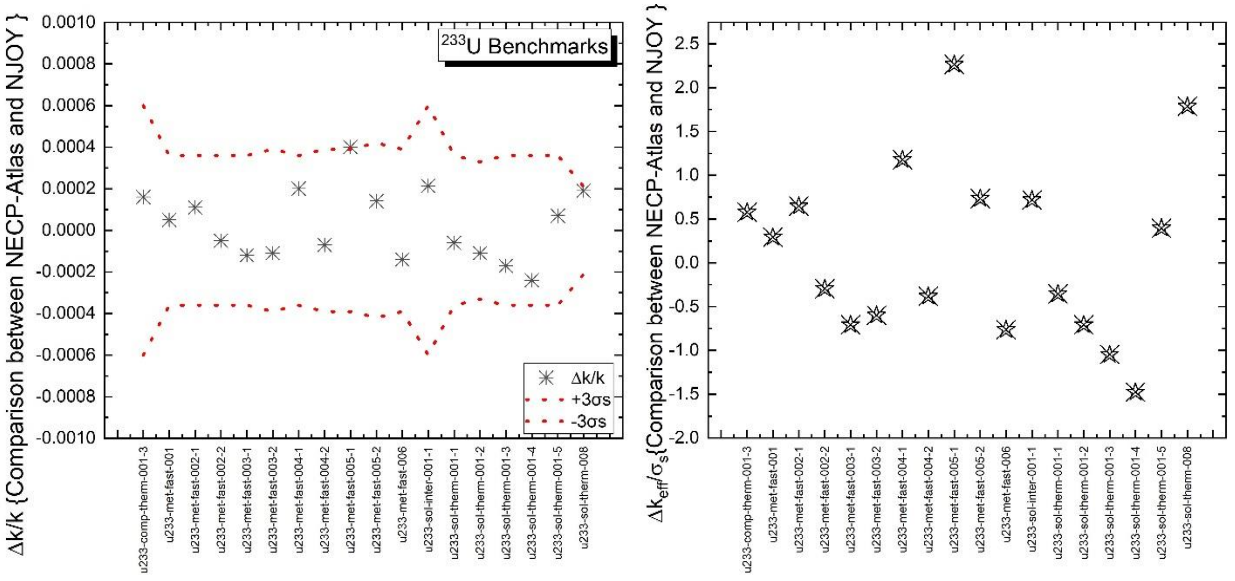

Figure 3. 45. $\frac{\Delta k_{eff}}{k_{eff}}$ and $\frac{\Delta_{keff}}{\sigma_s}$, comparison between NECP-Atlas and NJOY, U-233 benchmarks.

Table 3. 4. χ^2 goodness-of-fit, and the $\langle|\Delta|\rangle$ factors, comparison between NECP-Atlas, NJOY and the benchmarks results.

Benchmarks	Number of benchmarks in the category	NECP-Atlas		NJOY	
		χ^2	$\langle\|\Delta\|\rangle$	χ^2	$\langle\|\Delta\|\rangle$

LEU benchmarks	15	2.34	235.20	2.36	229.53
IEU benchmarks	11	6.71	346.00	6.61	347.55
HEU benchmarks	40	2.58	254.30	2.61	257.63
Pu benchmarks	36	1.44	270.75	1.48	268.86
U-233 benchmarks	18	1.70	204.39	1.68	204.72
Average	120	2.96	262.13	2.95	261.66

Table 3. 5. Weighted mean $\overline{k_{eff}}$ and S_p.

Benchmarks	Number of benchmarks in the category	NECP-Atlas		NJOY	
		$\overline{k_{eff}} \pm S_p$		$\overline{k_{eff}} \pm S_p$	
LEU benchmarks	15	0.99848	± 0.00292	0.99847	± 0.00299
IEU benchmarks	11	1.00036	± 0.00412	1.00036	± 0.00415
HEU benchmarks	40	0.99980	± 0.00389	0.99977	± 0.00390
Pu benchmarks	36	0.99995	± 0.00371	0.99995	± 0.00373
U-233 benchmarks	18	0.99939	± 0.00216	0.99937	± 0.00215

Results for the Doppler benchmark

The multiplication factors were calculated at HZP and HFP for various types of fuel. We choose to take as the reference the results obtained with the library ENDF/B-VII.0 the results are shown in **Figure 3.46** to **Figure 3.48** the relative error in the Doppler coefficient is also plotted in the mentioned figures.

When we compare the results from ENDF/B-VII.0 and ENDF/B-VIII.0 cross-sections, we find that there is no straight rule between the calculated k-infinity values (i.e. ENDF/B-VIII.0 values sometimes higher sometimes lower), besides, the maximum difference in k-infinity between the two libraries is up to 0.4% on an absolute basis. Conversely, there is a difference in the Doppler coefficient since ΔD_C is around 4%, 3%, and 3% on an absolute basis, for UO_2, reactor-recycled, and weapons-grade MOX fuel category, respectively, but they are mainly within the $\pm 3\sigma_s$ interval, near the ENDF/B-VII.0 values. Also, the maximum ΔD_C occurs for the Weapons-Grade MOX fuel case 1 (9% on an absolute basis).

The comparison between ENDF/B-VIII.0-NECP-Atlas and ENDF/B-VIII.0-NJOY indicates that the NECP-Atlas-based k-infinity values are slightly below the NJOY values (60% of the total values) but differences are below 0.04% on an absolute basis. On the other hand, more than 70% Dc calculated with ENDF/B-VIII.0-NECP-Atlas are higher than the values given by ENDF/B-VIII.0-NJOY. The maximum difference is 7.1% for UO_2 (enriched to 4.5%) this is generally acceptable since ΔD_C values are mainly (around 94%) within the $\pm 1\sigma_s$ interval, near the value given by NJOY.

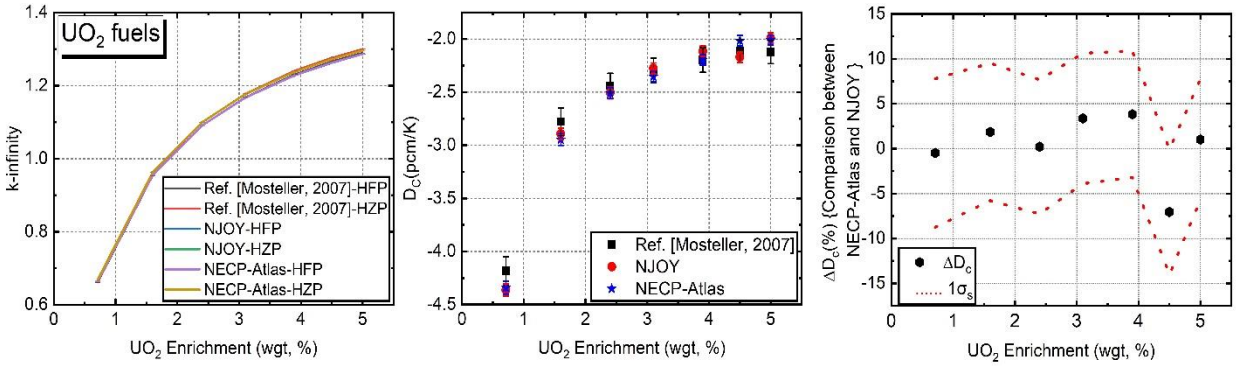

Figure 3. 46. Doppler Coefficients for UO_2 fuels.

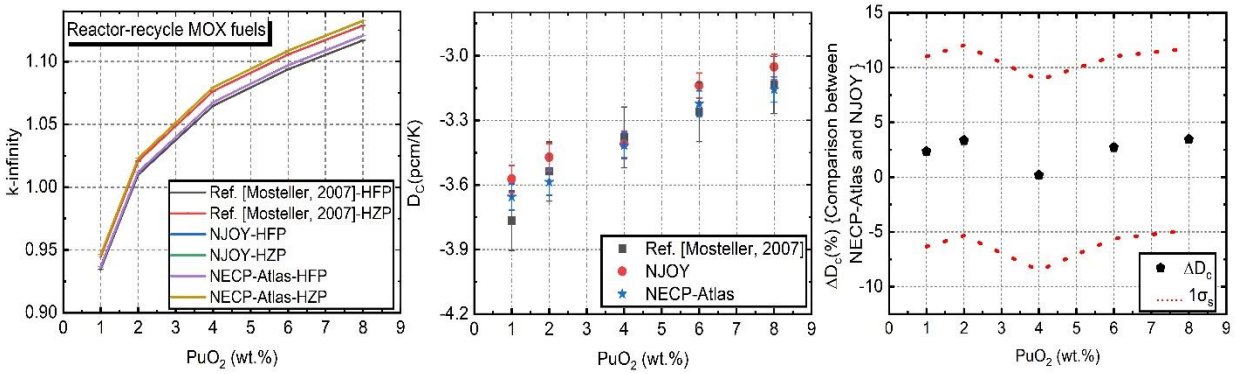

Figure 3. 47. Doppler Coefficients for Reactor-Recycle MOX fuels.

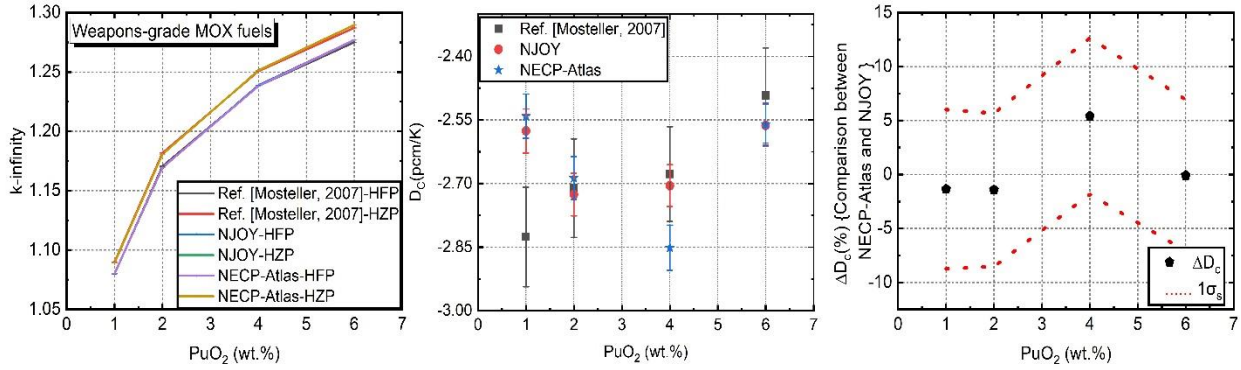

Figure 3. 48. Doppler Coefficients for Weapons-Grade MOX Fuels.

3.4.4. Summary

This work has focused on processing the entire recent release of the ENDF nuclear data library with the NECP-Atlas and NJOY processing codes. The subject is to perform a statistical inter-comparison between the produced neutron libraries. This study also demonstrates the way ACE

libraries are processed for MCNP codes. The verification and the mutual comparison of processed files are carried out by performing criticality calculations for 120 criticality safety benchmarks and additional benchmarks proposed by Russell D. Mosteller.

The results for criticality safety benchmarks are acceptable to good in the vast majority of cases, with only minor differences between the two processed libraries and the benchmark values. The largest deviations occurred for some known benchmarks, though such poor performances also have been reported for earlier ENDF/B releases.

For the benchmark experiments used, statistical analyzes based on $\frac{\Delta k_{eff}}{k_{eff}}$, χ^2, $\langle|\Delta|\rangle$, the weighted mean multiplication factor and the bias uncertainty were established and presented. Results show that the discrepancy between the values obtained for ENDF/B-VIII.0-NECP-Atlas and ENDF/B-VIII.0-NJOY libraries falls within a reasonable range.

The results for the Doppler coefficients are generally good, but in some cases, strong deviations from the benchmark values occur. The largest deviations are seen for Weapons-grade MOX fuels (especially case 1, both libraries). Yet the results showed good agreement with no substantial differences between NECP-Atlas and NJOY libraries.

3.4.5. Acknowledgments

The authors acknowledge gratefully Professor Tiejun Zu and the NECP-Atlas code developers at Xi'an Jiaotong University in China for providing NECP-Atlas code for this work.

3.4. Processing of JEFF-3.3 and ENDF/B-VIII.0 and testing with critical benchmark experiments and TRIGA Mark II research reactor using MCNPX

Modified from a paper published in Applied Radiation and Isotopes - Journal.

DOI: https://doi.org/10.1016/j.apradiso.2019.05.015

Ouadie Kabach [1,*], Abdelouahed Chetaine [1], Abdelfettah Benchrif [2]

[1)] Nuclear Reactor and Nuclear Security Group Energy Center, Nuclear Physics Laboratory, Physics Department, Faculty of Science, Mohammed V University, Rabat, Morocco.

[2)] National Centre of Sciences, Energy and Nuclear Techniques (CNESTEN/CENM), POB 1382, Rabat, Morocco.

*Corresponding author e-mail address: ouadie.kabach10@gmail.com

Abstract: A comparative study has been performed with the latest evaluated nuclear data libraries JEFF-3.3 and ENDF/B-VIII.0. The study has been conducted through the benchmark calculations for 120 criticality problems and the TRIGA Mark II research reactor with the libraries processed using NJOY21 for the MCNPX Monte Carlo transport code. The criticality benchmark assemblies, taken from the ICSBEP benchmark, cover Uranium (highly enriched uranium, intermediate enriched uranium, low enriched uranium, and U-233) and Plutonium fuel systems in various metal forms, and under various spectral conditions. The Moroccan TRIGA Mark II research reactor calculation is used to look into the predictive capability of those nuclear data libraries and then to compare the accuracy of the predicted results with the experimental data published elsewhere.

Actually, the purpose of this study is to investigate some neutronic and kinetic parameters of those benchmarks for both libraries. The formers consist of effective multiplication factor, heat distribution, neutron flux distribution, effective delayed neutron fraction (β_{eff}), prompt removal lifetime (τ_r), and the mean neutron generation time (Λ). The results show that the calculated effective multiplication factor, heat distribution, neutron flux distribution, and kinetic parameters are in good agreement with references. However, it is found that the computed values are strongly dependent on the nuclear data set used in calculations.

3.4.1. Introduction

The nuclear data evaluations have been separately released from different countries. ENDF/B-VI of Cross-Section Evaluation Working Group and JEFF of OECD/NEA have been widely

utilized in the nuclear community in light of the fact that these libraries include reliable, evaluated data for all neutron reactions. In the last years, new versions of the two nuclear reaction data libraries were released: JEFF-3.3 in 2017 [70] and ENDF/B-VIII.0 in 2018 [71] with a significant upgrade in data for several nuclides [72]. The ENDF-6 formats [11] are accessible on the IAEA website [73].

This work was intended to generate the continuous energy neutron data libraries for the MCNPX [29] based on the latest evaluated nuclear data and to analyze them through benchmarking with the 2 MW TRIGA Mark-II research reactor and the criticality benchmarks calculations. Application libraries have been independently created with the NJOY21(1.0.0.json) Nuclear Data Processing System [12] available at the LANL website [16]. A broad outline of this section begins with: i) testing the processed libraries of critical benchmark models defined in the International Criticality Safety Benchmark Evaluation Project (ICSBEP) handbook [41]. In this part of this work the effective multiplication factors (keff) are calculated and compared to the published benchmark values [41]; ii) benchmarking the processed libraries with the TRIGA Mark II research reactor for the well-known both neutronic and kinetic parameters. The complete 3D geometry of the TRIGA reactor core, using MCNPX, is implemented with high accuracy and details, exploiting all the available data about the geometry and materials. Finally, as part of the evaluation process, comparisons with the JEFF-3.2 [74] and ENDF/B-VII.1 [75] libraries were indeed carried out.

3.4.2. Results of criticality benchmark calculations

In this section, we report the keff results of the criticality benchmark using the MCNPX code. All results are given in graphical and in tabular form (see Appendix A). The following section contains:

i) The benchmark calculation values for keff and its uncertainty in pcm.

ii) The $\frac{C}{E}$ values for keff and their uncertainties using the following libraries: JEFF-3.3, ENDF/B-VIII.0, JEFF-3.2, and ENDF/B-VII.1.

iii) The χ^2 and $\langle|\Delta|\rangle$ metrics.

The results of the calculations using JEFF-3.3 and ENDF/B-VIII.0 libraries have been compared with the published results [41] and with those obtained with JEFF-3.2 and ENDF/B-

VII.1. Each calculation has used a total average of 3,000 active generations of 10,000 histories per generation. The results from the first 50 generations were excluded from the statistics. Subsequently, the reported results for each case are based on 29,500,000 active neutron histories. A statistical uncertainty between 10 pcm and 30 pcm is obtained. For the large majority of the cases studied, the criticality benchmarks calculations illustrate a good performance for the chosen latest libraries. As shown in **Figure 3.49** to **Figure 3.53**, the keff accuracy is quite dramatic. Seventy-eight (accounted for 65%) and sixty (50%) of the one-hundred-twenty values for keff have been improved for ENDF/B-VIII.0 and JEFF-3.3 libraries against ENDF/B-VII.1 and JEFF-3.2. For the rest of the cases, the two studied libraries produce values for keff, which are not significantly different from those produced by JEFF-3.2 and ENDF/B-VII.1 and the following remarks can be underlined:

For the HEU category, the computations have been made for 40 critical assemblies and the results are qualitatively good as demonstrated in **Figure 3.49**. With ENDF/B-VIII.0 cross-sections, the worst-case result is obtained for "heu-met-fast-003-case11", the calculated eigenvalue is too large by almost 860 pcm, for the JEFF-3.3 library a deviation of 980 pcm was obtained. Nonetheless, these results are still better than those calculated with ENDF/B-VII.1 and JEFF-3.2.

For both ENDF/B-VIII.0 and JEFF-3.3 IEU system category (15 calculated cases), it is worthy to note that the overall keff $\frac{C}{E}$ results are very good in which the average deviations are 55 pcm and 36 pcm for ENDF/B-VIII.0 and JEFF-3.3 cross-sections, respectively (**Figure 3.50**).

The $\frac{C}{E}$ keff results for LEU case, which is considered as an important benchmark category (10 studied cases); indicate that seven of the 10 assemblies are reduced with ENDF/B-VIII.0 and five of the 10 assemblies for the JEFF-3.3 library (**Figure 3.51**). The worst result was reported for "leu-sol-therm-001" in both libraries.

In the Pu category (37 cases), the performance of the new ENDF/B-VIII.0 and JEFF-3.3 libraries versus the performance of the ENDF/B-VII.1 and JEFF-3.2 demonstrate that 19 calculated $\frac{C}{E}$ keff's values for these experiments are improved for the two reviewed libraries. The worst values were observed for "mix-met-fast-008" and "pu-sol-therm-009-case3a" cases, by 2212 pcm and 1280 pcm, respectively (**Figure 3.52**).

The results for U-233 benchmarks (18 cases) show that keff values obtained with JEFF-3.3 nuclear data are higher than those obtained with ENDF/B-VIII.0. However, the keff's for 6

assemblies among 18 are reduced from JEFF-3.3 to JEFF-3.2. It is worth mentioning that a particular result has been deduced for benchmarks containing Beryllium (Be) such as for "U233-sol-inter-001-case1". The calculated eigenvalue, as shown in **3.53**, is too small by almost 1414 pcm and 1779 pcm for ENDF/B-VIII.0 and JEFF-3.3, respectively, but they still better than ENDF/B-VII.1 and JEFF-3.2. [18, 67] have reported that the beryllium is performing worse when it is used as a reflector. Therefore, it is strongly recommended that their cross-sections be reviewed. As demonstrated in **Tables 3.6** and **3.7**, it should be noted that the ENDF/B-VIII.0 produces excellent agreement with the experimental for the majority of cases than JEFF-3.3 except for a few benchmark cases, whereas for the rest of the cases a similar behavior between both libraries is highlighted.

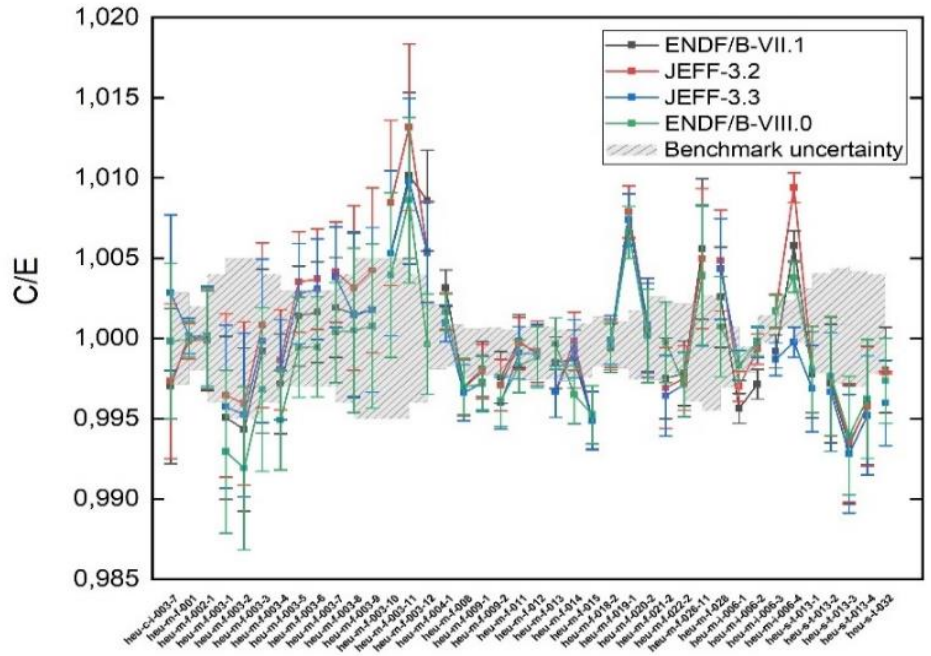

Figure 3. 49. $\frac{C}{E}$ results and their uncertainties for the HEU benchmarks.

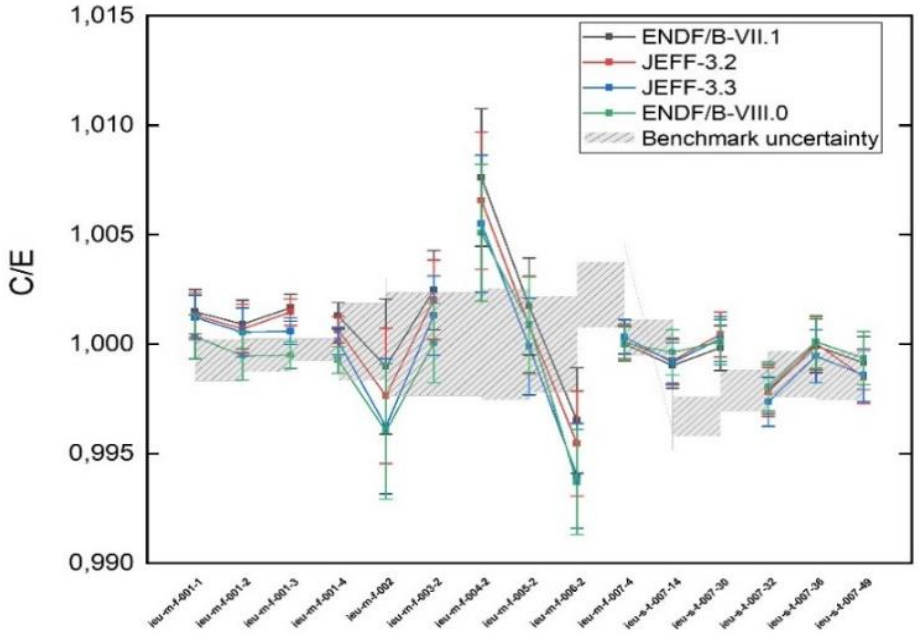

Figure 3. 50. $\frac{C}{E}$ results and their uncertainties for the IEU benchmarks.

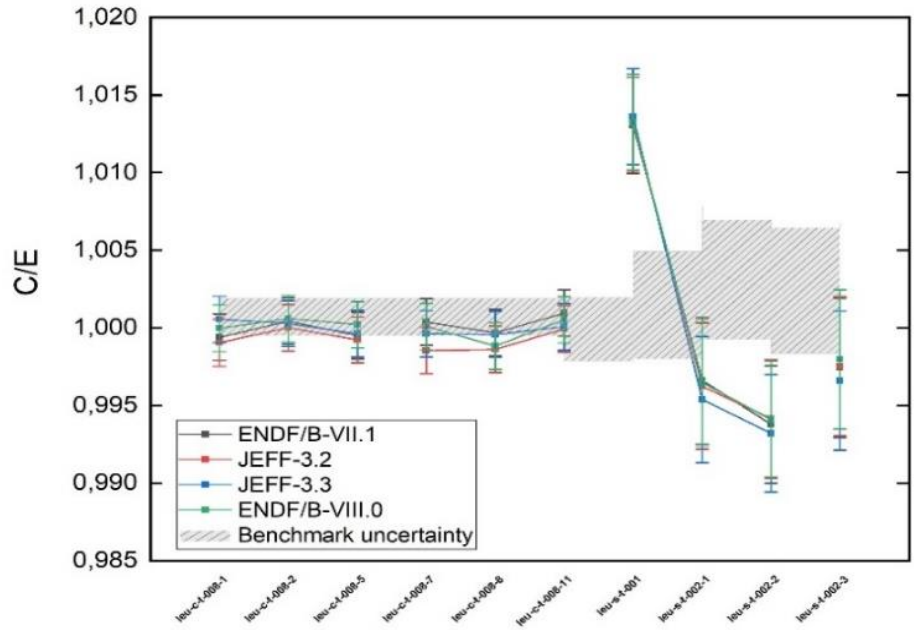

Figure 3. 51. $\frac{C}{E}$ results and their uncertainties for the LEU benchmarks.

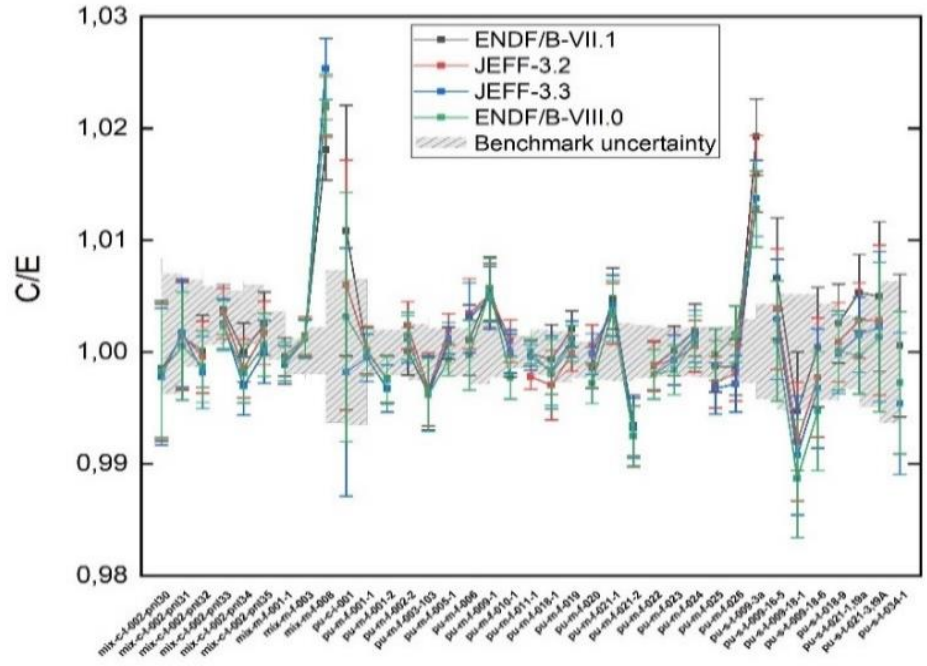

Figure 3. 52. $\frac{C}{E}$ results and their uncertainties for the Pu benchmarks.

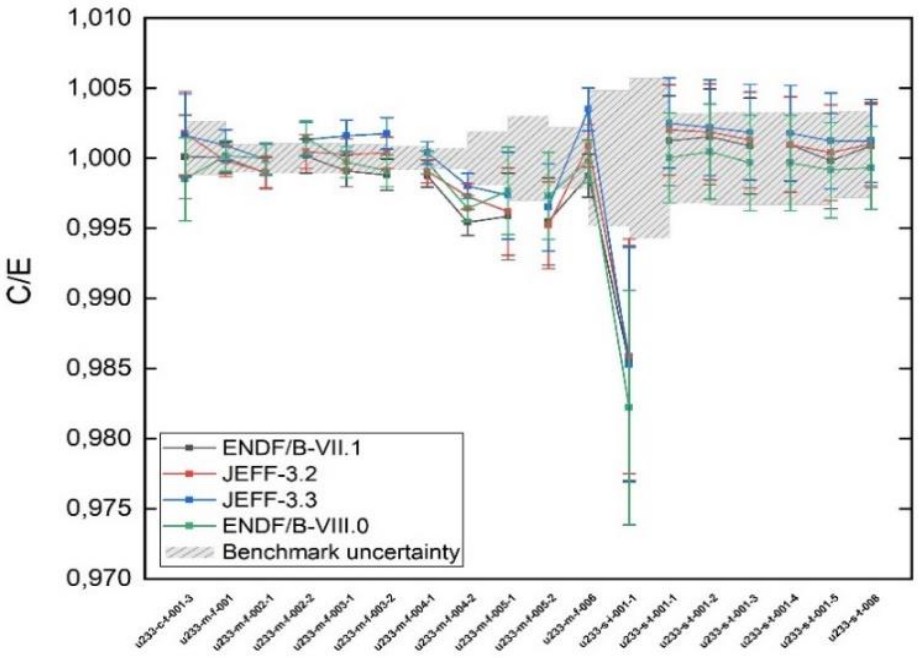

Figure 3. 53. $\frac{C}{E}$ results and their uncertainties for the U-233 benchmarks.

Table 3. 6. The χ^2 between calculated and benchmark keff.

	ENDF/B-VII.1	JEFF-3.2	JEFF-3.3	ENDF/B-VIII.0
All benchmarks	3.424	3.863	2.692	2.491
HEU benchmarks	4.535	6.140	2.344	2.533
IEU benchmarks	2.590	2.088	1.732	1.340
LEU benchmarks	2.549	2.826	2.787	2.586
Pu benchmarks	3.166	3.641	3.974	3.310
U-233 benchmarks	2.665	1.316	1.575	1.623

Table 3. 7. The average difference ($\langle|\Delta|\rangle$) in pcm between calculated and benchmark keff.

	ENDF/B-VII.1	JEFF-3.2	JEFF-3.3	ENDF/B-VIII.0
All benchmarks	280.968	294.209	283.524	245.591
HEU benchmarks	306.925	335.850	296.500	253.050
IEU benchmarks	172.000	170.067	167.867	144.133
LEU benchmarks	284.600	299.500	305.100	273.700
Pu benchmarks	325.976	335.759	327.024	298.997
U-233 benchmarks	219.556	216.778	249.667	188.167

3.4.3. TRIGA Mark II research reactor calculation

The TRIGA Mark II research reactor installed at Maamora Center of Nuclear Studies (CENM), in Morocco, is a research reactor operated at 2000 kW. It is a pool-type reactor cooled and moderated by light water. The fuel is composed of a mixture of uranium (8.5 wt.%, enriched at 19.7% with U-235), zirconium hydride, and encapsulated in a stainless steel cladding. Five control rods containing boron carbide control the reactor. The TRIGA core consists of 101 fuel elements and 17 graphite elements. Further description of TRIGA can be found in [76]. The model for these components was realized trying to preserve as far as possible all the characteristics related to the geometry, dimensions, and compositions. The MCNPX input was prepared (**Figure 3.54**) in such a way that a very quick setup of any desired core configuration with an adequate position of all control rods is possible. The MCNPX calculations were run with 50,000,000 active histories. 50,000 histories per generation were used and 1,050 generations of neutrons. The first 50 generations were skipped to obtain a well-distributed neutron source. To account for thermal neutron scattering and low-energy neutron interactions, the appropriate $s(\alpha,\beta)$ treatments were used for water, zirconium hydride, and crystalline graphite for all the studied libraries.

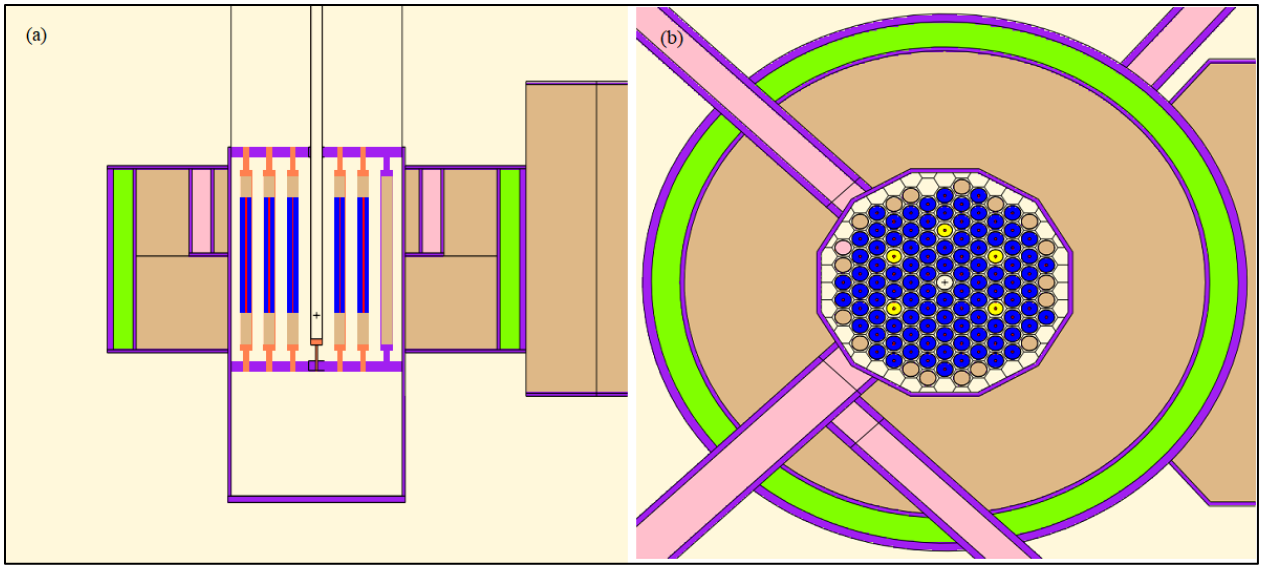

Figure 3. 54. Side (a) and Top (b) view of the MCNPX computational model of the TRIGA Mark II research reactor.

Neutronic parameters calculation results

The calculation results of all the neutronic parameters including the effective multiplication factor, heat distribution, neutron flux distribution, of the TRIGA Mark II reactor core using MCNPX code and both data libraries JEFF-3.3 and ENDF/B-VIII.0 are investigated in the following sections.

Effective multiplication factor (keff)

The calculations of the keff eigenvalue were performed in the core for three cases; the critical position, core in the operating position, and control rods that are withdrawn. The comparison between the MCNPX and the experimental results is shown in **Table 3.8**. The calculated $(\frac{C}{E} - 1)$ value of keff for the control rods at critical positions [77] were found to be overestimated by 474 pcm and 120 pcm for JEFF-3.3 and ENDF/B-VIII.0, respectively. For the operating position [78], the $(\frac{C}{E} - 1)$ value of keff were found also to be overestimated by 578 pcm for JEFF-3.3 and 254 pcm for ENDF/B-VIII.0. However, underestimated values of 51 pcm and 341 pcm for all control rods in withdrawn positions [79] have been deduced for JEFF-3.3 and ENDF/B-VIII.0, respectively. It can also be observed that the calculated keff using JEFF-3.3 are systematically higher than this using ENDF/B-VIII.0 except for rods that were completely withdrawn position.

Table 3. 8. Comparison between the experiment and calculated keff at different control rod positions using different cross-section libraries.

Control rods position	Core multiplication factor. keff							
	Reference	Calculation						
		ENDF/B-VII.1		JEFF-3.2		JEFF-3.3		ENDF/B-VIII.0	
Critical	1.00	0.99964	± 0.00010	1.00395	± 0.00011	1.00474	± 0.00010	1.00120	± 0.00010
Operating position	1.04957	1.05062	± 0.00010	1.05475	± 0.00011	1.05564	± 0.00010	1.05224	± 0.00011
Withdrawn (full-out-condition)	1.07902	1.07382	± 0.00010	1.07763	± 0.00010	1.07847	± 0.00010	1.07533	± 0.00011
Control rod worth (|**ρ**|) in pcm	-	6910,5	± 13,7	6810,3	± 14,4	6804,3	± 13,6	6885,4	± 14,3

Effect of graphite isotope density over TRIGA multiplication factors

The density of the graphite elements is not directly reported on the reactor documentation (the composition of the reflector is poorly documented). The value we used, equal to 1.65 g/cm^3, was found in [77]. However, other sources report different values, with the density ranging from 1.72 g/cm^3 [80] to 1.75 g/cm^3 [81]. To investigate the effects of nuclear graphite density on the core effective multiplication factor at different control rod positions, the PERT card was used [28]. This card allows perturbations in cell material density. This latter is estimated without actually changing the input material specifications. The calculation findings are presented in **Table 3.9**.

Table 3. 9. Effect of Graphite density over the calculated keff at different control rod positions using different cross-section libraries.

Control rods position	Graphite density ($\mathbf{g/cm^3}$)	Core multiplication factor							
		Calculation							
		ENDF/B-VII.1		JEFF-3.2		JEFF-3.3		ENDF/B-VIII.0	
Critical	1.75	1.00427	± 0.00016	1.00829	± 0.00017	1.00921	± 0.00016	1.00566	± 0.00017
	1.65	0.99964	± 0.00010	1.00395	± 0.00011	1.00474	± 0.00010	1.00120	± 0.00010
Operating position	1.75	1.05496	± 0.00016	1.05909	± 0.00017	1.06000	± 0.00010	1.05676	± 0.00016
	1.65	1.05062	± 0.00010	1.05475	± 0.00011	1.05564	± 0.00010	1.05224	± 0.00011
Withdrawn (full-out-condition)	1.75	1.07802	± 0.00017	1.08189	± 0.00017	1.08303	± 0.00016	1.07954	± 0.00017
	1.65	1.07382	± 0.00010	1.07763	± 0.00010	1.07847	± 0.00010	1.07533	± 0.00011

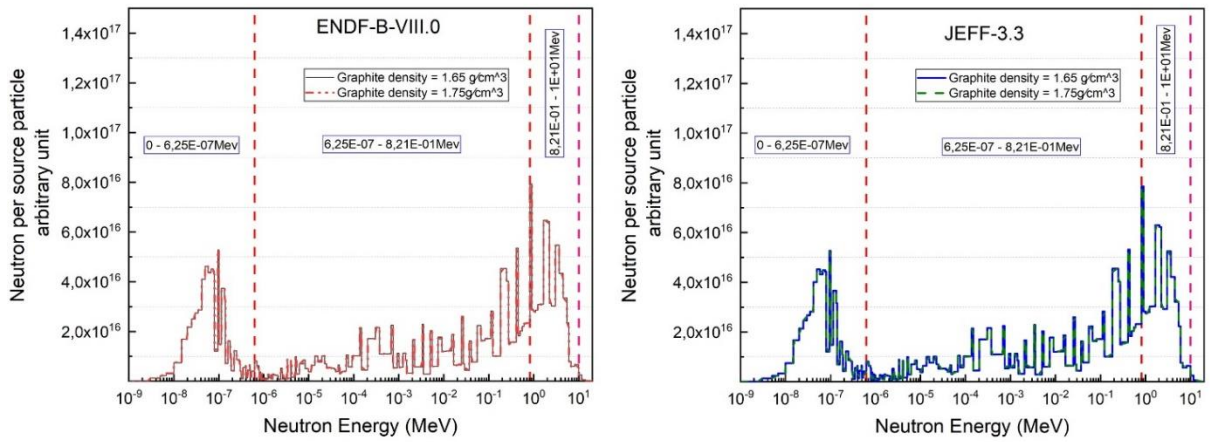

Figure 3. 55. Comparison of the neutron flux spectra obtained from different graphite densities using ENDF/B-VIII.0 and JEFF-3.3 libraries.

The initial calculated keff at different control rod positions predicted by the model were compared well with the reference values (**Table 3.8**). For the perturbation case as demonstrated in **Table 3.9**, the analysis of the simulation results with the control rods in different positions highlights that the core multiplication factors increase appreciably about (0.5 %) for all studied libraries. This increase can be explained by the fact that an increase in graphite density may allow more energetic neutrons to be better scattered which results in a rise in keff values. Nevertheless, as shown in **Figure 3.55**, no clear changes were exhibited by the comparison of the neutron flux spectra obtained with both graphite densities. The maximum neutron flux differences were found to be 0.13 % in the thermal region, 0.3 % in the epi-thermal region, and 0.43 % in the fast region for both ENDF/B-VIII.0 and JEFF-3.3 libraries. It can be concluded, therefore, that the graphite density change (from 1.65 g/cm^3 to 1.75 g/cm^3) does not significantly affect the neutron spectrum.

Neutron flux and power distributions analysis

For the neutron flux calculations, a comparison was made between the JEFF-3.3 and ENDF/B-VIII.0 (**Figure 3.56**). It is found that the MCNPX predicted values for both libraries have almost the same values as those in the reference core [79], and we observe that the flux evaluations by JEFF-3.3 are systematically slightly higher (about 1 % on average) than those by ENDF/B-VIII.0.

The plots in **Figures 3.57** and **3.58** show the power distributions in the core of TRIGA Mark-II by comparing the calculated results to the two studied libraries. In this study, the heat generated in each of the fuel elements is most likely due to two sources: non-fission neutron reactions (mainly elastic and inelastic scattering) and neutron-induced fission reactions. For tallying these results, F6: n Tally was used (track length estimator of fission energy deposition) and normalized to the full-power steady-state operating condition.

It is worth mentioning that the fuel elements in the middle rings generate more power than those in the external rings of the core. The maximum power produced in the hottest fuel element at full-power steady state was found to be 29.31 kW, 29.3 5kW, 29.20 kW, and 29.42 kW in the B3 fuel element for ENDF/B-VIII.0, JEFF-3.3, ENDF/B-VII.1, and JEFF-3.2, correspondingly. In general, there is good agreement between the power distribution values evaluated by both ENDF/B-VIII.0 and JEFF-3.3. We may see that the differences between them were observed to be 2 % in the core center and around 3 % in the boundaries of the core.

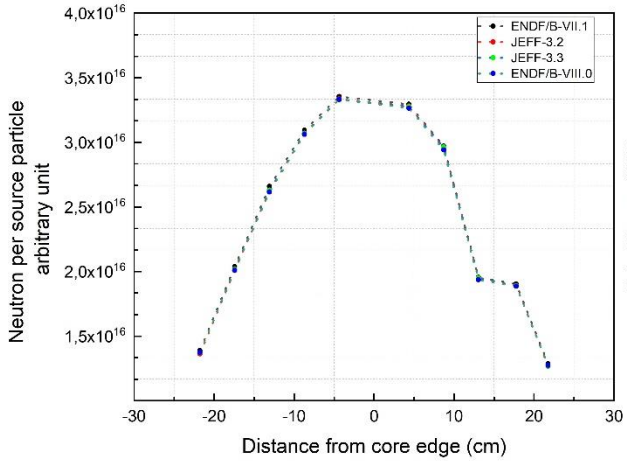

Figure 3. 56. Comparison between the measured radial flux using different cross-section libraries.

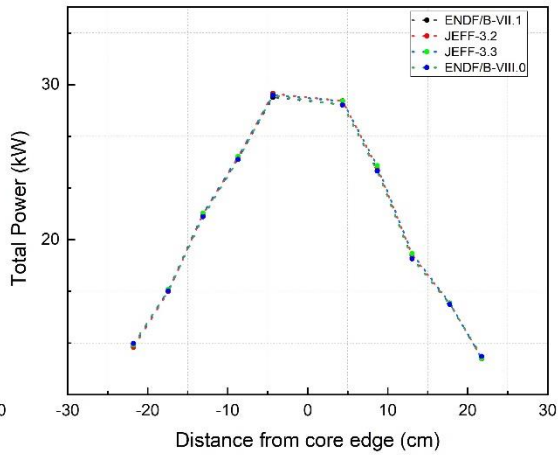

Figure 3. 57. Comparison between the measured radial power distribution using different cross-section libraries.

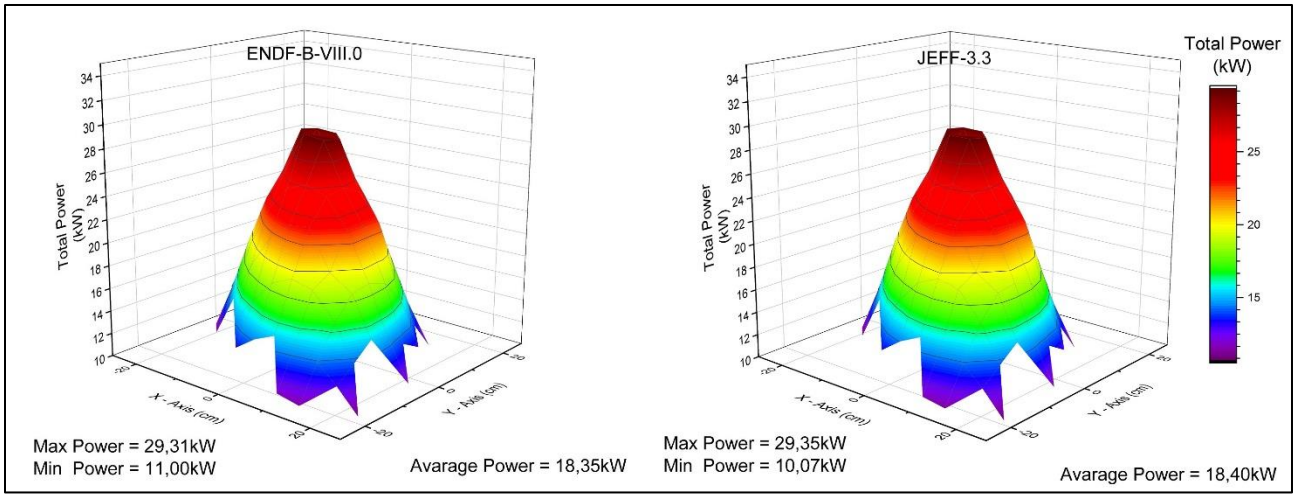

Figure 3. 58. Radial power distribution within the fuel and fuel follower produced using ENDF/B-VIII.0 and JEFF-3.3 libraries.

3.5.3.1. Kinetics parameters results

The principal analyzed kinetics parameters are effective delayed neutron fraction (β_{eff}), prompt removal lifetime (τ_r), and mean neutron generation time (Λ). They can determine the time-dependent behavior of reactor power after reactivity insertion. In research reactors, these parameters are usually provided by the manufacturer [82].

Effective delayed neutron fraction (β_{eff})

The effect of the nuclear data library on the calculated value of βeff was investigated for TRIGA MARK II at the critical position. The results are summarized in **Tables 3.10** and **3.11**. We notice that clearly the results of ν, ν_p, ν_d, and β_{eff} are strongly dependent on the nuclear data library used. However, we can see that the calculated values are close between (ENDF/B-VII.1, ENDF/B-VIII.0) and (JEFF-3.2, JEFF-3.3) and as expected, it is highly likely due to the original ENDF data evaluation process. It can be seen likewise that the values of ν, ν_p, ν_d, and β_{eff} are slightly closer to the reference values [82]. Anyway, both libraries agreed with a maximum relative error smaller than 3% with the reference value.

Table 3. 10. Predicted values of keff, k_p, k_d, and β_{eff} of various nuclear data libraries.

	Reference	ENDF/B-VII.1	JEFF-3.2	JEFF-3.3	ENDF/B-VIII.0
keff	-	0.99964 ± 0.00010	1.00395 ± 0.00011	1.00474 ± 0.00010	1.00120 ± 0.00010
k_p	-	0.99241 ± 0.00011	0.99643 ± 0.00010	0.99724 ± 0.00011	0.99396 ± 0.00010

k_d	-	0.00723 ± 0.00021	0.00752 ± 0.00021	0.00750 ± 0.00021	0.00724 ± 0.00020
β_{eff}	0.00730	0.00723 ± 0.00021	0.00749 ± 0.00021	0.00746 ± 0.00021	0.00723 ± 0.00020

Table 3. 11. The comparison of the estimated values of the average number of neutrons released per fission (ν), prompt neutron (νp), and delayed neutron yields (νd).

	Reference [83]	ENDF/B-VII.1	JEFF-3.2	JEFF-3.3	ENDF/B-VIII.0
ν	2.4300	2.4386	2.4272	2.4273	2.4314
νp	2.4142	2.4226	2.4108	2.4110	2.4155
νd	0.0158	0.0159	0.0164	0.0164	0.0159

Calculation of the mean neutron generation time (Λ).

The second important kinetic parameter that characterizes the time behavior of the neutron population is the mean neutron generation time. Using the prompt neutron lifetime τ_r, which is the average time from the emission of a prompt neutron in fission to the removal of the neutron by some physical process such as fission, capture, or escape, and keff. For Λ the reported value of mean neutron generation time for 8.5 wt.% fuel range from 49.2 to 54.8 μs [84], while our computed values are 52.250 μs and 52.623 μs utilizing JEFF-3.3 and ENDF/B-VIII.0 data libraries, respectively (**Table 3.12**). The maximum difference value between the reference value and JEFF-3.3 is 2 %. On the contrary, it can, therefore, be concluded that the mean neutron generation time Λ depends slightly on the nuclear data library used.

Table 3. 12. The comparison of the calculated values of τr and Λ between the libraries and also with the reference [82].

Kinetic parameters	Reference	Calculation							
		ENDF/B-VII.1		JEFF-3.2		JEFF-3.3		ENDF/B-VIII.0	
τr (μs)	-	53.315	± 0.39020	52.195	± 0.38781	52.250	± 0.40307	52.623	± 0.37948
Λ (μs)	53.000	53.335	± 0.44369	51.990	± 0.44325	52.003	± 0.45293	52.560	± 0.43152

3.4.4. Conclusion

A comparative study has been performed with the new continuous energy cross-section data JEFF-3.3 and ENDF/B-VIII.0, generated for MCNPX using the NJOY21 data processing system. The correlation has been carried out against some critically benchmarks lattices and the TRIGA Mark II research reactor.

Based on criticality calculations using both libraries, the agreement overall between experimentally measured and computed values of keff is very good for the benchmark calculations performed here. However, the largest deviations (more than 1000 pcm) were seen for “leu-sol-

therm-001", "mix-met-fast-008", "pu-sol-therm-009-case3a" and "u233-sol-inter-001-case1". Moreover, the beryllium is in particular considered as a problematic issue for different benchmarks e.g. for "u233-sol-inter-001-case1". For this reason, we strongly recommended that the cross-sections for beryllium could be assessed in future releases. It should be noted that ENDF/B-VIII.0 produces excellent agreement with the experimental for the majority of cases than JEFF-3.3 except for a few benchmark cases, whereas the rest of the cases show a similar behavior between both libraries.

For the TRIGA Mark II reactor, the objective of this study is to investigate the predictive capability of the recent nuclear data libraries JEFF-3.3 and ENDF/B-VIII.0 by analyzing both neutronic and kinetic parameters, and then to compare the accuracy of the predicted results with those of the published values. For the effective multiplication factors, the analysis of the simulation results with the control rods in different positions highlights that the absolute value of $(\frac{C}{E} - 1)$ is 374 pcm using the JEFF-3.3 cross-section library, and is 341 pcm using the ENDF/B-VIII.0. In general, the calculation results for JEFF-3.3 and ENDF/B-VIII.0 data libraries were found to be very encouraging. During the comparison calculation, it is worth pointing out that the performance of JEFF-3.3 and ENDF/B-VIII.0 data libraries is quite satisfying. However, their influence could be qualitatively assessed.

Conclusion

New neutron cross-section libraries have been processed using the NJOY and NECP-Atlas codes, as well as various nuclear data evaluations. The study focuses on ENDF/B and JEFF as the main data libraries and aims to assess the performances of the processed libraries through criticality calculations using MCNP code and numerous well-known consolidate benchmarks such as criticality benchmarks, Octavian Shielding benchmarks, Doppler reactivity, and TRIGA Mark II benchmarks. Based on the analysis of these benchmarks, we can draw the following conclusions:

For criticality calculations:

The results using different releases of ENDF/B libraries show that practically all our results are within the range of benchmarks uncertainties, except for a few cases. The poor performance of the excepted cases is not due to our processing methods, as other authors have reported the

same issues with the current and old data libraries. The cases are mainly reflected by Beryllium, Beryllium oxide, or fueled with uranium or plutonium nitrate solutions. In our published articles, we made some recommendations to improve the elastic scattering cross-section of Beryllium. However, the obtained ENDF/B-VIII.0 results improved in the majority of benchmark cases. Indeed, when compared to older evaluations, the calculated values of $\frac{C}{E} - 1$ and their uncertainties are better, especially for certain benchmark cases. The agreement between experimentally measured and computed values of keff is very good, based on calculations using both the ENDF/B and JEFF libraries. The greatest deviations (more than 1000 pcm) were observed for "leu-sol-therm-001," "mix-met-fast-008," "pu-sol-therm-009-case3a," and "u233-sol-inter-001-case1." It should be noted that, except for a few benchmark cases, ENDF/B-VIII.0 produces better agreement with the experimental in the majority of cases than JEFF-3.3, while the rest of the cases exhibit similar behavior. This thesis also provides an overview of the processing and preparation of ENDF/B-VIII.0 incident neutron data for implementation in the MCNP code using the NECP-Atlas and NJOY codes. Based on the calculations, the discrepancy between the values obtained for ENDF/B-VIII.0-NECP-Atlas and ENDF/B-VIII.0-NJOY libraries is within a reasonable range.

For shielding benchmarks calculations:

The TOF Oktavian experiments were used to benchmark ENDF/B VIII. 0β6 by comparing it to the other libraries, it is possible to conclude that ENDF/B VIII.06 is improved in some cases for each specific energy region. In the majority of applications, however, there are minor differences in values between the libraries. In many cases, the largest differences are most likely due to original nuclear data.

For Doppler benchmarks calculations:

In almost all cases, the Doppler coefficients behave similarly using different releases of the ENDF/B library. The coefficients and standard deviation (σ) from the libraries under consideration are statistically indistinguishable. However, there are differences in the values for keff'. In other words, when it comes to calculating Doppler coefficients, the keff parameter is unimportant. The results for a comparison between NECP-Atlas and NJOY code using ENDF/B-VIII.0 library are generally good, but in some cases, strong deviations from the benchmark

values occur. The largest deviations are seen for Weapons-grade MOX fuels. Yet the results showed good agreement with no substantial differences between

For TRIGA Mark II reactor benchmark calculations:

The analysis of the simulation results using JEFF-3.3 and ENDF/B-VIII.0 data libraries were found to be very encouraging in general. During the comparison calculation, it is worth noting that the performance of the data libraries JEFF-3.3 and ENDF/B-VIII.0 is quite satisfactory. Their impact, on the other hand, could be evaluated qualitatively.

Part II: Possible scenarios for a transition to a thorium-based fuel cycle in a pebble-bed high temperature reactor

Chapter 4: Basic functional requirements of a reactor

This chapter reviews the theory of the operational requirements of a reactor that will be required to clarify the findings of chapter 6. This chapter elaborates on nuclear physics concepts such as kinetic coefficients, temperature feedback coefficients, control rod effect, and nuclear poisons effect. Additional information on these concepts can be found in References [7, 3].

4.1. Stability and control of a reactor

4.1.1. Kinetic coefficients

4.1.1.1. Reactor kinetics

As is introduced in Chapter 1, most of the neutrons released in fission occur virtually at the time of fission (more than 99%); these are the prompt neutrons. Long after the fission event and due to beta decay that precedes neutron emission, a small fraction of the fission neutrons appears those fissions are delayed neutrons. A reactor's time behavior depends on the different properties of those two neutron types.

4.1.1.1.1. Neutron lifetime

After they are emitted and as a result of elastic and inelastic collisions with nuclei in the system the prompt fission neutrons slow down. Most of them attain thermal energies in thermal reactors without being absorbed or escaping from the system. They diffuse in the reactor as thermal neutrons; some are eventually absorbed and some leak out. The average time that a neutron spends in a reactor before it is absorbed or leaks out is called the total neutron lifetime (l). It represents the sum of the slowing downtime (l_s) and the thermal or diffusion time (l_{th}) in a thermal reactor [23].

$$l = l_s + l_{th} \tag{4.1}$$

The slowing down lifetime represents the time that a neutron spends while slowing down from fission energies to thermal energies. Whereas, the thermal lifetime corresponds to the time that neutrons spend diffusing before being absorbed. In an infinite thermal reactor the neutron lifetime is obtained as the ratio of the absorption mean free path ($\lambda_{th} = \frac{1}{\Sigma_a}$) and the average neutron velocity

($\overline{\boldsymbol{\nu}}$). The slowing down lifetime is neglected in the equation because it is much shorter than the thermal neutron lifetime in a finite thermal reactor [23].

$$l_{\infty} \approx l_{th\infty} = \frac{\lambda_{th}}{\overline{\boldsymbol{\nu}}} \tag{4.2}$$

If N represents the total of neutrons per generation, and $P_{\mathrm{NL}} = (1 + L^2B^2)^{-1}$ is the probability of non-leakage, then $N.P_{\mathrm{NL}}$ neutrons remain at the core to contribute to the effective neutron lifetime.

$$N.l_{th} = N.l_{th\infty}.P_{\mathrm{NL}}$$
$$l \approx l_{th} = l_{th\infty}.P_{\mathrm{NL}} = l_{th\infty}(1 + L^2B^2)^{-1} = \frac{1}{\overline{\boldsymbol{\nu}}.\Sigma_a.(1 + L^2B^2)} = \frac{1}{\overline{\boldsymbol{\nu}}.\Sigma_a.\mathrm{k_{inf}}} \tag{4.3}$$

where $B^2 = \frac{1}{D}\left(\frac{1}{k}\Sigma_f - \Sigma_a\right)$ is defined as the geometric buckling and $L^2 = \frac{D}{\Sigma_a}$ is the thermal diffusion area [1]. Examples of the slowing and thermal lifetimes in thermal reactors for the most common moderator materials are shown in **Table 4.1**.

Table 4. 1. Neutron lifetime in thermal reactors [23].

Moderator	Slowing down time (s)	Thermal time (s)
Carbon (**C**)	1.5×10^{-4}	1.8×10^{-2}
Light water ($\mathbf{H_2O}$)	5.6×10^{-6}	2.1×10^{-4}
Heavy water ($\mathbf{D_2O}$)	4.3×10^{-5}	1.4×10^{-1}
Beryllium (**Be**)	5.7×10^{-5}	3.7×10^{-3}

Another important parameter to be taken into account is the neutron generation time (Λ) and is defined as the time required for neutrons from one generation to cause the fissions that produce the next generation of neutrons.

$$\Lambda = \frac{\lambda_{th}}{\overline{\boldsymbol{\nu}}} = \frac{1}{\overline{\boldsymbol{\nu}}.\nu.\Sigma_f} \tag{4.4}$$

where λ_{th} represents the mean free path for neutron production.

If G represents the number of neutron generations or the number of neutron lifetimes, between 0 and time t, the neutron density and neutron flux in a thermal infinite reactor will change as follows:

$$n(t) = n(0)(\mathrm{k_{eff}})^{G}$$
$$\text{therefore} \tag{4.5}$$
$$\phi(t) = \phi(0)(\mathrm{k_{eff}})^{G}$$

where $\phi(0)$ is the steady-state neutron flux, $G = \frac{t}{l_\infty}$ and $\mathrm{k_{eff}}$ can be written as $\mathrm{k_{eff}} = 1 + \Delta\mathrm{k_{eff}}$.

Thus, the flux change can be expressed as **Equation (4.6)**, and for a very small change in the multiplication factor, **Equation (4.6)** reduces to **Equation (4.7)** [23].

$$\ln\left(\frac{\phi(t)}{\phi(0)}\right) = \frac{t}{l_\infty}\ln(1 + \Delta\mathrm{k_{eff}}) = \frac{t}{l_\infty}\left\{\Delta\mathrm{k_{eff}} - \frac{1}{2}\Delta{\mathrm{k_{eff}}}^{2} + \cdots\right\} \tag{4.6}$$

$$\ln\left(\frac{\phi(t)}{\phi(0)}\right) = \frac{t}{l_\infty}\Delta\mathrm{k_{eff}} \Rightarrow \phi(t) = \phi(0)e^{\frac{\Delta\mathrm{k_{eff}}}{l_\infty}.t} \tag{4.7}$$

The reactor period taking into account only prompt neutrons for ε folding time (T), is defined as the time needed for the flux to change by a factor $\varepsilon = \frac{\Delta\mathrm{k_{eff}}}{l_\infty}.t$ **Equation (4.7)**. As can be seen from the equation, the reactor period has to be long enough to prevent a dangerous reactor power excursion. In fact, all reactors employ automatic safety systems to suddenly shutdown the reactor if the period becomes too short.

4.1.1.1.2. Delayed neutrons

The delayed neutrons are released immediately after a fission fragment has first β decay also known as a delayed neutron precursor (**Figure 4.1**). Although delayed neutrons represent a very small fraction of the total neutron number, they play an extremely important role in reactor control. Beta delayed neutron emission is improved when the emitted neutron binding energy is minimum. Beta delayed neutrons are characterized by their yields of β_i, in theory, six families can be calculated with delayed neutrons. Even though there are many more than six delayed neutron precursors, but they decay constants λ_i can be conveniently represented by no more than six decay constants that differ slightly with the fission species (**Table 4.2**), the total delayed yield of neutrons per fission in a reactor can be specified as:

$$\beta = \sum_{i=1}^{6} \beta_i \tag{4.8}$$

The average half-life ($t_{\frac{1}{2}}$) of the delayed neutrons can be defined by **Equation (4.9)**, and the average decay constant λ by **Equation (4.10)**.

$$t_{\frac{1}{2}} = \frac{1}{\beta} \sum_{i=1}^{6} \beta_i t_{i,\frac{1}{2}} \tag{4.9}$$

$$\lambda = \left(\frac{1}{\beta} \sum_{i=1}^{6} \beta_i \frac{1}{\lambda_i} \right)^{-1} \tag{4.10}$$

The delayed neutrons do not have the same properties as the prompt neutrons released directly from the fission since the average energy of the prompt neutrons is about 2 MeV, much larger than the average energy of the delayed neutrons, ~0.5 MeV. But the lower energy has two significant impacts on the way they proceed through the neutron life cycle; (i) Delayed neutrons have a much lower probability of causing fast fissions than prompt neutrons because their average energy is less than the minimum required for fast fission to take place; (ii) Delayed neutrons are less likely to leak out of the core while at fast energies because they are born at lower energies and then travel a shorter distance as fast neutrons [23]. A term called the importance Factor (I) takes account of these two considerations. The importance factor includes the average delayed neutron fraction (β) to the effective delayed neutron fraction (β_{eff}).

$$I = \frac{\beta_{eff}}{\beta} \tag{4.11}$$

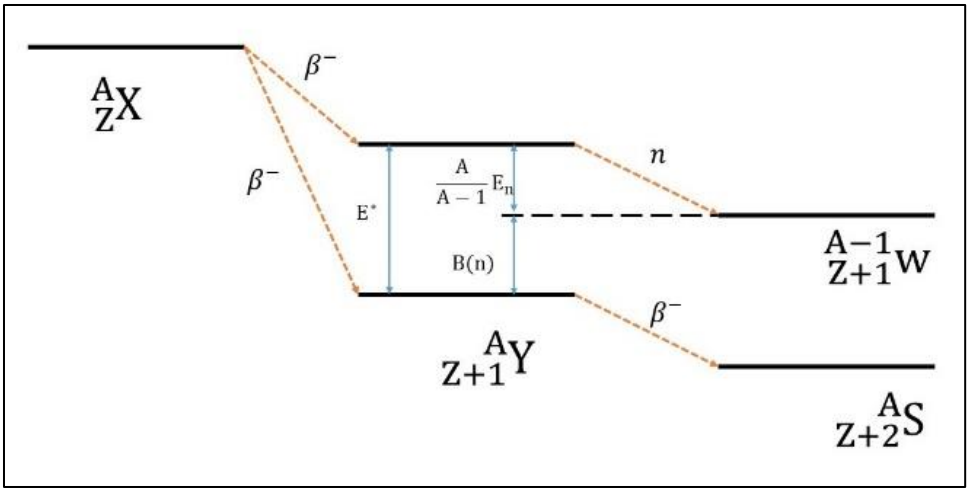

Figure 4. 1. Illustration of the mechanism of delayed neutron generation**.**

Table 4. 2. Delayed neutron parameters for the main fissile and fertile isotopes [3].

Group	Fast Neutrons		Thermal Neutrons	
	Decay Constant $\lambda_i(s^{-1})$	Relative Yield (β_i/β)	Decay Constant $\lambda_i(s^{-1})$	Relative Yield (β_i/β)
^{233}U		ν_d = 0.00731		ν_d = 0.00667
		β = 0.0026		β = 0.0026
1	0.0125	0.096	0.0126	0.086
2	0.0360	0.208	0.0337	0.299
3	0.138	0.242	0.139	2.252
4	0.318	0.327	0.325	0.278
5	1.22	0.087	1.13	0.051
6	3.15	0.041	2.5	0.034
****				
^{235}U		ν_d = 0.01673		ν_d = 0.01668
		β = 0.0064		β = 0.0067
1	0.0127	0.038	0.0124	0.033
2	0.0317	0.213	0.0305	0.219
3	0.115	0.188	0.11	0.196
4	0.311	0.407	0.301	0.395
5	1.40	0.128	1.14	0.115
6	3.87	0.036	3.01	0.042
****				
^{239}Pu		ν_d = 0.0063		ν_d = 0.00645
		β = 0.0020		β = 0.0022
1	0.0129	0.038	0.0128	0.035
2	0.0311	0.280	0.0301	0.298
3	0.134	0.216	0.124	0.211
4	0.331	0.328	0.325	0.326

5	1.26	0.103	1.12	0.086
6	3.21	0.035	2.69	0.044
****				
^{241}Pu		v_d = 0.0152		v_d = 0.0157 β = 0.0054
1	-	-	0.0128	0.010
2	-	-	0.0297	0.299
3	-	-	0.124	0.173
4	-	-	0.352	0.390
5	-	-	1.61	0.182
6	-	-	3.47	0.016
****				
^{232}Th		v_d = 0.0531 β = 0.0203		
1	0.0124	0.034		
2	0.0334	0.150		
3	0.121	0.155		
4	0.321	0.446		
5	1.21	0.172		
6	3.29	0.043		
****				
^{238}U		v_d = 0.0460 β = 0.0164		
1	0.0132	0.013		
2	0.0321	0.137		
3	0.139	0.162		
4	0.358	0.388		
5	1.41	0.225		
6	4.02	0.075		
****				
^{240}Pu		v_d = 0.0090 β = 0.0029		
1	0.0129	0.028		
2	0.0313	0.273		
3	0.135	0.192		
4	0.333	0.350		
5	1.36	0.128		
6	4.04	0.029		

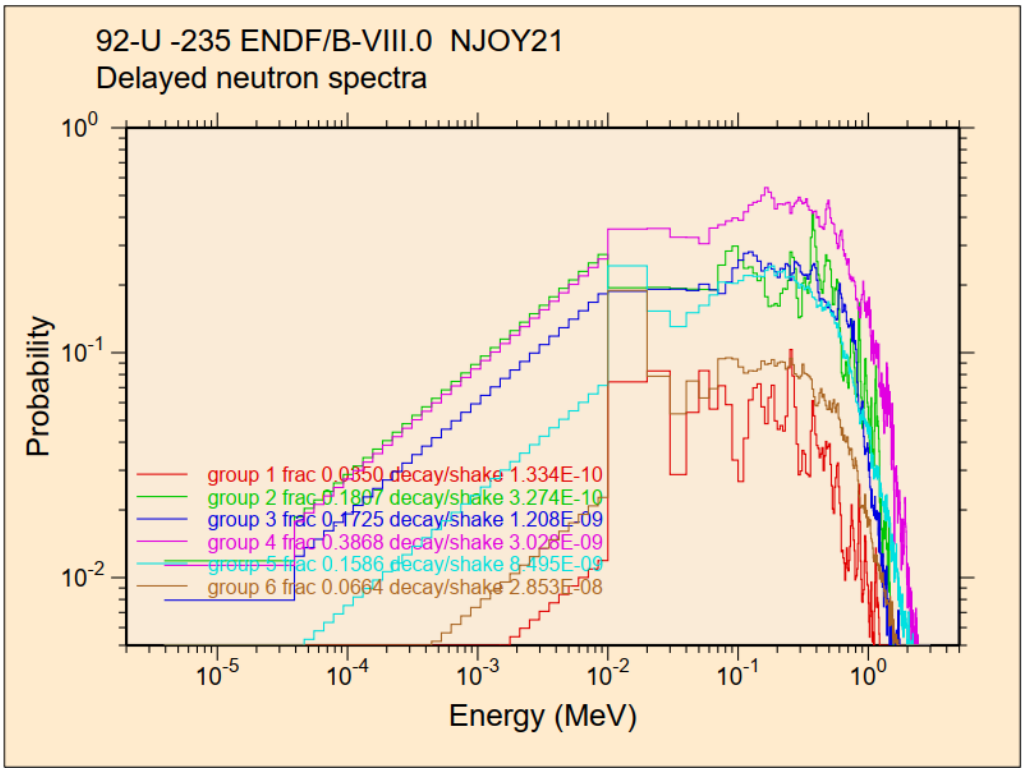

Figure 4. 2. Delayed neutron spectra for U-235.

4.1.1.1.3. MCNP evaluation of β_{eff} and Λ

The effective delayed neutron fraction β_{eff} is calculated by MCNP using the prompt method, which requires two calculations with and without the TOTNU NO card [28]. The TOTNU NO card was used to calculate the effective multiplication factor taking into account just the prompt neutron contribution **Equation (4.12)**. Using the prompt neutron lifetime τ_r, which is the average time from the emission of a prompt neutron in fission to the removal of the neutron by some physical process such as fission, capture, or escape, and keff, Λ parameter can be determined as demonstrated in **Equation (4.13)**. The difference between the mean neutron generation time Λ and neutron prompt neutron lifetime τ_r is that Λ only takes into account the neutron absorptions inducing fission [20].

$$\beta_{\text{eff}} \cong 1 - \frac{k_{\text{eff,(prompt)}}}{k_{\text{eff,(total)}}} \tag{4.12}$$

$$\Lambda = \frac{\tau_r}{k_{\text{eff}}}. \tag{4.13}$$

4.1.1.2. Temperature feedback coefficients

The fission heat in the fuel region that radiates outwards through the constituent material to the coolant and moderator causes the temperature gradient in the reactor. This gradient affects the reactivity that again stimuli the reaction rate that influences the temperature, which is known as a feedback mechanism. Moreover, due to the various reactor materials having different temperatures during reactor operation, several different coefficients of temperature are used. The two significant temperature coefficients are typically the fuel and the moderator temperature reactivity coefficients [2, 23]. The importance of the reactivity mechanism if it became uncontainable, the reactor may become unstable and uncontrollable e.g. the RBMK reactors.

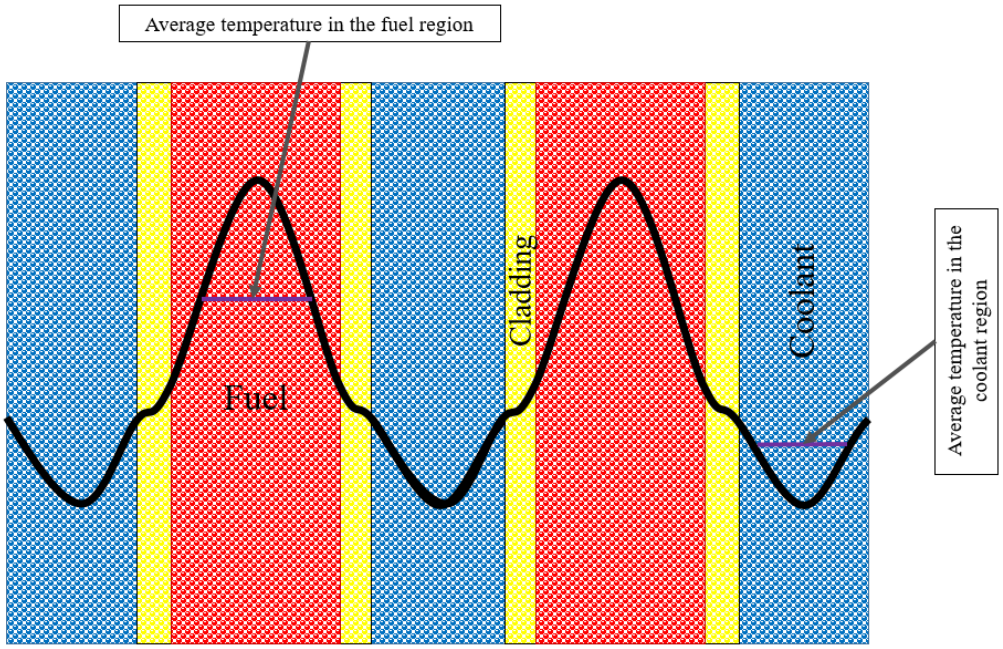

Figure 4. 3. The temperature profile in a nuclear reactor.

The temperature coefficient of reactivity (α_T) also named the prompt coefficient is expressed as **Equation (4.13)**. The coefficients can be consequences of temperature modification of the fuel or moderator or any other component, each acting differently. The reactor's response to a temperature change depends on the algebraic sign of the feedback factor. If there is positive feedback, increases or decreases in temperature will cause the same effect on reactivity. Similarly, negative feedback happens when a temperature increase or decrease causes the reactivity to get the opposite effect.

$$\alpha_T \equiv \frac{\delta\rho}{\delta T} = \frac{\delta}{\delta T}\left(\frac{k-1}{k}\right) = \frac{1}{k^2}\frac{\delta k}{\delta k} \cong \frac{1}{k}\frac{\delta k}{\delta T} \tag{4.13}$$

4.1.1.2.1. Fuel temperature coefficient

4.1.1.2.1.1. Physical process a background study

The Doppler Effect (or Doppler defect) is directly caused by a change in the temperature of the fuel. The resonance capture e.g. in U-238 increases as the fuel heats up for the following reason. The absorption cross-section of U-238 in the resonance range includes a set of sharp peaks as shown in **Figure 4.4**. In the resonance range, the probability that a stationary nucleus absorbs a neutron depends on the fact that the energy kinetics of the neutron is or is not identical to the resonance energy. The nucleus and neutron start moving, so the most important variable is the neutron velocity relative to the nucleus when determining the probability of absorption. An increase in the temperature of the system causes the atoms to become more agitated so the relative velocities of neutrons and nuclei change.

To illustrate this effect, let us examine the scenario drawn on the top of **Figure 4.5** (Stationary nucleus). The probability that a neutron with a velocity corresponding to the resonance peak will be absorbed is highest, while it is unlikely that the stationary nucleus will capture a neutron that spreads slightly slower or faster than that velocity. Now let us look at what happens when the fuel gets heated and the nuclei become extremely agitated. A neutron whose velocity is such that it was sufficiently far from the peak will hit a nucleus that moves at this moment in such a way that the velocity of the neutron relative to the nucleus corresponds with the peak.

If we represent the neutron's kinetic energy by E_n, and the energy at resonance peak by $E_{\text{resonance}}$. The three neutrons tend to have the same nuclei resonance energy. The scenario in the center of the figure illustrates a neutron whose energy is higher than that at the bottom of the figure. However, the neutron approaches a nucleus moving at a velocity that makes the neutron’s approach velocity the same as in the first diagram. For the nucleus, this neutron tends to be in the resonance peak energy. The same thing happens to a neutron whose velocity is lower than the peak of a resting nucleus, but which strikes a "hot" nucleus moving towards it exactly at the velocity as indicated in the scenario at the bottom of the figure. The fuel heating actually “broadens or expands” the resonances as seen in **Figure 4.6**. In the meantime, the increased movement of nuclei has decreased the peak height since neutrons moving exactly at the first velocity no longer move

at this velocity concerning the moving nuclei. The overall absorption may not change much if the reduced rate of absorption at the peak is to offset the increased absorption away from the peak. Moreover, the cross-section of the resonant nuclei is so high in all scenarios that a neutron in the peak area will almost certainly be absorbed. In other words, the peaks are sharper when the fuel is not as hot. When the peak is sharp, the resonant neutrons are absorbed near the surface of the fuel and the neutrons that are far from the peak energy can pass through the fuel and continue until they are slowed down. The hotter fuel exposes a significant amount of the resonant nuclei to neutrons whose energies are slightly different from the resonant peak and many of them are absorbed in addition to the resonant neutrons absorbed. The net result of heating is to broaden the neutron energy spectrum, for which resonance capture is highly likely. Hence, the reduced resonance escape probability (p) results in less reactivity. The two nuclides present in large amounts in the fuel with large resonant peaks that dominate the Doppler Effect are U-238 and Pu-240.

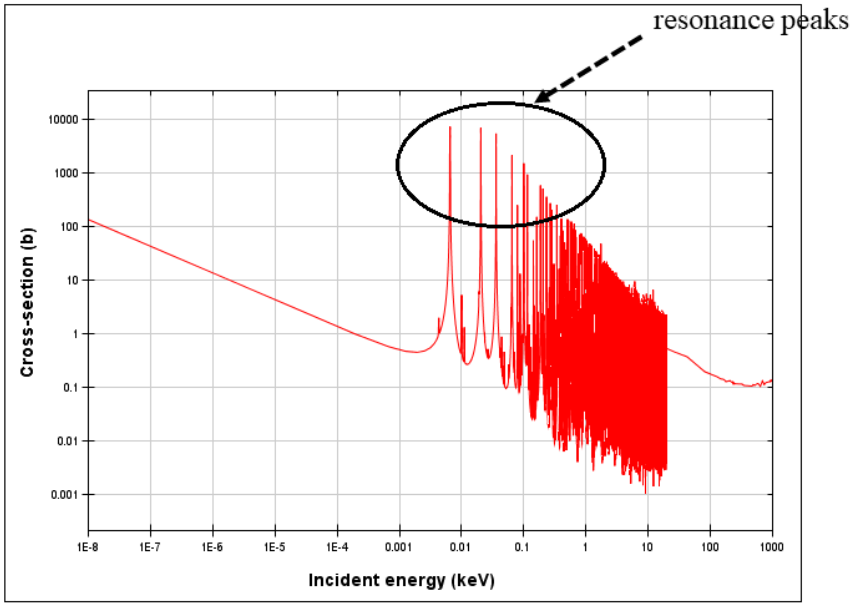

Figure 4. 4. Capture cross-section for U-238.

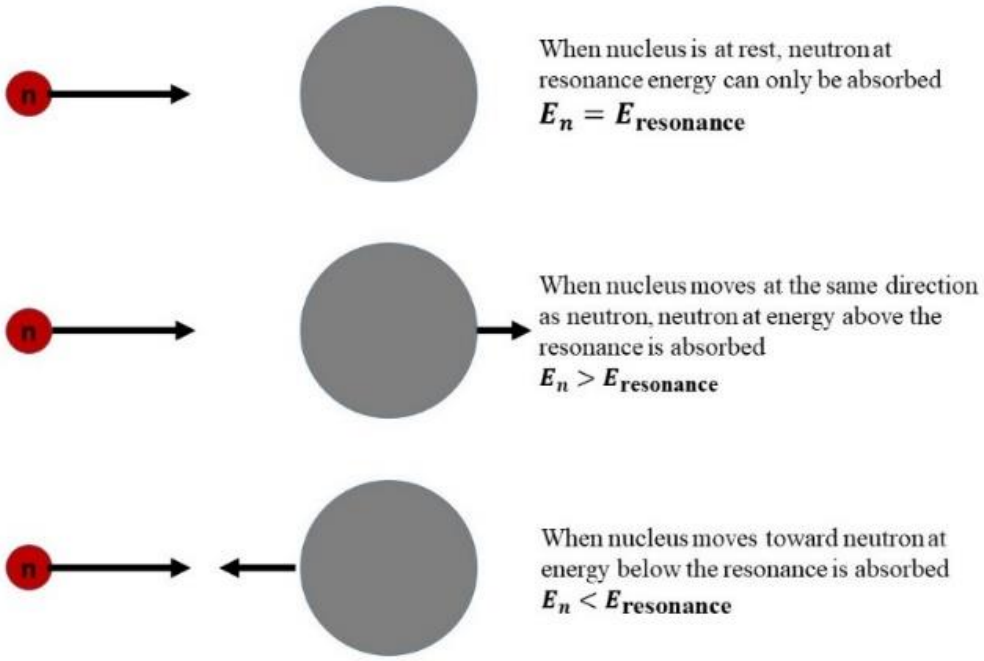

Figure 4. 5. Interaction between neutron and nucleus concerning the resonance absorption.

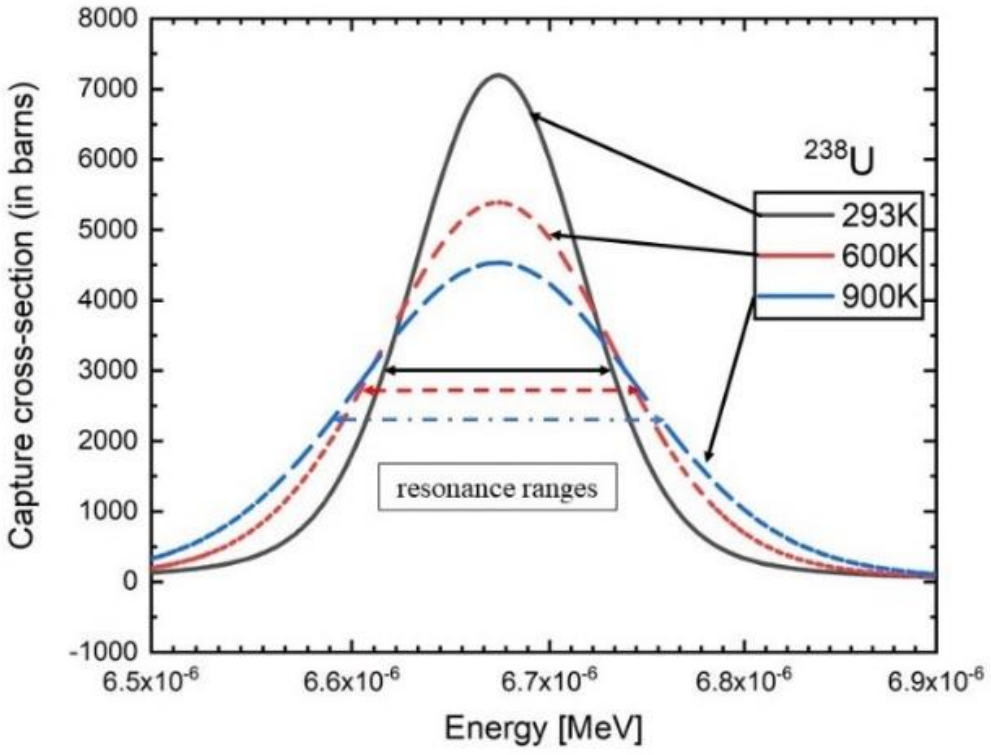

Figure 4. 6. Doppler broadening of the capture cross-section (U-238) at resonance from 293K to 900 K.

4.1.1.2.1.2. Formalism

In the nuclear theology industry, the fuel temperature coefficient (FTC) noted α_F (F= Fuel), is defined as:

$$\alpha_F \approx \frac{1}{k}\frac{\delta k}{\delta T_F} \tag{4.14}$$

δk is the difference between the core effective multiplication factors which corresponds to the temperature variation (δT_F) in the fuel region. The temperature remains the same for other components (moderator temperature, coolant, etc.)

For example, to calculate the FTC in a light water reactor (LWR) pin cell benchmark (U-235 3.1 wt.%) as a function of burnup, two sets of calculations were carried out using the DRAGON code. The first was in hot zero power conditions, where the fuel, the cladding, and the moderator were set at a temperature of 600 K. The second set of calculations was carried out under Hot Full Power conditions where the fuel temperature was set at 900 K and the cladding and moderator temperatures were set at 600 K. The full benchmark specification is described in **Chapter 2**. The results are present in **Figures 4.7 to 4.9**.

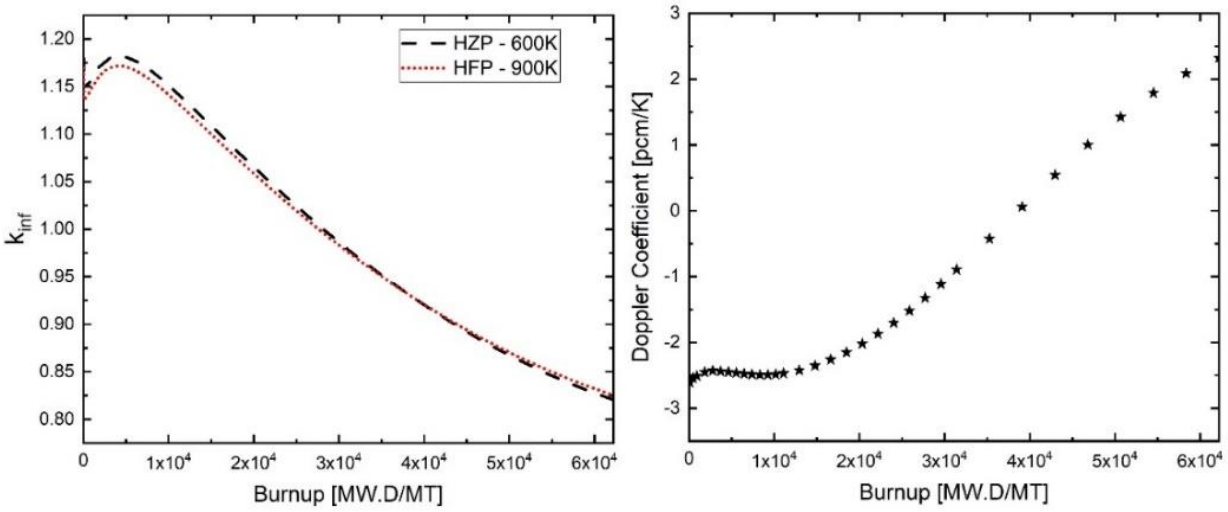

Figure 4. 7. K-infinity and fuel temperature coefficients for the LWR pin cell.

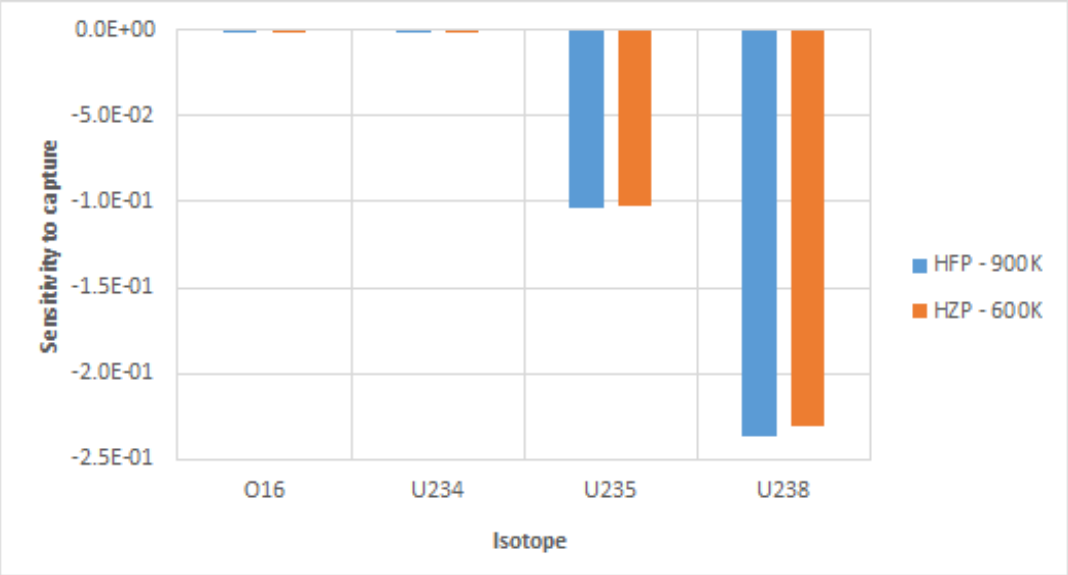

Figure 4. 8. Sensitivity to capture for the LWR pin cell evaluated by DRAGON code. A sensitivity coefficient represents a relative change in the value of the multiplication factor to a change in the cross-section.

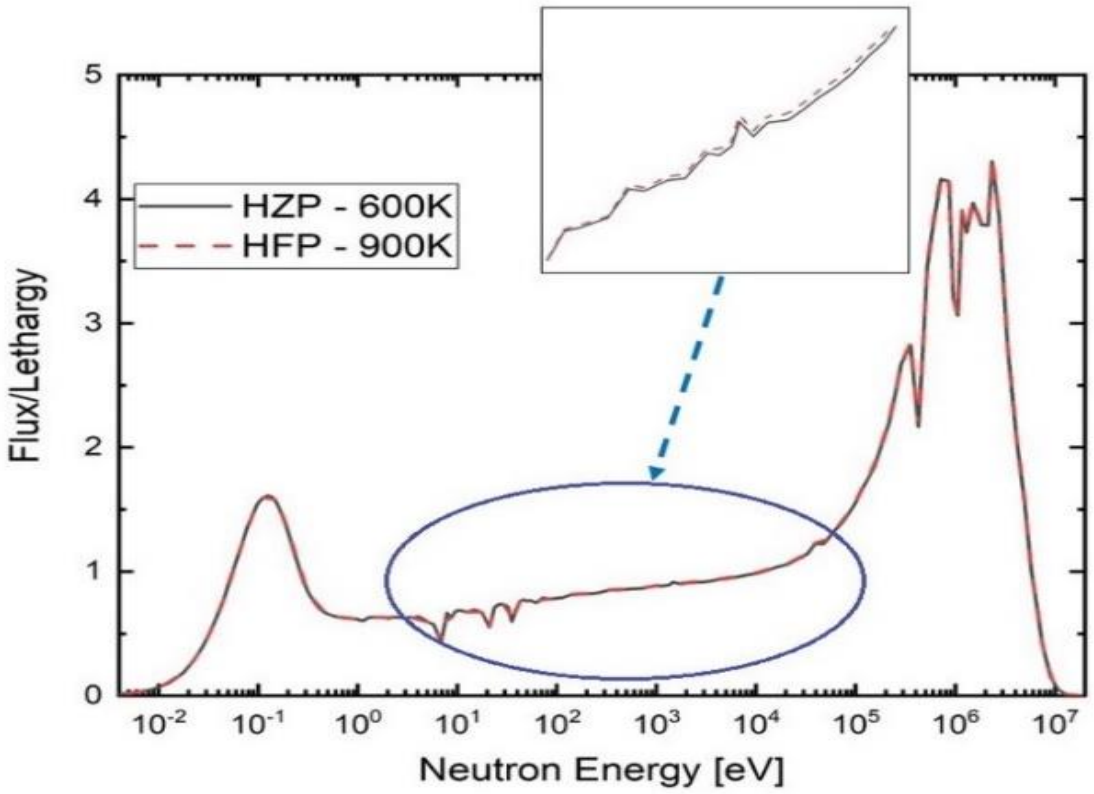

Figure 4. 9. Neutron spectrum at 600 K and 900 K

4.1.1.2.2. Moderator temperature coefficient

4.1.1.2.2.1. Physical phenomena

To explain this effect, we first introduce an important parameter that mainly contributes to the thermal utilization factor ($f = \frac{1}{1+\frac{\sigma_{a,M}}{\sigma_{a,F}}.r}$), therefore, in the multiplication factor and the reactivity change in a thermal reactor. This parameter is called the moderation ratio (r). This ratio reflects the ratio between the moderator quantity compared ($N_{\text{Moderator}}.V_{\text{Moderator}}$) to the fuel quantity ($N_{Fuel}.V_{Fuel}$) as expressed in **Equation (4.15)**.

$$r = \frac{N_{Fuel}.V_{Fuel}}{N_{\text{Moderator}}.V_{\text{Moderator}}} \tag{4.15}$$

According to the four factors formula, the infinite multiplication factor can be expressed as: $k_{\text{inf}} = \epsilon f p \eta$. So when the moderator is heated (i.e. water in the light water-moderated reactors), N_F and V_F do not vary (we assume that the increase in temperature occurs only in the moderator region). On the other hand, N_{M} decreases because there is water dilation (changes in moderator temperature result in changes in density), however, when the water is heated its volume increases (pressurizer) but on the other hand V_{M} does not vary (because water is the moderator and the coolant). Thus in the r expression, only N_{M} decreases when the temperature of the moderator increases. Therefore, we conclude that an increase in moderator temperature causes a drop in the reactivity of the reactor.

4.1.1.2.2.2. Formalism

Much like the fuel temperature coefficient, that of the moderator (MTC), noted α_M, is defined as:

$$\alpha_M \approx \frac{1}{k}\frac{\delta k}{\delta T_M} \tag{4.16}$$

Therefore, the MTC is the component of reactivity that measures the effect of change in moderator temperature (delayed temperature coefficient). Changes in moderator temperature result in changes in density, decreasing density with increasing temperature results in reduced moderation and increased leakage which adds to negative reactivity in the under moderated light water reactors, and positive reactivity in the over moderated light water reactors.

A combination of the FTC and the MTC is called the overall temperature coefficient, which gives the overall effect of the temperature parameter on the total reactivity of the core.

4.2. Reactor control

4.2.1. Control rods

In order to control the chain reaction, it is necessary to have control rods in the reactor core, i.e. neutron absorbers that can be withdrawn or inserted according to the operating sequences. In particular, these rods ensure the automatic shutdown of the reactor in the event of any failure detected by a safety system.

Several types of neutron absorbers are used for the control rods. Typically, the selected material should have a strong neutron absorption cross-section and have a long life as an absorber (i.e. not burning out rapidly), e.g. boron, cadmium, and hafnium. The choice of the control rods also depends closely on the choices made for the fuel. Their number depends on their efficiency and the variations in core reactivity that they must be able to control. The three main functions of the control rod system are:

- Reactor control, discrepancies, shutdowns, power level changes,
- Compensation for reactivity variations resulting from fuel consumption,
- Safety, automatic shutdown of the reactor, whatever its condition, in the event of a malfunction.

Control rod effectiveness

The effectiveness of a control rod is mainly based upon the value of the neutron flux ratio at the rod's position to the reactor's average neutron flux. The control rod inserts the most negative reactivity when it is positioned inside the reactor core where the maximum flux is. If a reactor only has one control rod, the rod should be placed in the reactor core center (see **Figure 4.10**). If additional rods are inserted into this reactor, the most effective position is where the maximum flux is. A reactor, which has a large amount of excess reactivity, requires additional control rods. The exact amount of reactivity inserted by each control rod depends upon the design of the reactor. The change in reactivity caused by control rod motion is referred to as control rod worth (ρ_w) **Equation (4.17)** [8].

$$\rho_w = \frac{k_{in} - k_{out}}{k_{in}} \tag{4.17}$$

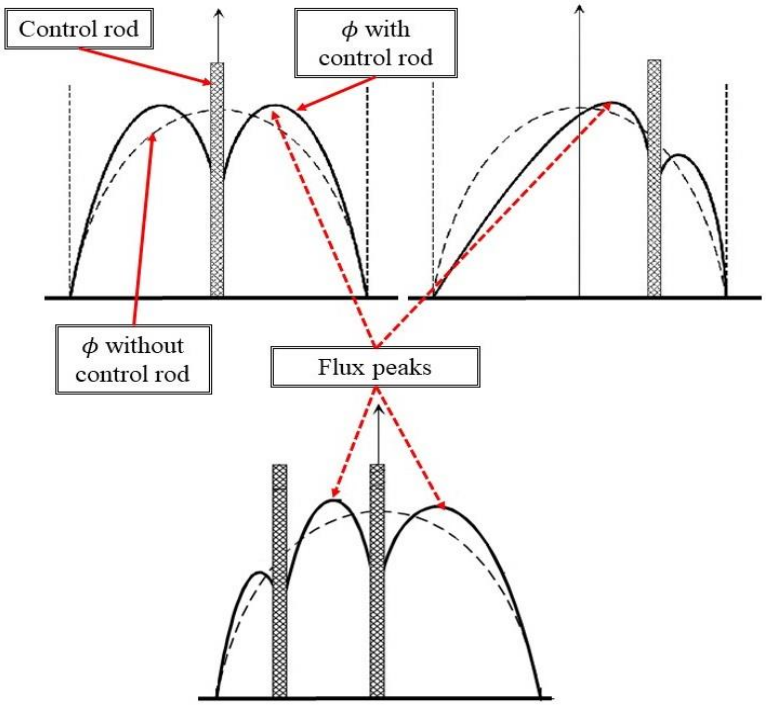

Figure 4. 10. Effect of control rod on radial flux distribution; (modified from *http://neutronique.free.fr/Genie_Atomique*).

4.2.2. Shutdown margin (SDM)

A safety analysis of any reactor will invariably include the determination of the shutdown margin. The shutdown margin (SDM) is defined by the United States Nuclear Regulatory Commission (NRC) as: "The instantaneous amount of reactivity by which the reactor is subcritical or would be subcritical from its present condition assuming all control rods are fully inserted except for the single rod of highest reactivity worth that is assumed to be fully withdrawn"[85]. The SDM is evaluated as the difference between the core excess reactivity and the combined reactivity of (N-1) out of the N control rods of the reactor and assuming that the highest worth rod is stuck. Therefore, it is necessary to determine which control rod is the highest worth rod, this can be done using **Equation (4.18)** [86]:

$$\rho^i_{w,rod} = k^i_{out} - k_{in} \tag{4.18}$$

k^{i}_{out} is the multiplication factor when the highest worth rod is inserted; k_{in} the combined multiplication factor in the case that all control rods fully inserted; $\rho^{i}_{w,rod}$ the worth of that rod.

4.2.3. Burnable absorbers

It is also possible to reduce, at least partially the fuel consumption or control the reactivity margin if it is required before the reactor startup by introducing absorbent materials, materials whose consumption (by neutron capture) will lead to a decrease in reactivity during irradiation. These absorbers are fixed in the core, either mixed with the fuel in certain elements or introduced in the form of independent elements (rods, pellets, etc.). These materials called burnable absorbers (e.g. boron, hafnium, europium, gadolinium, samarium, and cadmium) [7, 1]. The main problem determining the choice of a burnable poison is its relative consumption rate, which must be chosen in such a way as to avoid two major issues. (1) Rapid combustion of poison that would bring the core reactivity back to a state identical to the core without poison; (2) Slow combustion that could affect the fuel's life, an excessive residual amount of poison at the end of life making the core prematurely subcritical.

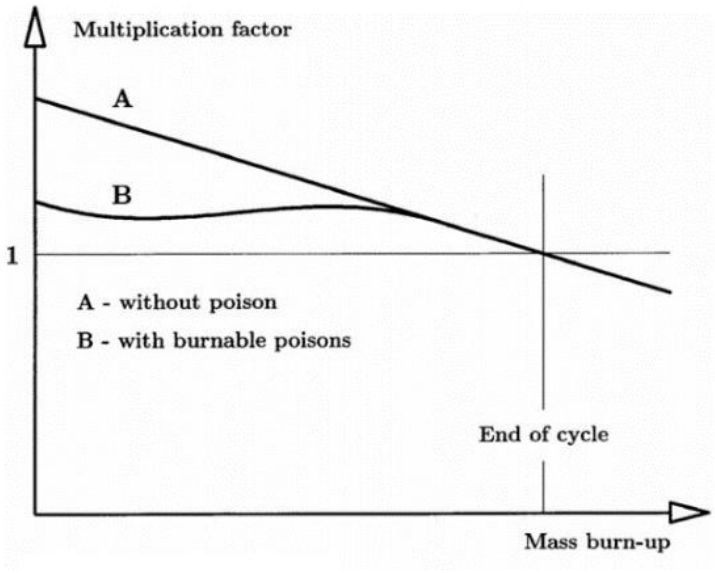

Figure 4. 11. Multiplication factor evolution with and without burnable poison [3].

In the case where the burnable poison evolves independently, we can get an idea of its relative speed of disappearance of the poison compared to U-235. If we note N_P is the poison concentration and σ_a^P its microscopic cross-section with ϕ_P the total flux at the location of the consumable poison. The rate of disappearance of the poison concentration can be as follow:

$$\underbrace{\frac{dN_P}{dt}}_{\text{rate of disappearance}} = -\underbrace{\sigma_a^P N_P \phi_P}_{\text{Poison burnup}} \tag{4.19}$$

and

$$\frac{dN_{^{235}\mathrm{U}}}{dt} = -\sigma_a^{^{235}\mathrm{U}} N_{^{235}\mathrm{U}} \phi_{^{235}\mathrm{U}} \tag{4.20}$$

If the poison is poorly self-shielded, i.e. if its absorption cross-section is not too high enough, which would lead to a significant drop in the flux($\phi_P/\phi_{^{235}\mathrm{U}} \ll 1$), therefore, its relative rate of disappearance can be expressed by:

$$\frac{N_P}{N_{\mathrm{p}}^0} = \left[\frac{N_{^{235}\mathrm{U}}}{N_{^{235}\mathrm{U}}^0}\right]^{(\sigma_a^P/\sigma_a^{^{235}\mathrm{U}})} \tag{4.21}$$

Several materials have been utilized for burnable absorbers for example:

- Boron, the most studied because of its large application as a control rod absorbent and as a burnable poison. It is found in the form of Pyrex glass, which contains approximately 12 wt. % boron oxide (B_2O_3), as carbide (B_4C), or as zirconium boride in the coating of fuel pellets. The B-10 isotope produces lithium and helium, which are both stable isotopes [87, 88]. Yet, B_4C has many unique properties, such as high neutron worth, chemical stability, high melting temperature, low density, and low cost. Furthermore, the main aim of using B_4C as a burnable poison is to reduce the number of control rods in the core of the reactor, because control rod systems are expensive [89].
- Gadolinium, used in the form of gadolinium oxide i.e. Gadolinia (Gd_2O_3) or grains in the fuel. Gadolinium has the largest thermal absorption cross-section followed by boron. However, only two gadolinium isotopes have the largest thermal neutron absorption cross-section among other isotopes (Gd-155 and Gd-157). The natural abundance of the Gd-155 equals 15%, while for Gd-157 is 16%. The neutron capture on ^{155}Gd and ^{157}Gd follows the formation of Gd-156 and Gd-158 with much lower absorption cross-sections [90].

- There are six naturally occurring Erbium isotopes: Er-162 (0.14%), Er-164 (1.61%), Er-166 (33.6%), Er-167 (22.93%), Er-168 (26.78%), and Er-170 (14.93%); however, Er-167 is the only strong absorber. Generally, Erbium used as erbium-oxide Er_2O_3 (Erbia) [91].
- Hafnium, often in combination with other absorbers, for special applications (e.g. utilization in the naval nuclear propulsion program), whose use cannot be retained for power reactors because of its low consumption under irradiation. Also, hafnium produces a larger number of decay isotopes.

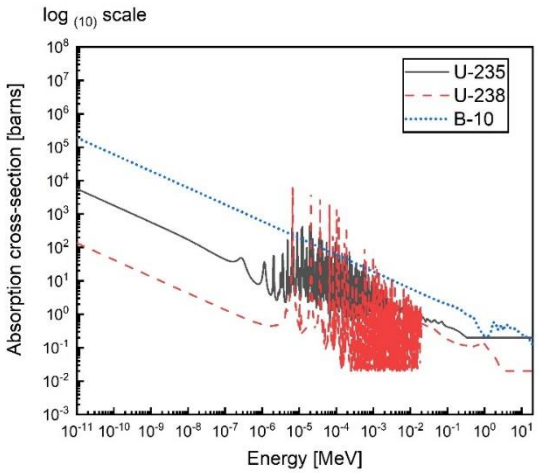

Figure 4. 12. Pointwise absorption cross-sections of B-10.

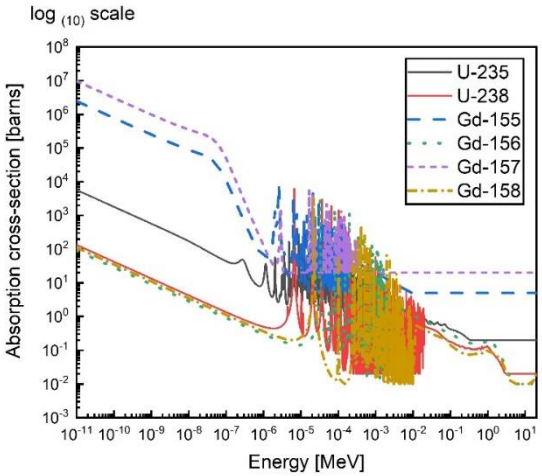

Figure 4. 13. Pointwise absorption cross-sections of Gd-155, Gd-156, Gd-157, and Gd-158.

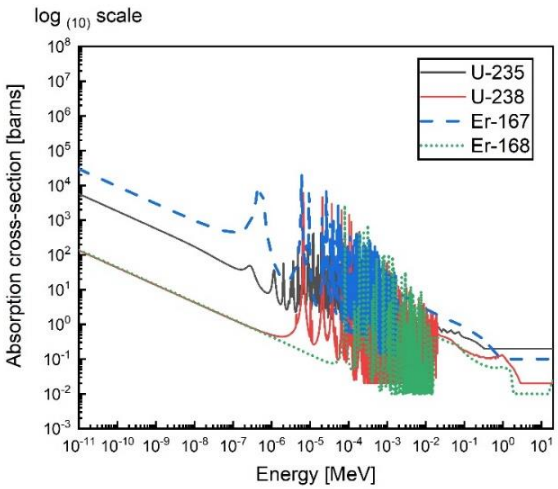

Figure 4. 14. Pointwise absorption cross-sections of Er-167 and Er-168.

Table 4. 3. Characteristics of some burnable absorbers [92].

Absorber	Density	Melting point (k)	Isotope of Interest	Abundance	Absorption cross-section	Resonance Integral
B_4C	2.49	2623	B-10	19.9%	3837	1722
Gd_2O_3	7.35	2612	Gd-155	14.8%	60900	1447
			Gd-157	15.7%	254000	700
Er_2O_3	8.57	2617	Er-167	22.9%	659	2970
HfO_2	9.62	3073	Hf-177	18.6%	380	7173

4.2.4. Fission product poisons

So far, in chapter 1, we have seen that two fission fragments are produced virtually in every fission. Due to their highly positive charge, they have a very short path inside the reactor at the time of their formation. Once stopped, fission fragments are named fission products. They deposit their kinetic energy instantaneously in the form of heat. These fission products are mostly unstable atoms, thereby producing other products more or less quickly by radioactive decay. Some of these fission products have remarkable neutronic properties and thus interrupt core functionality. Although some fission products have substantial neutron absorption cross-sections, Xe-135 and samarium-149 have the most important impact on the function and operation of the reactor. Because these two fission product poisons remove reactor neutrons, they will influence the thermal utilization factor and therefore keff and reactivity [1].

The reactivity equivalent of poisons in a previously critical reactor situation can be written as,

$$\rho = \frac{k - k_0}{k} = \frac{f - f_0}{f} \tag{4.22}$$

where

$$f_0 = \frac{\bar{\Sigma}_{a,F}}{\bar{\Sigma}_{a,F} + \bar{\Sigma}_{a,M}} \quad \text{and} \quad f = \frac{\bar{\Sigma}_{a,F}}{\bar{\Sigma}_{a,F} + \bar{\Sigma}_{a,M} + \bar{\Sigma}_{a,P}} \tag{4.23}$$

where $\bar{\Sigma}_{a,F}$, $\bar{\Sigma}_{a,M}$, and $\bar{\Sigma}_{a,P}$ are the macroscopic thermal absorption cross-sections of the fuel, everything else except the fuel and the poison, respectively.

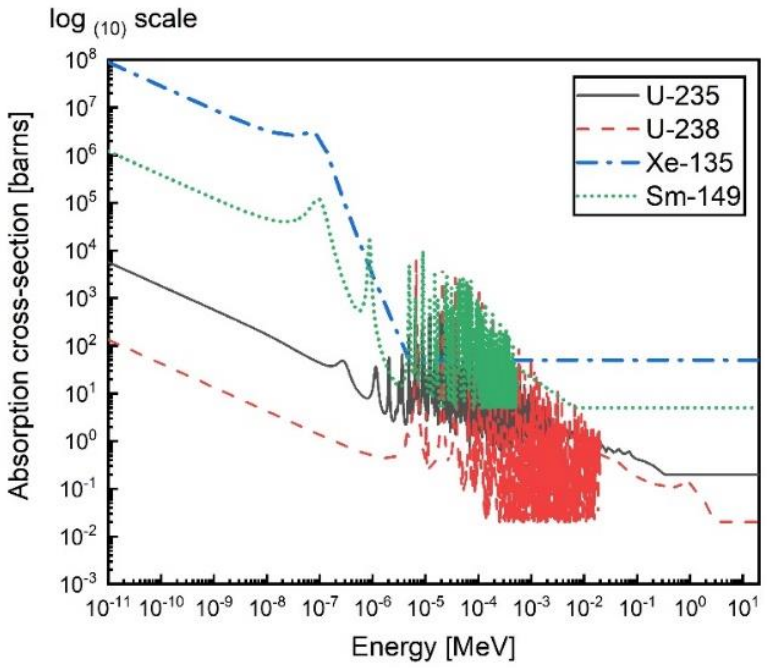

Figure 4. 15. Absorption cross-section for Xe-135 and Sm-149 compared to U-235 and U-238.

4.2.4.1. Buildup and removal of Xenon-135

Xenon-135 (Xe-135) is the most important fission product poison and has a significant impact on nuclear reactor operations. Therefore, to predict how the reactor will respond to changes in the concentration of xenon, it is important to know its production and removal rate. Xe-135 has a 2.6×10^6 barns neutron absorption cross-section. It is produced directly by some fissions but is more commonly a product of the tellurium-135 decay chain shown below. The fission yield (γ) for Xe-135 is about 0.3%, while γ for tellurium-135 is about 6%.

$$\text{Fission} \Rightarrow {}^{135}_{51}\text{Sb} \xrightarrow[0.8\text{ sec}]{\beta^-} {}^{135}_{52}\text{Te} \xrightarrow[19\text{ sec}]{\beta^-} {}^{135}_{53}\text{I} \xrightarrow[6.57\text{ h}]{\beta^-} {}^{135}_{54}\text{Xe} \xrightarrow[9.1\text{ h}]{\beta^-} {}^{135}_{55}\text{Cs} \xrightarrow[2.3\times10^6\text{ yr}]{\beta^-} {}^{135}_{55}\text{Ba (stable)}$$

Tellurium-135's half-life is so short, so it can be assumed that iodine-135 is produced directly from fission. Iodine-135 is not a strong neutron absorber but decays to form the neutron poison Xe-135. In fact, ninety-five percent of all produced Xe-135 comes from iodine-135 decay. Consequently, the half-life of iodine-135 plays an important role in the amount of Xe-135 present. The rate of change in iodine concentration is based on a simple balance of nuclear densities expressed as follows:

$$\underbrace{\text{Iodine concentration}}_{\text{Variation}} = \underbrace{\text{Yield from fission}}_{\text{Appearances}} - \underbrace{(\text{Decay rate} + \text{Burnup rate})}_{\text{Disappearances}}$$

$$\underbrace{\frac{dN_I}{dt}}_{\text{Variation}} = \underbrace{\gamma_I \Sigma_f^{\text{fuel}} \phi}_{\text{Appearances}} - \underbrace{(\lambda_I N_I + \sigma_a^I N_I \phi)}_{\text{Disappearances}} \tag{4.24}$$

Where:

N_I: I-135 concentration.
γ_I: Fission yield of ^{135}I.
Σ_f^{fuel}: Macroscopic fission cross-section fuel.
ϕ: Thermal neutron flux.
λ_I: Decay constant for ^{135}I.
σ_a^I: Microscopic absorption cross-section ^{135}I.

Since the iodine absorption cross-section is very small, the burnup rate term may be ignored, and the expression for the rate of change of iodine concentration is modified as shown below.

$$\frac{dN_I}{dt} = \gamma_I \Sigma_f^{\text{fuel}} \phi - \lambda_I N_I \tag{4.25}$$

When the rate of iodine production equals the rate of iodine removal, there is equilibrium. The concentration of iodine remains constant and is $N_{I(eq)}$. From the preceding equation, the following equation for the equilibrium concentration of iodine can be determined by setting the two terms one equal to the other and resolving for $N_{I(eq)}$.

$$N_{I(eq)} = \frac{\gamma_I \Sigma_f^{\text{fuel}} \phi}{\lambda_I} \tag{4.26}$$

Because the Xe-135 concentration consists of 5% that comes directly from fission and 95% comes from the decay of iodine-135. The rate of change of xenon concentration is expressed by the following equations.

$$\underbrace{\frac{dN_{Xe}}{dt}}_{\text{Variation}} = \underbrace{\gamma_{Xe} \Sigma_f^{\text{fuel}} \phi}_{^{135}\text{Xe yield from fission}} + \underbrace{\lambda_I N_I}_{^{135}\text{I decay}} - \underbrace{\lambda_{Xe} N_{Xe}}_{^{135}\text{Xe decay}} - \underbrace{\sigma_a^{Xe} N_{Xe} \phi}_{^{135}\text{Xe burnup}} \tag{4.27}$$

The burnup term refers to neutron absorption by Xe-135 $\left\{ {}^{135}_{54}\text{Xe} + {}^{1}_{0}\text{n} \rightarrow {}^{136}_{54}\text{Xe} + \gamma \right\}$. However, Xe-136 is not a significant neutron absorber, therefore, the neutron absorption by Xe-135 leads to the removal of poison from the reactor. Besides, the Xe-135 burnup rate depends on the neutron flux and the concentration of Xe-135. The Xe-135 equilibrium concentration at the equilibrium of iodine-135 is designated as $N_{Xe(eq)}$, and is represented as shown below.

$$N_{Xe(eq)} = \frac{(\gamma_{Xe} + \gamma_I)\Sigma_f^{\text{fuel}}\phi}{\lambda_{Xe} + \sigma_a^{Xe}\phi} \tag{4.28}$$

4.2.4.2. Buildup and removal of Samarium-149

Because of its high thermal neutron absorption cross-section of 4.1×10^4 barns, samarium-149 is the second most important fission-product poison. Sm-149 is formed from the decay of the fission fragment of neodymium-149 as shown in the decay chain below [23].

$$\text{Fission} \Rightarrow {}^{149}_{60}\text{Nd} \underbrace{\xrightarrow{\beta^-}}_{1.72\text{ h}} {}^{149}_{61}\text{Pm} \underbrace{\xrightarrow{\beta^-}}_{53.1\text{ h}} {}^{149}_{62}\text{Sm (stable)}$$

Since the neodymium-149 half-life (1.73h) is sufficiently shorter than that of promethium-149 (53.1h), promethium-149 can be considered as being formed directly from fission. This assumption and neglecting the small amount of promethium burnup permits describing the promethium rate of change as follows.

$$\underbrace{\frac{dN_{Pm}}{dt}}_{\text{Variation}} = \underbrace{\gamma_{Pm}\Sigma_f^{\text{fuel}}\phi}_{{}^{149}\text{Pm yield from fission}} - \underbrace{\lambda_{Pm}N_{Pm}}_{{}^{149}\text{Pm decay}} \tag{4.29}$$

Solving for the equilibrium value of promethium-149 gives the following.

$$N_{Pm(eq)} = \frac{\gamma_{Pm}\Sigma_f^{\text{fuel}}\phi}{\lambda_{Pm}} \tag{4.30}$$

Because of the fission yield of Sm-149 ($\gamma_{Sm}\Sigma_f^{\text{fuel}}\phi$) is virtually zero, the rate of Sm-149 formation can be described as follows.

$$\underbrace{\frac{dN_{Sm}}{dt}}_{\text{Variation}} = \underbrace{\lambda_{Pm}N_{Pm}}_{^{149}\text{Pm decay}} - \underbrace{\sigma_a^{Sm}N_{Sm}\phi}_{^{135}\text{Xe burnup}} \tag{4.31}$$

Taking into account the equilibrium value of promethium-149 ($N_{Pm(eq)}$), the equilibrium concentration of Sm-149 can be written as flow:

$$N_{Sm(eq)} = \frac{\gamma_{Pm}\Sigma_f^{\text{fuel}}}{\sigma_a^{Sm}} \tag{4.32}$$

Table 4. 4. Fission product yields (atoms per fission) from thermal fission [1].

Isotopes	^{233}U	^{235}U	^{239}Pu
^{135}I	0.0475	0.06390	0.0604
^{135}Xe	0.0107	0.00237	0.0105
^{149}Pm	0.00795	0.01071	0.0121

Table 4. 5. Decay constants for fission product poisoning calculations [1].

Isotopes	λ_s (sec^{-1})
^{135}I	2.87×10^{-5}
^{135}Xe	2.09×10^{-5}
^{149}Pm	2.87×10^{-5}

Chapter 5: Background – Thorium

This chapter provides an introduction to thorium as a nuclear fuel based on the literature. More details are included in the articles (chapter 6).

5.1. Introduction

The interest in using thorium as a nuclear fuel started in the 1950s. In the early 1960s, the Elk River boiling water reactor in Elk River and the Indian Point 1 pressurized water reactor were the first two reactors loaded with thorium-uranium (high-enriched uranium in combination with thorium dioxide) fuel but uranium was the preferred choice due to the success of the simpler uranium fuel cycle. However, the dwindling availability of uranium and the inherent advantages of using thorium have prompted renewed interest and research in thorium over the last years. Thorium is also found naturally on the surface of the earth (mainly in the form of monazite and thorite). It is estimated 3 to 4 times more abundant than uranium. Thorium consists mainly of Th-232 (almost 100%), which is considered a fertile isotope, similar to U-238.

The use of thorium is different from the use of uranium or plutonium in a nuclear reactor. Uranium requires enrichment to achieve a sustainable fission reaction, since the natural concentration of fissile U-235 is too low, with a high amount of fertile material in the form of U-238. Thorium has no fissile isotope to assist in maintaining the initial chain reaction and thus producing a fissile isotope requires more time than the U-238 absorption chain, Therefore, a fissile element such as plutonium extract from weapons or spent fuel or enriched uranium should be added to thorium to ensure a stable neutron economy initially. On the other hand, the neutron capture of Th-232 creates a fissile U-233 (**Figure 5.1**), which has a reduced probability of reproducing plutonium when used in a nuclear reactor. U-233 also has very favorable fission to capture ratio superior to U-235, Pu-239, or Pu-241 (**Figure 5.2**). Moreover, thorium-based fuels offer quite a lot of potential advantages over uranium fuels such as higher fissile conversion rates, higher thermal fission factor (η) [93], lower capture-to-fission ratio (**Table 5.2**), low actinides (americium and curium) production [94, 95] and chemically very stable. In addition, one attraction of using the thorium-based fuel in fissile nuclear reactors is its relatively improved thermo-physical properties, such as higher melting points (340ºC higher than that of UO_2), higher thermal

conductivity (about 50% higher), lower coefficient of thermal expansion and negative reactivity feedback [86, 96, 97, 98, 99, 100, 33].

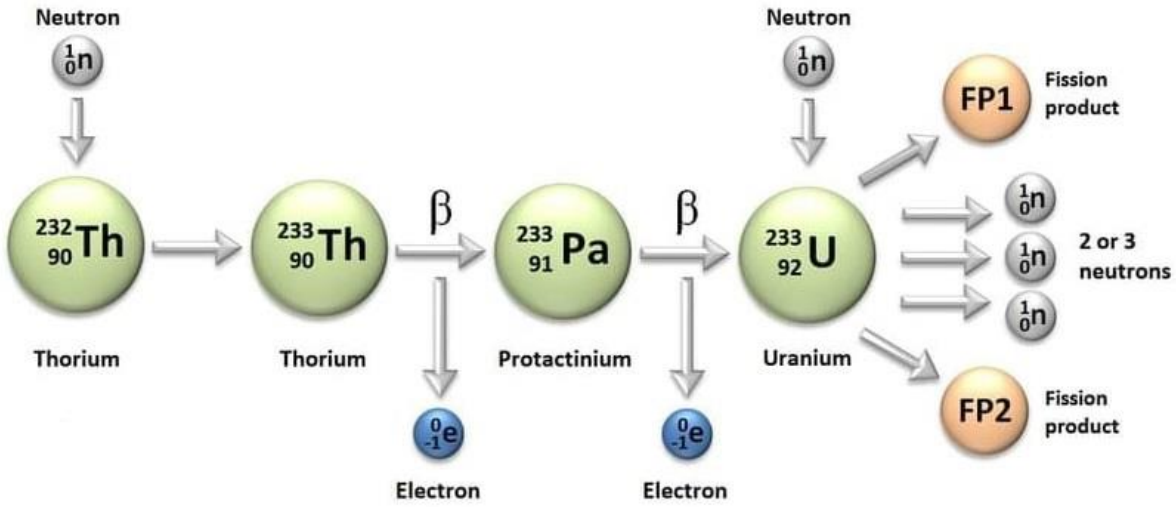

Figure 5. 1. Conversion chain of Th-232 to U-233.

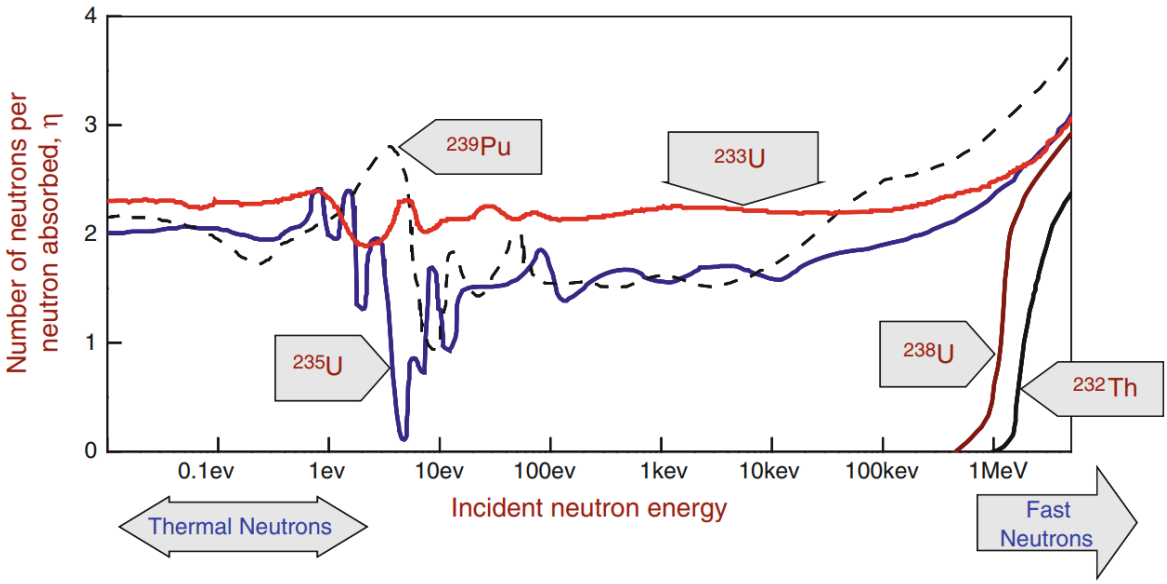

Figure 5. 2. Energy dependence of η for U-233 compared to and U-235 and Pu-239.

Based on the literature reviews [94, 100, 101, 102], thorium-based fuels have been studied for their potential applications in almost all types of reactors including pressurized water reactors (PWRs), boiling water reactors (BWRs), pressurized heavy water reactors (PHWRs) and fast breeder reactors (FBRs). It has already been established that $(Th, U)O_2$ and $(Th, Pu)O_2$ fuels can

be used in PWRs without any significant change in the reactor design. Todosow et al. presented calculation results and a comparison of the potential utilization of thorium-based mixed oxide fuel in LWRs using two configuration types for both the seed-blanket unit (SBU) and the whole assembly seed and blanket (WASB). According to their results, the SBU and the WASB designs provide reductions of 30% in the volume of spent fuel and of 60 to 70% in the mass of plutonium produced during nuclear power generation [103]. Tucker et al. have reported the possibility of converting the UO_2-fueled Westinghouse-type 17x17 PWR to a novel ThMOX configuration. As it is mentioned in both studies, it appears feasible from a neutronic point of view to integrate ThMOX fuel into the fuel supply for a conventional PWR [95, 86]. Likewise, Akbari-Jeyhouni et al. considered that $(Th, U)O_2$ is a good fuel option for the upcoming Small Modular Reactors (SMRs) [104]. In addition to LWR reactor scenarios, two types of reactors were suggested for the future thorium fuel breeding process (Generation-IV): high-temperature reactors (HTRs) and molten salt reactors (MSRs). Chapter 6 aims to determine the effects of the introduction of thorium with different 'engine/driver' fissile materials and multiple configurations into a high-temperature pebble-bed reactor.

Table 5. 1. Parameters of fissile and fertile nuclei.

Properties	U	Pu	Th	UO_2	PuO_2	ThO_2
Melting point (°C)	1130	632	1750	2760	2400	3300
Theoretical density (g/cm3)	19.10	19.80	11.70	10.96	11.50	10.00
Crystalline structure				FCC (CaF2 type)	FCC (CaF_2 type)	FCC (CaF_2 type)

Table 5. 2. Mean fissile and fertile nuclei parameters in a thermal neutron spectrum.

	Th-232	U-233	U-235	U-238	Pu-239	Pu-241
Thermal						
σ capture (barns)	4.62	364	405	1.73	1045	1121
σ fission (barns)	0	332	346	0	695	842
$\alpha = {}^{\sigma_c}/_{\sigma_f}$		0.096	0.171		0.504	0.331
η_{th}		2.26	2.08		1.91	2.23
Epithermal Resonance	0	764	0	275	301	
I.R: integral resonance in infinite dilution						
RI capture	85.6	882	405	278	474	740

RI fission		746	272		293	571
$\alpha = {RI_c}/{RI_f}$		0.182	0.489		0.618	0.296
η_{epi}		2.1	1.63		1.77	2.29
Neutron Yield υ		2.48	2.43		2.87	2.97
Delayed Neutron Yield β		0.0031	0.0069		0.0026	0.005
Capture:						
2 200 m/s value	7.6	54	100	2.7	267	
Resonance integral	85	140	144	275	200	
Neutron/fission		2.5	2.4			2.9

Chapter 6: Numerical results

This chapter discusses the various scenarios for employing thorium fuel in the high-temperature pebble-bed reactor (HTR-10). This chapter's contents have been published in international peer-reviewed journals [105, 106].

6.1. A comparative analysis of the neutronic performance of thorium mixed with uranium or plutonium in a high-temperature pebble-bed reactor

Modified from a paper published in the International Journal of Energy Research.

DOI: https://doi.org/10.1002/er.6935

Ouadie Kabach [1,*], Abdelouahed Chetaine [1], Abdelfettah Benchrif [2], Hamid Amsil [1, 2], Fadi El Banni [3]

[1)] Nuclear Reactor and Nuclear Security Group Energy Centre, Department of Physics, FSR, Mohammed V University, Rabat, Morocco

[2)] National Centre of Nuclear Energy Sciences and Techniques, Rabat, Morocco

[3)] LASMES, SSMT, Felix Houphouet Boigny University, Abidjan, Ivory Coast

*Corresponding author e-mail address: ouadie.kabach10@gmail.com; ouadie_kabach@um5.ac.ma

Abstract: High-temperature gas-cooled reactors (HTGRs) present an interesting concept for the next generation of nuclear reactors due to them having many advantages. In particular, their fuel is based on coated particles known as tri-structural-isotropic (TRISO) particles, and these provide a strong container capacity for fission products. Solid graphite acts as a moderator by delaying the transient temperature in the event of an accident, while neutronically inert helium acts as a coolant. What is more, several TRISO particle models are in various stages of development. Nowadays, numerous studies have sought to investigate the integration of thorium as a fertile absorber with a driver fuel (i.e. U-233, U-235, or Pu-293) in nuclear reactors due to its natural abundance and its potential for producing fissile material (U-233). In addition, there are numerous perspectives for recycling and reusing the fissile isotopes released during thorium irradiation and the spent fuels from current reactors, with the main goal being to dispose of the world's growing stocks of radioactive waste and surplus weapons material. The primary objective of this study is not just to discuss the advantages of using thorium in a (pebble-bed type) HTGR but also to investigate how thorium can be incorporated into the fuel with different drivers and how this affects the neutronic parameters in comparison to the nominal HALEU (UO_2 17 wt.%) fuel. These parameters include the burnup behavior, spent fuel compositions, effective delayed neutron

fractions, neutron spectra and temperature coefficients. The investigated fuel mixtures include thoria (ThO_2) fuel mixed with high-assay, low enriched uranium (HALEU 20 wt.%), reactor-grade plutonium ($RGPuO_2$), weapons-grade plutonium ($WGPuO_2$), and U-233. Neutronic analyses show that cores fueled by $(Th+^{233}U)O_2$ and ThO_2+$WGPuO_2$ achieved higher excess reactivity at the beginning of cycle (BOC), compared with the UO_2 core which achieves higher discharge burnups. Cores fueled by ThO_2+$RGPuO_2$, in contrast, can achieve higher discharge burnup despite having the lowest excess reactivity at BOC. Further comparisons of the examined fuel mixtures reveal that the $(Th+^{233}U)O_2$ and ThO_2+PuO_2 mixtures have less favorable effective delayed neutron fractions and temperature coefficients than the UO_2. However, the moderator temperature coefficients of the $(Th+^{233}U)O_2$ mixtures were sufficiently negative for all time steps.

Keywords: Pebble-bed reactor, Thorium-based fuel, TRISO; Neutronic analyses, Discharge burnup, MCNP6.2, ENDF/B-VIII.0 library.

6.1.1. Introduction

There is a considerable interest at present in using thorium-based fuels in various nuclear reactors to ensure the safety and sustainability of nuclear energy. Natural thorium, mostly in the form of the fertile Th-232 isotope, is three to four times more abundant than uranium [104]. Th-232 also has a greater capture cross-section for thermal neutrons than U-238, so it has a higher conversion ratio for converting it to U-233 than when converting U-238 to Pu-239. The interest in thorium is also driven by its unique chemical properties [24]. On the other hand, the process for recycling the nuclear waste produced by commercial reactors is also one of the key problems facing the nuclear industry, both in terms of the sustainability of fuel and nuclear non-proliferation [107]. As a result, several existing scenarios are available for using Th-232 with recycled waste in the fuel cycle (e.g., $Th+^{233}U$ and Th+Pu).

Indeed, thorium-based fuels have been widely investigated for use in pressurized water reactors (PWRs/SMRs) [86, 108], water-water energetic reactors (VVERs) [109], boiling water reactors (BWRs)[100], and advanced heavy-water reactors (AHWRs) [110]. In most of these reactors, one of two thorium assembly designs has been considered, namely heterogeneous or homogeneous. The heterogeneous design concept, also known as the seed and blanket (S&B) concept, uses the driver fuel in the seed region and thorium in the blanket region, while the homogeneous design uses a mixture of the driver fuel and thorium [93]. In addition, research into the use of thorium-

based fuels has progressed beyond traditional water reactors to include molten salt reactors (MSRs) [111, 112, 113], breeder reactors (BR) [114, 115, 116], and high-temperature gas reactors (HTGRs) [117].

The HTGR concept is one of six concepts for the fourth generation of nuclear reactors [118]. There are several types of HTGR (e.g., the pebble-bed and the prismatic block types), but all these concepts are fundamentally based on TRISO particles. Due to their advantages, such as inherent safety, HTGRs have attracted considerable interest, because helium (the coolant) is neutronically inert and stays in single-phase under all conditions. In addition, there is the presence of a large amount of graphite (a moderator and reflector), which has a high heat capacity and can delay the transient temperature during accidents [119]. Furthermore, HTGRs may be a better choice than the other potential reactors for using thorium-based fuels because the use of TRISO particles retains the fission product and resists irradiation very well, thus allowing for a very high fuel burnup [120, 121]. Unlike block-type reactors, one of the major challenges in incorporating thorium in pebble-bed reactors (PBR **Figure 6.1** to **6.3**) is the difficulty in implementing the S&B concept, because the pebbles are randomly packed in the cylindrical cavity of the reactor core. As a result, the most practical option is to add the driver fuel with thorium into a TRISO particle known as mixed oxide (MOX) fuel [122, 123].

Historically, the use of Th-232 as a fertile material in HTGRs has been commonly suggested as a potential way to increase the burnup of the fuel element or recycle the nuclear waste produced by reactors. The main HTGR model comes in a variety of fuel cycles, designs, and variants. The current reactors can use highly enriched uranium [124, 125], high-assay low enriched uranium [126, 127], or low enriched uranium with thorium as the fertile material [128]. Plutonium [125, 122] can be used as a fissile driver in thorium-based fuels, as well as U-233 from other reactors. The fuel element in an HTGR reactor can be cylindrical, such as in the Dragon reactor [129]; spherical, such as in the AVR, Xe-100 and HTR-PM reactors [130, 131, 132, 133, 134]; or block-type, as is the case with the AHTR reactor [123].

According to the literature review, studies comparing the use of thorium-based fuel with various driver materials in HTGRs have often been conducted in prismatic block-type HTRs because of the flexible core that can support a wide range of fuel cycles [135, 136, 137]. Studies for PBR, on the other hand, have been conducted separately, and ThO_2+UO_2 or ThO_2+PuO_2 fuels have been widely used [124, 125, 138, 139]. A recent comparative analysis between using HALEU (17 wt.%)

and ThO_2+$RGPuO_2$ ($RGPuO_2$ content-37.6 wt.%) in the PBR-HTR-10 reactor was conducted by Alzamly et al.[140]. Their results showed that core a fueled by ThO_2+$RGPuO_2$ achieves a 24% longer fuel cycle than one fueled by HALEU (17 wt.%). The focus of their study, however, was limited to discharge burnup behavior and spent fuel composition without any consideration of other safety parameters. This current study, therefore, aims to investigate the neutronic differences between using the nominal (HALEU 17 wt. %) fuel in the PBR-HTR-10 reactor and other possible candidate fuels based on thorium. These proposed fuels include ThO_2 mixed with HALEU (20 wt. %), $RGPuO_2$, $WGPuO_2$, or U-233. As a reference, we also simulate a reactor core fueled by nominal HALEU [UO_2 (17 wt.%)]. The neutronic comparison takes into account the discharge burnup behavior, spent fuel compositions, effective delayed neutron fractions, and temperature coefficients.

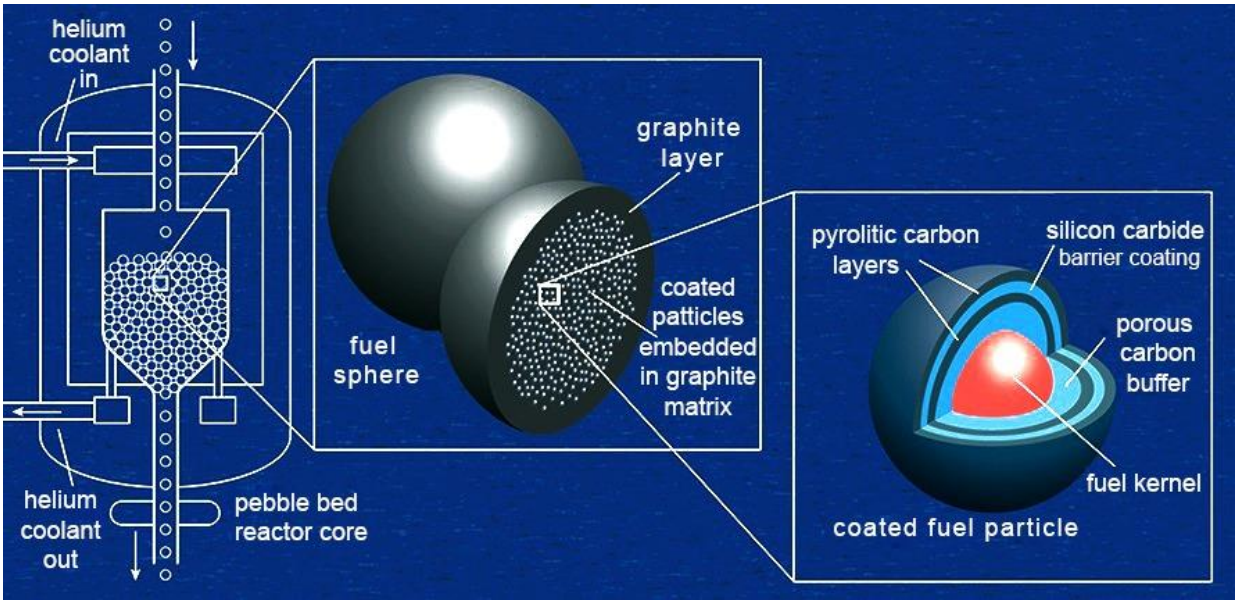

Figure 6. 1. A representative pebble-bed HTGR core, pebble model, and TRISO fuel particle [141].

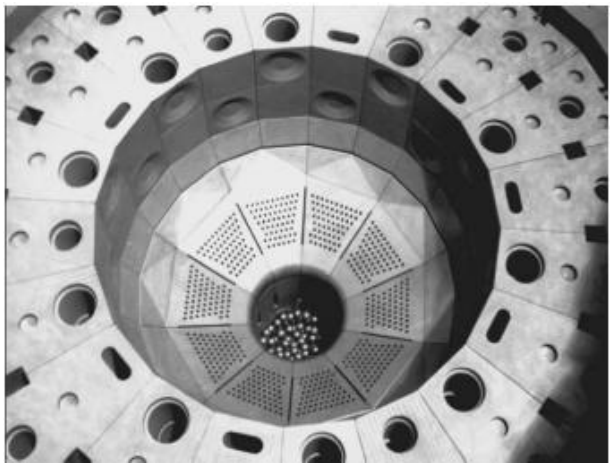

Figure 6. 2. HTR-10 horizontal core view [119].

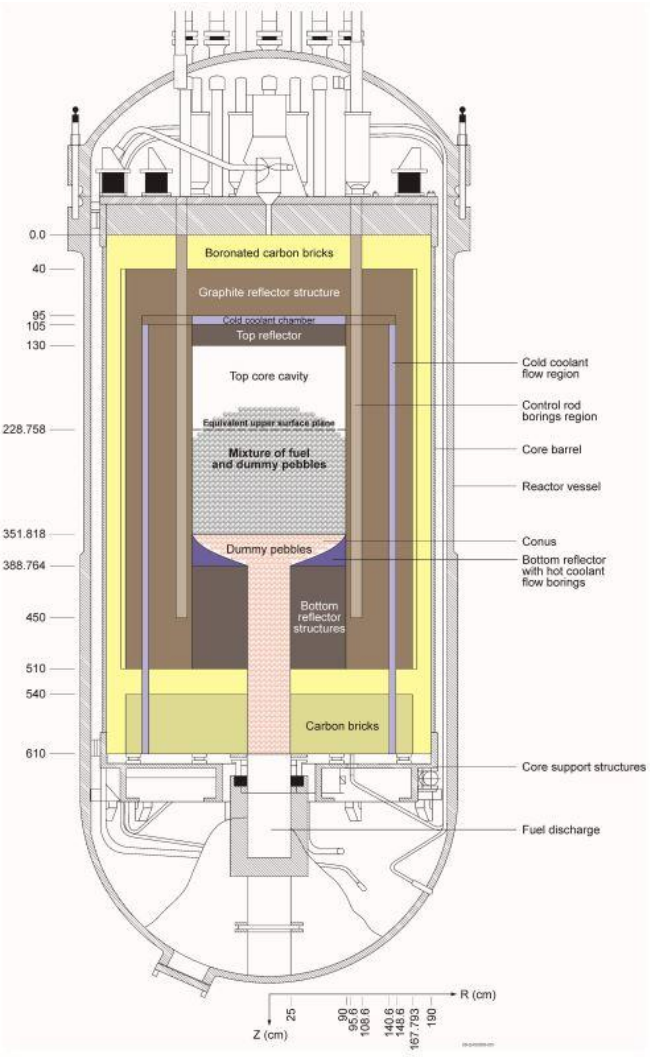

Figure 6. 3. HTR-10 vertical core view [142][119].

6.1.2. Description of the HTR-10

The HTR-10 is an experimental reactor based on the pebble-bed design. It was constructed, and is operated, by the Institute of Nuclear and New Energy Technology (INET) in China. Despite its low power capacity (10 MW), the diameter of the HTR-10 reactor vessel is approximately equal to that of the 250 MW HTR-PM (HTR-MODUL) [143, 144, 145, 146], and both reactors can be operated with little excess reactivity since it is possible to adjust reactivity during operation [119, 147]. The HTR-10 reactor core is surrounded by an arrangement that comprises a graphite reflector and a borated carbon shield. The core itself comprises spherical fuel pebbles containing coated fuel particles and moderator pebbles. The fuel and moderator pebbles have the same diameter (6 cm) and are loaded at a ratio of 0.57/0.43. The reactor core is filled with approximately 27,000 fuel pebbles, with these being packed in a cylindrical cavity with a height of 197 cm and a diameter of 180 cm [148]. One of the most essential aspects of the PBR concerns the online refueling schemes, which can significantly increase fuel burnup. In general, three refueling schemes can be used:

1) The pebbles are loaded into the top of the core and then fall down due to gravity. The pebbles can be then discharged after one cycle. This is known as the Once-Through-Then-Out (OTTO) scheme [149].
2) The pebbles are continuously loaded into the core to sustain criticality until the core is completely filled, after which they are completely discharged and replaced. This is called the "Peu-a-Peu" scheme [118].
3) The pebbles are continuously extracted, tracked for burnup, and transported back to the top of the reactor core if they have not yet met the burnup target. This process is known as the multi-pass scheme, and it is commonly used in reactors like the HTR-10 [133, 138, 150].

A fuel pebble in the HTR-10 core contains an average of 8,335 coated particles. These coated particles are of a TRISO type and contain HALEU fuel (17 wt.%) surrounded by four outer layers for structural integrity and the containment of fission products [151]. More specifically, these are the Porous Carbon Buffer, the Inner Pyrolytic Carbon (I-PyC), the Silicon Carbide (SiC), and the Outer Pyrolytic Carbon (O-PyC). The HTR-10 core has two separate shutdown mechanisms, 10 boron carbide control rods, and 7 absorber balls. The control rods comprise five-ring segments of boron carbide (B_4C) contained in steel sleeves, joints, and upper and lower ends, while the absorber

balls are homogeneous mixtures of boron carbide (≈ 25%) and graphite (≈ 75%). Both the control rods and the absorber balls are positioned in the side reflector, and they are capable of bringing the reactor to a cold shutdown condition [152]. In addition, the absorber balls were designed to shut down the reactor in an emergency when the main control rods are out of control [153]. The key parameters of the HTR-10 reactor are described in **Table 6.1**.

Table 6. 1. Key parameters of a typical HTR-10 reactor [148].

Reactor thermal power	10 MW
Power of residual heat removal system	250 kW
Design lifetime	20 years
Reactor core volume	5 m3
Reactor core diameter	180 cm
BCC unit-cell size	6.877 cm
Fuel	UO2
UO2 density	10.4
Fresh fuel U-235 enrichment	17 wt.%
Diameter of a fuel pebble	6 cm
Diameter of fueled region	5 cm
Moderator pebble diameter	5.462 cm
Total number of pebbles loaded	27,000
Number of coted particles in a pebble	8333
Heavy metal content of each pebble	~ 5 g
U-235 content of each pebble	~ 0.9 g
Diameter of the fuel kernel	0.05 cm
Coating layers	PyC/ I-PyC/SiC/O-PyC
Densities	1.1/1.9/3.18/1.9 (g/cm3)
Thickness	90/40/35/40 (μm)
Fuel temperature coefficient	-2.13 pcm/K
Position of control rods	Side Reflector
Control rod channels	10
Absorbing ball channels	7

6.1.3. Description of the TRISO particle

All HTR fuel concepts are based on the idea of a coated fuel particle in which a small kernel is covered with several layers. Coated particles are a fundamental safety feature of HTR reactors, act as the first barrier to the retention of fission products, and are the basis for the inherent safety features of modular HTRs. As the core of the HTR contains thousands of coated fuel particles, if a small fraction of them fails, the total release of radioactivity would remain within acceptable values. Besides, the micro-particles are very well resistant to irradiation and thus make it possible

to achieve a very high fuel burn. Due to their central role in all key concepts of HTRs. TRISO, particles consist of a spherical kernel, which is surrounded by four concentrated coating layers. The first layer that surrounds the kernel is a layer of porous carbon known as the buffer. An internal layer of high-density pyro-carbon (IPyC), a layer of silicon carbide (SiC), and an outer layer of high-density pyro-carbon (OPyC) follow this layer.

The following bullets describe the main features of each component of a TRISO particle (**Figure 6.4**)

- Buffer layer, this first layer in contact with the kernels is known as the buffer layer and has three main roles:
  - Mitigate the decline in fission products; i.e. to slow down the fission products with very high energies resulting from fission. However, the recoil path of fission products is very long in a low-density material such as porous carbon; therefore, the thickness of this layer is comparable to the recoil path.
  - Ensuring an empty space for gaseous fission products. The porous layer ensures a space for the retention of the generated gases and good control of the internal pressure of the kernel.
  - It can deform to compensate for the enlargement of the fuel kernel.
- Inner pyro-carbon layer (IPyC): the inner high-density, isotropic layer of pyrolytic carbon. The IPyC layer form the first load-bearing barrier against the pressure exerted by fission products within the fuel kernel and the buffer layer, thus reducing the pressure on the next layer, which consists of SiC.
- Silicon carbide layer (SiC): the SiC acts as a barrier to the diffusion of solid fission products, in particular cesium, silver, and strontium, a major innovation brought by the TRISO in terms of high-performance fission retention of products. It has two key functions:
  - Provide structural support to meet internal gas pressure.
  - To serve as an effective shield for solid and gaseous fission products.
- Outer pyro-carbon layer (OPyC): the purpose of this layer is to protect the SiC layer against damage during the fuel production process regarding the coating process. It also provides pre-

stress from the outside of the SiC layer due to its interaction with the IPyC layer under fast neutron during the reactor lifetime.

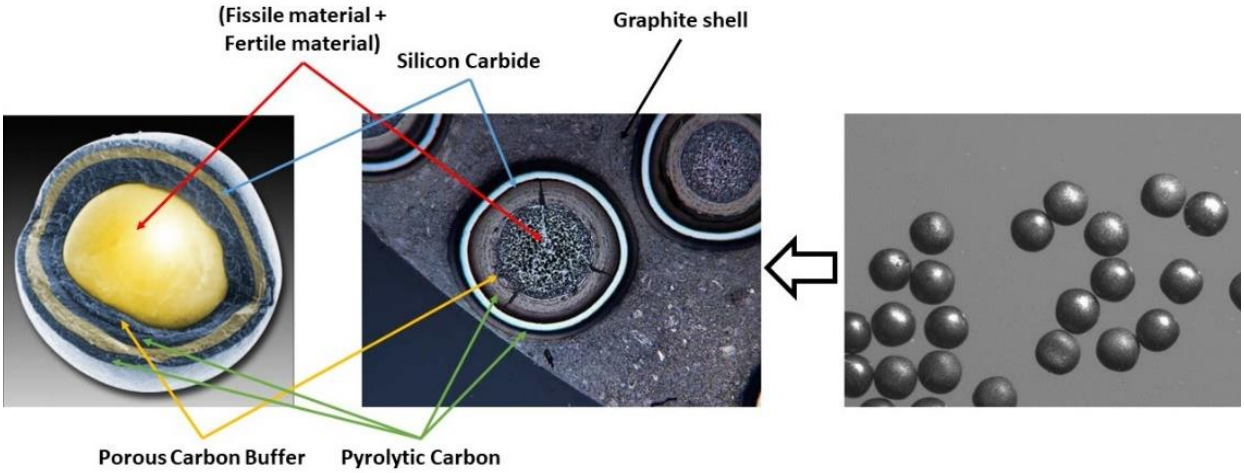

Figure 6. 4. TRISO particles showing detailed features (modified from *www-zmescience-com*).

6.1.4. Calculation model and methods

The core simulations presented here were performed using the Monte Carlo transport code of MCNP version 6.2 [30]. MCNP6 can be accurately described as a combination of the capabilities of MCNP5 [34] and MCNPX [32]. Using the "BURN" option of the input file, MCNP6 can perform individual criticality calculations for each time step and handle complex geometries, such as the PBR's double heterogeneity, which consists of TRISO particles surrounded by graphite matrix and pebbles distributed in the core. The "BURN" option, which is responsible for burnup calculations, allows the user to pre-define the power level, the duration, and the burnable materials, as well as specify the fission products that MCNP6 should track and the omitted list of isotopes for which cross-section data does not exist in the MCNP6 library. MCNP6 uses the CINDER90 library to perform depletion/burnup calculations and generate new number densities that correspond to the end of each time step. One of the most essential features of the "BURN" option is the three "Tiers" of fission products that are available to the user. These three Tiers have an increasing number of fission products, ranging from the 12 most-common fission products in Tier 1, through all fission products for which neutron cross-sections exist in the cross-section directory, and to all fission products for which CINDER90 has fission yield data in Tier 2 and Tier 3, respectively [30].

Establishing an accurate model for predicting the neutronic behaviors of HTR-10 and PBR cores is difficult due to the double heterogeneity of the system, so the following approximations were used in this work (**Figures 6.5** and **6.6**):

- A simple cubic lattice was used to model the TRISO particles in the pebble, and a repeated structure was used to generate the particles in the pebble.
- The fuel pebbles were arranged in a BCC lattice, with each lattice containing 1 is placed in the center and 1/8 in each corner of the cube.
- The repeated structure was used to model the reactor core using LATTICE and FILL options.
- The edging effects caused by the repeated structure (i.e. pebbles clipped by inner surfaces) were minimized by adjusting the packing fraction (0.61 is reduced to 0.59).

Finally, in this analysis, Tier 3 fission products were used. In the MCNP KCODE option, the criticality calculations were set to perform 300 cycles with 50,000 neutrons per cycle, as well as 100 discarded cycles for converging the source distribution using the ENDF/B-VIII.0 cross-section library [71]. The discarded cycles were verified using the Shannon entropy convergence test.

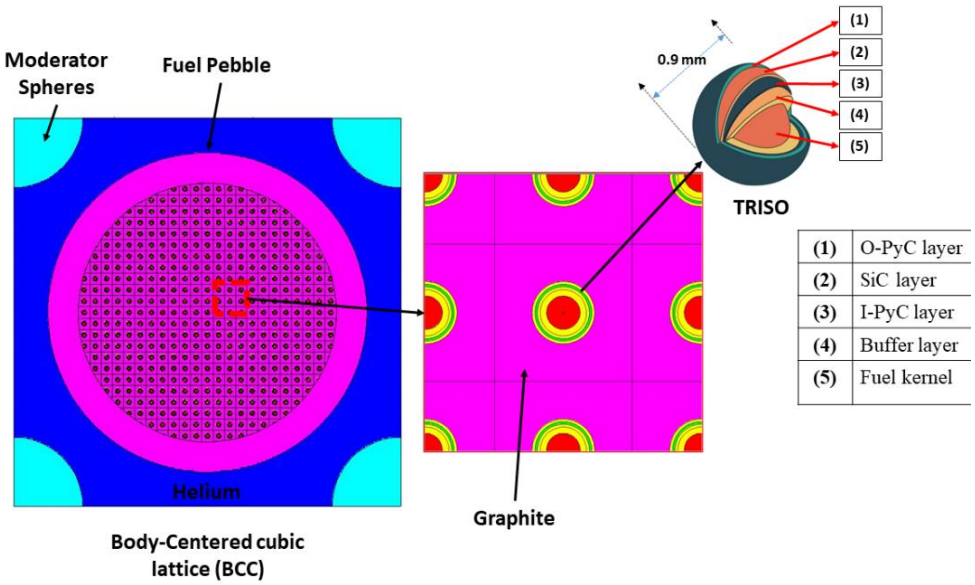

Figure 6. 5. Geometrical shape of a fuel pebble in a BCC structure and TRISO particle. Most of these figures were generated using Visual Editor and are schematic.

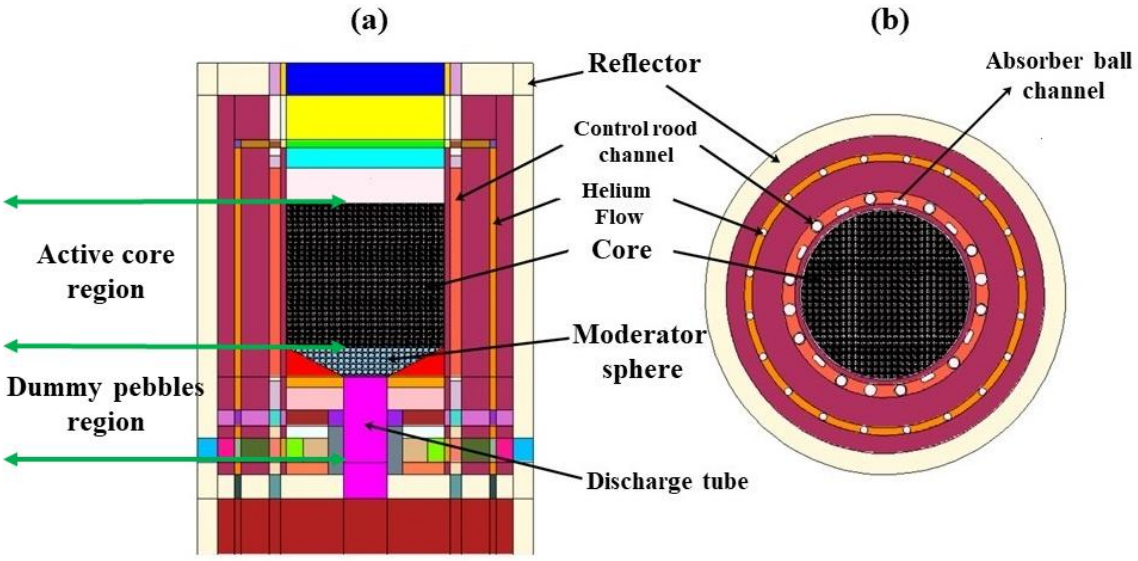

Figure 6. 6. (a) Cross-section and (b) top view of the simulation model exported by MCNP.

6.1.5. Model verification

To ensure that our model's geometry was acceptable, we conducted a benchmark test by comparing multiplication factors (keff) at beginning of cycle (BOC) using UO_2 (17 wt.%) fuel against the benchmark value with 16,890 fuel pebbles [142] and the values given in the IAEA reference with 27,000 fuel pebbles [154]. The benchmarking outcomes for 16,890 and 27,000 fuel pebbles are included in **Tables 6.2** and **6.3**, respectively. The results indicate that there is fairly good agreement with the reference values, thereby providing an initial validation of the designed model. The difference in the keff values observed across ENDF/B releases is caused by a significant change in the carbon cross-section (**Figure 6.7**). It is known that PBRs (HTR-10/HTR-PM) have a high carbon content in their fuel pebbles and reflector materials, so the results will be sensitive to carbon thermal absorption cross-section and graphite thermal scattering data. As argued by Bostelmann et al.[155], when moving from the ENDF/B-VII.0 library to ENDF/B-VII.1, keff changes by more than 1%, while between the ENDF/B-VII.1 and ENDF/B-VIII.0 libraries, the change is approximately 0.4%. Furthermore, by changing the graphite porosity to 10% and 30% in ENDF/B-VIII.0, keff is increased by about 0.4% and 0.7%, respectively.

Table 6. 2. Verification of the initial critical configuration of the HTR-10 loaded with approximately 16,890 pebbles.

Code	**Library**	**K_{eff}**		$\Delta k/k$
MCNP6 (present work)	ENDF/B-VIII.0	1.00632	± 0.00022	0.63%
MCNP-4B [147]	ENDF/B-VI	1.00479	-	0.48%
KENO [155]	ENDF/B-VIII.0	1.00582	± 0.00008	0.58%
Benchmark value [142]		1.00000	± 0.00037	-

Table 6. 3. Verification of the HTR-10 reactor loaded with 27,000 pebbles.

	S(α; β) data used for graphite	k_{eff}		$\Delta k/k$
ENDF/B-VII.0 (present work)	Graphite	1.12832	± 0.00021	0.13%
ENDF/B-VII.1 (present work)	Graphite	1.11701	± 0.00022	1.13%
ENDF/B-VIII.0 (present work)	Graphite	1.12033	± 0.00023	0.83%
	10% porous graphite	1.12588	± 0.00022	0.34%
	30% porous graphite	1.12348	± 0.00022	0.56%
Previous study [154] (MCNP4C with ENDF/B-VI library)		1.12976	± 0.00086	-

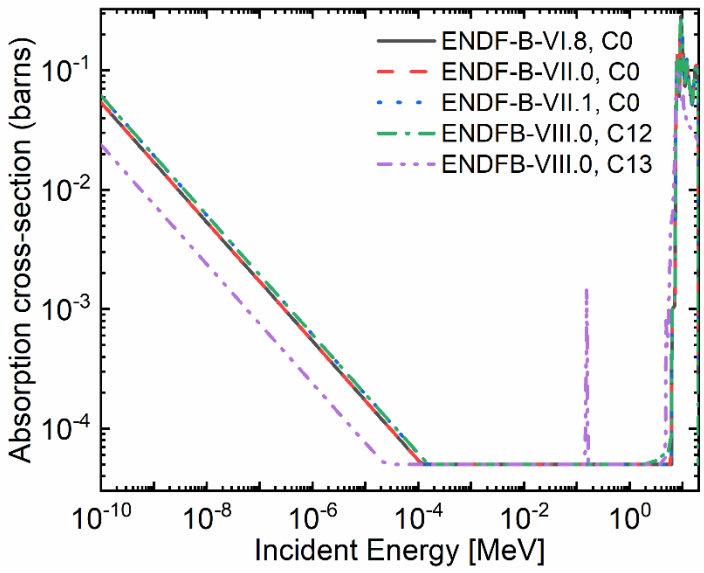

Figure 6. 7. Comparison of carbon absorption cross-sections with ENDF/B-VI.8, ENDF/B-VII.0, ENDF/B-VII.1 and ENDF/B-VIII.0.

6.1.6. Results and discussion

6.1.6.1. The effect of thorium content on the effective multiplication factor

The key motivation behind this work is to compare the behavior when using ThO_2 fuel mixed homogeneously with HALEU, $RGPuO_2$, $WGPuO_2$, and U-233 instead of the nominal UO_2 (17 wt.%) fuel in the HTR-10 reactor. This subsection provides a general evaluation of the criticality behaviors of thorium fuel mixed with various fissile contents (%) at BOC. (The scenarios are described below.) The objective is to identify the mixtures that will be investigated in the following sections. The physical properties of uranium, plutonium, and thorium are given in **Table 6.4** [98], while **Table 6.5** shows the isotopic compositions of the plutonium used in RGPu and reactor WGPu.

The preliminary scenarios for evaluation were determined as follows:

- The first scenario is based on the use of (ThO_2+UO_2) fuel with an increase of 1% to 100% for the UO_2 ratio and an increase in the enrichment value from (17 wt.%) to the HALEU limit value (20 wt.%).
- The second scenario is based on (ThO_2+$RGPuO_2$) fuel with an increase in the ratio of $RGPuO_2$ from 1% to 100%.
- The third scenario is based on (ThO_2+$WGPuO_2$) fuel with an increase in the $WGPuO_2$ ratio from 1% to 100%.
- The final scenario is based on (Th+^{233}U)O_2 fuel with an increase in the U-233 ratio from 1% to 100%.

Table 6. 4. Physical properties of uranium, plutonium, and thorium fuel (metallic and ceramic).

Properties	U	Pu	Th	UO_2	PuO_2	ThO_2
Melting point (°C)	1130	632	1750	2760	2400	3300
Theoretical density (g/cm^3)	19.10	19.80	11.70	10.96	11.50	10.00
Crystalline structure				FCC (CaF2 type)	FCC (CaF_2 type)	FCC (CaF_2 type)

Table 6. 5. The isotopic compositions of the suggested WGPu and RGPu fuels [124, 140].

Isotope	WGPu composition (wt.%)	RGPu composition (wt.%)
Pu-238	-	1.81
Pu-239	94.0	59.14
Pu-240	6.0	22.96
Pu-241	-	12.13
Pu-242	-	3.96

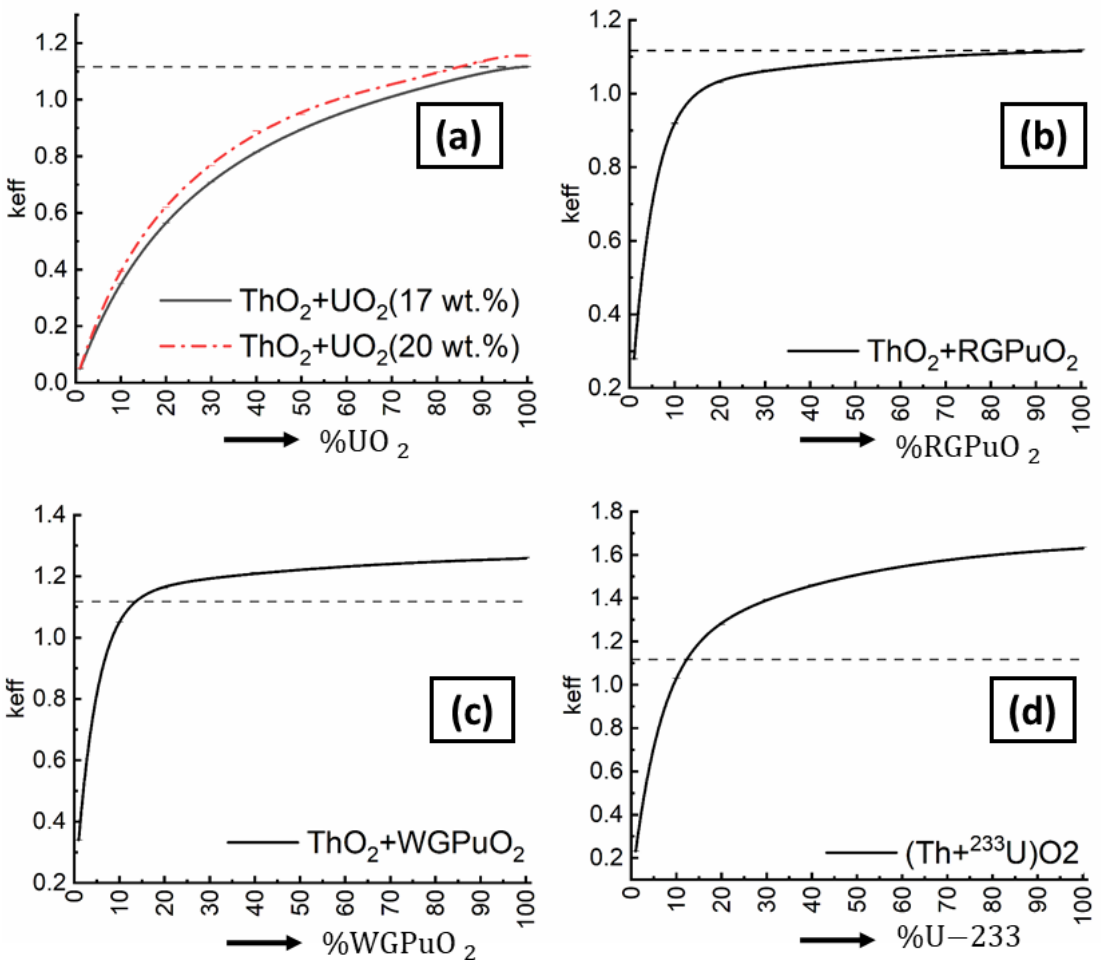

Figure 6. 8. Effective multiplication factor curves with mixed charges consisting of (a) ThO_2+UO_2 fuels; (b) ThO_2+$RGPuO_2$ fuels; (c) ThO_2+$WGPuO_2$ fuels; and (d) (Th+^{233}U)O_2 fuels. The dashed line reflects the keff result for the reference core, which is referred to as keff [UO_2].

Figure 6.8 illustrates the relationship between the keff values and the fissile fuel content as represented in the given scenarios. The main findings are summarized below:

- The first series of criticality calculations performed with the ThO_2 and UO_2 (20 wt.%) fuel mixture shows that the reactor becomes critical (keff ≈ 1) at 56% UO_2 content, while keff ≥ keff [UO_2] occurs at more than 85% UO_2 content. The reason for the substantial quantity of UO_2 that is required to achieve keff ≈ keff [UO_2] mainly relates to the decrease in the fission-to-capture ratio (σ_f/σ_a) that is caused by the higher absorption cross-section of Th-232, which is about three times greater than that of U-238 [33].
- In the second sequence of criticality calculations performed with the ThO_2 and $RGPuO_2$ fuel mixture, the reactor is critical with 15% $RGPuO_2$ content. As can be seen in **Figure (6.8.b)**,

however, keff > keff [UO_2] cannot be achieved with $RGPuO_2$, and this is due to the presence of plutonium and Th-232 isotopes with higher neutron absorption.

- In the third set of criticality calculations for the fuel mixture of ThO_2 and $WGPuO_2$, it is interesting to observe how keff rises rapidly with greater $WGPuO_2$ content. As depicted in **Figure (6.8.c)**, the reactor becomes critical with less than 8% $WGPuO_2$ content, while keff ≥ keff [UO_2] is achieved using just under 14% $WGPuO_2$ content.
- Just like with ThO_2+$WGPuO_2$ mixtures, the reactor can become critical with less than 8% U-233 content in the (Th+^{233}U)O_2 mixture. Furthermore, at around 13% U-233 content, the reactor can achieve keff ≥ keff [UO_2] (**Figure 6.8.d**).

6.1.6.2. Burnup calculation

Evolution of the effective multiplication factor with burnup

Figure 6.9 shows the neutronic behavior (keff) in terms of the burnup function (GWd/ton) for some of the considered fuel mixtures, which were selected based on the results presented in the previous section. The neutronic behaviors for these fuel types were compared with that of the nominal fuel, and all the investigations were conducted with a one-batch discharge burnup with a realistic power of 10 MW in the "BURN" option. As predicted, in the first phase after reactor start-up, the keff values for all the considered fuels decreased due to fission poison build-up (i.e. Xenon-135 and Samarium-149), and then decreased smoothly again due to fuel burnup.

As can also be seen from the figure, although the cores fueled with $RGPuO_2$ have the smallest keff values at BOC (due to the higher absorption cross-sections of Th-232 and Pu-240), they also show the lowest descent during burn time. Their keff's also achieve the critical condition at approximately 42 GWd/ton and 45 GWd/ton for 38% $RGPuO_2$ and 40% $RGPuO_2$, respectively, compared with 36 GWd/ton for UO_2 fuel. In contrast, in the case of 85%ThO_2+15%$WGPuO_2$ and (87%Th+13%^{233}U)O_2 mixtures, despite the BOC values being 355 pcm and 1,234 pcm higher than the estimated value using UO_2 fuel, criticality is achieved at just 23 GWd/ton and 26 GWd/ton, respectively. The reasons for this are explained below:

The lower discharge burnup of the 85% ThO_2 with 15% $WGPuO_2$ mixture versus the ThO_2 with $RGPuO_2$ mixtures is due to the Pu-239, which is the most abundant isotope in ThO_2+$RGPuO_2$ mixtures and primarily responsible for maintaining the fission chain (**Figure 6.10**). Furthermore, investigations into a simplified configuration using the BCC lattice (an infinite medium with a

reflective boundary condition, as presented in **Figure 6.5**) indicate that the ThO_2+$RGPuO_2$ mixture preserves a relatively higher average fission-to-capture ratio during burnup, which also contributes to increasing the cycle length and subsequently the burnup (**Figure 6.11**).

For the 87% Th with 13% $^{233}UO_2$ fuel mixture, the keff behavior results from rapid burning of the initial U-233, and it does not generate more fissionable material. It is also clear that increasing the initial fissile content in ThO_2+$WGPuO_2$ and (Th+^{233}U)O_2 fuel mixtures may help to increase the cycle length, for example, 80%ThO_2+20%$WGPuO_2$ and (85%Th+15%^{233}U)O2 mixtures retain their criticality at 46 GWd/ton and 45 GWd/ton, respectively. However, increasing the fissile content of the latter fuels increased the BOC reactivity, but this issue can be resolved by introducing a certain amount of burnable absorbents to the TRISO particles as a reactivity control method. Concerning the ThO_2+UO_2 (20%) fuel, both suggested mixtures achieve greater discharge burnup than with the UO_2 fuel (38 GWd/ton and 42 GWd/ton for the 86% UO_2 and 90% UO_2 fuels, respectively), but including Th-232 in the fuel mixture requires more of the U-235 fissile isotope to at least retain the same discharge burnup.

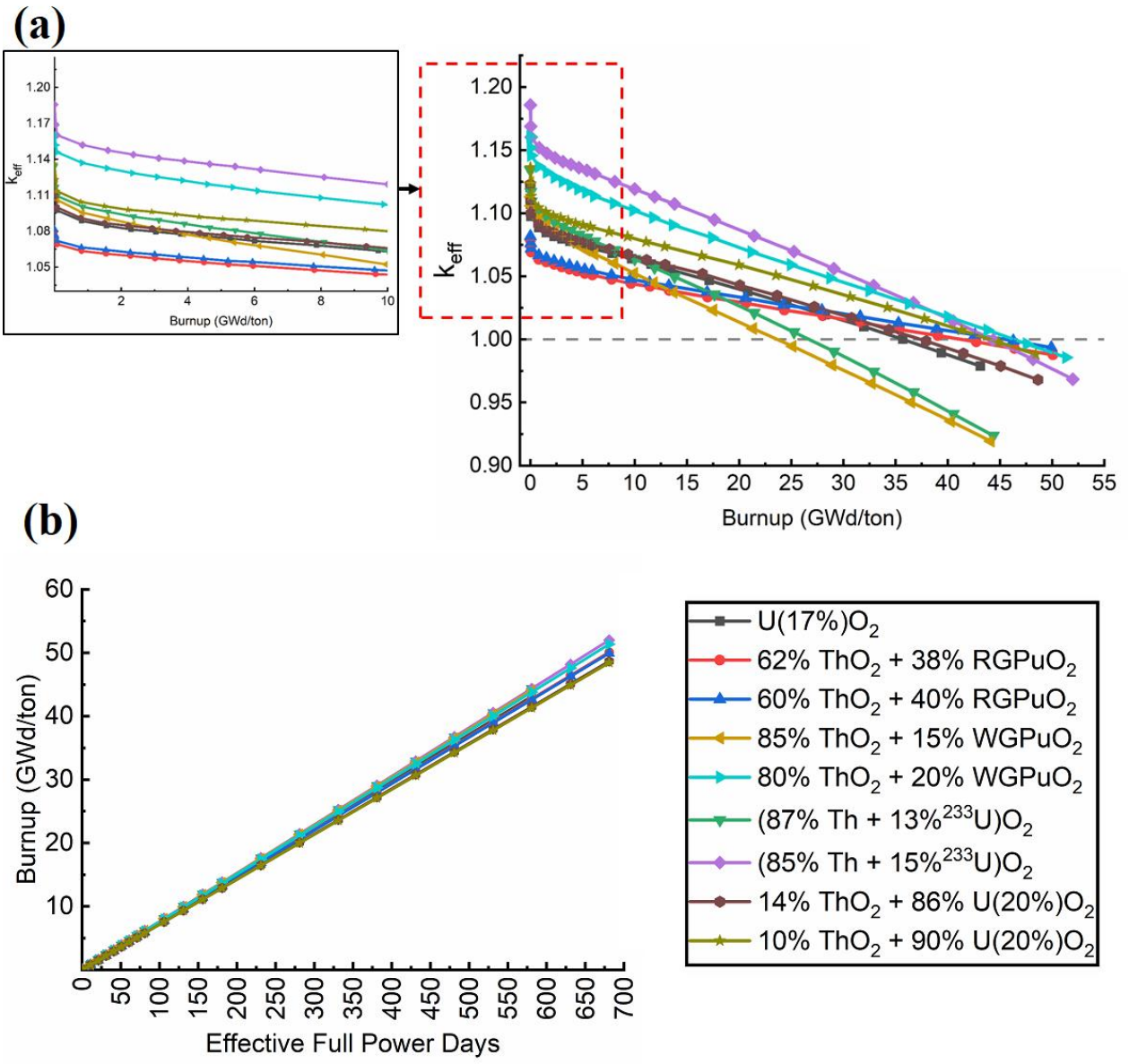

Figure 6. 9. (a) Dependence of keff on the burnup for different fuel mixtures, (b) burnup as a function of effective full power days.

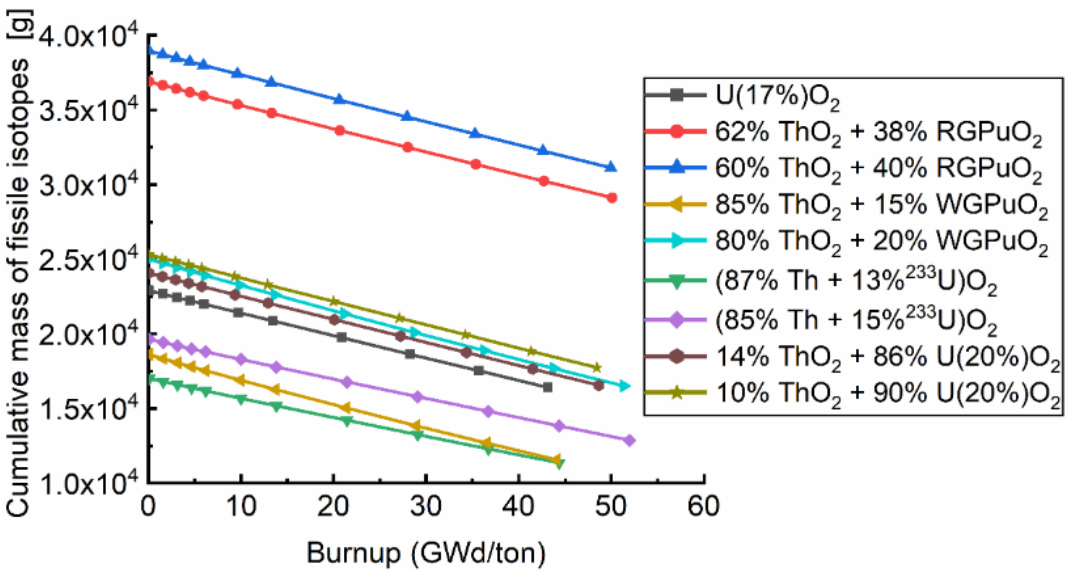

Figure 6. 10. Burnup-dependent variation of the accumulated masses of fissile isotopes (U-233, U-235, Pu-239, and Pu-241).

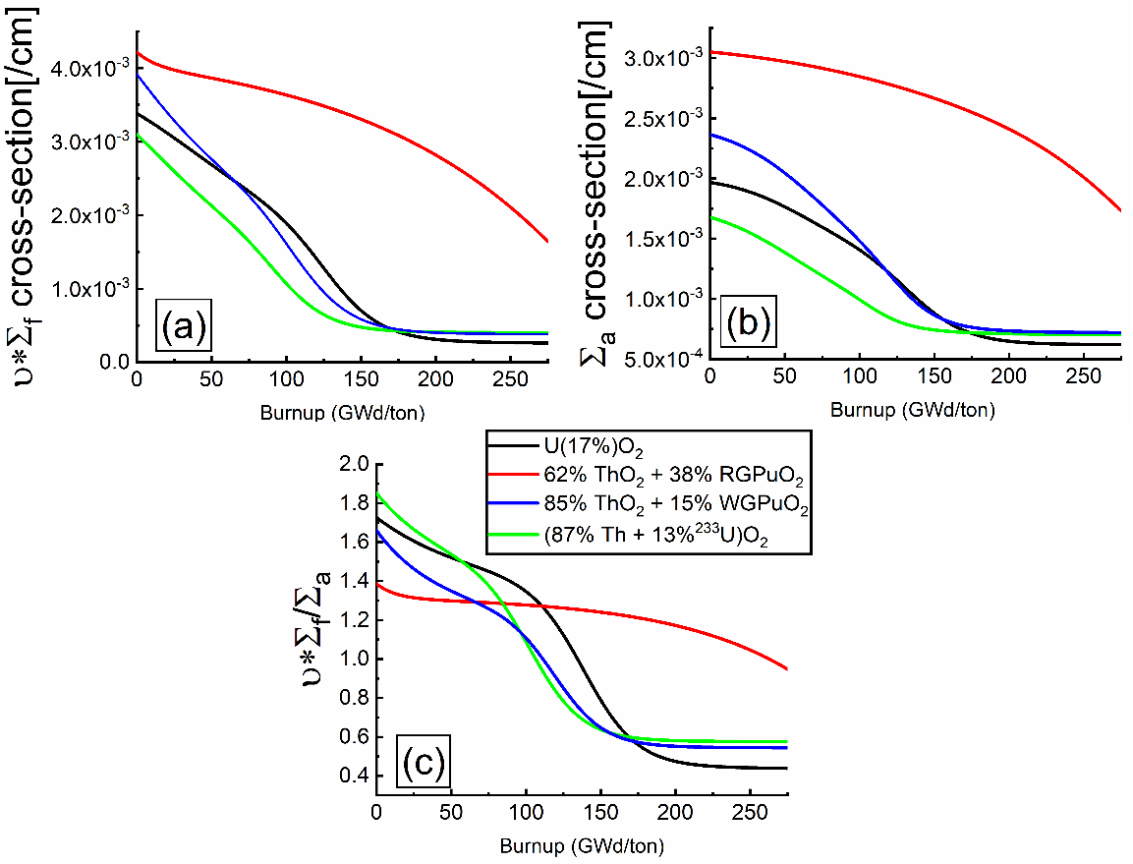

Figure 6. 11. Burnup-dependent macroscopic (a) nu* fission cross-sections, (b) absorption cross-sections, and (c) fission-to-capture ratios in a simplified configuration using a BCC lattice.

Depleted fuel and the evolution of masses

In this subsection, a comparative analysis of the evolution of the mass concentrations of uranium and plutonium isotopes is provided to determine how much of these materials are created or depleted for each fuel mixture as a function of burnup. The results of this are shown in **Figure 6.12**.

As expected, the production of Pu-239 increased with burnup in UO_2 fuel. For ThO_2+$RGPuO_2$ fuel, however, the mass of Pu-239 and Pu-241 decreased by almost 26% and 2%, respectively, mainly due to the fission process and the absence of U-238. The mass of Pu-238 decreased by 5%. In addition, due to neutron capture in the Th-232, the mass of U-233 increases with burnup, albeit only by a small amount.

As with ThO_2+$RGPuO_2$ fuels, the mass of Pu-239 in ThO_2+$WGPuO_2$ fuels decreased by 45% due to it being burned. This fuel, on the other hand, exhibited different behaviors, because the mass of the other plutonium isotopes increased after the reactor was started. As a result, the production of Pu-240 (approximately 289.5 barns) leads to greater absorption of neutrons and thus decreases core reactivity during burnup. However, in the ThO_2+$WGPuO_2$ cases, a lower Pu-239 content is required to achieve keff ≈ keff [UO_2] at BOC, resulting in a higher fertile load of Th-232 and greater U-233 production than with ThO_2+$RGPuO_2$ fuels, although this increase in U-233 content is insufficient to preserve constant reactivity during burnup. The most significant observation in all ThO_2+PuO_2 cases concerns how the concentration of Pu-239 decreases with burnup due to fission after the absorption of neutrons, while the concentration of Pu-293 increases with other UO_2 fuels, which is important from a non-proliferation point of view.

Figure 6.12 also indicates that there is a degeneration in U-233 for (Th+^{233}U)O_2 mixtures because it is the main fissile isotope. In addition, the production of Pu-239 and other plutonium isotopes in this kind of fuel is virtually non-existent, because plutonium and U-238 are initially absent in the mixture.

The burnup analysis shows that plutonium buildup is much lower in ThO_2+UO_2(20%) cores than it is in the UO_2 core due to the lower proportion of U-238 in these fuels and greater U-235 enrichment. Conversely, the total mass actinide inventory in ThO_2+UO_2 (20%) mixtures is much higher than with other candidate mixtures, and it increases as UO_2 content increases (**Figure 6.13**). For U-233 production, ThO_2+UO_2 (20%) mixtures produce less because of the lower fertile load.

Table 6.6 compares the actinides mass inventory of various spent fuels at 43.13 GWd/ton (EOC of UO_2 case). According to the burnup prediction, the concentration of neptunium isotopes in the spent UO_2 fuel, followed by the ThO_2+UO_2 (20%) fuels, was considerably higher than with the other investigated fuel mixtures. This difference can be attributed to the presence of UO_2. The decrease in the ThO_2+UO_2 (20%) mixtures is due to the longer time it takes Th-232 to produce U-237 and U-239 isotopes, which in turn produce Np-237 and Np-239 isotopes through beta decay [156].

Frequently the existence of both americium and curium isotopes, mainly Am-243 and Cm-244, in Pu-based fuels and thus ThO_2+PuO_2 mixtures is a concern. The neutron capture in Am-243 and the subsequent decay of Am-244 are the primary sources of Cm-244. The formation of Am-243 is caused by the neutron capture of Pu-242 and the subsequent decay of Pu-243. Mixing Th-232 and Pu may therefore slightly reduce the formation of americium and curium isotopic compositions in spent fuels. Cm-244 has an 18-year half-life before decaying to Pu-240, while Am-243 has a 7,370-year half-life before decaying to Pu-239 [124].

Actinides are formed in far lower concentrations in the (Th+^{233}U)O_2 mixtures than in other mixtures, thus minimizing the radiotoxicity of spent fuel. However, certain radionuclides, such as Protactinium (Pa-233 with a half-life of 27 days) and U-232 (a gamma emitter), may have long-term radiological effects [157].

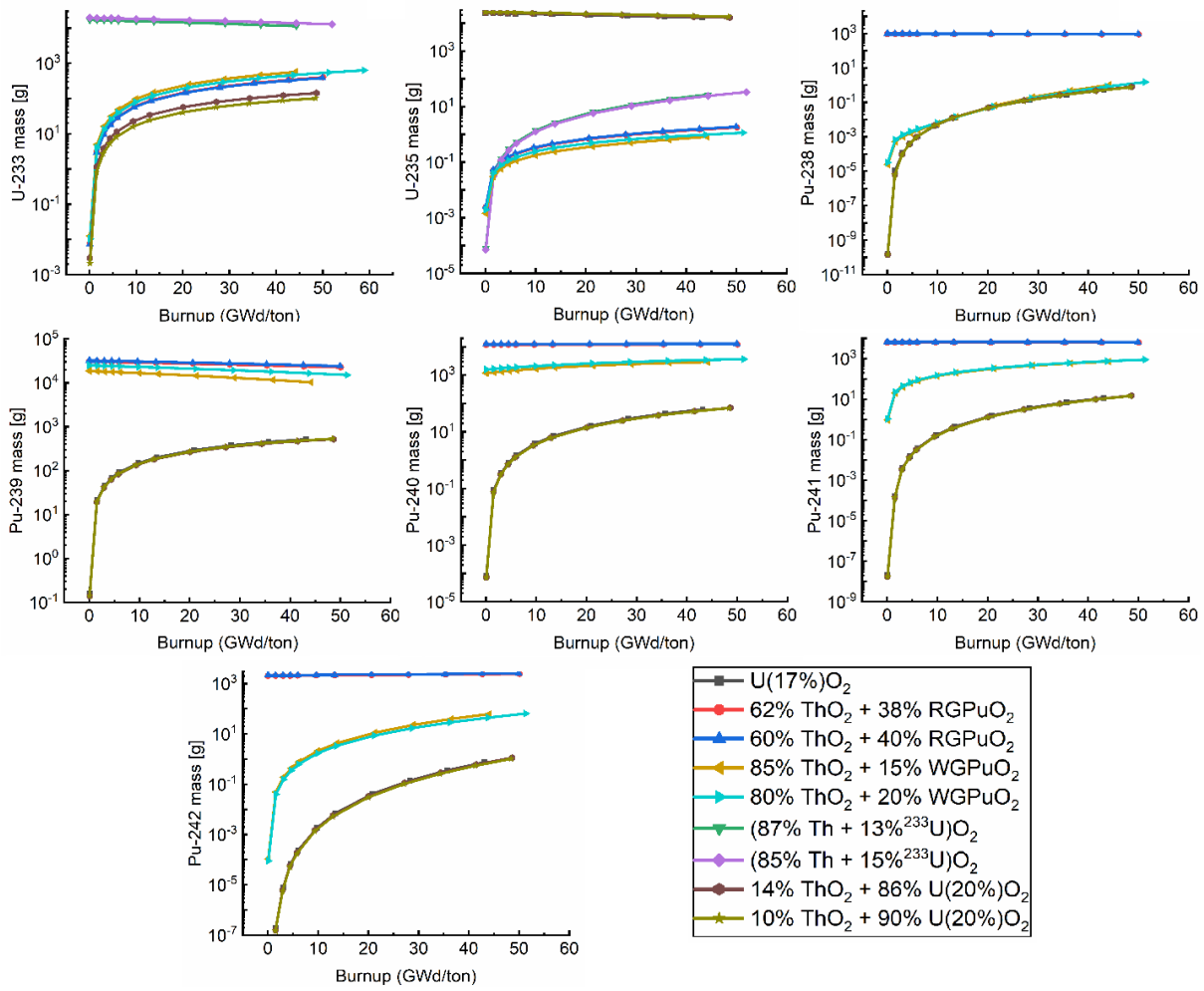

Figure 6. 12. Isotopic depletion and heavy metal utilization in HTR-10 core fueled with the suggested mixtures. The y-axis represents the mass densities on a log $_{(10)}$ scale.

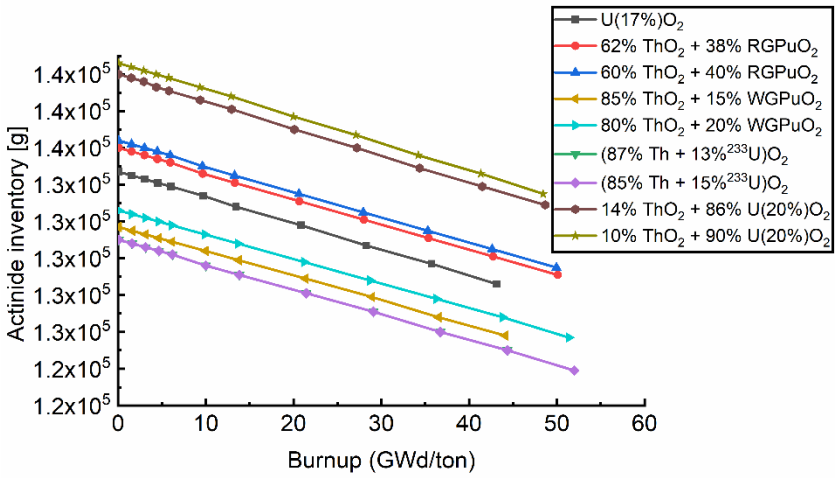

Figure 6. 13. Evolution of heavy metal inventories of fuel with burnup.

Table 6. 6. Comparison of mass inventory of actinides in different spent fuels (burnup = 43.13 GWd/ton).

Nuclide	Fuel type mass [g]								
	UO_2	38%RGPu	40%RGPu	15%WGPu	20%WGPu	13%^{233}U	15%^{233}U	86%UO_2	90%UO_2
Th-231	6.479E-08	8.109E-04	7.789E-04	1.155E-03	1.002E-03	9.152E-04	8.266E-04	1.301E-04	9.168E-05
Th-232	2.792E-05	8.379E+04	8.133E+04	1.112E+05	1.055E+05	1.130E+05	1.105E+05	1.940E+04	1.392E+04
Th-233	1.327E-11	1.559E-02	1.487E-02	3.136E-02	2.315E-02	4.287E-02	3.588E-02	6.452E-03	4.522E-03
Th-234	1.648E-06	9.538E-14	9.978E-14	-	-	-	-	1.419E-06	1.492E-06
Pa-231	-	-	-	-	-	2.798E-01	2.615E-01	-	-
Pa-232	2.019E-08	9.441E-05	8.722E-05	2.493E-04	1.636E-04	2.539E-04	2.024E-04	3.042E-05	2.064E-05
Pa-233	3.680E-07	2.704E+01	2.580E+01	5.413E+01	4.008E+01	7.397E+01	6.201E+01	1.117E+01	7.832E+00
U-232	-	-	-	-	-	3.780E-02	3.205E-02	-	-
U-233	-	3.391E+02	3.252E+02	5.720E+02	4.631E+02	1.133E+04	1.381E+04	1.228E+02	8.734E+01
U-234	3.664E-02	1.460E+01	1.498E+01	1.049E+01	6.519E+00	5.480E+02	5.582E+02	2.463E+00	1.687E+00
U-235	1.588E+04	1.485E+00	1.564E+00	8.245E-01	9.760E-01	2.707E+01	2.430E+01	1.705E+04	1.826E+04
U-236	1.115E+03	1.988E+00	2.096E+00	3.720E-01	4.437E-01	7.895E-01	5.912E-01	1.121E+03	1.128E+03
U-237	4.059E-01	8.771E-04	9.134E-04	1.796E-04	1.868E-04	-	-	3.987E-01	3.901E-01
U-238	1.111E+05	6.419E-03	6.741E-03	7.231E-05	5.368E-05	-	-	9.565E+04	1.006E+05
U-239	3.350E-02	4.529E-09	4.704E-09	-	-	-	-	2.972E-02	2.976E-02
U-240	-	6.870E-14	6.415E-14	-	-	-	-	-	-
Np-235	2.167E-09	1.990E-10	2.002E-10	-	-	1.337E-11	8.746E-12	2.085E-09	2.022E-09
Np-236	9.589E-07	1.018E-07	1.075E-07	2.652E-09	2.944E-09	1.050E-10	7.148E-11	9.535E-07	9.404E-07
Np-237	1.133E+01	5.761E-01	6.101E-01	2.257E-02	2.474E-02	-	-	1.114E+01	1.096E+01
Np-238	9.125E-03	2.280E-04	2.330E-04	1.658E-05	1.348E-05	-	-	8.527E-03	7.990E-03
Np-239	4.838E+00	1.028E-04	1.056E-04	1.396E-06	9.374E-07	-	-	4.293E+00	4.298E+00
Pu-236	8.937E-08	-	-	-	-	2.506E-11	1.607E-11	8.708E-08	8.473E-08
Pu-237	1.008E-07	3.296E-05	3.436E-05	-	-	5.035E-12	2.856E-12	8.883E-08	9.106E-08
Pu-238	5.152E-01	8.920E+02	9.441E+02	1.022E+00	8.320E-01	-	-	4.836E-01	4.560E-01
Pu-239	5.155E+02	2.370E+04	2.539E+04	1.028E+04	1.647E+04	-	-	4.679E+02	4.784E+02
Pu-240	6.177E+01	1.216E+04	1.282E+04	2.920E+03	3.465E+03	-	-	5.353E+01	5.235E+01
Pu-241	1.155E+01	6.192E+03	6.536E+03	7.137E+02	7.479E+02	-	-	9.859E+00	9.440E+00
Pu-242	7.568E-01	2.375E+03	2.484E+03	6.237E+01	4.439E+01	-	-	6.078E-01	5.482E-01
Pu-243	-	7.172E-02	7.326E-02	-	-	-	-	-	-
Pu-244	-	2.763E-03	2.748E-03	-	-	-	-	-	-
Am-241	-	4.285E+02	4.545E+02	2.250E+01	2.467E+01	-	-	-	-
Am-242	-	1.902E+00	2.004E+00	8.678E-02	9.233E-02	-	-	-	-
Am-243	-	1.192E+02	1.224E+02	1.551E+00	1.002E+00	-	-	-	-
Am-244	-	1.191E-02	1.200E-02	-	-	-	-	-	-
Cm-241	-	2.841E-07	2.834E-07	2.331E-08	1.689E-08	-	-	-	-
Cm-242	-	1.972E+01	1.988E+01	1.713E+00	1.331E+00	-	-	-	-
Cm-243	-	7.976E-02	7.872E-02	7.036E-03	4.477E-03	-	-	-	-

Cm-244	-	7.301E+00	7.382E+00	6.046E-02	3.404E-02	-	-	-	-

Fission product poisons

Fission product poisons are nuclei with large absorption cross-sections and a considerable capacity to capture neutrons without leading to the fission process. Xe-135 and Sm-149 are the most significant poisons (2,700,000 barns and 42,000 barns, respectively) that affect the safety of the reactor due to their ability to extract neutrons from the reactor, so they will have an impact on reactivity [107, 158]**.**

Figure 6.14 shows the variation in the Xe-135 mass for each fuel mixture with burnup. It can be seen that the Xe-135 mass increases in the beginning until it reaches a peak and then stays constant during burnup. Due to its large absorption cross-section, Xe-135 plays a critical role in overall reactivity insertion in the reactor core. Furthermore, the delayed accumulation of Xe-135 resulting from Iodine-135 beta decay makes it difficult to control the reactor during shutdown [159]. As shown in the figure, the equilibrium concentration of Xe-135 is much higher with the ThO_2+ PuO_2 (i.e. RGPu and WGPu) cores than the UO_2 and (Th+^{233}U)O_2 cores. The reason for this is that the yield of fission products affecting reactor poisoning during operation is significantly higher for plutonium than it is for U-235 and U-233 [160].

Figure 6.14 also shows the accumulation of Sm-149. The main source for this in a reactor is the neodymium-149 decay chain. As shown in the figure, Sm-149 shows a similar behavior to Xe-135 for all the examined fuel mixtures, with the only major difference being that due to its longer half-life and lower absorption cross-section, it slowly decreases before reaching equilibrium. In addition, because it is a stable isotope, it does not degrade over time.

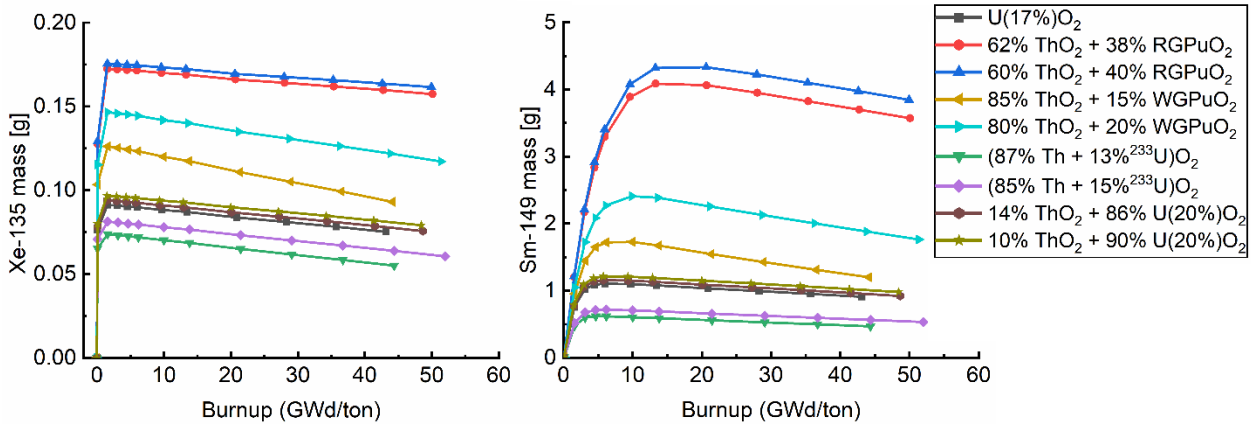

Figure 6. 14. Variation of Xe-135 and Sm-149 masses with burnup.

Neutron energy spectrum

Figure 6.15 shows the calculated neutron spectra averaged over the whole reactor, for the considered thorium-based fuels and the nominal fuel. The spectra were calculated using the F4 tally in MCNP6, while the Monte Carlo source normalization factor was estimated as described in reference. [33] In general, the neutron spectrum in the reactor depends upon the neutron absorption cross-section of the mixture used in the fuel and the average neutrons produced per fission. A couple of features are noteworthy in the figure. Firstly, all the ThO_2+PuO_2 mixtures, but especially ThO_2+$RGPuO_2$, maintain lower thermal neutron spectra than UO_2 for all the considered burnups. In addition, the ThO_2+$RGPuO_2$ spectra have two near-identical peaks that differ from one of the UO_2 fuels. This is due to the greater cross-sections and lower resonance peaks of Pu-239 and Pu-240, which largely determine the spectrum shape, especially in the thermal region [124] The second feature that can be observed is that (Th+^{233}U)O_2 fuel spectra are harder than UO_2 because the thermal neutron absorption cross-section of Th-232 (7.35 barns) is higher than that of U-238 (2.683 barns) [33]. This behavior can also be seen with ThO_2+UO_2 fuels.

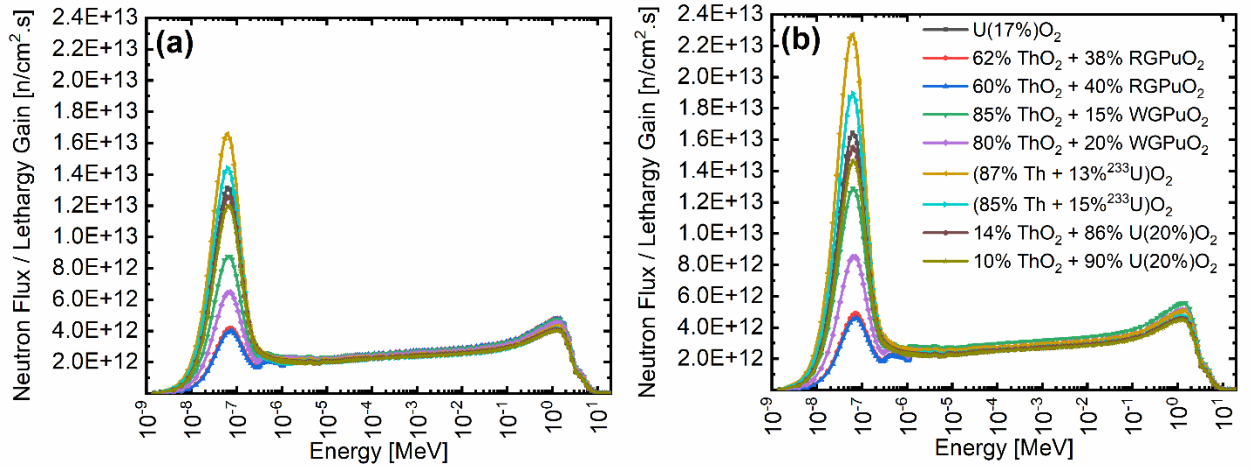

Figure 6. 15. Comparison of core-average neutron spectra at BOC (a) and the end of cycle (b) of the UO_2 fuel.

Effective delayed neutron fraction

The effective delayed neutron fraction (β_{eff}) is one of the most critical parameters for use in feasibility calculations because it is the kinetics parameter that determines the time-dependent reaction of the reactor. More specifically, the delayed neutrons provide the ability to control the rate at which power increases in the reactor. If there were only prompt neutrons, control over the

reactor would not be possible due to rapid power changes causing damage over a short period of operation [158]. In addition, a lower β_{eff} value means that the reactor's kinetic response is quicker. In contrast, a higher β_{eff} value implies that the core will have a slower response [161].

Figure 6.16 illustrates the effective delayed neutron fraction for the investigated mixtures. As can be seen from this figure, the β_{eff} values for cores fueled with plutonium or U-233 are lower than for those fueled with U-235. More precisely, the fractions decreased on average by 56%, 58%, and 51% for ThO_2+$WGPuO_2$, (Th+^{233}U)O_2, and ThO_2+$RGPuO_2$ cores, respectively. Obviously, the lower delayed neutron fraction of Pu-239 and U-233 (260 pcm and 310 pcm, respectively), when compared to that of U-235 (650 pcm) [24, 162], is the main reason for why these cores have lower β_{effs} than UO_2 core. The addition of Th-232, which is pure fertile material, also contributes to the reduced β_{eff} values. However, as reported by Zuhair et al.[163], the incorporation of Th-232 into plutonium cores increases both the prompt neutron lifetime and the generation time, so it may improve reactor safety. For the ThO_2+UO_2 cores, the introduction of ThO_2 also decreased the fractions of β_{eff} by 1%. This decrease occurs despite Th-232 having a higher delayed neutron yield than U-238 because it has a slightly lower fission rate contribution in the thermal spectrum. On the other hand, U-238 has a relatively high delayed neutron yield, and this, along with its significant fission contribution, increases β_{eff} for UO_2 cores [164].

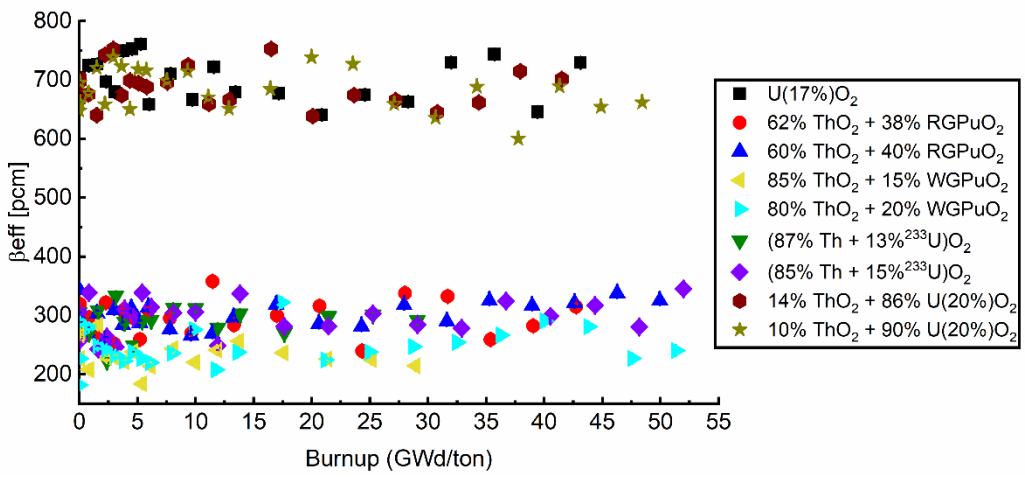

Figure 6. 16. Variation in the β_{eff} fractions with burnup for the examined fuel mixtures.

Temperature reactivity coefficients

The change in the temperature of the reactor leads to a change in the system's reactivity, and this is defined as the reactivity temperature coefficient. In reality, the temperature of the reactor

does not change uniformly, because an increase in reactor power will first cause an increase in the temperature of the fuel before affecting other components of the reactor such as the moderator. The two widely considered reactivity coefficients are therefore the fuel temperature coefficient (FTC), which relates to the change in reactivity according to a change in fuel temperature, and the moderator temperature coefficient (MTC), which relates to the change in reactivity according to the temperature of the moderator. In general, the temperature coefficients are assessed as follows: If there is negative feedback, an increase or decrease in temperature would have the opposite effect on reactivity. In contrast, positive feedback occurs when an increase or decrease in temperature has the same effect on reactivity [86, 165].

Figure 6.17 depicts the FTC values when a change in temperature ($\Delta T \approx 300$ K) is applied (i.e. 293.6 K up to 600 K). The first thing that can be gleaned from this figure is that all the FTCs are negative. Using $WGPuO_2$ or U-233, however, results in less negative coefficients, and this is attributable to the following:

For ThO_2+$WGPuO_2$ cores, as the fuel temperature rises, fewer neutrons are captured in the capture resonances of Pu-240 and Pu-242 (initially absent), as well as the lower resonance absorption integral of Th-232, resulting in less negative FTCs. The feedback parameters for ThO_2+$RGPuO_2$ are significantly more negative than those for ThO_2+$WGPuO_2$ due to the presence of a large amount of Pu-240 in ThO2+$RGPuO_2$ mixtures.

For the (Th+^{233}U)O_2 cores, this effect can be attributed to the lower resonance absorption integral of Th-232 (about three times lower than that of U-238) [90]. What is more, with a high U-233 content, the FTC values became less negative. Therefore, to obtain more negative FTCs, the resonance absorption must be increased by adding a resonant nucleus [162].

In the case of ThO_2+UO_2(20%) cores, adding Th-232 and increasing the enrichment of U-235 displaces the U-238, significantly decreasing the epithermal resonance absorption of neutrons in the fuel and, as a result, the FTC's of ThO_2+UO_2(20%) cores are less than those of UO_2 cores.

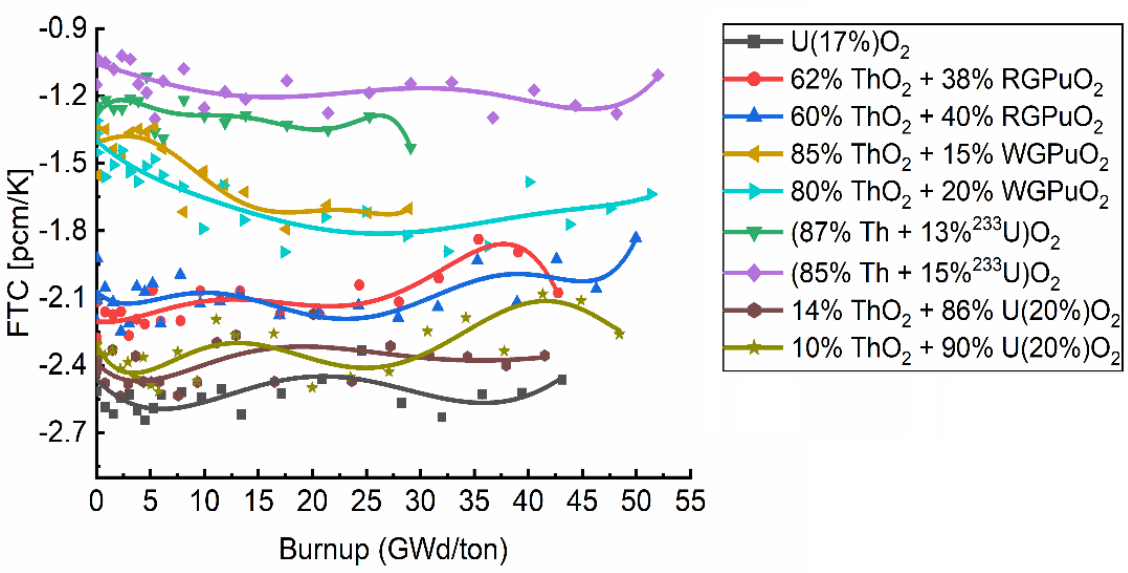

Figure 6. 17. Fitted curves: Fuel temperature coefficients as a function of burnup. The 1σ statistical uncertainty bars range from around 0.0004– 0.0030 pcm of the figure values.

Similarly, the MTCs of the investigated fuel mixtures were determined by changing the temperature in the moderator region (Graphite) from 293.6 K to 600 K while keeping the temperature in the fuel and other regions unchanged. The MTCs are all negative across the temperature range, as shown in **Figure 6.18**. Furthermore, with increased fuel burnup and combustion of fissionable nuclide, the coefficient curves show a more negative trend for most of the investigated fuel mixtures.

Compared to the UO_2 core, the moderator coefficients for ThO_2+PuO_2 cores are also less negative. According to Richards et al [166], less negative MTC values for Th+Pu systems may be due to an upshift of the thermalized Maxwellian neutron flux spectrum into the thermal fission and capture resonances of Pu-239 and Pu-241 (at 0.3 eV) as moderator temperature increases. Yet, as depicted in the figure, a higher fertile Th-232 content and decreased Pu loading result in slightly more negative MTCs (e.g. ThO_2+$WGPuO_2$).

Unlike FTCs, MTC values are high in (Th+^{233}U)O_2 cores. This is because increasing the fuel temperature decreases the number of neutrons that get thermalized (i.e. the resonance escape probability), while increasing the moderator temperature just changes the neutron velocity and hence the flux. As a result, more neutrons are absorbed in Th-232. This behavior is also observed with ThO_2+UO_2(20%) cores. Furthermore, the capture resonance integrals for U-233 and U-235 are nearly equal [24].

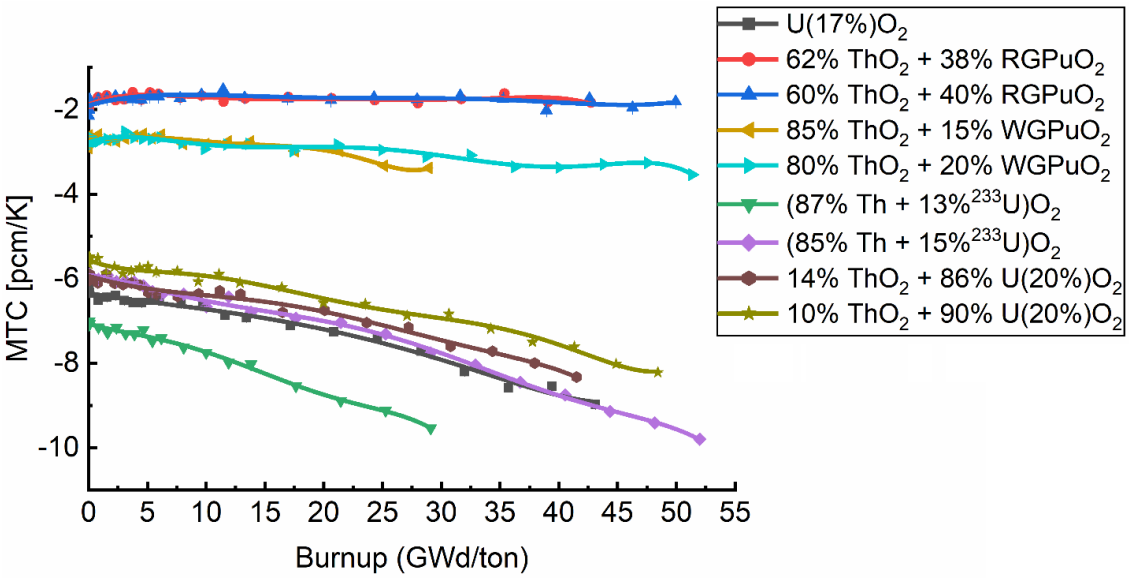

Figure 6. 18. Fitted curves: Moderator temperature coefficients as a function of burnup. The 1σ statistical uncertainty bars range from around 0.0004– 0.0030 pcm.

6.1.7. Summary and conclusions

PBR-HTRs use spherical fuel pebbles packed into a dynamic pebble-bed consisting of TRISO-coated UO_2 fuel kernels with different U-235 enrichments. Moreover, numerous HTGRs have also been tested to establish their ability to burn most fuel combinations including thorium fuel cycles and deep burning of minor actinides while preserving favorable safety characteristics. The main objective of this study was to investigate the potential utilization of alternative thorium-based fuels in HTR-10. The suggested fuel mixtures included in the analyses were 1) ThO_2+HALEU; 2) ThO_2+$RGPuO_2$; 3) ThO2+$WGPuO_2$; and 4) (Th + $^{233}U)O_2$. In this context, several scenarios were created to determine how the reactor would interact with different thorium contents in the proposed fuel mixtures. The analysis was then accompanied by determining reactor parameters, such as discharge burnup behavior, spent fuel composition, effective delayed neutron fractions, neutron spectra and temperature coefficients.

When comparing keff results, it was found that despite the fact that ThO_2+$RGPuO_2$ cores achieved lower keff values at BOC, they had the lowest descent over the irradiation period and deeper discharge burnups than UO_2, allowing for full plutonium fission and thus minimizing the proliferation danger in the use of this fuel. ThO_2+$WGPuO_2$ and (Th + $^{233}U)O_2$ cores, on the other hand, required more fissile materials to achieve deeper discharge burnup, even though they had higher keff values at BOC, therefore, this level would require the use of burnable absorbers for

reactor safety and control in order to prevent higher reactivities. Likewise, it was observed that mixing UO_2 with ThO_2 requires more U-235 enrichment and lower Th-232 content to achieve the same discharge burnup as it consumes and more fissile nuclides to maintain reactivity, especially (BOC).

From the perspective of plutonium disposition, the results show that thoria-based fuels have a lower Pu-239 inventory. This results from (i) the absence of U-238 in the ThO_2+PuO_2 fuels, thus breeding additional plutonium during irradiation; and (ii) the absence of plutonium in (Th+^{233}U)O_2. As a result, this study supports the possibility of incorporating ThO_2 into PBR cores, as well as its ability in burning stockpiled plutonium. The masses of the fission product poisons, on the other hand, indicate that the inventory of Xe-135 and Sm-149 products increased when using the ThO_2+PuO_2 fuels. This is because the yield of fission products affects reactor poisoning during operation, and this is significantly higher for plutonium when compared with U-235 and U-233.

The effective delayed neutron fraction is a major determinant of the temporal response of a reactor. The results showed that during burnup the ThO_2+PuO_2 and (Th+^{233}U)O_2 fuel mixtures have lower delayed neutron fractions than that of the UO_2 fuel. Therefore, greater attention would have to be taken during the operation of the core fueled by these mixtures, as they are likely to have a shorter reactor period and thus be more difficult to control.

Regarding the temperature coefficients, there were differences in the behaviors of the investigated fuel mixtures. It was found, for example, that ThO_2+WGPuO_2 and ThO_2+RGPuO_2 cores produced less negative values for the fuel and moderator temperature coefficients. With a high Pu content, they became even less negative. The values of the fuel temperature coefficients in (Th+^{233}U)O_2 cores, on the other hand, are strongly influenced by the resonance absorption integral of Th-232 and the U-233 content in the fuel. The moderator temperature coefficients, however, were found to be more negative, and even more negative than the UO_2 core. As a result, the overall temperature coefficients of reactivity (fuel plus moderator) are likely to become sufficiently negative. These sufficiently negative coefficients may help compensate for the reduced controllability of (Th+^{233}U)O_2 cores due to lower delayed neutron fractions.

6.2. The use of burnable absorbers integrated into TRISO/QUADRISO particles as a reactivity control method in a pebble-bed HTR reactor fueled with (Th,^{233}U)O_2

Modified from a paper published in Nuclear Engineering and Design.

DOI: https://doi.org/10.1016/j.nucengdes.2021.111476

Ouadie Kabach [1,*], Abdelouahed Chetaine [1], Abdelfettah Benchrif [2], Hamid Amsil [1, 2]

[1)] Nuclear Reactor and Nuclear Security Group Energy Centre, Department of Physics, FSR, Mohammed V University, Rabat, Morocco

[2)] National Centre of Nuclear Energy Sciences and Techniques, Rabat, Morocco

*Corresponding author e-mail address: ouadie.kabach10@gmail.com; ouadie_kabach@um5.ac.ma

Abstract: There are two HTGR concepts, one based on a pebble-bed core, and the other is a prismatic core. One of the key differences between the pebble-bed core and the prismatic core is the complexity of applying the seed-blanket (SB) concept to the internal production of U-233 from Th-232 in order to extend the cycle length of the reactor. Actually, an enhancement of the operating cycle length in the pebble-bed reactors fueled with (Th,^{233}U)O_2 can be reached by using high U-233 ratios, but these ratios could result in high excess reactivity at the BOC. In order to suppress the excess reactivity phenomenon at the early stage of the fuel cycle, to flatten the reactivity curve as a function of time, a new reactivity control method has been investigated by incorporating burnable absorbers into the fuel particles. This purpose is set up by introducing two varieties of BAs, including Gadolinia and Erbia, either as a homogeneous mixture with the fuel kernel in the TRISO particles or as an additional layer next to the fuel kernel producing the quadruple isotropic (QUADRISO) particles. The present work aims at characterizing the effect of these different loading patterns on some neutronic parameters that define the reactor core under BOC conditions as well as during burnup. In this attempt, the nominal UO_2 (17 wt.% U-235) fueled core was used as a reference, while the other models adopt (Th,^{233}U)O_2 (17 wt.% U-233) fuel with Gadolinia and/or Erbia with different loading patterns. The calculation results show that excess reactivity can be compensated during the early stages of core life and flattened during the cycle by adding Erbia doped with a few ppm of Gadolinia to the TRISO/QUADRISO particles. In these updated configurations, the new core life achieved is approximately 678 Effective Full Power Days (EFPDs), equivalent to 52.5 GWd/t on a single-batch discharge burnup. This means that from the

core fueled with UO_2, which has a core life of 537 EFPDs (37 GWd/ton), an average period of 141 EFPDs is extended.

Keywords: Pebble-bed reactor; Thorium fuel; Burnable absorber; TRISO, QUADRISO.

6.2.1. Introduction

Natural thorium has only one fertile isotope, which is Thorium-232, Th-232 can absorb thermal neutrons and subsequent nuclear reactions create fissile U-233. A sustainable Th-^{233}U cycle can be achieved under optimized breeding conditions, but the thorium cycle requires a trigger fissile, which can be based on uranium or plutonium fuel cycle (e.g. U-233, U-235, Pu-239, or Pu-241). U-233 is advantageous as a fissile nucleus in a reactor for several reasons. First, it has the smallest value of α (the capture-to-fission ratio) among the fissile nuclides, which is responsible for the highest thermal value of η (ratio of neutrons produced per neutrons absorbed in the fuel of each fission reaction) [138, 157]. Second, xenon and samarium yields are about 20% lower from U-233 fission relative to other fissionable isotopes, which decreases the number of absorptions of non-fuel [1, 160]. In addition, the use of the Th-^{233}U mixture significantly decreases the amount of highly radioactive transuranic isotopes which is for instance produced from U-235 or Pu-239 fissions and that may mitigate some of the existing long-term disposal concerns [167]. Historically, Th-^{233}U fuel mixture has been investigated for different types of reactors, including light water reactors (LWRs) [168], pressurized heavy water reactors (PHWRs) [169], breeder reactors (BRs) [170], molten salt reactors (MSRs), and accelerator-driven reactors (ADRs) [113], as well as high-temperature gas-cooled reactors (HTGRs).

The HTGRs appear as good candidates for the next generation of nuclear reactors due to them having many advantages. In particular, solid graphite, with its large specific heat capacity, acts as a moderator by delaying the transient temperature in the event of an accident, while neutronically inert helium acts as a coolant. Regarding fuel type, the HTGR employs two main types: prismatic block and pebble-bed types. Both types are moderated by graphite and fueled by TRISO particles. The refueling mode is one of the primary differences between a prismatic block and a pebble-bed HTGR core [171]. The latter design, which uses continuously moving pebbles, can be loaded randomly online during operation. According to the studies, thorium can be used in reactors in two ways: heterogeneously (seed-blanket) and homogeneously. However, optimal thorium use as nuclear fuel can be achieved in a heterogeneous configuration. The structured loading patterns of

prismatic block-type reactors can help in the implementation of the heterogeneous concept since thorium and the driver fuels can be separated. On the other hand, the heterogeneous concept is incompatible with continuously moving pebbles in the pebble-bed type (as if tennis ball-sized fuel spheres vertically traverse the core). This indicates that it might be difficult to achieve high discharge burnup with a sustaining Th-^{233}U system. Therefore, to avoid the highest descending sloop in effective multiplication factor (keff) caused by the rapid burning of the initial U-233 content, it is found that increasing the effective enrichment may efficiently increase keff, and therefore the discharged burnup. However, such an increase in the initial enrichment tends to significantly increase the reactivity at the BOC (see **Figure 6.19**). To address this problem, an effective burnable absorber (BA) must be loaded to manage the excess reactivity at the early stage of the cycle. It is also important to account for flattening the reactivity curve overtime or reducing excess reactivity during core life. Given the fact that a fixed BA is the only feasible way to reduce excess reactivity in helium-cooled HTGRs [172], there have been few studies on how to incorporate BAs into HTGRs published in the literature. Currently, two BA applications are being observed: QUADRISO fuel particle, and particle-type BA.

The QUADRISO fuel particle concept differs from the TRISO particle concept in that it includes an extra layer of BA next to the fuel kernel. Argonne National Laboratory has conducted many research studies on the QUADRISO concept [173, 136, 171, 174]. Their studies concentrated on thorium-plutonium fuel cycles, as well as transmute neptunium and plutonium fuel cycles and excess reactivity control in prismatic VHTR fuel blocks. The use of QUADRISO particles in a VHTR, according to the studies, can significantly reduce the initial excess reactivity and flatten the reactivity curve as compared to cases without a BA, as well as improve the homogeneity of the BA distribution.

Most studies on BA particles, which are spherical particles distributed uniformly in the fuel pebble [128], were carried out in a Once-Through-Then-Out (OTTO) refueled pebble-bed reactor to reduce the high axial power peaking factor when the reactor is refueled with fresh pebbles, as well as reactivity control [175, 176, 177]. Results in a pebble-bed HTGR suggested that using BA particles could help minimize reactivity swing and improve power density distribution [178]. However, using both QUADRISO and particle-type BA concepts will have an impact on fuel burnup performance, i.e. the target burnup would be reduced and higher enrichment will be needed to achieve the same discharge burnup [178, 179, 180].

The objective of this study is to manage excess reactivity at the early stage of the cycle and suppress the reactivity swing during burnup time, while also improving discharge burnup as much as possible, when it compared to the UO_2 case, by finding the optimum BA implementation scheme. These were conducted by utilizing two BAs, Gadolinia and Erbia, mixed in the TRISO or as an extra layer in QUADRISO particles fueled with (Th,^{233}U)O_2 fuel. Future studies, we will screen other potential absorbers for incorporation into TRISO/QUADRISO fuel particles or as particles-type BA, while also taking refueling schemes into account. In this article, the (Th,^{233}U)O_2 enrichment is 17 wt.% (U-233), and the three-dimensional HTR-10 reactor was designed using Monte Carlo MCNP6.2 code without any geometrical homogenization. Based on the desired goal, the calculation methods are described in the first part of this paper and the results are illustrated in the second part. The concepts for TRISO/QUADRISO fueled particles are shown in **Figure 6.20**. It should be noted that TRISO particle dimensions and all QUADRISO particle dimensions, except for the absorber layer, were kept constant between models.

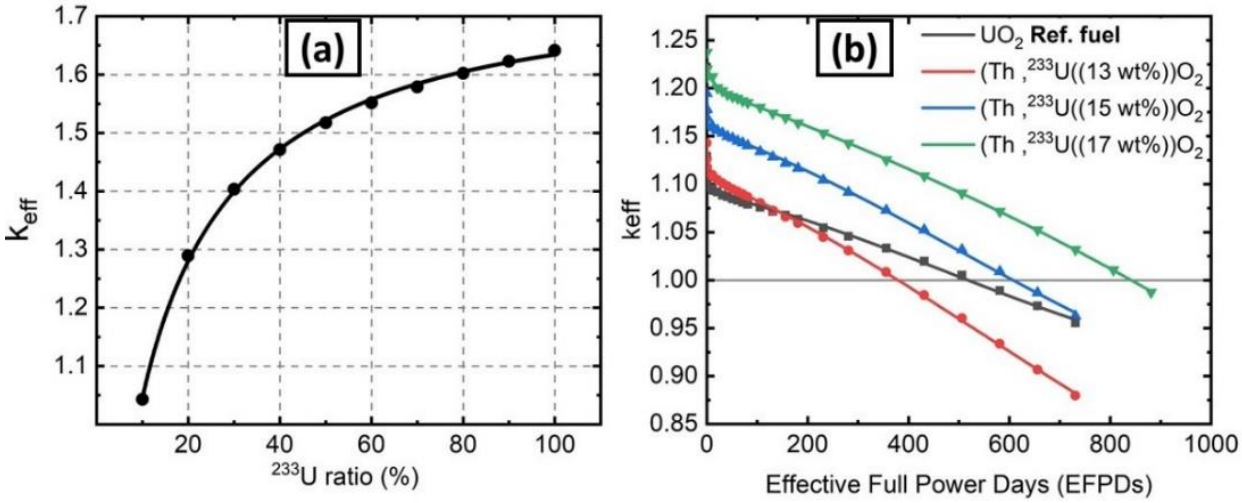

Figure 6. 19. (a) Multiplication factor as a function of U-233 ratio in (Th,^{233}U)O_2 fuel, (b) keff as a function of EFPDs for the (Th,^{233}U)O_2 with 13 wt.%, 15 wt.% and 17 wt.% U-233 compared to the UO_2 fuel.

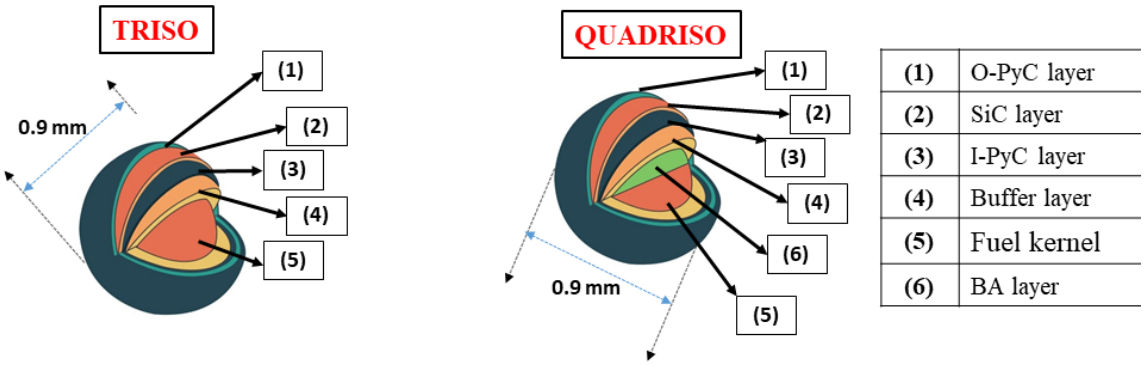

Figure 6. 20. Schematic of TRISO and QUADRISO particles [179].

6.2.2. Burnable absorbers selection

The period during which the reactor has sufficient over-reactivity to enable start-up with full power operation is generally determined by the amount of fuel material initially loaded into the reactor core. This amount will depend on the excess reactivity that reactor control mechanisms can properly compensate for (e.g. control rods). On the other hand, to increase the initial possible fuel load of the core, it is common to incorporate the core with materials characterized by high neutron absorption cross-sections (i.e. BA) which compensate for such excess reactivity in the early stages of core life by capturing neutrons to contribute to negligible negative reactivity later in core life. As a result, these BAs can nearly match the temporal behavior of excessive fuel reactivity as they decrease over the lifetime of the core, allowing for larger initial fuel inventories without a corresponding increase in control requirements [88].

In general, the selection of BAs is determined by their chemical, physical, and nuclear properties. i.e., absorption cross-section isotopes (**Figure 6.21**) and the composition of the main absorbing. Boron carbide (B_4C) and gadolinia (Gd_2O_3) are commonly used as BA materials in thermal reactors to control long-term reactivity. Materials containing nuclides with a relatively high microscopic absorption cross-section, such as cadmium, samarium, europium, dysprosium, erbium, and hafnium (Cd-113, Sm-149, Eu-151, Dy-161, Dy-164, Er-167, and Hf-177), can be used as BA in addition to B_4C and Gd_2O_3 [181, 176, 182]. It was found, however, that HfO_2 produces a greater number of decay isotopes. CdO, Sm_2O_3, Gd_2C_3, and Gd_2O_3 were discovered to deplete quickly, while Er_2O_3, Eu_2O_3, and Dy_2O_3 deplete slowly [179].

Although the philosophy of using BAs in LWRs is well known, there are few approaches for using BAs in HTGRs since, as addressed in the introduction section, the only feasible way to

minimize excess reactivity is to use a fixed BA. Among these approaches are mixing the absorber with the fuel kernel (homogeneous mixture) in TRISO particles, applying the absorber as a thin layer in QUADRISO particles, or using fixed particle-type absorbers in the fuel pebbles.

For this study, we begin with two common BAs, Gadolinia and Erbia, which will be applied to TRISO and QUADRISO particles. Other potential absorbers will be examined in future studies for incorporation into TRISO/QUADRISO fuel particles or as particles-type BAs. In the calculations presented in this paper, the natural composition of each BA material was used; some of the physical properties of these materials are specified in the following sub-sections.

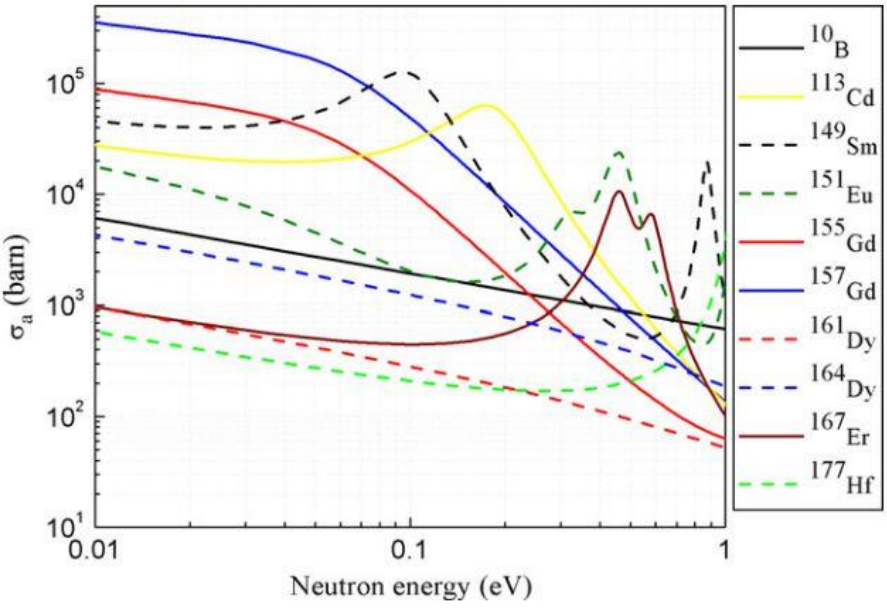

Figure 6. 21. Microscopic absorption cross-section of B-10, Cd-113, Sm-149, Eu-151, Gd-155, Gd-157, Dy-161, Dy-164, Er-167 and Hf-177 in the thermal energy range 0.01–1 eV [176].

Gadolinium

Gadolinium is generally used as gadolinium oxide (Gadolinia) or gadolinium carbide in the nuclear industry. Gadolinium has the largest thermal absorption cross-section compared to other BAs such as boron. However, only two gadolinium isotopes have extremely high thermal neutron absorption cross-sections among other isotopes i.e. Gd-155 and Gd-157 (see **Table 6.7**). The natural abundance of the Gd-155 equals 15%, while for Gd-157 is 16%. The neutron capture on Gd-155 and Gd-157 follows respectively the formation of Gd-156 and Gd-158 which are poor thermal neutron absorbers [90].

Erbium

There are six naturally occurring erbium isotopes: Er-162 (0.14%), Er-164 (1.61%), Er-166 (33.61%), Er-167 (22.93%), Er-168 (26.78%), and Er-170 (14.93%). Yet, Er-167 is the only strong thermal neutron absorber in this series of isotopes, but it is smaller compared to Gd-155 and Gd-157 as shown in **Figure 6.22**. Generally, erbium is used as erbium oxide (Erbia). Based on the literature review, Erbia has two advantages over Gadolinia when it is used as a BA in light water reactors: i) low neutron absorption cross-section results in a smooth redistribution of power when Erbia is consumed, and ii) depletes more slowly than gadolinium, thus providing reactivity control over extended cycle lengths [183].

Table 6. 7. Major properties of the selected BA materials [179, 184].

Absorber	Theoretical density (g/cm^3)	Molar mass (g/mol)	Macroscopic absorption cross-section of thermal neutron (cm^{-1})	Melting point (K)	Isotope(s) of interest
Gadolinia (Gd_2O_3)	7.4	362.5	1196	2612	Gd-155 Gd-157
Erbia (Er_2O_3)	8.64	382.5	4.2	2617	Er-167

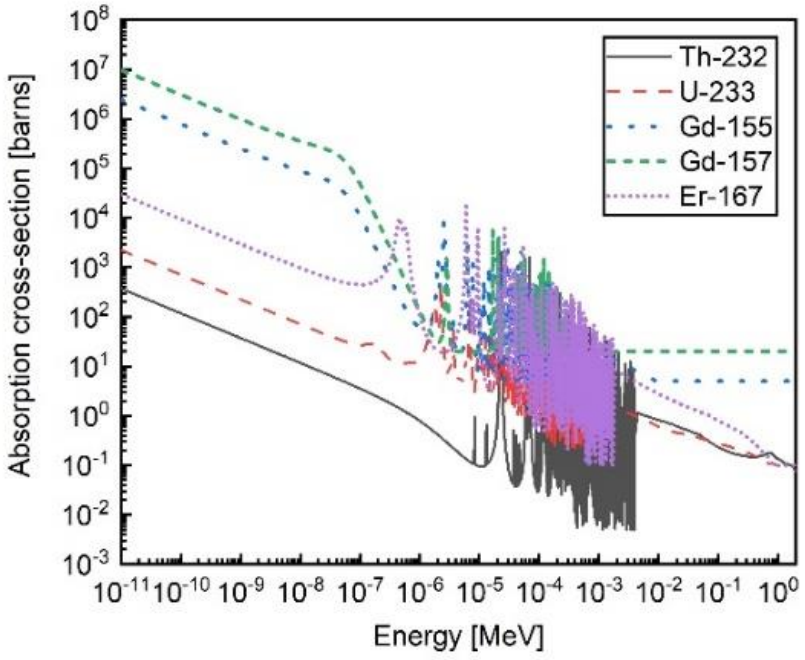

Figure 6. 22. Neutron absorption cross-sections of Th-232, U-233, Gd-155, Gd-157 and Er-167 according to the ENDF-B/VII library.

6.2.3. Results and discussions

Survey on the loading of the BAs in TRISO/QUADRISO particles

The general objective of this first section is to find optimal configurations for the use of two absorbers in the proposed two forms of particles. In other words, we change the BA ratios (in TRISO) and BA layer thicknesses (in QUADRISO). The target is to suppress the excess reactivity at the BOC and achieve keff almost equivalent to the conventional HTR-10 fueled with UO_2. The mixture densities were calculated using **Equation (6.1)**. The results of this first investigation will be graphically presented in the following sub-sections and the dashed line in the figures represents keff at BOC for the UO_2 (17 wt.%) fueled reactor.

$$\rho_{mix} = \left(\frac{W_{(Th,^{233}U)O_2}}{\rho_{(Th,^{233}U)O_2}} + \frac{W_{BA}}{\rho_{BA}} \right)^{-1} \quad (6.1)$$

where:

ρ_{mix}: The density of the mixture $(Th, {}^{233}U)O_2$ with BA; $W_{(Th,^{233}U)O_2}$: the weight percent of $(Th, {}^{233}U)O_2$ fuel; W_{BA}: The weight percent of BA; ρ_{BA}: The density of BA.

Keff sensitivity to BA ratio in TRISO particles

Figure 6.23 illustrates the dependency of keff on the BA ratio for both proposed absorbents. For Gadolinia, it can be observed that keff decreases by a factor of 2.96% on average for every 0.01% increase in the Gadolinia ratio. As for Erbia, it can be noted that with each 0.8% increase in the Erbia ratio, keff decreases by an average factor of 2.66%. This was expected due to the high absorption cross-section of gadolinium isotopes. Besides, by adding approximately 0.03% or 3.0% of Gadolinia or Erbia, respectively, to the $(Th,^{233}U)O_2$ fuel, we can attain keff fit with that of UO_2 fuel at BOC.

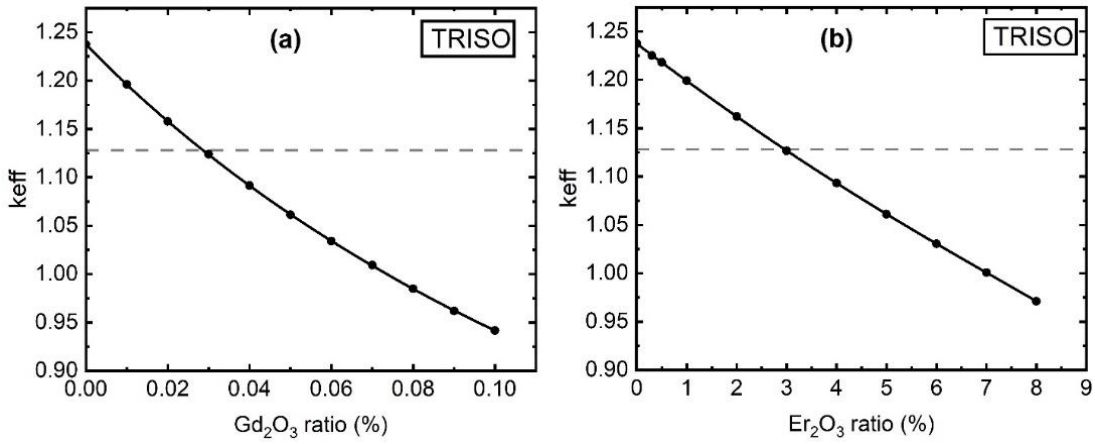

Figure 6. 23. Variation of the multiplication factor with BA ratio in the (Th,^{233}U)O_2 fuel, (a) with Gadolinia (b) with Erbia. The dashed line represents keff at BOC for the UO2 (17 wt.%) fueled reactor.

Keff sensitivity to BA thickness in QUADRISO particles

Figure 6.24 depicts keff 's reliance on the BA layer thickness in QUADRISO particles. For Gadolinia, it can be observed that for every 0.01 μm increase in the thickness of the Gadolinia layer keff decreases by 2.29% on average. For Erbia, it can be seen that keff decreases by 2.60% on average for every 0.8 μm increase in the thickness of the Erbia layer. Moreover, by covering the fuel by approximately 0.03 μm or 3.0 μm of Gadolinia or Erbia, respectively, we can also obtain keff comparable to that of UO_2 fuel at BOC.

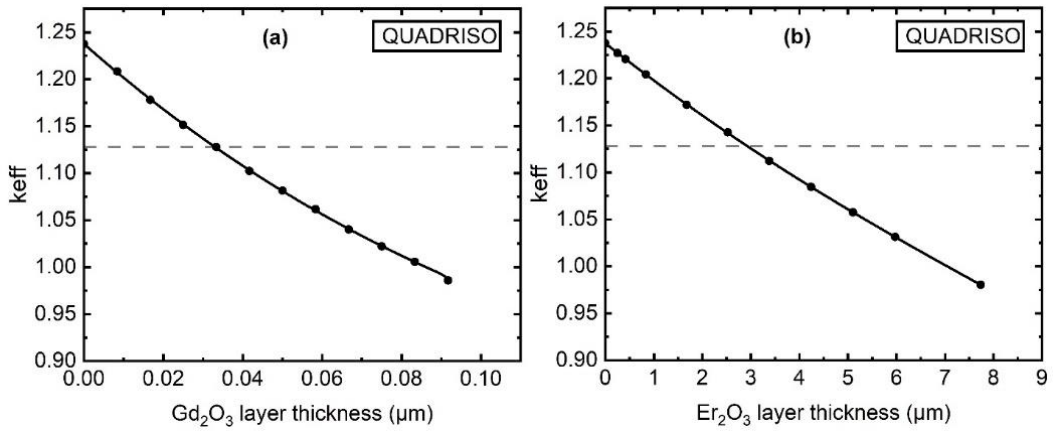

Figure 6. 24. Variation of the multiplication factor for the (Th,^{233}U)O_2 fuel as a function of BA thickness, (a) with Gadolinia (b) with Erbia. The dashed line represents keff at BOC for the UO2 (17 wt.%) fueled reactor.

So far, in this first assessment, we can conclude that reactivity can be suppressed at BOC by introducing a certain amount of BAs.

Investigation of the variation of keff with burnup

This sub-section is interested in investigating the keff results as a function of fuel burnup with BA materials and compared to the reference. In other words, we aimed at investigating the degree of ability of the use of BAs to suppress the reactivity as a function of burnup. The investigations were carried out on a single-batch discharge burnup at a power density of 10 MW. The first assessment was conducted using the ratios/thicknesses as described in the previous section, and yet these data may change as our next objectives are:

1. Suppress the reactor's excess reactivity throughout the cycle, this means that the BAs should burn slowly and release the reactivity gradually;
2. The multiplication factor results (as a function of burnup) should not significantly exceed the target multiplication factor set as keff for UO_2 fuel at the beginning of the reactor life **Equation (6.2)**;
3. Maximize the discharge burnup as far as possible.

Figure 6.25 illustrates the variation of the keff and reactivity with burnup (EFPDs) for the selected ratios/thicknesses and **Table 6.8** shows the predicted reactor operational lifetime of the suggested configurations. The calculated reactivities (ρ) can be defined as follows.

$$\rho = \rho_0 - \rho_i = \left(1 - \frac{1}{k_{eff,\,UO2_{BOC}}}\right) - \left(1 - \frac{1}{k_{eff,(Th,^{233}U)O2}}\right) \qquad (6.2)$$

where $k_{eff,UO2_{BOC}}$ and $k_{eff,(Th,^{233}U)O2}$ are the effective multiplication factor for the UO_2 fuel at BOC and (Th,^{233}U)O_2 fuel (with and without the BAs).

Figure 6.25 shows that the estimated average cycle length of the (Th,^{233}U)O_2 fuel-loaded HTR-10 reactor without any BA was almost 1.56 times higher than that of the standard UO_2 loaded core, approximately is about 537 EFPDs. In the depletion calculation for the BA-loaded (Th,^{233}U)O_2 configurations mentioned in the previous sub-section, it is clear that Gadolinia and Erbia, either in TRISO or QUDRISO particles, give desirable results at BOC. However, it is observed that Gadolinia exhibits a very fast depletion rate (**Figure 6.26**) which leads to a sudden increase in keff, but the associated discharge burnup is quite significant (**Table 6.8**). Contrariwise, Erbia can flatten

the reactivity curve during the cycle, but the discharge burnup is very small compared to the (Th,^{233}U)O_2 fuel without any BA since Erbia's ratio/thickness lowered the fuel load (**Figure 6.27**). Furthermore, the comparison between TRISO and QUADRISO loaded with materials indicates the same pattern as they have the same consumption rate for all isotopes in both the Gadolinia and Erbia configurations. Indeed, these behaviors are due to the differences in absorption cross-sections of both absorbers. Gadolinia's high thermal cross-section enables it to suppress BOC's initial high reactivity at a lower ratio/thickness, but its consumption is very fast, so Gadolinia cannot play a further active role in the regulation of reactivity during burnup. On the other hand, due to higher residual activity during burnup, Erbia's function becomes more significant.

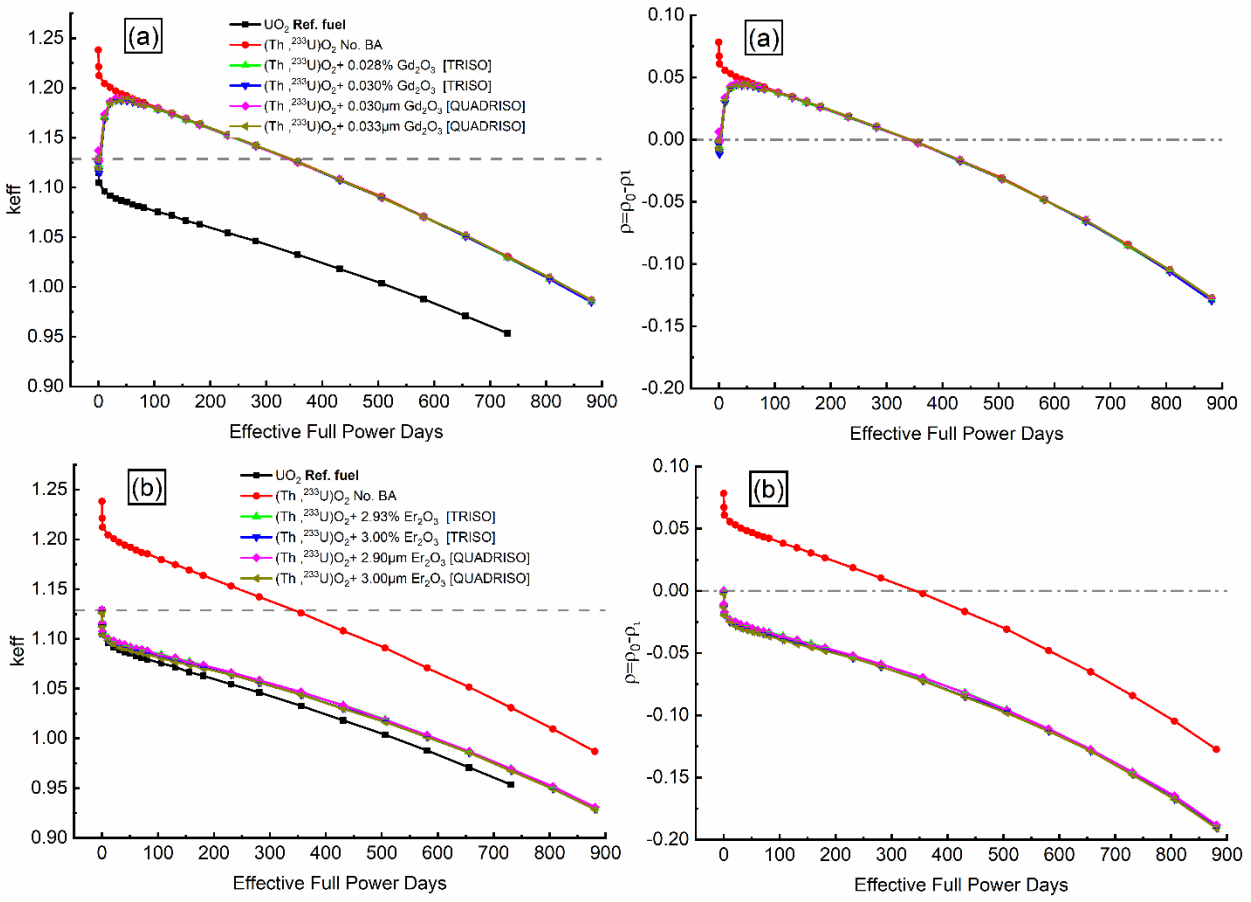

Figure 6. 25. Multiplication factor and reactivity profiles versus EFPDs for (a) Gadolinia (b) Erbia configurations. The dashed line in the figures represents keff at BOC for the UO_2 fuel.

Table 6. 8. Predicted reactor operational lifetime for various Gadolinia and Erbia configurations.

Fuel Description	Cycle length (Day)	Difference between the Ref. fuel (+Day)
UO2 Ref. fuel	537	-
(Th,^{233}U)O_2, No BA	837	300
Gadolinia configurations		
(Th,^{233}U)O_2 +0.028% [TRISO]	836	299
(Th,^{233}U)O_2 +0.030% [TRISO]	832	295
(Th,^{233}U)O_2 +0.030 μm [QUADRISO]	842	305
(Th,^{233}U)O_2 +0.033 μm [QUADRISO]	864	327
Erbia configurations		
(Th,^{233}U)O_2 +2.93% [TRISO]	604	67
(Th,^{233}U)O_2 +3.00% [TRISO]	597	60
(Th,^{233}U)O_2 +2.90 μm [QUADRISO]	605	68
(Th,^{233}U)O_2 +3.00 μm [QUADRISO]	594	57

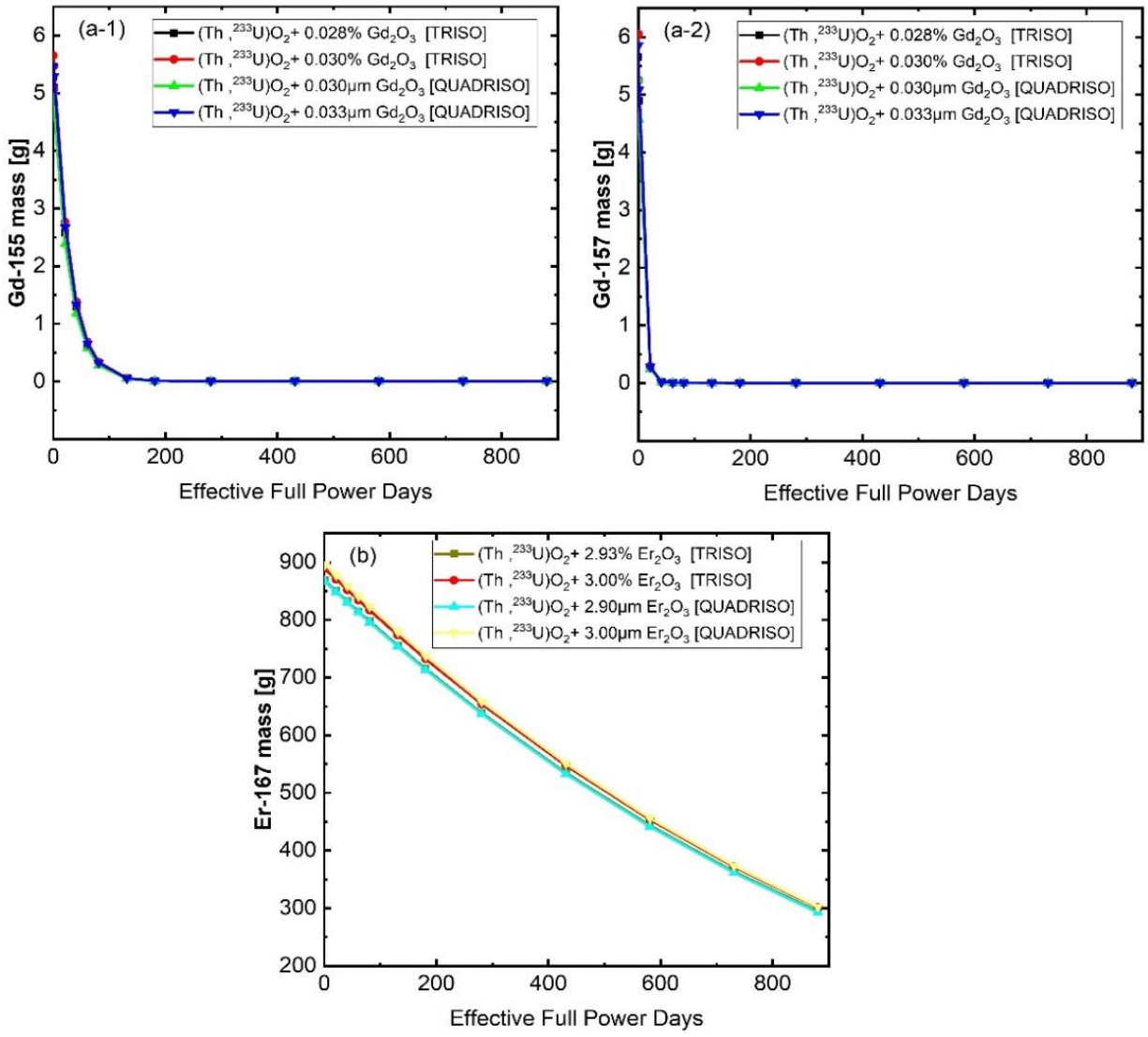

Figure 6. 26. Isotopic inventories of gadolinium and erbium as a function of burnup in (a) Gadolinia (b) Erbia configurations, respectively (**most vital isotopes**).

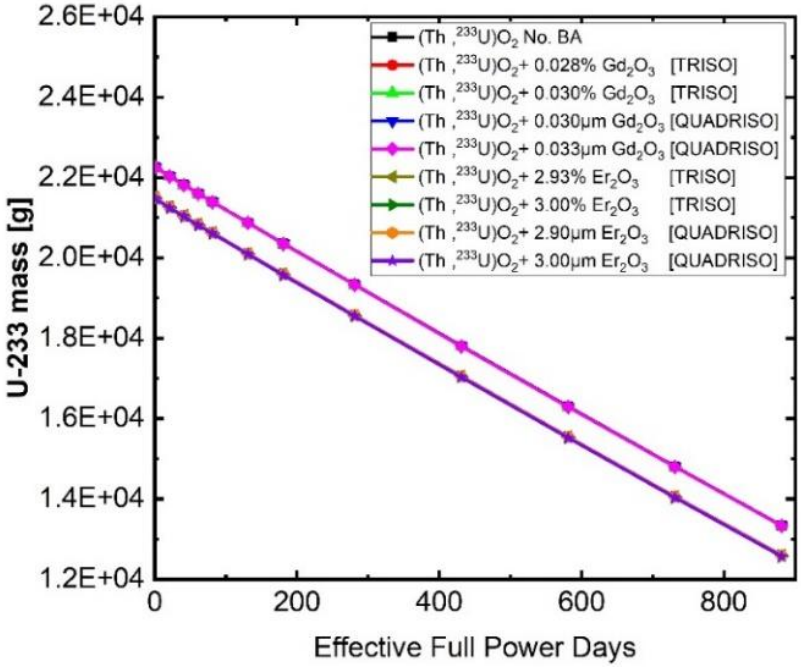

Figure 6. 27. Variation of U-233 mass with EFPDs in Gadolinia and Erbia configurations.

Based on the findings discussed above and with a view to achieving a better and more feasible configuration of BA materials in the HTR-10 reactor, it seems appropriate to use Erbia (with a reduced ratio/thickness) doped with a few ppm of Gadolinia in TRISO or QUADRISO to enhance the life cycle. Actually, Gadolinia suppresses the initial high reactivity and during the cycle, Erbia helps regulate the reactivity. New optimized configurations are specified for this purpose; the Erbia ratio varies from 1.6 % to 2.0 % in the TRISO configuration, while the Erbia thickness varies from 1.6 μm to 2.0 μm in the QUADRISO configuration. In these patterns, Erbia ratio and thickness are loaded as much as possible to suppress excess reactivity near the middle of life (MOL i.e. first 50 days) and the 10000 ppm of gadolinia has been introduced to suppress the reactivity around BOC. The analysis results are presented in **Figure 6.28**.

As expected, the figure shows that a very smooth and stable reactivity curve is obtained when Erbia and Gadolinia are mixed into TRISO or QUADRISO particles. Besides, increasing the ratio or thickness of Erbia resulted in an improvement in the stability of the reactivity curve. However, due to the decrease in fuel loading and the high remaining Er-167 content at the end of life, there is still a deficit in fuel burnup efficiency as compared to (Th,^{233}U)O_2 (**Figures 6.29** and **6.30)**. Even so, the new core lifetime is about 52.5 GWd/ton, and this corresponds to 678 EFPDs, which means that an extension of 141 EFPDs (**Table 6.9)** is obtained from one with UO_2 of 17 wt.%

enrichment, whose core lifetime is 537 EFPDs (37 GWd/ton). Yet, in order to address the decrease in fuel burnup efficiency in (Th,^{233}U)O_2 mixture, Tran and Liem proposed adding fertile material that acts as BA in the early stages of the cycle. Later, the material is transmuted to fissile fuel to maximize neutron economy (e.g., Pa-231 to U-233), and the fuel burnup performance improves as a result. According to the findings, burnup performance improved by around 37% as compared to the fuel without Pa-231[138].

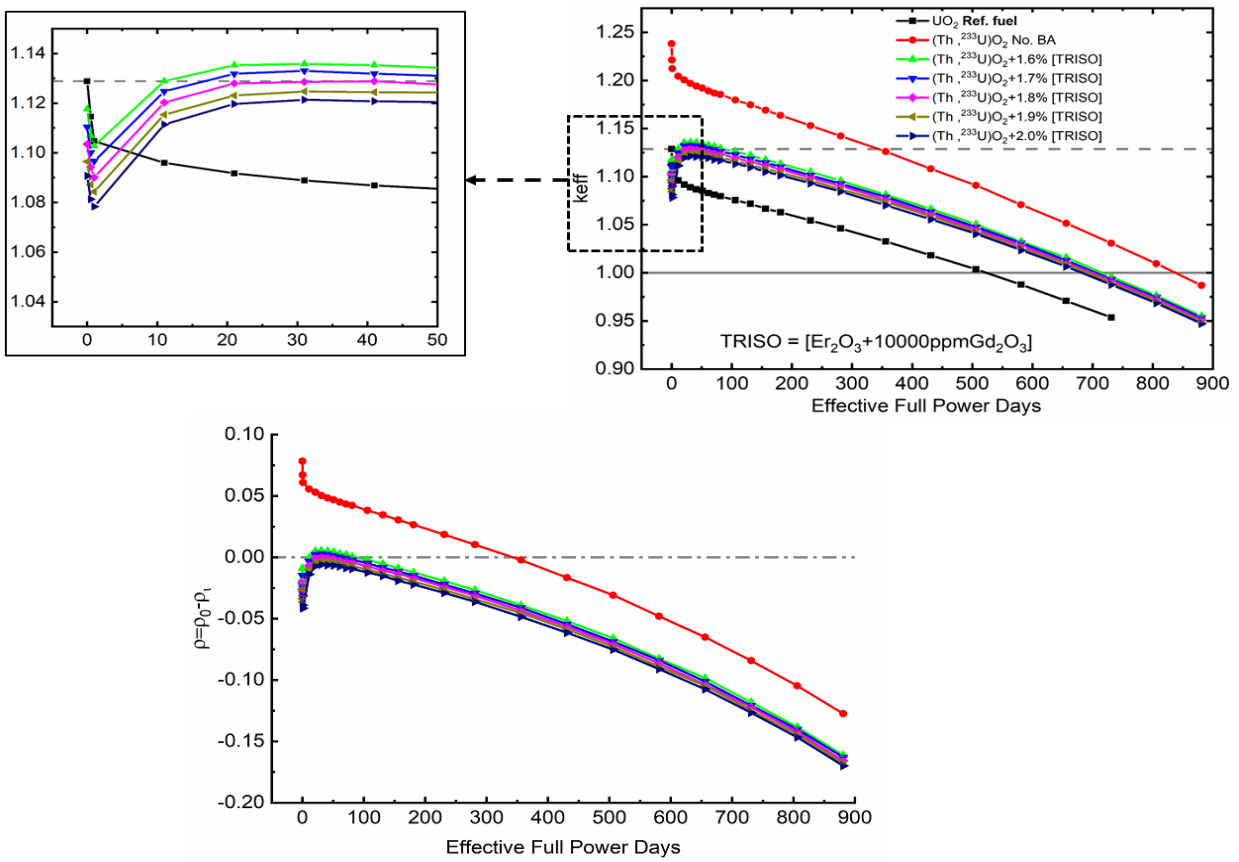

(a) TRISO configurations.

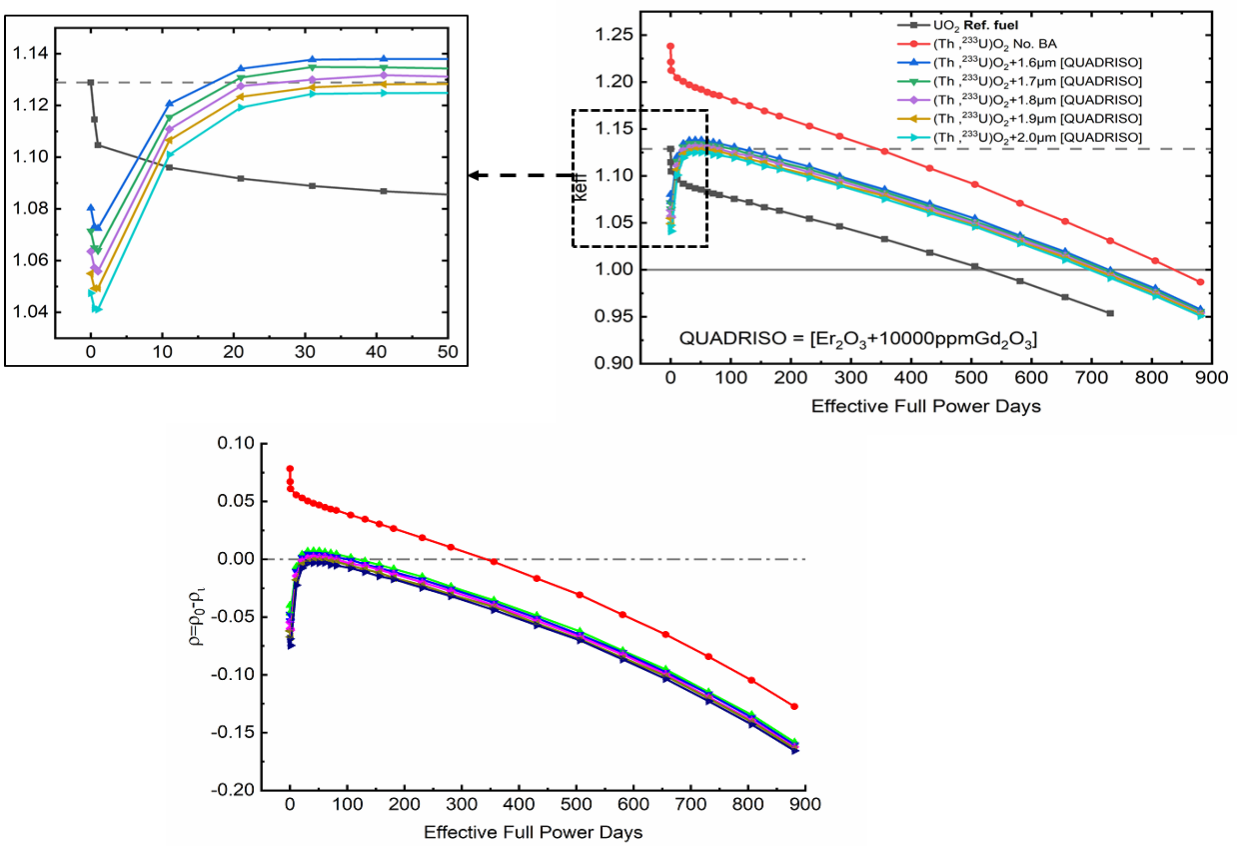

(b) QUADRISO configurations.

Figure 6. 28. Multiplication factor as a function of burnup time for various [Er_2O_3+ 10000 pm Gd_2O_3] configurations in (a) TRISO and (b) QUADRISO particles.

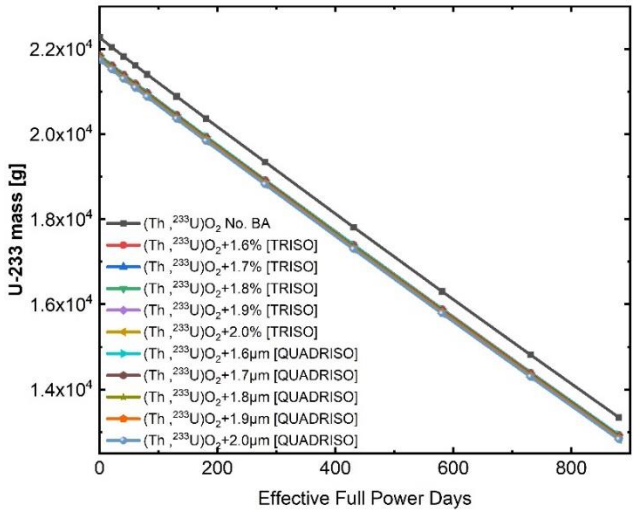

Figure 6. 29. Variation of U-233 mass for various [Er_2O_3+ 10000 ppm Gd_2O_3] configurations.

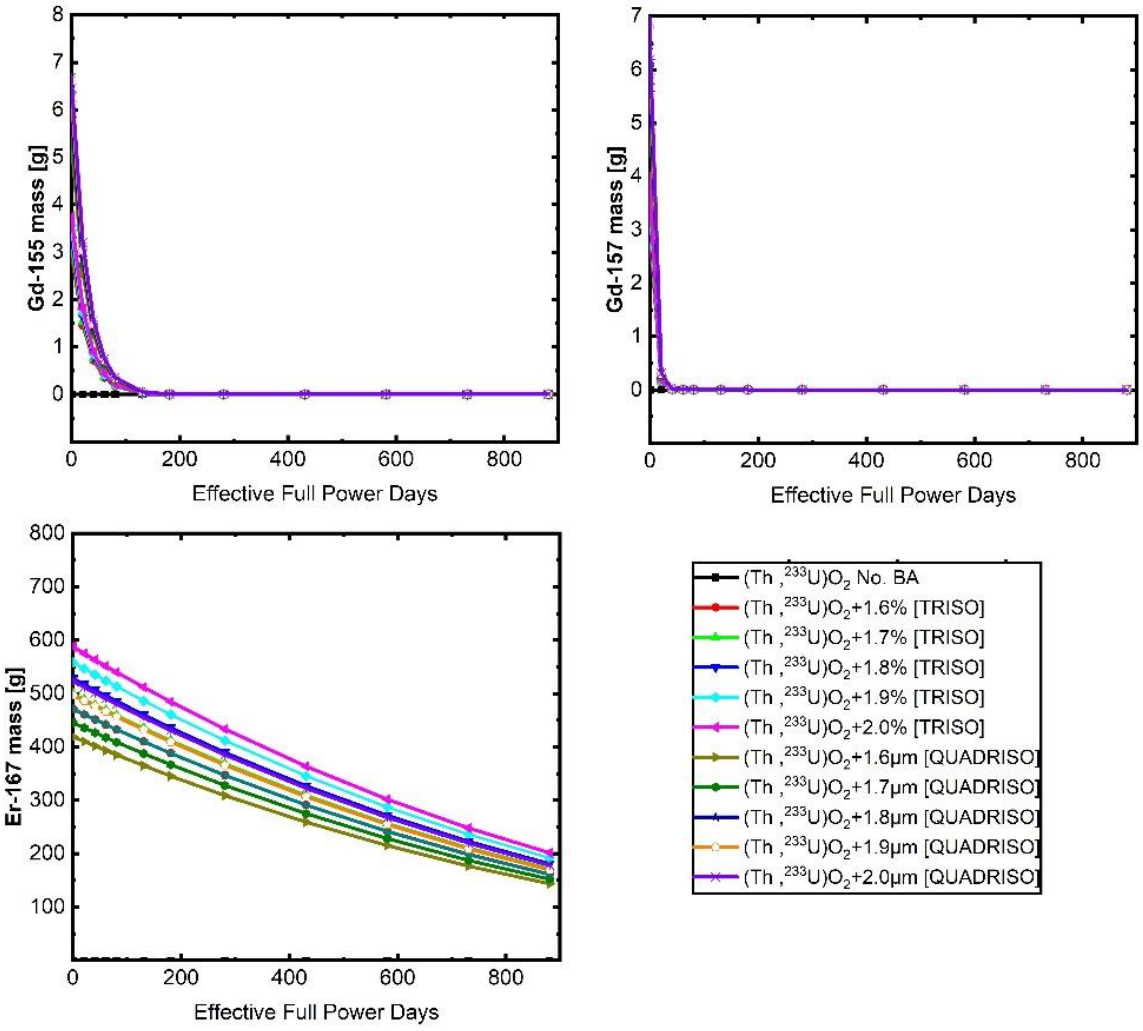

Figure 6. 30. Depletion performance of gadolinium and erbium isotopes for various [Er2O3+ 10000 ppm Gd2O3] configurations.

Table 6. 9. Predicted reactor operational lifetime for various [Er_2O_3+ 10000 ppm Gd_2O_3] configurations.

Fuel Description	Cycle length (Day)	Difference between the Ref. fuel (+Day)
UO_2 Ref. fuel	537	-
(Th,^{233}U)O_2 No BA	837	300
[Er_2O_3+ 10000 ppm Gd_2O_3] configurations		
(Th,^{233}U)O_2 +1.6% [TRISO]	701	164
(Th,^{233}U)O_2 +1.7% [TRISO]	690	153
(Th,^{233}U)O_2 +1.8% [TRISO]	680	143
(Th,^{233}U)O_2 +1.9% [TRISO]	670	133
(Th,^{233}U)O_2 +2.0% [TRISO]	659	122
(Th,^{233}U)O_2 +1.6 μm [QUADRISO]	692	155

(Th,^{233}U)O_2 +1.7 μm [QUADRISO]	687	150
(Th,^{233}U)O_2 +1.8 μm [QUADRISO]	675	138
(Th,^{233}U)O_2 +1.9 μm [QUADRISO]	664	127
(Th,^{233}U)O_2 +2.0 μm [QUADRISO]	660	123
Average	**678**	**141**

Power distribution

In order to determine the differences between operating a core with and without burnable absorbers, a characterization of the power density profiles needs to be provided. However, since the repeated structure was used to fill the BCC lattices into the cylindrical core geometry, the core was assumed to consist of five axial fuel layers or five radial fuel cortices, with each fuel layer or cortex having the same volume (i.e. equivalent to 1/5 of the core volume) for simplicity of the power density distribution analysis [149]. **Figure 6.31** shows the axial and radial power distributions at BOC (a, b) and after 537 days of full-power operation (c, d). The relative power differences of each (Th,^{233}U)O_2 configuration from UO_2 are shown in **Figure 6.32**. According to these comparisons, at BOC, the addition of Er_2O_3+Gd_2O_3 to the (Th,^{233}U)O_2 fuel gradually increases the axial power density in the edges of the core while slightly decreasing it in the center of the core because the gadolinium and erbium atoms absorb neutrons without fission. On the contrary, the addition of the burnable absorbers increases the radial power density in the inner region and decreases it in the outer. On the other hand, after 537 days of full-power operation (c and d figures), both axial and radial power profiles are very comparable, and the differences from the normal UO_2 are within 2.5% on an absolute basis. Likewise, the comparison between neutron spectra in the fuel region shows that incorporating Er_2O_3+Gd_2O_3 into (Th,^{233}U)$_{O2}$ fuel slightly thermalized the spectra, and shifted the spectra to the UO_2 spectra (**Figure 6.33**). However, it should be noted that the actual power profiles would be quite different from **Figure 6.31** when the possible refueling schemes are taken into account.

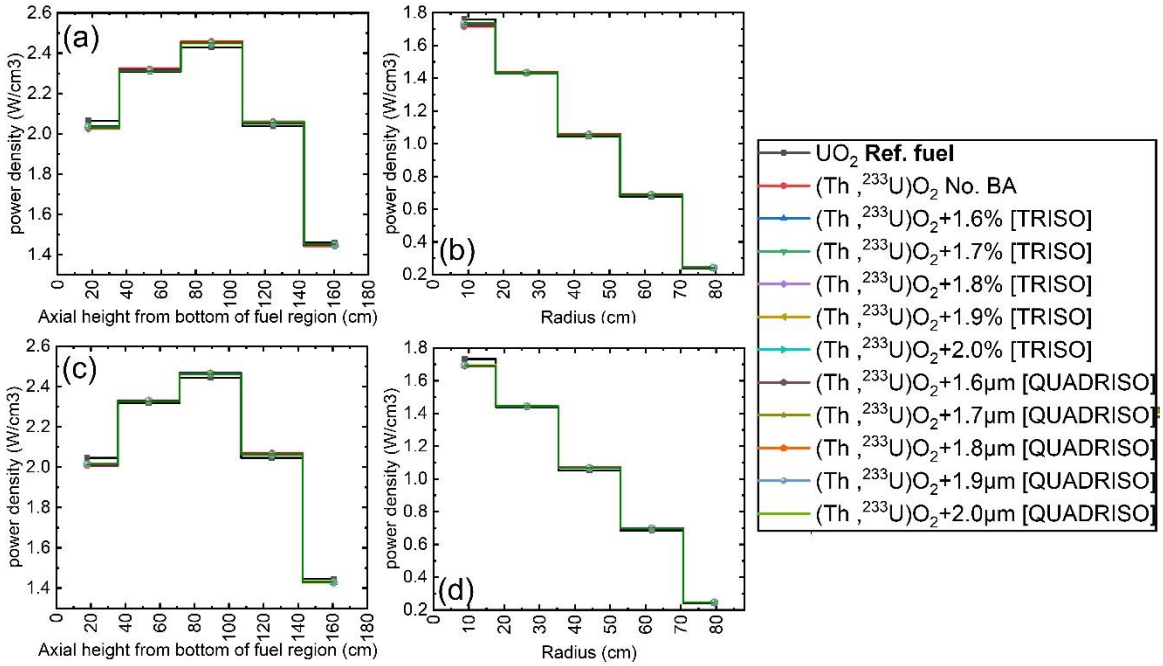

Figure 6. 31. Axial and radial neutronic power density distributions at 10 MW, (a, b) BOC and (c, d) 537 EFPDs.

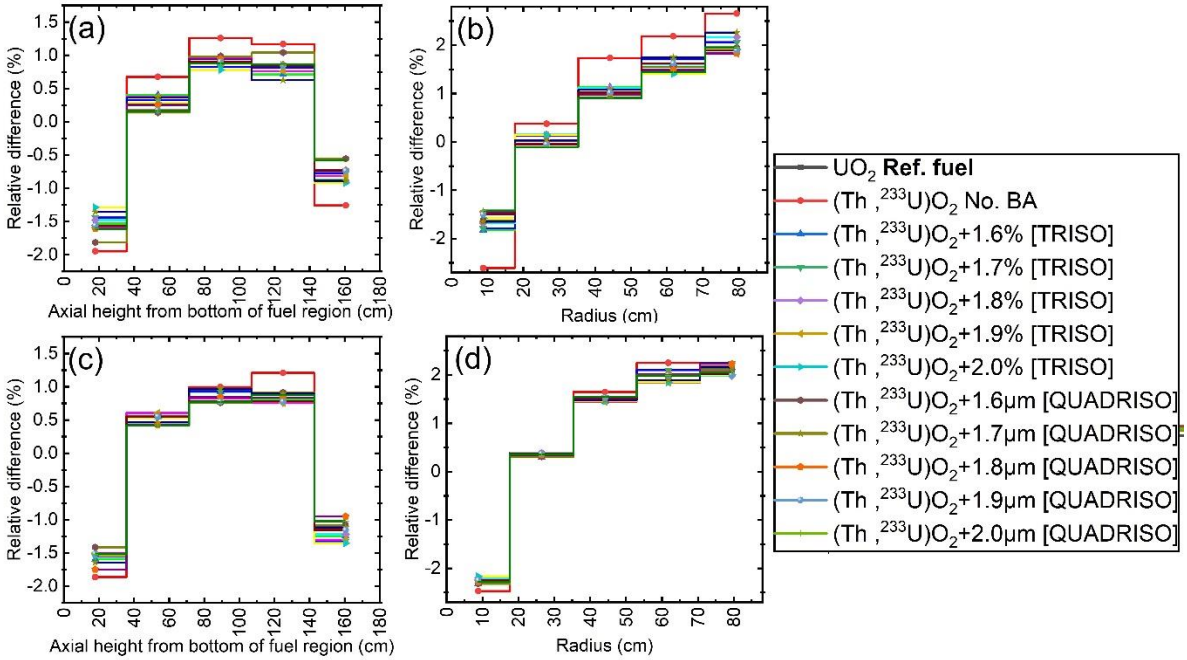

Figure 6. 32. Relative power differences of each (Th,^{233}U)O_2 + BA configuration from UO_2 configuration; (a, b) BOC and (c, d) 537 EFPDs.

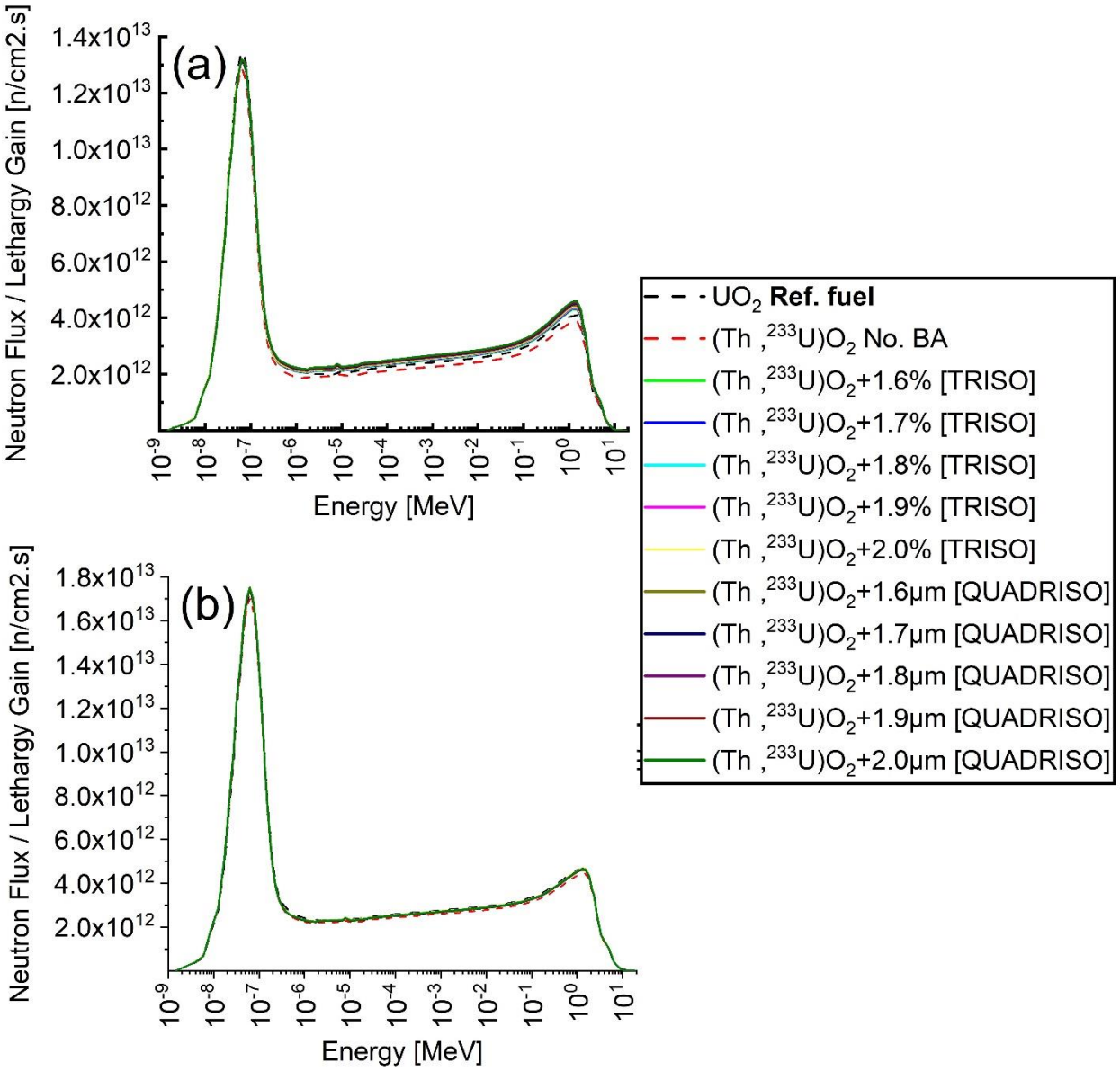

Figure 6. 33. Core-average neutron spectra at (a) BOC and (b) 537 EFPDs.

Fuel temperature coefficients

The fuel temperature coefficient (FTC) can be calculated by changing the temperature of the fuel region while keeping the temperature of the other regions constant. As is known, the core temperature coefficients should be negative for the inherent safety of the high-temperature reactor core mainly the fuel temperature coefficients, while BA loading may generally affect the core reactivity coefficients. In particular, the FTCs can be significantly modified if BA contains resonant absorbers such as Gd-155, Gd-157 and Er-167 [172].

Figure 6.34 displays the FTC dependence on burnup and the increase in the fuel temperature from 293.6 K to 1200 K of the (Th,^{233}U)O_2 based fuel with different absorber loading in TRISO/ QUADRISO particles presented in **Figure 6.28**. For comparison, the FTC for the UO_2 fuel is also plotted. Obviously, less negative fuel temperature coefficients for (Th,^{233}U)O_2 fuels depend on less neutron capture resonances of Th-232 than U-238, while the comparison between the ten BA-based fuel compositions showed that the FTCs were slightly less negative for the cases with a greater BA amount in QUADRISO configurations. However, the most significant result is that for all fuel compositions, the negative temperature coefficients during burnup are achieved.

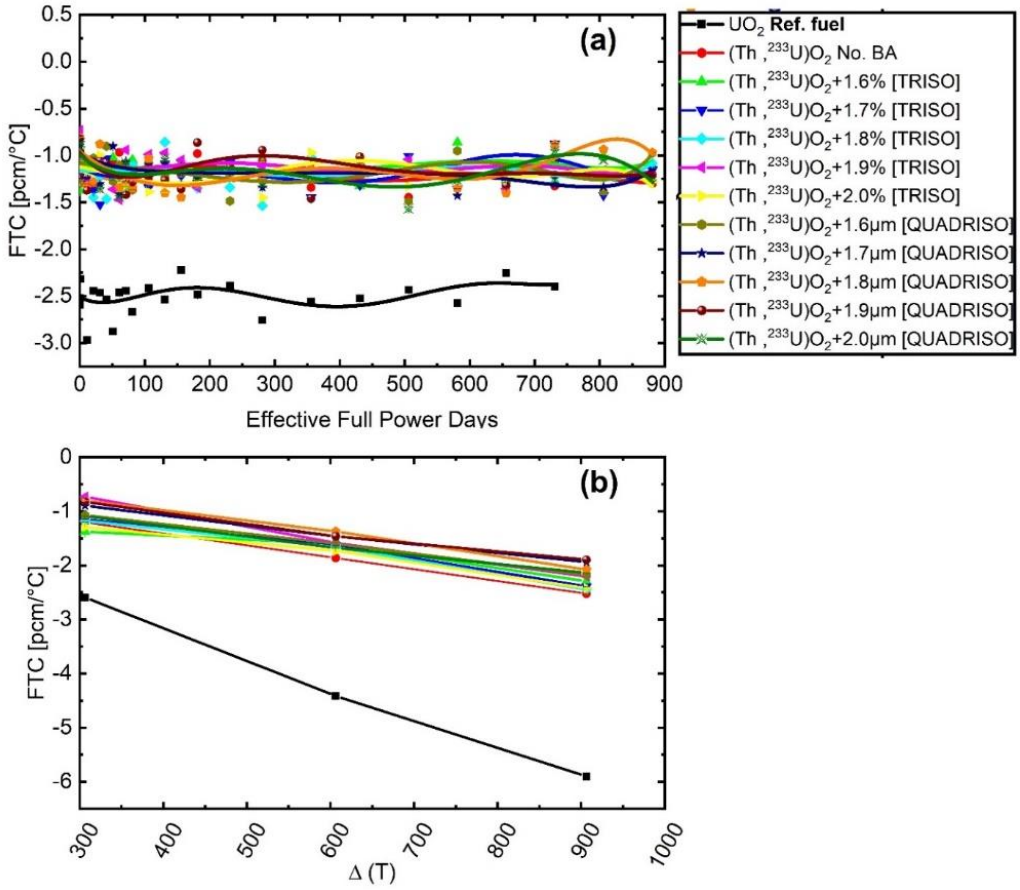

Figure 6. 34. FTC of various [Er_2O_3+ 10000 ppm Gd_2O_3] configurations (a) as a function of burnup and (b) as a function of temperature change (ΔT) at BOC.

6.2.4. Summary and conclusion

In this paper, we investigate from a neutronic point of view a core behavior with two different BAs, either mixed with the fuel kernel (i.e. TRISO) or as an additional layer (i.e. QUADRISO), in

the fuel particles of a pebble-bed HTR reactor fueled with (Th,^{233}U)O_2 for potential long-cycle operation. In this type of fuel, the initial excess reactivity is much higher than the standard UO_2 fuel due to the highest thermal value (η) for U-233 and its higher necessary ratios to achieve the target discharge burnup. For this purpose, the use of a BA is very essential to handle the excess reactivity throughout the cycle length. In the light of the study performed in this paper, we have selected Gadolinia/Erbia with different loading patterns in TRISO/QUADRISO particles in a way that the obtained multiplication factors did not exceed that obtained for UO_2 fuel at the beginning of the reactor life, and stabilize the reactivity curve during burnup. The subsequent results are the outcomes of this neutronic investigation:

- The excess reactivity present at the beginning of life can be controlled by the use of the two BAs.
- The use of Erbia materials in the TRISO/QUADRISO particles lowers the cycle length due to a reduction in fuel loading.
- Gadolinia is only useful for initial high reactivity suppression as it depletes very quickly, while Erbia is more effective for the middle of life.
- The use of Erbia doped with a few ppm (e.g. 10000 ppm) of Gadolinia in TRISO or QUADRISO can stabilize the reactivity curve during burnup.
- Although the discharge burnup for the [Er_2O_3+ 10000 ppm Gd_2O_3] loaded configurations decreased by an average of 19% of the fuel without BAs, it was still 26% higher than that of the standard UO_2 fuel.
- The FTC values for the QUADRISO configurations are slightly less negative for cases with a higher content of BAs, but the most important result is the negative temperature coefficients obtained during burnup.
- It is worth noting that none of the simulations discussed here account for fuel recirculation, refueling, or coolant flow; therefore, a thorough study using a coupled neutronic and thermos-hydraulic code, such as VSOP, is needed to fully understand the impact of BA implementation on the behavior of the pebble-bed HTR reactor [180].

Conclusion

The fundamental reactor neutronic properties of thorium-fueled pebble-bed HTR-10 reactor cores have been studied in the first section of this chapter (article 1). Thorium was combined with

several fissile materials to create feasible nuclear bundle designs, and the neutronic properties of these fuels were investigated using the Monte Carlo N-Particle code. The fuels investigated in the study were ThO_2 + HALEU (20 wt.%), ThO_2 + $RGPuO_2$, ThO_2 + $WGPuO_2$, and (Th + $^{233}U)O_2$. Additionally, the neutronic comparison of the different investigated fuel types was also performed for different initial content of fissile isotopes. Because the study is a comparative analysis of the neutronic performance of thorium-based fuels, the reactor physics parameters (i.e. Effective multiplication factors, neutron spectra, and delayed neutron fractions) and reactor safety-related parameters were determined (i.e. temperature reactivity coefficients, fission product poisons). Furthermore, the mass inventory of actinides in various spent fuels was examined.

Through the comparison between the ThO_2 + $RGPuO_2$ and UO_2 (17 wt.%) fuels, it was found that the ThO_2 mixed with $RGPuO_2$ achieved higher keff in the EOC and therefore deeper discharge burnup than UO_2 fuel despite the lower Keff values at BOC. For example, when the weight percent's were 38% and 40% keff's achieved the critical condition at approximately 42 GWd/ton and 45 GWd/ton, respectively, compared with 36 GWd/ton for UO_2 fuel. In contrast, the ThO_2 + $WGPuO_2$, and (Th + $^{233}U)O_2$ fuels achieved the critical condition at approximately 46 GWd/ton and 45 GWd/ton, respectively, but with suggested mixtures that realize higher reactivity at BOC (i.e. 80%ThO_2+20%$WGPuO_2$ and (85%Th+15%^{233}U)O2). In the next article of this chapter, we will deal with some methods to decrease the reactivity of the U-233 mixture but the principle is also applicable to the WGPu. The ThO_2+UO_2 (20%) mixtures also achieve a higher discharge burnup (38 GWd/ton and 42 GWd/ton for the 86% UO_2 and 90% UO_2 fuels, respectively) because of the enrichment used, which provides a sufficient number of fissile nuclei.

The addition of the fertile nuclide Th-232, as well as the fissile isotopes Pu-293 and U-233, alters the coefficients of relevance to the safe operation of pebble-beds to a minor degree, with values lower than the domain of UO2 fuel. There are two exceptions: delayed neutron fractions and fuel temperature coefficients are less favorable when Pu-293 and U-233 are the dominant fissile elements. The delayed neutron fractions raise serious concerns about the technical feasibility of using any of the fuel types in a reactor. However, to fully comprehend the implications of the observed differences between the investigated thorium-based fuel types and the reference fuel types, a more thorough analysis of dynamic core behavior is required.

Two burnable absorbers were used in the study conducted in the second section of this chapter (article 2) to reduce the excess reactivity at BOC of the pebble-bed HTR-10 fueled with (Th + $^{233}U)O_2$ and to increase the discharge burnup. This is Erbia doped with 10000 ppm of Gadolinia (Er_2O_3+Gd_2O_3) in TRISO or QUADRISO. A second calculation of the pebble-bed HTR-10 fueled with (Th + $^{233}U)O_2$ will allow us to quantify the impact of two absorbers on the various neutronic parameters. Results show that, when mixed with (Th + $^{233}U)O_2$ fuel, the two burnable absorbers can indeed suppress the excess reactivity at BOC. The suggested configurations reach criticality after an average burnup of 52.5 GWd/ton, implying a 26% extension from one with a UO_2 enrichment of 17 wt.% (37 GWd/ton). Furthermore, a comparison of neutron spectra and power distributions in the fuel region reveals that incorporating Er_2O_3+Gd_2O_3 into (Th,$^{233}U)O_2$ fuel slightly thermalized the spectra and shifted the spectra and power distributions to UO_2 ones (due to the increase in absorption due to the burnable absorbers), which are favorable from a safety point of view.

Chapter 7: Summary and outlooks for future work

The previous chapter is summarized in this final chapter, and the results are discussed. Finally, some relevant research projects are described that might be used to supplement and extend the work presented.

Summary

High-temperature gas-cooled reactors (HTGRs), also known as very-high-temperature reactors (VHTRs), have been chosen as generation IV reactor options due to their remarkable safety characteristics and huge potential for nuclear process heat application. Safety features are provided, for example, by so-called TRISO particles that withstand high temperatures (over 1,400 °C) in accident scenarios without significant damage, and by a large amount of graphite and low energy density in the reactor core. Pebble-bed type HTGRs, which are one of the HTGR designs, also have online refueling features, allowing them to burn a wide range of fuel combinations, including thorium fuel cycles while maintaining favorable safety characteristics.

The thesis presents a detailed investigation into the possibility of thorium-based fuels in a small pebble-bed HTGR (HTR-10) reactor from a neutronic point of view. The goal is to operate for a reasonably long period of time and maintain the well-known safety features of the HTGR reactors. As mentioned in the introduction section, examining thorium-based in HTR reactors is not a novel concept; however, there is no comprehensive cross-comparison of multiple prospective pebble-bed HTR reactor thorium fuels in the open literature. Thus, this thesis investigates how thorium can be incorporated into the fuel with different drivers and how this affects the neutronic parameters in comparison to the nominal/standard HALEU (UO_2 17 wt.%) fuel. The investigated thorium-based fuels include ThO_2 (Thoria/Thorium Dioxide) mixed with high-assay, low enriched uranium (HALEU 20 wt.%), reactor-grade plutonium ($RGPuO_2$), weapons-grade plutonium ($WGPuO_2$), and U-233. The study sought to assess specific neutronic parameters, for example, the effective multiplication factor, the impact of fission products on reactivity, the neutron spectrum, isotopic composition and fluctuation of effective delayed neutron fractions and temperature coefficient during burnup. Finally, the influence of burnable absorbers on reactor performance is discussed. The core performance and the burnup analysis were conducted using MCNP6 code.

In the first section of this study (i.e. first article in chapter 6), six thorium variants were proposed. Based on the simulations, it is possible to infer that all six-core configurations are at least possible in the sense that they produce results within the realm of possibility for the pebble-bed type HTR. These cores, however, behave in a very different way than others, for example, cores fueled by (Th + $^{233}U)O_2$ and ThO_2 + $WGPuO_2$ achieved higher excess reactivity at the beginning of the cycle, and cores fueled by ThO_2 + $RGPuO_2$ can achieve higher discharge burnup despite having the lowest excess reactivity at beginning of the cycle. Yet, thorium-based fuels have some advantages that can improve the safety of the HTR reactor. When mixed with U-233, U-235, or smaller concentrations of PuO_2, thorium fuels produce less fission product poisons, notably lower concentrations of Xe-135 and Sm-149. Additionally, thorium can be used to reduce plutonium and uranium-233 stockpiles. Even though a thorium-fueled reactor has some enhanced safety features, certain safety problems must be addressed. Because of the slightly lower delayed neutron fractions, the thorium mixed with Plutonium or U-233 reactor can generate rapid criticality at a lower reactivity insertion than the UO_2 reactor. The thorium cores have an additional safety concern. The long absorption chain of Th-232 produces a sizable inventory of the intermediate isotope Protactinium-233 (half-life of 27 days) and U-232 (a gamma emitter) which may have long-term radiological effects.

In the second section of this study (i.e. second article in chapter 6), a mixture of two burnable absorbers (Erbia and Gadolinia) was proposed in order to reduce the excess reactivity of the (Th, $^{233}U)O_2$ fueled reactor discussed in the first article. In the light of this study, we have selected Gadolinia/Erbia with different loading patterns in TRISO/QUADRISO particles in a way that the obtained multiplication factors did not exceed that obtained for UO_2 fuel at the beginning of the reactor life and stabilized the reactivity curve during burnup. The results showed that the use of Erbia doped with a few ppm (e.g. 10000 ppm) of Gadolinia in TRISO or QUADRISO can stabilize the reactivity curve during burnup. however, due to the decrease in fuel loading and the high remaining Er-167 content at the end of life, there is a deficit in fuel burnup efficiency as compared to (Th,$^{233}U)O_2$ without burnable absorber. Despite this, the new core discharge burnup is around 52.5 GWd/ton on average, without taking into account the refueling schemes, implying a 15.5 GWd/ton extension from the core fueled with UO_2, whose discharge burnup is around 37 GWd/ton.

Outlooks for future work

While the preceding analysis described in the thesis represents a significant portion of the research required to demonstrate the viability of integrating thorium with different fissile materials and the designs of burnable absorbers integrated into TRISO/QUADRISO particles to reduce the excess reactivity noted at the beginning of the (Th + ^{233}U)O_2 fueled reactor's life. Even so, this study raises several points that could be expanded on to round out the findings. As a result, we can identify the following points that will be addressed further in future works:

- First, the next objectives will be to perform complete analyses of (ThO_2+WGPuO_2) and (Th + ^{233}U)O_2 fuel mixtures with different Th-232 ratios and using:
  - Different absorbers (e.g. boron, cadmium, europium, dysprosium, hafnium and samarium). As well as quantification of the influence of these absorbers on the various neutronic/kinetic parameters.
  - Different implementation approaches (e.g. including the particle-type burnable absorber).
  - Improving some safety parameters, such as fuel temperature coefficient, by incorporating zirconium, zirconium hydride, or zirconium carbide, for example.
- Validate the results using different simulation codes.
- Since the key features of the pebble-bed reactors are pebble recirculation and the refueling scheme, a detailed thermal-hydraulic analysis is required.

References

[1] J. R. Lamarsh and A. J. Baratta, *Introduction to Nuclear Engineering*. 2001.

[2] A. Klimov, *Nuclear Physics and Nuclear Reactors*. 1975.

[3] W. M. Stacey, *Nuclear Reactor Physics: Second Edition*. 2007.

[4] P. Reuss, *Neutron Physics*. 2008.

[5] D. G. Cacuci, *Handbook of Nuclear Engineering, Vol. 1: Nuclear Engineering Fundamentals*. 2010.

[6] J. Bussac and P. Reuss, *Traité de neutronique: physique et calcul des réacteurs nucléaires avec application aux réacteurs à eau pressurisée et aux réacteurs à neutrons rapides*. Hermann, 1978.

[7] J. J. Duderstadt and L. J. Hamilton, *Nuclear Reactor Analysis*, vol. 66, no. 5. 1976.

[8] B. Zohuri, *Neutronic Analysis For Nuclear Reactor Systems*. Cham: Springer International Publishing, 2019.

[9] Nuclear Power, "Thermal Neutron," *Thermal Neutron*, 2020. [Online]. Available: https://www.nuclear-power.net/nuclear-power/reactor-physics/atomic-nuclear-physics/fundamental-particles/neutron/thermal-neutron/. [Accessed: 04-May-2020].

[10] CSEWG, "ENDF-102 data formats and procedures for the evaluated nuclear data file ENDF-6," 2001.

[11] CSEWG, "ENDF-6 Formats Manual Data,Data Formats and Procedures for the Evaluated Nuclear Data Files ENDF/B-VI, ENDF/B-VII and ENDF/B-VIII," 2018.

[12] R. Macfarlane, D. W. Muir, R. M. Boicourt, A. C. Kahler, III, and J. L. Conlin, "The NJOY Nuclear Data Processing System, Version 2016," 2017.

[13] T. Zu *et al.*, "NECP-Atlas: A new nuclear data processing code," *Ann. Nucl. Energy*, vol. 123, pp. 153–161, Jan. 2019.

[14] D. E. Cullen, "PREPRO 2019: 2019 ENDF/B Pre-processing Codes", report IAEA-NDS-229," 2019.

[15] D. Wiarda, M. E. Dunn, N. M. Greene, M. L. Williams, and C. Celik, "AMPX-6 : A Modular Code System for Processing ENDF / B," 2016.

[16] Los Alamos National Laboratory, "NJOY21—NJOY for the 21st Century," *Los Alamos National Laboratory*, 2016. [Online]. Available: https://github.com/njoy/NJOY21.git. [Accessed: 25-Mar-2017].

[17] R. E. MacFarlane and A. C. Kahler, "Methods for Processing ENDF/B-VII with NJOY," *Nucl. Data Sheets*, vol. 111, no. 12, pp. 2739–2890, 2010.

[18] O. Kabach, A. Chetaine, A. Jalil, A. Darif, and A. Saidi, "Processing and benchmarking of evaluated nuclear data file/b-viii.0β4 cross-section library by analysis of a series of critical experimental benchmark using the monte carlo code MCNP(X) and NJOY2016," *Nucl. Eng. Technol.*, vol. 49, no. 8, pp. 1610–1616, Dec. 2017.

[19] O. Kabach *et al.*, "Processing of the ENDF/B-VIII.0β6 neutron cross-section data library and testing with critical benchmarks, oktavian shielding benchmarks and the doppler reactivity defect benchmarks," *Ann. Univ. Craiova, Phys.*, vol. 28, pp. 78–98, 2018.

[20] O. Kabach, A. Chetaine, and A. Benchrif, "Processing of JEFF-3.3 and ENDF/B-VIII.0 and testing with critical benchmark experiments and TRIGA Mark II research reactor using MCNPX," *Appl. Radiat. Isot.*, vol. 150, no. February, pp. 146–156, Aug. 2019.

[21] J. Xu, T. Zu, and L. Cao, "Development and verification of resonance elastic scattering kernel processing module in nuclear data processing code NECP-Atlas," *Prog. Nucl. Energy*, vol. 110, no. September 2018, pp. 301–310, Jan. 2019.

[22] T. Zu, J. Xu, and L. Cao, "A processing method of generating S(α, β, T) tables considering resonance elastic scattering kernel for the Monte Carlo codes," *Prog. Nucl. Energy*, vol. 122, p. 103262, Apr. 2020.

[23] T. Jevremovic, *Nuclear Principles in Engineering*. Boston, MA: Springer US, 2009.

[24] IAEA, “Thorium Fuel Cycle - Potential Benefits and Challenges IAEA TECDOC 1450,” 2005.

[25] T. Yamamoto and Y. Miyoshi, “Reliable Method for Fission Source Convergence of Monte Carlo Criticality Calculation with Wielandt’s Method,” *J. Nucl. Sci. Technol.*, vol. 41, no. 2, pp. 99–107, Feb. 2004.

[26] Y. Azmy and E. Sartori, *Nuclear Computational Science*, vol. 53, no. 9. Dordrecht: Springer Netherlands, 2010.

[27] S. A. Dupree and S. K. Fraley, *A Monte Carlo Primer*. Boston, MA: Springer US, 2002.

[28] X-5 Monte Carlo Team, “MCNP — A General Monte Carlo N-Particle Transport Code, Version 5,” 2003.

[29] D. B. Pelowitz, “MCNPX: user’s manual, v2. 6.0,” 2008.

[30] C. J. Werner, “MCNP® USER’S MANUAL Code Version 6.2,” 2017.

[31] M. L. Fensin, “Development of the MCNPX depletion capability: a monte carlo linked depletion method that automates the coupling between MCNPX and CINDER90 for high fidelity burnup calculations,” University of Florida, 2008.

[32] D. B. Pelowitz *et al.*, “MCNPX 2.7.D Extensions,” 2010.

[33] O. Kabach, A. Chetaine, A. Benchrif, and H. Amsil, “Neutronic investigation of the thorium-based mixed-oxide as an alternative fuel in the TRIGA Mark-II research reactor – Part I: A beginning of life calculations,” *Ann. Nucl. Energy*, vol. 140, no. xxxx, p. 107075, Jun. 2020.

[34] X-5 Monte Carlo Team, “MCNP — A General Monte Carlo N-Particle Transport Code, Version 5.,” 2003.

[35] M. Mattes and J. Keinert, “Thermal Neutron Scattering Data for the Moderator Materials H2O, D2O and ZrHx in ENDF-6 Format and as ACE Library for MCNP(X) Codes,” *IAEA Rep. INDC NDS0470*, no. April, 2005.

[36] T. R. England, “CINDER--A ONE-POINT DEPLETION AND FISSION PRODUCT PROGRAM,” West Mifflin, PA (United States), Aug. 1962.

[37] W. B. Wilson, S. T. Cowell, T. R. England, A. C. Hayes, and P. Moller, “‘A Manual for CINDER’90 version 07. 4 Codes and Data,’ Tech. Rep. LA-UR-07-8412, Los Alamos National Laboratory,” 2007.

[38] Z. Artstein and R. A. Vitale, “A Strong Law of Large Numbers for Random Compact Sets,” *Ann. Probab.*, vol. 3, no. 5, pp. 879–882, 1975.

[39] F. B. Brown, “On the use of shannon entropy of the fission distribution for assessing convergence of Monte Carlo criticality calculations,” in *PHYSOR-2006 - American Nuclear Society’s Topical Meeting on Reactor Physics*, 2006, vol. 2006, pp. 1–6.

[40] D. J. Koch, “Investigation and improvement of criticality calculations in MCNP5 involving Shannon entropy convergence,” Georgia Institute of Technology, 2014.

[41] Nuclear Energy Agency, *International Handbook of Evaluated Criticality Safety Benchmark Experiments*, 2010th ed. 2010.

[42] W. J. Marshall and B. T. Rearden, “Criticality Safety Validation of SCALE 6.1 with ENDF/B-VII.0 Libraries-ORNL/TM-2011/450,” 2013.

[43] C. Ichihara, K. Kobayashi, S. A. Hayashi, I. Kimura, J. Yamamoto, and A. Takahashi, “FENDL-2 BENCHMARKS SUBLIBRARY Leakage Neutron Spectra from Various Sphere Piles with 14 MeV Neutrons,” 1988. .

[44] K. Sumita, A. Takahashi, T. Iida, and J. Yamamoto, “Status of OKTAVIAN I and proposal for OKTAVIAN II,” *Nucl. Sci. Eng.*, vol. 106, no. 3, pp. 249–265, 1990.

[45] C. Ichihara, I. Kimura, S. A. Hayashi, J. Yamamoto, and A. Takahashi, “Measurement of leakage neutron spectra from a spherical pile of zirconium irradiated with 14mev neutrons and validation of its nuclear data,” *J. Nucl. Sci. Technol.*, vol. 40, no. 6, pp. 417–422, 2003.

[46] S. C. van der Marck, “Shielding Benchmark Calculations with MCNP-4C3 Using JEFF-3.1 Nuclear Data,” 2005.

[47] D. H. Kim, C. S. Gil, and Y. O. Lee, “Nuclear data sensitivity analyses of OKTAVIAN shielding benchmark experiments,” *J. Nucl. Sci. Technol.*, vol. 45, no. March, pp. 70–73, 2008.

[48] Z. H. Y. and C. W. H., “Integral Test of CENDL-3.1 with Shielding Benchmarks,” *J. Korean Phys. Soc.*, vol. 59, no. 23, p. 1166, 2011.

[49] R. D. Mosteller, L. D. Eisenhart, R. C. Little, W. J. Eich, and J. Chao, “Benchmark Calculations for the Doppler Coefficient of Reactivity,” *Nucl. Sci. Eng.*, vol. 107, no. 3, pp. 265–271, Mar. 1991.

[50] F. Rahnema and H. N. M. Gheorghiu, “ENDF/B-VI benchmark calculations for the doppler coefficient of reactivity,” *Ann. Nucl. Energy*, vol. 23, no. 12, pp. 1011–1019, Aug. 1996.

[51] J. L. Conlin, “Computational benchmark of the doppler reactivity defect,” *Jt. Int. Top. Meet. Math. Comput. Supercomput. Nucl. Appl. M C + SNA 2007*, 2007.

[52] R. D. Mosteller, “The Doppler-defect benchmark: Overview and summary of results,” *Jt. Int. Top. Meet. Math. Comput. Supercomput. Nucl. Appl. M C + SNA 2007*, pp. 1–13, 2007.

[53] O. Kabach *et al.*, “PROCESSING OF THE ENDF/B-VIII.0B6 NEUTRON CROSS-SECTION DATA LIBRARY AND TESTING WITH CRITICAL BENCHMARKS AND OKTAVIAN SHIELDING BENCHMARKS,” in *The Fourth International Conference on Physics and Technology of Reactors and Applications*, 2018.

[54] O. Kabach, A. Chetaine, A. Benchrif, and H. Amsil, “An inter-comparison between ENDF/B-VIII.0-NECP-Atlas and ENDF/B-VIII.0-NJOY results for criticality safety benchmarks and benchmarks on the reactivity temperature coefficient,” *Nucl. Eng. Technol.*, vol. 53, no. 8, pp. 2445–2453, Aug. 2021.

[55] National Nuclear Data Center, “ENDF/B-VIII.0beta4 US Evaluated Nuclear Data Library,” 2017. [Online]. Available: https://ndclx4.bnl.gov/gf/project/endf/. [Accessed: 28-Feb-2017].

[56] Los Alamos National Security, “NJOY,” *Los Alamos National Laboratory*, 2016. [Online]. Available: http://www.njoy21.io/. [Accessed: 28-Feb-2017].

[57] P. Balaji *et al.*, “MPICH2 Installer’s Guide, Mathematics and Computer Science Division,” *Argonne Natl. Lab.*, 2012.

[58] R. D. Mosteller, F. B. Brown, and B. C. Kiedrowski, “An Expanded Criticality Validation Suite for MCNP,Tech. Rep. LA-UR-10-04170,” 2011.

[59] National Nuclear Data Center, “Library, Endf/B-Viii.0Beta6 US Evaluated Nuclear Data,” 2018. [Online]. Available: https://ndclx4.bnl.gov/gf/project/endf/.

[60] R. D. Mosteller, “ENDF/B-V, ENDF/B-VI, and ENDF/B-VII.O results for the doppler-defect benchmark,” in *Joint International Topical Meeting on Mathematics and Computations and Supercomputing in Nuclear Applications, M and C + SNA 2007*, 2007.

[61] W. L. Oberkampf and T. G. Trucano, “Verification and validation benchmarks,” *Nucl. Eng. Des.*, vol. 238, no. 3, pp. 716–743, 2008.

[62] J.-C. Jaboulay *et al.*, “TRIPOLI-4® Monte Carlo code ITER A-lite neutronic model validation,” *Fusion Eng. Des.*, vol. 89, no. 9–10, pp. 2174–2178, Oct. 2014.

[63] M. Cornock, “Benchmarking of ENDF/B-VII.1 and JENDL-4.0 in the Fast Neutron Range,” *Nucl. Data Sheets*, vol. 118, no. 1, pp. 430–432, Apr. 2014.

[64] R. H. H. Smith, J. Keener, J. F. DeClue, A. W. Krass, and V. R. Cain, “Bias and Uncertainty of Critical Experiment Models with CSAS25 from SCALE4.4a for Criticality Safety Analyses On the HP J-5600 (CMODB) Workstation,” 2001.

[65] J. Clarity and W. B. J. Marshall, “Assessment of normality for criticality safety bias and bias uncertainty calculation,” in *ICNC 2019 - 11th International conference on Nuclear Criticality Safety September 15-20, 2019 – Paris, France*, 2019.

[66] Y. Nomura and T. Shimooke, “A Multiple Regression Equation for Calculated k eff Bias Errors by Criticality Code System,” *Nucl. Technol.*, vol. 65, no. 2, pp. 340–349, May 1984.

[67] R. Mosteller, “Comparison of ENDF/B-VII.1 and ENDF/B-VII.0 Results for the Expanded Criticality Validation Suite for MCNP and for Selected Additional Criticality Benchmarks,” *Nucl. Data Sheets*, vol. 118, no. 1, pp. 442–445, 2014.

[68] R. D. Mosteller, S. C. Frankle, and P. G. Young, “Data Testing of ENDF/B-VI with MCNP: Critical Experiments, Thermal-Reactor Lattices, and Time-of-Flight Measurements,” *Adv. Nucl. Sci. Technol.*, vol. 24, pp. 131–195, 2005.

[69] A. C. Kahler, “Monte Carlo eigenvalue calculations with ENDF/B-VI.8, JEFF-3.0, and JENDL-3.3 cross sections for a selection of international criticality safety benchmark evaluation project handbook benchmarks,” *Nucl. Sci. Eng.*, vol. 145, no. 2, pp. 213–224, 2003.

[70] O. Cabellos *et al.*, “Benchmarking and validation activities within JEFF project,” *EPJ Web Conf.*, vol. 146, p. 06004, 2017.

[71] D. A. Brown *et al.*, “ENDF/B-VIII.0: The 8th Major Release of the Nuclear Reaction Data Library with CIELO-project Cross Sections, New Standards and Thermal Scattering Data,” *Nucl. Data Sheets*, vol. 148, pp. 1–142, 2018.

[72] A. D. Carlson *et al.*, “Evaluation of the Neutron Data Standards,” *Nucl. Data Sheets*, vol. 148, pp. 143–188, 2018.

[73] International Atomic Energy Agency, “ENDF-Archive,” *IAEA web site*, 2018. [Online]. Available: https://www-nds.iaea.org/public/download-endf/. [Accessed: 25-Jan-2017].

[74] O. Cabellos, “Processing of the new JEFF-3.2T4 Cross Section Library with the NJOY Code System into Various Formats for Testing Purposes,” no. February, 2014.

[75] M. B. Chadwick *et al.*, “ENDF/B-VII.1 nuclear data for science and technology: Cross sections, covariances, fission product yields and decay data,” *Nucl. Data Sheets*, vol. 112, no. 12, pp. 2887–2996, 2011.

[76] IAEA, “History, Development and Future of TRIGA Research Reactors,” *Tech. Reports Ser. No. 482*, no. 482, 2016.

[77] M. Q. Huda, M. Rahman, M. M. Sarker, and S. I. Bhuiyan, “Benchmark analysis of the TRIGA MARK II research reactor using Monte Carlo techniques,” *Ann. Nucl. Energy*, vol. 31, no. 11, pp. 1299–1313, 2004.

[78] B. El Bakkari *et al.*, “Fuel burnup analysis for the Moroccan TRIGA research reactor,” *Ann. Nucl. Energy*, vol. 51, pp. 112–119, Jan. 2013.

[79] E. Chham *et al.*, “Neutronic and thermal–hydraulic analysis of new irradiation channels inside the Moroccan TRIGA Mark II research reactor core,” *Appl. Radiat. Isot.*, vol. 116, pp. 178–184, 2016.

[80] T. Matsumoto, “Benchmark analysis of criticality experiments in the TRIGA mark II using a continuous energy monte carlo code MCNP,” *J. Nucl. Sci. Technol.*, vol. 35, no. 9, pp. 662–670, 1998.

[81] G. B. Engle, “Assessment of Grade H-451 Graphite for Replaceable Fuel,” no. 17, 1977.

[82] Y. Boulaich *et al.*, “Steady-state thermal-hydraulic analysis of the Moroccan TRIGA MARK II reactor by using PARET/ANL and COOLOD-N2 codes,” *Nucl. Eng. Des.*, vol. 241, no. 1, pp. 270–273, 2011.

[83] G. R. Keepin, “Physics of nuclear kinetics,” in *Addison-Wesley series in nuclear science and engineering*, Addison-Wesley Pub. Co; 1st edition (1965), 1965, pp. 161–186.

[84] M. Hassanzadeh and S. A. H. Feghhi, “Analysis of burn up effects on kinetic parameters in an Accelerator Driven Subcritical TRIGA reactor,” *Ann. Nucl. Energy*, vol. 62, pp. 280–283, 2013.

[85] U.C.NRC, “Shutdown margin,” 2019. [Online]. Available: https://www.nrc.gov/reading-rm/basic-ref/glossary/shutdown-margin.html. [Accessed: 21-Mar-2019].

[86] L. P. Tucker and S. Usman, “Thorium-based mixed oxide fuel in a pressurized water reactor: A burnup analysis with MCNP,” *Ann. Nucl. Energy*, vol. 111, pp. 163–175, Jan. 2018.

[87] C. Subramanian, A. Suri, and T. Murthy, “Development of Boron-based materials for nuclear applications,” 2010.

[88] A. H. Fadaei, “Investigation of burnable poisons effects in reactor core design,” *Ann. Nucl. Energy*, vol. 38, no. 10, pp. 2238–2246, 2011.

[89] A. A. Galahom, “Study of the possibility of using Europium and Pyrex alloy as burnable absorber in PWR,” *Ann. Nucl. Energy*, vol. 110, pp. 1127–1133, 2017.

[90] S. F. Mughabghab, “The thermal neutron capture cross sections resonance integrals and G-factors,” 2003.

[91] F. Franceschini and B. Petrović, “Fuel with advanced burnable absorbers design for the IRIS reactor core: Combined Erbia and IFBA,” *Ann. Nucl. Energy*, vol. 36, no. 8, pp. 1201–1207, 2009.

[92] D. R. Lide, W. M. “Mickey” Haynes, Grace Baysinger, L. I. Berger, M. Frenkel, and R. N. Goldberg, “CRC Handbook of Chemistry and Physics Internet Version 2010,” p. 2010, 2010.

[93] A. Radkowsky and A. Galperin, “The Nonproliferative Light Water Thorium Reactor: A New Approach to Light Water Reactor Core Technology,” *Nucl. Technol.*, vol. 124, no. 3, pp. 215–222, Dec. 1998.

[94] J. Breza, P. Dařílek, and V. Nečas, “Study of thorium advanced fuel cycle utilization in light water reactor VVER-440,” *Ann. Nucl. Energy*, vol. 37, no. 5, pp. 685–690, 2010.

[95] L. P. Tucker, A. Alajo, and S. Usman, “Thorium-based mixed oxide fuel in a pressurized water reactor: A beginning of life feasibility analysis with MCNP,” *Ann. Nucl. Energy*, vol. 76, pp. 323–334, 2015.

[96] P. Boczar *et al.*, “Thorium fuel-cycle studies for CANDU reactors,” in *Thorium fuel utilization: Options and trends, IAEA-TECDOC-1319*, 2002, pp. 25–41.

[97] IAEA, “Thermophysical Properties Database of Materials for Light Water Reactors and Heavy Water Reactors, IAEA-TECDOC-1496,” Aug. 2006.

[98] IAEA, “Summary for Policymakers,” Cambridge University Press, Cambridge, 2008.

[99] J. Liu, Z. Dai, X. Yang, Y. Zhao, and S. Meng, “Lattice thermodynamic behavior in nuclear fuel ThO2 from first principles,” *J. Nucl. Mater.*, vol. 511, pp. 11–17, 2018.

[100] K. Insulander Björk and C. Netterbrant, “Thorium as an additive for improved neutronic properties in boiling water reactor fuel,” *Ann. Nucl. Energy*, vol. 113, pp. 470–475, Mar. 2018.

[101] P. Boczar, G. R. Dyck, P. S. W. Chan, and D. B. Buss, “Recent advances in thorium fuel cycles for CANDU reactors,” in *Thorium fuel utilization: Options and trends, IAEA-TECDOC-1319*, 2002, pp. 104–120.

[102] T. Takei and A. Yamaji, “Core design of PWR-type seed-blanket core breeder reactor with tightly packed fuel assembly,” *Nucl. Eng. Des.*, vol. 333, no. October 2017, pp. 45–54, 2018.

[103] M. Todosow, A. Galperin, S. Herring, M. Kazimi, T. Downar, and A. Morozov, “Use of Thorium in Light Water Reactors,” *Nucl. Technol.*, vol. 151, no. 2, pp. 168–176, 2005.

[104] R. Akbari-Jeyhouni, D. Rezaei Ochbelagh, J. R. Maiorino, F. D’Auria, and G. L. de Stefani, “The utilization of thorium in Small Modular Reactors – Part I: Neutronic assessment,” *Ann. Nucl. Energy*, vol. 120, pp. 422–430, Oct. 2018.

[105] O. Kabach, A. Chetaine, A. Benchrif, H. Amsil, and F. El Banni, “A comparative analysis of the neutronic performance of thorium mixed with uranium or plutonium in a high-temperature pebble-bed reactor,” *Int. J. Energy Res.*, vol. 45, no. 11, pp. 16824–16841, Sep. 2021.

[106] O. Kabach, A. Chetaine, A. Benchrif, and H. Amsil, “The use of burnable absorbers integrated into TRISO/QUADRISO particles as a reactivity control method in a pebble-bed HTR reactor fuelled with (Th,233U)O2,” *Nucl. Eng. Des.*, vol. 384, no. December, p. 111476, Dec. 2021.

[107] E. H. Uguru, S. F. A. Sani, M. U. Khandaker, and M. H. Rabir, “Investigation on the effect of 238U replacement with 232Th in small modular reactor (SMR) fuel matrix,” *Prog. Nucl. Energy*, vol. 118, no. July 2019, p. 103108, Jan. 2020.

[108] G. L. de Stefani, J. R. Maiorino, and J. M. de Losada Moreira, “The AP-Th 1000 - An advanced concept to use MOX of thorium in a closed fuel cycle,” *Int. J. Energy Res.*, no. November 2019, pp. 1–14, Apr. 2020.

[109] A. A. Galahom, “Improvement of the VVER-1200 Fuel Cycle by Introducing Thorium with Different Fissile

Material in Blanket-Seed Assembly," *Nucl. Sci. Eng.*, vol. 193, no. 6, pp. 638–651, 2019.

[110] A. Kumar, R. Srivenkatesan, and R. K. Sinha, "On the Physics Design of Advanced Heavy Water Reactor (AHWR)."

[111] A. Waris, V. Richardina, I. K. Aji, S. Permana, and Z. Su'Ud, "Preliminary study on plutonium and minor actinides utilization in thorims-nes minifuji reactor," *Energy Convers. Manag.*, vol. 72, pp. 27–32, 2013.

[112] A. Waris, I. K. Aji, S. Pramuditya, Novitrian, S. Permana, and Z. Su'ud, "Comparative Studies on Plutonium and Minor Actinides Utilization in Small Molten Salt Reactors with Various Powers and Core Sizes," *Energy Procedia*, vol. 71, pp. 62–68, May 2015.

[113] C. Y. Zou, C. Z. Cai, C. G. Yu, J. H. Wu, and J. G. Chen, "Transition to thorium fuel cycle for TMSR," *Nucl. Eng. Des.*, vol. 330, pp. 420–428, Apr. 2018.

[114] S. PERMANA, N. TAKAKI, and H. SEKIMOTO, "Feasible Region of Design Parameters for Water Cooled Thorium Breeder Reactor," *J. Nucl. Sci. Technol.*, vol. 44, no. 7, pp. 946–957, Jul. 2007.

[115] S. Permana, N. Takaki, and H. Sekimoto, "Breeding capability and void reactivity analysis of heavy-water-cooled thorium reactor," *J. Nucl. Sci. Technol.*, vol. 45, no. 7, pp. 589–600, 2008.

[116] S. Permana, "Basic design parameter optimization on water cooled thorium breeder reactor," *Ann. Nucl. Energy*, vol. 139, p. 107218, May 2020.

[117] R. Bäumer, I. Kalinowski, E. Röhler, J. Schöning, and W. Wachholz, "Construction and operating experience with the 300-MW THTR nuclear power plant," *Nucl. Eng. Des.*, vol. 121, no. 2, pp. 155–166, Jul. 1990.

[118] F. Carré, P. Hildebrandt, A. C. Kadak, W. Naughton, B. Seidel, and S. Sorrell, "Generation IV Roadmap Description of Candidate Gas-cooled Reactor Systems Report," 2002.

[119] IAEA, "Evaluation of High Temperature Benchmark Analysis Related to the PBMR-400, PBMM, the ASTRA Critical Facility-IAEA-TECDOC-1694G," 2013.

[120] A. M. Attom, J. Wang, C. Yan, and M. Ding, "Neutronic analysis of thorium MOX fuel blocks with different driver fuels in advanced block-type HTRs," *Ann. Nucl. Energy*, vol. 129, pp. 101–109, 2019.

[121] T. Aoki, S. S. Chirayath, and H. Sagara, "Proliferation resistance evaluation of an HTGR transuranic fuel cycle using PRAETOR code," *Ann. Nucl. Energy*, vol. 141, p. 107325, Jun. 2020.

[122] S. Şahin, H. M. Şahin, and A. Acir, "Criticality and burn up evolutions of the Fixed Bed Nuclear Reactor with alternative fuels," *Energy Convers. Manag.*, vol. 51, no. 9, pp. 1781–1787, 2010.

[123] A. M. Attom, J. Wang, J. Huang, C. Yan, and M. Ding, "Comparison of homogeneous and heterogeneous thorium fuel blocks with four drivers in advanced high temperature reactors," *Int. J. Energy Res.*, vol. 44, no. 7, pp. 5713–5729, Jun. 2020.

[124] IAEA, "Potential of thorium based fuel cycles to constrain plutonium and reduce long lived waste toxicity," 2003.

[125] J. C. Kuijper *et al.*, "HTGR reactor physics and fuel cycle studies," *Nucl. Eng. Des.*, vol. 236, no. 5–6, pp. 615–634, Mar. 2006.

[126] D. Irwanto, S. Permana, and S. Pramuditya, "Preliminary Study of 20 MWth Experiment Power Reactor based on Pebble Bed Reactor," *J. Phys. Conf. Ser.*, vol. 877, no. 1, pp. 5–9, 2017.

[127] D. Irwanto, S. Permana, A. Pramutadi, and S. Pramuditya, "Preliminary Design Study of Small Power 30-50 MWt Experiment Power Reactor based on High Temperature Pebble Bed Gas Cooled Reactor Technology," *J. Phys. Conf. Ser.*, vol. 1127, no. 1, 2019.

[128] J. L. Kloosterman, "Application of boron and gadolinium burnable poison particles in UO2 and PUO2 fuels in HTRs," *Ann. Nucl. Energy*, vol. 30, no. 17, pp. 1807–1819, 2003.

[129] IAEA, "High Temperature Gas Cooled Reactor Fuels and Materials," 2010.

[130] Z. Zhang *et al.*, "Current status and technical description of Chinese 2 × 250 MWth HTR-PM demonstration plant," *Nucl. Eng. Des.*, vol. 239, no. 7, pp. 1212–1219, 2009.

[131] G. Locatelli, M. Mancini, and N. Todeschini, “Generation IV nuclear reactors: Current status and future prospects,” *Energy Policy*, vol. 61, pp. 1503–1520, 2013.

[132] M. J. Wang, R. J. Sheu, J. J. Peir, and J. H. Liang, “Criticality calculations of the HTR-10 pebble-bed reactor with SCALE6/CSAS6 and MCNP5,” *Ann. Nucl. Energy*, vol. 64, pp. 1–7, 2014.

[133] E. J. Mulder and W. A. Boyes, “Neutronics characteristics of a 165 MWth Xe-100 reactor,” *Nucl. Eng. Des.*, vol. 357, no. March 2019, p. 110415, Feb. 2020.

[134] Zuhair, Suwoto, S. Permana, and T. Setiadipura, “Study on Control Rod Reactivity of Small Pebble Bed Reactor with Wallpaper Fuel Design,” *J. Phys. Conf. Ser.*, vol. 1772, no. 1, p. 012021, Feb. 2021.

[135] A. Talamo, W. Gudowski, J. Cetnar, and F. Venneri, “Key physical parameters and temperature reactivity coefficients of the deep burn modular helium reactor fueled with LWRs waste,” *Ann. Nucl. Energy*, vol. 31, no. 16, pp. 1913–1937, 2004.

[136] A. Talamo, “A novel concept of QUADRISO particles - Part III: Applications to the plutonium-thorium fuel cycle,” *Prog. Nucl. Energy*, vol. 51, no. 2, pp. 274–280, 2009.

[137] M. H. Rabir, A. F. Ismail, and M. S. Yahya, “Review of the microheterogeneous thoria-urania fuel for micro-sized high temperature reactors,” *Int. J. Energy Res.*, no. August, p. er.5923, Sep. 2020.

[138] H. N. Tran and P. H. Liem, “Neutronic feasibility study of U-Th-Pa based high burnup fuel for pebble bed reactors,” *Prog. Nucl. Energy*, vol. 80, pp. 17–23, 2015.

[139] P. A. Demkowicz, B. Liu, and J. D. Hunn, “Coated particle fuel: Historical perspectives and current progress,” *J. Nucl. Mater.*, vol. 515, pp. 434–450, Mar. 2019.

[140] M. A. Alzamly, M. Aziz, A. A. Badawi, H. A. Gabal, and A. R. A. Gadallah, “Burnup analysis for HTR-10 reactor core loaded with uranium and thorium oxide,” *Nucl. Eng. Technol.*, vol. 52, no. 4, pp. 674–680, Apr. 2020.

[141] L. Langston, “A Path for Nuclear Power,” *Am. Sci.*, vol. 102, no. 2, p. 90, 2014.

[142] W. K. Terry *et al.*, “Evaluation of the Initial Critical Configuration of the Htr-10 Pebble-Bed Reactor,” 2007.

[143] Z. Zhang, Z. Wu, Y. Sun, and F. Li, “Design aspects of the Chinese modular high-temperature gas-cooled reactor HTR-PM,” *Nucl. Eng. Des.*, vol. 236, no. 5–6, pp. 485–490, 2006.

[144] C. Fang, X. Bao, C. Yang, Y. Yang, and J. Cao, “The R&D of HTGR high temperature helium sampling loop: From HTR-10 to HTR-PM,” *Nucl. Eng. Des.*, vol. 306, pp. 192–197, 2016.

[145] J. Zhang, F. Li, and Y. Sun, “Physical Analysis of the Initial Core and Running-In Phase for Pebble-Bed Reactor HTR-PM,” *Sci. Technol. Nucl. Install.*, vol. 2017, 2017.

[146] J. Zhang, J. Guo, F. Li, and Y. Sun, “Research on the fuel loading patterns of the initial core in Chinese pebble-bed reactor HTR-PM,” *Ann. Nucl. Energy*, vol. 118, pp. 235–240, 2018.

[147] V. Şeker and Ü. Çolak, “HTR-10 full core first criticality analysis with MCNP,” *Nucl. Eng. Des.*, vol. 222, no. 2-3 SPEC, pp. 263–270, 2003.

[148] Q. Zhenya, “General design of the 10 MW HTR,” in *Proceedings of the 3rd JAERI symposium on HTGR technologies*, 1996, pp. 149–160.

[149] S. R. Wu, S. C. Wu, D. S. Chao, and J. H. Liang, “Burnup computations of online-refueling process for pebble-bed reactors using layer-mixed-shell fuel movement model,” *Appl. Radiat. Isot.*, vol. 147, no. February, pp. 1–6, 2019.

[150] S. Jiang, J. Tu, X. Yang, and N. Gui, “A review of pebble flow study for pebble bed high temperature gas-cooled reactor,” *Exp. Comput. Multiph. Flow*, vol. 1, no. 3, pp. 159–176, 2019.

[151] A. Benchrif, A. Chetaine, and H. Amsil, “Benchmark results for the ‘BWR-PB’ fuel assembly based on pebble-bed coated particles with uranium dioxide and gadolinia poison,” *Nucl. Eng. Des.*, vol. 239, no. 6, pp. 1148–1154, Jun. 2009.

[152] xu Yuanhui, “The HTR-10 project and its further development,” 2000.

[153] N. Jakiyah, Suharyana, Riyatun, and A. Khakim, "The dependency of shutdown margin values of the HTR-10 on packing fraction absorber," in *AIP Conference Proceedings*, 2018, vol. 2014, no. September, p. 020045.

[154] IAEA, "the High Temperature Gas Cooled Reactor Test," no. March 1993, 2000.

[155] F. Bostelmann, M. L. Williams, C. Celik, R. J. Ellis, G. Ilas, and B. T. Rearden, "Assessment of scale capabilities for high temperature reactor modeling and simulation," *Trans. Am. Nucl. Soc.*, vol. 119, pp. 1073–1076, 2018.

[156] E. H. Uguru, S. F. A. Sani, M. U. Khandaker, M. H. Rabir, and J. A. Karim, "A comparative study on the impact of Gd2O3 burnable neutron absorber in UO2 and (U, Th)O2 fuels," *Nucl. Eng. Technol.*, vol. 52, no. 6, pp. 1099–1109, 2020.

[157] M. Bourquin, "Thorium Energy for the World," in *Thorium Energy for the World*, 2016.

[158] A. A. Galahom, "Minimization of the fission product waste by using thorium based fuel instead of uranium dioxide," *Nucl. Eng. Des.*, vol. 314, pp. 165–172, 2017.

[159] R. W. Dodson and R. D. Fowler, "Products of the Uranium Fission. Radioactive Isotopes of Iodine and Xenon," *Phys. Rev.*, vol. 57, no. 11, pp. 966–971, Jun. 1940.

[160] D. Greneche and M. Chhor, "Development of the thorium fuel cycle," in *Nuclear Fuel Cycle Science and Engineering*, Elsevier, 2012, pp. 177–202.

[161] J. Carbajo, "Issues in the use of Weapons-Grade MOX Fuel in VVER-1000 Nuclear Reactors: Comparison of UO2 and MOX Fuels," Oak Ridge, TN, May 2005.

[162] IAEA, "Proceedings of three IAEA meetings held in Vienna in 1997, 1998 and 1999," in *Thorium fuel utilization: Options and trends, IAEA-TECDOC-1319*, 2002, no. November.

[163] Zuhair, Suwoto, T. Setiadipura, and J. C. Kuijper, "Study on the Characteristics of Effective Delayed Neutron Fraction (β eff) for Pebble-Bed Reactor with Plutonium Fuel," *Iran. J. Sci. Technol. Trans. A Sci.*, vol. 43, no. 6, pp. 3037–3045, 2019.

[164] C. Fiorina *et al.*, "Comparative analysis of thorium and uranium fuel for transuranic recycle in a sodium cooled Fast Reactor," *Ann. Nucl. Energy*, vol. 62, pp. 26–39, Dec. 2013.

[165] M. Rahgoshay and O. Noori-Kalkhoran, "Calculation of control rod worth and temperature reactivity coefficient of fuel and coolant with burn-up changes for VVRS-2MWth nuclear reactor," *Nucl. Eng. Des.*, vol. 256, pp. 322–331, Mar. 2013.

[166] G. A. Richards and D. E. Serfontein, "The influence of thorium on the temperature reactivity coefficient in a 400 MW th pebble bed high temperature plutonium incinerating reactor (HTR2014-51384)," in *Proceedings of the HTR 2014*, 2014.

[167] M. Lung and O. Gremm, "Perspectives of the thorium fuel cycle," *Nucl. Eng. Des.*, vol. 180, no. 2, pp. 133–146, 1998.

[168] D. Baldova, E. Fridman, and E. Shwageraus, "High conversion Th-U233 fuel for current generation of PWRs: Part I – Assembly level analysis," *Ann. Nucl. Energy*, vol. 73, pp. 552–559, Nov. 2014.

[169] S. M. Mirvakili, M. Alizadeh Kavafshary, and A. Joze Vaziri, "Comparison of neutronic behavior of UO 2 , (Th- 233 U)O 2 and (Th- 235 U)O 2 fuels in a typical heavy water reactor," *Nucl. Eng. Technol.*, vol. 47, no. 3, pp. 315–322, Apr. 2015.

[170] S. Permana, N. Takaki, and H. Sekimoto, "Preliminary study on feasibility of large and small water cooled thorium breeder reactor in equilibrium states," *Prog. Nucl. Energy*, vol. 50, no. 2–6, pp. 320–324, Mar. 2008.

[171] A. Talamo, "A novel concept of QUADRISO particles. Part II: Utilization for excess reactivity control," *Nucl. Eng. Des.*, vol. 240, no. 7, pp. 1919–1927, 2010.

[172] C. K. Jo, Y. Kim, and J. M. Noh, "Burnable poison for reactivity management in a very high temperature reactor," *Ann. Nucl. Energy*, vol. 36, no. 3, pp. 298–304, 2009.

[173] A. Talamo, "A novel concept of QUADRISO particles Part I: Transmutation of Neptunium and Plutonium,"

Ann. Nucl. Energy, vol. 35, no. 10, pp. 1944–1953, Oct. 2008.

[174] A. Talamo, "Conceptual design of QUADRISO particles with europium burnable absorber in HTRs," 2010.

[175] H. N. Tran, Y. Kato, and Y. Muto, "Optimization of burnable poison loading for HTGR cores with OTTO refueling," *Nucl. Sci. Eng.*, vol. 158, no. 3, pp. 264–271, 2008.

[176] H. N. Tran and Y. Kato, "An optimal loading principle of burnable poisons for an OTTO refueling scheme in pebble bed HTGR cores," *Nucl. Eng. Des.*, vol. 239, no. 11, pp. 2357–2364, 2009.

[177] W. Chunlin, Z. Jing, Z. Jian, and X. Bing, "Study of the effect of burnable poison particles applying in a pebble bed HTR," in *Proceedings of the HTR 2014*, 2014, pp. 1–4.

[178] H. N. Tran and V. K. Hoang, "Neutronic characteristics of an OTTO refueling PBMR," *Nucl. Eng. Des.*, vol. 253, pp. 269–276, 2012.

[179] J. Washington, J. King, and Z. Shayer, "Selection and evaluation of potential burnable absorbers incorporated into modified TRISO particles," *Nucl. Eng. Des.*, vol. 278, pp. 377–386, 2014.

[180] M. Tchonang Pokaha and D. E. Serfontein, "Different techniques for reducing DLOFC fuel temperatures in a PBMR-DPP-400 core," *Nucl. Eng. Des.*, vol. 335, no. January, pp. 210–218, 2018.

[181] A. Talamo, "Effects of the burnable poison heterogeneity on the long term control of excess of reactivity," *Ann. Nucl. Energy*, vol. 33, no. 9, pp. 794–803, 2006.

[182] T. Obara and T. Onoe, "Flattening of burnup reactivity in long-life prismatic HTGR by particle type burnable poisons," *Ann. Nucl. Energy*, vol. 57, pp. 216–220, 2013.

[183] R. A. Khrais, G. V. Tikhomirov, I. S. Saldikov, and A. D. Smirnov, "Neutronic analysis of VVER-1000 fuel assembly with different types of burnable absorbers using Monte-Carlo code Serpent," *J. Phys. Conf. Ser.*, vol. 1189, no. 1, 2019.

[184] J. Wang *et al.*, "Multiobjective genetic algorithm strategies for burnable poison design of pressurized water reactor," *Int. J. Energy Res.*, vol. 45, no. 8, pp. 11930–11942, Jun. 2021.

Résumé

Les bibliothèques de données nucléaires fiables et la durabilité de l'énergie nucléaire, avec l'évacuation des stocks de croissance en monde tel que les déchets radioactifs et les matières nucléaires de qualité militaire en excès, sont les deux défis les plus actuels auxquels fait face la recherche en ingénierie nucléaire. Par conséquent, cette thèse est divisée en deux grandes parties : la première partie concentrée sur le traitement des bibliothèques de sections efficace en utilisant des évaluations de données nucléaires base sur les bibliothèques ENDF/B et JEFF et traitées par les systèmes de codes NJOY et NECP-Atlas. Les bibliothèques traitées ont été validées à l'aide d'expériences incluses dont le guide ICSBEP puis par rapport à d'autres expériences consolidées telles que les benchmarks d'effet Doppler qui sont basées sur des cellules de réacteur PWR (élargissement doppler dans le combustible) et de blindage Oktavian. Une fois les bibliothèques développées, les analyses préliminaires ont été effectuées sur le réacteur TRIGA afin d'évaluer les paramètres-clés de réacteur (le facteur de multiplication effective des neutrons, la fraction effective de neutrons retardés, le temps effectif de génération de neutrons, les coefficients de sûreté…etc.). La deuxième partie de cette thèse examine les potentiels combustibles à base de thorium avec divers isotopes 'driver' pour les intégrer dans l'une des conceptions les plus prometteuses des réacteurs, le réacteur à lit de boulets refroidi par gaz (HTR) basé sur les particules TRISO, pour identifier les mélanges potentiels et pour analyser leurs performances neutroniques et physiques. Les combustibles évalués dans cette thèse incluent le combustible à dioxyde de thorium mélangé avec l'uranium faiblement enrichi à dosage élevé (High-Assay Low-Enriched Uranium), le plutonium issu du recyclage de combustible de réacteur utilise, le plutonium issu de combustible militaire et U-233. De plus, tous les paramètres ont été évalués en utilisant nos bibliothèques générées. Enfin, dans cette thèse, les nouvelles méthodes de contrôle de réactivité pour le combustible (Th,^{233}U)O_2 ont été proposées en utilisant les absorbeurs consommables incorporés dans TRISO/QUADRISO afin de disposer d'une anti-réactivité neutronique au début de cycle, de réduire l'excédent de réactivité et d'augmenter les longueurs de cycle de fonctionnement.

Mots- clés : Codes de traitement nucléaires, Bibliothèques données nucléaires, Benchmarks, Réacteur TRIGA, Combustibles à base de thorium, Réacteur HTR.

Abstract

Reliable nuclear data libraries and the sustainability of nuclear energy, with the disposal of the world's growth stocks as radioactive waste or surplus weapons material, are two of the most current challenges facing nuclear engineering research. Hence, this thesis is divided into two major parts: the first part deals with neutron cross-section libraries using state-of-the-art nuclear data evaluations (ENDF/B and JEFF) processed by the NJOY and NECP-Atlas code systems. The processed libraries have been validated using integral experiments from the ICSBEP Handbook and expansively validated against other consolidated experiments such as Oktavian shielding and the Doppler reactivity defect benchmarks. Once libraries were developed, preliminary analyses were carried out for the TRIGA reactor to estimate the reactor key parameters (effective neutron multiplication factor, effective delayed neutron fraction, effective neutron generation time, safety coefficients …). The second part of this thesis examines potential thorium-based fuels with various 'driver' isotopes in one of the most promising reactor designs, the high-temperature pebble-bed reactor (HTR) based on TRISO coating particles, to identify the potential mixtures and to analyze their physical performance. The fuels evaluated in this thesis include thoria fuel mixed with High-Assay Low Enriched Uranium, reactor-grade plutonium, weapon-grade plutonium and U-233. Moreover, all parameters were evaluated using our generated libraries. Additionally, in this thesis, new reactivity control methods for the (Th,^{233}U)O2 fuel were proposed using burnable absorbers incorporated into TRISO/QUADRISO to enhance de discharge burnup in this type of reactor.

Key Words: Processing codes, libraries, Benchmarks, TRIGA reactor, thorium-based fuels, HTR Reactor